Molecular control of charge recombination dynamics in dye sensitised solar cells

Narukuni Hirata

Submitted to the University of London in partial fulfilment
for the degree of Doctor of Philosophy

2005

Centre for Electronic Materials and Devices
Department of Chemistry
Imperial College London

Abstract

Dye sensitised solar cells (DSSCs) have attracted extensive research over the last decade because of their potential for low cost production. However, fundamental studies aimed at direct practical application of the devices have been relatively limited to date. In the work presented in this thesis, fundamental studies based upon transient absorption spectroscopy (TAS) are employed to address the potential of a range of novel molecular materials for practical device development. These studies of charge transfer dynamics for novel molecular dyes and hole transport materials in DSSCs have revealed some key issues about controlling these kinetics for efficient energy conversion.

This thesis was divided into two parts; research on liquid electrolyte and solid state dye sensitised solar cells. In the first part, a range of dyes have been studied, including not only analogues of the established dye, $Ru(dcbpy)_2(NCS)_2$, but also alternative dyes such as Platinum complexes. Such studies have in particular focused on lengthening the distance between injected electrons and the dye cations in order to slow interfacial charge recombination. Of particular interest, it was shown that a supermolecular analogue of the $Ru(dcbpy)_2(NCS)_2$ which included the addition of a secondary electron donor moiety, tri-methoxy phenyl amine, showed the longest-lived charge-separated state reported to date, with decay half time of 0.7 s.

Research on solid cells has concentrated on both polymer electrolyte and molecular hole conductors, including a range of novel materials supplied by both industrial and academic partners. For the polymer electrolyte devices, it was determined that kinetic competition between charge recombination and dye cation re-reduction was critical in limiting device efficiency. In contrast, for molecular hole conductor, electron recombination with the holes in the HTMs was found to be of primary concern. A range of strategies were employed to address this issue. In particular a charge transfer cascade was developed based upon a bi-layer of two hole conductors differing in ionization potential resulting in a significant retardation of interfacial charge recombination.

Acknowledgements

The author would like to thank Prof. James R Durrant for his guidance throughout my PhD studies and also thank Dr Emilio Palomares, Dr Saif A Haque and Dr Jessica E Kroeze for useful discussions. Financial support from Bridgestone Corporation is grateful acknowledged. Thanks go to Prof Michael Grätzel group at EPFL, Prof Andrew B Holmes group at the University of Melbourne, Prof Neil Robertson group at the University of Edinburgh and the Energy Research Centre of the Netherlands (ECN) for the supply of materials. The author is also grateful to all co-workers in James R Durrant group.

Contents

Abstract 2

Acknowledgements 3

Contents 4

List of figures, schemes and tables 8

Abbreviations 18

1. Introduction 20

1.1 The Need of alternative energy sources to fossil fuels 20

1.2 The dye sensitized solar cells 22

1.2.1 Overview of DSSCs 22

1.2.2 Comparison with silicon solar cells 27

1.2.3 Features of DSSCs 28

1.2.4 Improvement of solar cell performance 31

1.3 This Thesis 33

1.4 References 35

2. Experimental 40

2.1 Sample preparation 40

2.1.1 Preparation of nanocrystalline TiO_2 films 40

2.1.1.1 Preparation of TiO_2 colloidal paste 40

2.1.1.2 Deposition of TiO_2 on glass substrates 42

2.1.1.3 Film sintering 43

2.1.2 Dye sensitisation 45

2.1.2.1 Preparation of sensitising solution 45

2.1.2.2 The sensitisation procedure 45

2.1.2.3 Calculation of dye coverage 46

2.1.2.4 Storage of sensitised films 47

2.1.3 Fabrication of dye-sensitised solar cells 47

2.2 Transient absorption spectroscopy 50

2.2.1 Principle 50

2.2.2 Apparatus 50

2.2.3 Calculation of ΔOD 52

2.2.4 Comparison with other apparatus 53

2.2.5 Types of experiments 54

2.3 Other Experimental Techniques 55

2.3.1 Steady state UV / visible absorption spectroscopy 55

2.3.2 Photocurrent measurements under AM 1.5 solar simulation 55

2.4 References 57

3. Electron transfer reactions on ruthenium based molecular dyes with different protonation degree 58

3.1 Introduction 58

3.2 Experimental 62

3.3 Results with same dye loading 63

3.4 Results under varied dye loading condition 66

3.5 Discussion 70

3.5.1 Influence of dye loading upon proton content 70

3.5.2 Correlation between TAS and I/V data 70

3.6 References 74

4. Supermolecular sensitisation of nanocrystalline TiO_2 films 76

4.1 Introduction 76

4.2 Experimental 79

4.3 Results and discussion 80

4.3.1 Semiempirical calculations 80

4.3.2 Transient absorption study 82

4.3.2.1 Recombination dynamics 82

4.3.2.2 Assignment of dye cation 83

4.3.2.3 Electron injection yield 84

4.3.2.4 Monoexponential decay 84

4.4 Conclusion 86

4.5 References 87

5. Optimisation of sensitiser function in dye sensitised solar cells 92

5.1 Introduction 92

5.2 Characterisation of a series of ruthenium complexes with long alkyl chains 94

5.2.1 Introduction 94

5.2.2 Experimental 96

5.2.3 Results 98

5.2.3 Discussion 103

5.3 Characterisation of a series of ruthenium complexes with unsaturated side chains 106

5.3.1 Introduction 106

5.3.2 Experimental 108

5.3.3 Results 109

5.3.4 Discussion 112

5.4 Characterisation of a series of platinum complexes 114

5.4.1 Introduction 114

5.4.2 Experimental 115

5.4.3 Results and Discussion 116

5.4.3.1 Sensitization of nanocrystalline TiO_2 films 116

5.4.3.2 Device optimization and comparison with Ruthenium complex (dye **2**) 121

5.4.3.3 Conclusions 123

5.5 References 124

6. Parameters influencing charge separation in solid-state dye sensitized solar cells using novel hole conductors 128

6.1 Introduction 128

6.2 Experimental 133

6.3 Results and discussion 134

6.3.1 Recombination dynamics 134

6.3.2 Hole transfer yield 135
6.3.3 Effect of additives and $\Delta G_{dye\text{-}HTM}$ 139
6.3.4 Device characterization 141
6.4 Conclusions 143
6.5 References 144

7. Interface engineering for solid-state dye sensitised nanocrystalline solar cells: the use of an organic redox cascade 147
7.1 Introduction 147
7.2 Experimental 151
7.2.1 Materials 151
7.2.2 Experimental procedures 152
7.2.2.1 CV measurements of P1 through P4 152
7.2.2.2 Sample fabrication 152
7.3 Results and discussion 153
7.4 Conclusion 156
7.5 References 157

8. Kinetic competition in flexible dye sensitised solar cells employing a series of polymer electrolytes 159
8.1 Introduction 159
8.2 Experimental 161
8.3 Results and discussion 162
8.4 Conclusion 167
8.5 References 168

9. General conclusions and future work 171

List of figures and schemes and tables

Chapter 1 Introduction

Figure 1.1 22

The schematic illustration of the structure of DSSCs

Figure 1.2 23

A schematic representation of the key reactions contributing to photocurrent in the dye sensitised solar cell.

Figure 1.3 25

Diagram depicting the reactions occurring at the TiO_2 / dye / redox couple interface

Figure 1.4 29

The molecular structures of two different sensitiser dyes and Incident Photon to Current Efficiency (IPCE) spectra for DSSCs employed nanocrystalline TiO_2 films sensitised with those dyes.

Figure 1.5 30

Charge transfer processes between the $RuL_2(NCS)_2$ dye and the TiO_2 lattice

Figure 1.6 31

A summary of the kinetics of the DSSC

Chapter 2 Experimental

Figure 2.1 41

High Resolution Transmission Spectroscopy image of two nanoparticles of TiO_2 before autoclaving the sol-gel solution

Figure 2.2 43

"Doctor blade" technique of preparing nanocrystalline TiO_2 films.

Table 2.1 44

Characteristics of both IC and ECN35

Figure 2.3 45

SEM picture of the surface of a ~5 μm thick nanocrystalline TiO_2 film made from IC paste (a) and ECN35 paste (b)

Figure 2.4 49

Schematic structure of a dye-sensitised solar cell

Figure 2.5 51

The microsecond to millisecond transient absorption system

Figure 2.6 55

Current-voltage characteristics for a nanocrystalline TiO_2 dye-sensitised solar cell under simulated AM 1.5 solar radiation

Chapter 3 Electron transfer reactions on ruthenium based molecular dyes with different protonation degree

Figure 3.1 58

Plot of conduction band energetics of nanocrystalline TiO_2 as a function of pH the electrolyte composition, in agreement with a Nernstein shift (reproduced from [1]).

Figure 3.2 60

Chemical structures for dye **1** $[Ru(dcbpyH_2)_2(NCS)_2]$, dye **2** $(Bu_4N)_2[Ru(dcbpyH)_2(NCS)_2]$, and dye **3** $(Bu_4N)_4[Ru(dcbpyH)_2(NCS)_2]$.

Figure 3.3 61

Device performance for the dye series reported by Nazeeruddin, showing that that the photovoltage is improved as the dye proton content reduces, while the photocurrent is decreased.

Figure 3.4 63

Uv-Visible measurements for nanoporous TiO_2 sensitised samples a) dye **1**, fully protonated dye, b) dye **2**, partially protonated dye and c) dye **3**, non-protonated dye.

Figure 3.5 64

IV-characterization for dye **1**, dye **2** and dye **3** with efficiencies (η) of 1.9 %, 2.2 %, and 2.5 % respectively under AM1.5 one sun illumination.

Figure 3.6 65

Transient absorption data monitoring photoinduced absorption of the dye cation. All data were collected under conditions of excitation at 550 nm and detection at 800 nm.

Figure 3.7 66

Adsorption maxima for dye **1** (bold line), dye **2** (thin line) and dye **3** (dashed line) as a function of sensitizing time in the dye solution at 23 °C.

Figure 3.8 68

IV characterizations for the cells sensitised by dye **1** (bold line), dye **2** (thin line) and dye **3** (dashed line) as a function of dye loadings, as monitored by film absorbance at 525, 530 and 531 nm respectively, showing the effect of dye loading upon device performance.

Figure 3.9 69

ΔOD for nanocrystalline TiO_2 films sensitised by dye **1** (bold line), dye **2** (thin line) and dye **3** (dashed line), monitoring at 800 nm in 1 μs after excitation at 550 nm

Figure 3.10 69

The half-time of decay for nanocrystalline TiO_2 films sensitised by dye **1** (bold line), dye **2** (thin line) and dye **3** (dashed line), monitored at 800 nm after excitation at 550 nm

Figure 3.11 72

Schematic picture regarding the electron recombination dynamics at the condition of lower dye coverage (a), at optimal dye layer coverage (OD_{opt}) (b) and at higher dye coverages, OD > OD_{opt} (c), showing faster dynamics due to lateral diffusion of dye cations.

Chapter 4 Supermolecular sensitisation of nanocrystalline TiO_2 films

Scheme 4.1 78

Schematic representation of electron-transfer (ET) processes in dye-sensitised solar cells showing photogeneration of the dye excited state

Figure 4.1 78

Chemical structure of [RuLL'$(NCS)_2$] (dye **4**), showing a secondary electron-donor moiety.

Figure 4.2 80

Comparison of bond (black) distances and angles (red) calculated using ZINDO/1 for the cation state of dye **2** with the corresponding experimental X-ray data [15]. The values in parentheses correspond to the X-ray data.

Table 4.1 81

Comparison of bond lengths (Å) and angles (^{0}) of crystallographic data for cis-$Ru(L)_2$ ($NCS)_2$ with ZINDO/1-optimized geometries for the cation states of dye **2** and dye **4**.

Figure 4.3 81

Graphical representation of the HOMOs of a) dye **2** and b) dye **4**.

Figure 4.4 82

Transient absorption data monitoring charge-recombination dynamics for TiO_2 films sensitised with dye **2** (black trace) and dye **4** (grey trace).

Figure 4.5 84

Transient absorption spectra shown in left hand side (4.5a) were collected for TiO_2 films sensitised with dye **4** monitored at 8 μs after excitation at 516 nm and the data shown in right hand side (4.5b) were for 4-(diphenylmaino) benzaldehyde (optical absorbance $\lambda_{410\ nm}$=0.35) monitored at 8 μs after excitation at 400 nm

Figure 4.6 87

Transient absorption data for dye **4** adsorbed on TiO_2 films, collected with the 650 nm optical probe (a), 700 nm (b), 750 nm (c) and 950 nm (d) respectively, after the 550 nm optical excitation.

Figure 4.7 88

Transient absorption data for dye **4** adsorbed on 4 μm thick nonporous TiO_2 films as a function of dye coverage. The data were collected under 516 nm optical excitation and 700 nm detection.

Figure 4.8 89

Transient absorption spectra of dye **4** on TiO_2 film under steady light illumination. The transient absorption spectra of dye **4** are shown at 10^{-6} s (filled circle) and at 10^{-4} s (open circle) after excitation at 550 nm.

Chapter 5 Optimisation of sensitiser function in dye sensitised solar cells

Figure 5.1 94

Chemical structure of $[Ru(H_2dcbpy)(mhdbpy)(NCS)_2]$ (where the ligands H_2dcbpy = 4,4'-dicarboxy-2,2'-bipyridine, mhdbpy = 4-methyl-4'-hexadecyl-2,2'-bipyridine)

Figure 5.2 96

Schematic diagram showing the different interfacial electron transfer processes: regeneration of the dye cation by electron transfer from the redox couple (*RG*)

Figure 5.3 97

Chemical structure of the four dyes employed, where R = CH_3 (dye **5.1**), n-C_6H_{13} (dye **5.2**), n-$C_{13}H_{27}$ (dye **5.3**), n-$C_{18}H_{37}$ (dye **5.4**).

Figure 5.4 98

UV-visible absorption spectra for nanocrystalline TiO_2 films sensitised with a series of dyes with different side chain lengths.

Figure 5.5 99

Overall cell performances both under AM1.5 one sun illumination (a) and under dark conditions (b)

Figure 5.6 100

A series of transient absorption data for nanocrystalline TiO_2 films sensitised with dyes **5.1-5.4** with different length of alkyl chain monitoring the dye cation absorption at 775 nm. In the figure (a), signal amplitude is corrected based on the densities of absorbed photons determined from sample optical densities. The data in Figure (b) were normalised for the same signal amplitudes at 10^{-6} s to compare the kinetics.

Figure 5.7 101

A series of transient absorption data for complete sandwich type cells employing sensitiser dyes with different length of alkyl chain lengths monitoring the injected electrons in TiO_2 at 1000 nm

Figure 5.8 102

Transient absorption data monitored at 775 nm for complete DSSC cells employing sensitiser dyes with different length of alkyl chains.

Figure 5.9 103

A plot of the half-time of the interfacial electron transfer reactions, *CR1*(circle), *CR2*(triangle) and *RG*(square), as a function of the alkyl chain length.

Figure 5.10 104

A plot of V_{oc} and I_{sc} for the dye series versus the alkyl chain length, showing the length of C_{13} resulted in the highest performance out of them, highly consistent with the TAS studies.

Figure 5.11 107

Chemical structure of a series of dyes, showing the dye **1** with no introduced side chain spacer, and dye **5.5**, dye **5.6**, dye **5.7** and dye **5.8** having vinyl, thiophene, vinyl thiophene, and vinyl phenyl groups as spacers between the pyridine group and carboxyl groups.

Table 5.1 107

Absorption maximum for the series of sensitizer dyes

Figure 5.12 109

UV-visible absorption spectra of the nanocrystalline TiO_2 films sensitised with a series of dyes with different spacers: dye **5.5** (red), dye **5.6** (green), dye **5.7** (blue), dye **5.8** (grey) and dye **1** (black).

Figure 5.13 110

Transient absorption data monitoring at 1000 nm after excitation at 540 nm for TiO_2 films sensitised with the dyes: dye **5.5** (red), **5.6** (green), **5.7** (blue) and **1** (black). The data are assigned to absorption of the injected electrons in the TiO_2 electrode.

Figure 5.14 113

A plot of initial amplitude of transient absorption for dye sensitised TiO_2 films taken from Figure 5.13(a), indicating the electron injection yield, as a function of HOMO-LUMO energy gap based on absorption in dye solution from Table 5.1.

Figure 5.15 115

Chemical structure of [Pt{X,X'$(CO_2H)_2$-2,2'-bipyridyl}(maleonitriledithiolate)] (X,X'=3,3'(pt**1**), 4,4'(pt**2**), or 5,5'(pt**3**))

Figure 5.16 116

UV-visible measurement for nonporous TiO_2 sensitized by pt**1** (black solid line), **2** (grey solid line) and **3** (black dashed line).

Table 5.2 117

Summary of UV/Vis spectroscopy results obtained for nanocrystalline TiO_2 films sensitised with pt1, pt 2 and pt 3.

Figure 5.17 118

Comparison of the difference absorption spectra of pt1 (black solid line), pt2 (grey solid line) and pt3 (black dashed line) on nanocrystalline TiO_2 film

Figure 5.18 119

Transient absorption data monitoring the charge recombination kinetics for 4 μm TiO_2 films sensitized with pt**1** (black) and pt**2** (grey). Experiments employed 550 nm excitation and all data were collected at 900 nm probe wavelength.

Figure 5.19 120

IV characterization for the liquid DSSC with pt**1** (black solid line), **2** (grey solid line) and **3** (black dashed line) under 1 sun AM1.5 light illumination

Figure 5.20 121

Comparison of cell performance obtained for DSSCs with sensitised pt**2** using electrolyte **A** (containing t-butyl pyridine (t-BP)) (black solid line) and electrolyte **B** (without t-butyl pyridine) (black dashed line). A cell employed the Ru dye **2** and electrolyte **A** was also measured as a control sample (grey solid line).

Figure 5.21 122

Comparison of transient absorption decays between the cell using electrolyte **A** (containing t-butyl pyridine (t-BP)) (a) and electrolyte **B** (without t-butyl pyridine) (b). A cell employed the dye **2** and electrolyte **A** was also measured as a control sample (c).

Chapter 6 Parameters influencing charge separation in solid-state dye sensitized solar cells using novel hole conductors

Figure 6.1 129

Schematic diagram of the charge-transfer processes occurring at the dye-sensitized nanocrystalline TiO_2/organic HTM heterojunction.

Table 6.1 132

Characteristics of the organic HTMs studied. Hole mobilities are FET mobilities.

Figure 6.2 134

Transient absorption data of the dye **2** / nanocrystalline TiO_2 films in the absence (black trace) and presence (grey trace) of HTM**1**, monitoring recombination dynamics at (a) 520 nm following 620 nm excitation, and (b) 800 nm following 530 nm excitation.

Figure 6.3 136

Schematic figure of the TAS measurements undertaken for quantitative determination of pore penetration. The excitation light is arriving at the front or back side of the sample.

Table 6.2 137

Hole transfer yields determined by probing the transient absorption of the dye cation at 800 nm upon front- and backside excitation at 530 nm.

Figure 6.4 138

Hole transfer yield as a function of the average molecular weight (M_w) of the hole conductor.

Figure 6.5 139

Schematic energetic diagram showing relationship between possible variation of the HOMO of dye **2** by additives and the HOMO level of the HTMs.

Table 6.3 141

Device parameters of solid-state dye-sensitized solar cells using different hole conductors.

Figure 6.6 142

Short-circuit current (I_{sc}) as a function of the hole transfer yield determined by using transient absorption spectroscopy.

Chapter 7 Interface engineering for solid-state dye sensitised nanocrystalline solar cells: the use of an organic redox cascade

Figure 7.1 148

Illustration of the organic redox cascade strategy addressed in this study to retard interfacial charge recombination.

Figure 7.2 149

Transient absorption data monitoring charge recombination dynamics of (a) a $RuL_2(NCS)_2$ sensitised TiO_2 film, (b) the same film covered in redox electrolyte and (c) the same film following addition of spiro-OMeTAD.

Figure 7.3 151

Chemical structures of the ion ligating hole transport polymers employed in this chapter and corresponding HOMO energy level determined by cyclic voltammetry.

Figure 7.4 153

Transient absorption data monitoring charge recombination dynamics of TiO_2 / dye / polymer / spiro-OMeTAD films as a function of polymer employed. Data collected in dark monitoring TiO_2 electron absorption at 1000 nm following optical excitation at 530 nm.

Figure 7.5 154

Recombination half times determined from transient absorption data such as that shown in Figure 5.4 as a function of polymer ionisation potential. Data shown with the inclusion (•) and omission (o) of lithium triflamide from the polymer dipping solution.

Figure 8.1 161

Chemical structure of the poly (epichlorohydrin-co-ethylene oxide) co polymers employed in this study

Figure 8.2 162

A comparison of the J-V characteristics of the typical flexible DSSCs using polymer redox electrolytes with EP-50, EP-16 and PEO in the dark (thin lines) and under 10 mW cm-2 AM1.5 simulated irradiation (bold lines).

Figure 8.3 163

Transient absorption for $Ru(dcpby)_2(NCS)_2$ sensitised TiO_2 films covered in polymer electrolytes with EP-50 (black) and EP-16 (grey). Data collected at a probe wavelength of 800nm, in the absence (a) or presence (b) of ~ 25 mW cm^{-2} of continuous white light irradiance.

Figure 8.4 165

I/V characteristics (solid lines) of the flexible DSSCs using polymer redox electrolytes with (a) EP-16 and (b) EP-50 as a function of irradiation intensity.

Abbreviations

Å	Angstrom (10^{-10} metre)
a.u.	Arbitrary units
Ag/AgCl	Silver / silver chloride electrode
Al_2O_3	Aluminium oxide
BET	Brunauer- Emmett-Teller analysis
CTRW	Continuous Time Random Walk model
ΔOD	Change in optical density
ΔG	Gibbs free energy difference
DAP	*N*,*N*-(di-*p*-anisylamino)phenoxymethyl
dcbpy	2,2'-bipyridyl-4,4'-dicarboxylate ligand
e^-	Electron
E_f	Fermi level
eV	Electron volt
ff	Fill factor
$h\nu$	Incident radiation
HOMO	Highest occupied molecular orbital
I_{sc}	Short circuit current
I^- / I_3^-	Iodide / triiodide redox couple
I_2	Iodine
IPCE	Incident photon to current conversion efficiency
λ	Reorganisation energy , also wavelength
LUMO	Lowest occupied molecular orbital
$LiClO_4$	Lithium perchlorate
LiI	Lithium iodide
MLCT	Metal-to-ligand charge-transfer
M, mM	Mole, mllimole
μs, ms	Microsecond, millisecond
μJ, mJ	Microjoule, millijoule
nm, μm	Nanometre, micrometre
n	TiO_2 electron density
PC	Propylene carbonate

r	TiO_2 - dye cation distance
SCE	Standard calomel electrode
SEM	Secondary electron microscopy / micrograph
SiO_2	Silicon oxide
SnO_2	Tin oxide
TEM	Transmission electron microscopy / micrograph
TiO_2	Titanium dioxide
$t_{50\%}$	Transient decay half-life
V and mV	Volt and millivolt
V_{oc}	Open circuit voltage
η	Overall cell efficiency

1

Introduction

1.1 The Need for alternative energy sources to fossil fuels

It is no exaggeration to state that most people living in developed countries live a life of pleasure bought continuously from the energy of fossil fuels, and in particular from oil. In addition to the obvious example of cars, it is easy to find products made from oil in our daily lives, such as in computers, clothes and houses. Approximately 5 million barrels of oil are consumed worldwide everyday [1]. As a result, we are now confronted by the serious environmental challenge of global warming, with estimates indicating global surface temperature have increased about 0.6°C (plus or minus 0.2°C) since the late-19th century [2]. Moreover, like all fossil fuels, oil is a finite resource and the potential exhaustion of oil reserves is providing further motivation for the development of alternative sustainable-energy sources to oil such as nuclear power, biomass and photovoltaic solar cells. The development and implementation of such alternative energy sources has now become one of the top priority issues for the world.

In terms of direct solar energy conversion, photovoltaic devices based upon crystalline silicon have dominated the field to date, due largely to their highly developed technological base. Energy conversion efficiencies of 21% have been reported for such devices, close to the theoretical thermodynamic maximum for single junction devices [3]. However, the relatively high cost of device production limits their suitability for widespread use. The function of silicon solar cells is based upon minority carrier transport, as photogenerated electrons and holes must move a significant distance through a high concentration of oppositely charged majority carriers without recombining. In order to minimise recombination losses in these

cells, it is therefore essential to keep impurities or defects in the crystal structure of the semiconductor to a minimum, resulting in requirement for relatively high purity and therefore high cost materials and production techniques. Attention is therefore increasingly focusing on alternative solar cell technologies. Of these, those fabricated from organic materials are of particular interest because of their potential merit of low cost production. Such devices include polymer-polymer [4-6], polymer-fullerene [7] and small organic molecule cells [8]. In addition to these all organic devices, photovoltaic devices based on dye sensitized nanocrystalline semiconductors, a system established by O'Regan and Grätzel in 1991, has attracted much attention in the renewable energy research area [9]. Such devices are called dye sensitized solar cells (DSSCs).

1.2 The dye sensitized solar cells

1.2.1 Overview of DSSCs

In the early 1990's at the laboratory of Prof. Michael Grätzel in EPFL (Laussane, Switzerland), the successful combination of efficient panchromatic dyes with high yields of electron injection and the extraordinary properties of high surface area transparent semiconductor electrodes allowed the development of a dye sensitised solar cell with an energy conversion efficiency exceeding 8% [9]. This important achievement initiated the development of a strong academic and industrial programme in the function and development of dye sensitised solar cells. Several recent reviews summarize this progress [10-13].

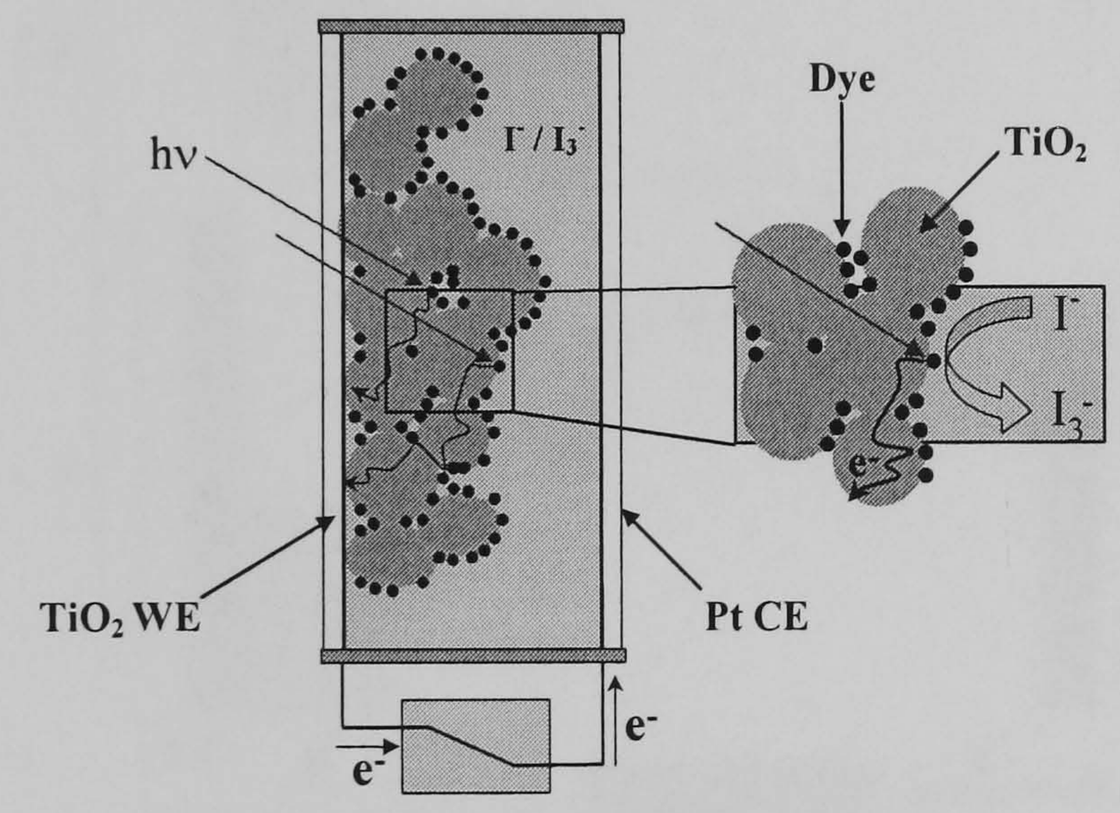


Figure 1.1 The schematic illustration of the structure of DSSCs

A typical DSSC comprises a dye sensitised, mesoporous, nanocrystalline titanium dioxide film interpenetrated by a liquid electrolyte containing I^-/I_3^- as a redox couple. A schematic structure of the DSSC, illustrating the the TiO_2 /dye/electrolyte interface is depicted in Figure 1.1. The following three steps summarise the key elements of device function: (i) Visible light is absorbed by the sensitiser dye (*e.g.*: $RuL_2(NCS)_2$, where L represents 4,4'-dicarboxy-2,2'-bipyridyl throughout this thesis). (ii) Electron injection from the excited state of the dye into the conduction band of the TiO_2 (referred to as *INJ* in this thesis) is followed by the subsequent regeneration of the dye ground state by the I^-/I_3^- redox couple (referred to as *RG* in

this thesis). (iii) Under illumination the cell produces voltage and a current through an external load connected to the electrodes.

More details are explained below. Figure 1.2 shows a schematic representation of the processes occurring in the dye sensitised solar cell which contribute to the generation of photocurrent. The energy levels of the various components of the dye sensitised solar cell are designed to allow electron migration through the device in the direction indicated in this diagram.

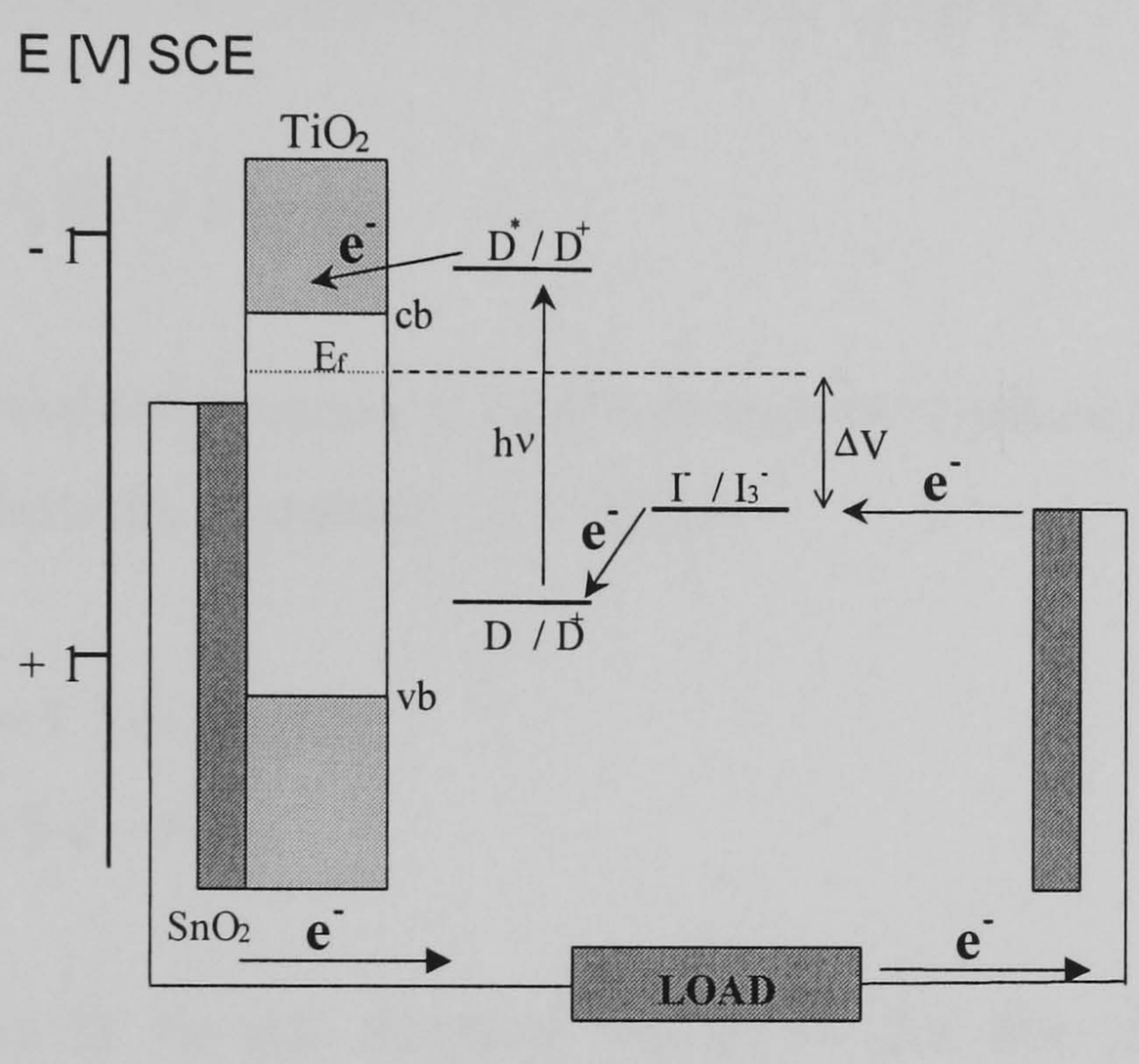


Figure 1.2 A schematic representation of the key reactions contributing to photocurrent in the dye sensitised solar cell.

The operation of the dye sensitised solar cell is initiated by the absorption of light at the working electrode. The monolayer of dye on the TiO_2 film intercepts photons of solar radiation. Light absorption results in generation of dye molecule excited states (Equation 1.1), which inject electrons into the conduction band (cb) of the TiO_2 (*INJ*) (Equation 1.2):

$$D + h\nu \rightarrow D^* \qquad (1.1)$$

$$D^{*} \rightarrow e^{-}_{TiO2} + D^{+} \qquad (1.2)$$

The injected electrons travel across the metal oxide film to the conducting glass where they are collected and pass through an external circuit where they can perform work. Hence, in contrast to the conventional *p-n* junction, the dye sensitised solar cells separates out the functions of light absorption (dye) and charge transport (TiO_2).

The dye cations that result following electron injection into the TiO_2 are reduced by the redox couple (*RG*) (Equation 1.3) [14]:

$$D^{+} + 2I^{-} \rightarrow D + I_2^{-} \qquad (1.3)$$

This oxidised redox couple is itself subsequently reduced by electrons at the platinum counter electrode (Equation 1.4, 1.5) [15].

$$I_2^{-} \rightarrow I^{-} + I_3^{-} \qquad (1.4)$$

$$I_3^{-} + 2\,e^{-} \rightarrow 3I^{-} \qquad (1.5)$$

There is no net chemical change in the dye sensitised solar cell during operation. Equations 1.1 to 1.5 show the reactions which contribute to photocurrent in the solar cell and these represent one cycle or turnover of the device. For the dye sensitised solar cell to be a viable means of producing electrical energy, this cycle needs to be repeated many times. Studies by Grätzel et al. [16] employing cells fabricated from $RuL_2(NCS)_2$ sensitised TiO_2 have shown these devices to produce a high number of turnovers (at least 10^7 cycles measured) without significant loss of performance or degradation of the sensitiser dye.

The maximum photovoltage obtainable from this device is defined as the Gibbs free energy difference between the quasi-Fermi level (E_f) of the TiO_2 under illumination and the chemical potential of the redox couple in the electrolyte.

As mentioned, Equations 1.1 to 1.5 show the reactions in the dye sensitised solar cell which are responsible for the production of photocurrent. However, there are many other reactions in the solar cell which can occur but are non-beneficial to cell performance. These other reactions are the loss pathways within the cell. They include the loss of dye excited states through radiative and non-radiative decay. Other important loss mechanisms include the loss of injected electrons in the TiO_2 through recombining with *either* dye cations (charge recombination 1, referred to as *CR1* in this thesis) *or* the oxidised form of the redox couple (also called the "dark reaction", referred to as *CR2* in this thesis). These reactions all occur at the TiO_2 / dye / redox species interface and are summarised in the Figure 1.3 below.

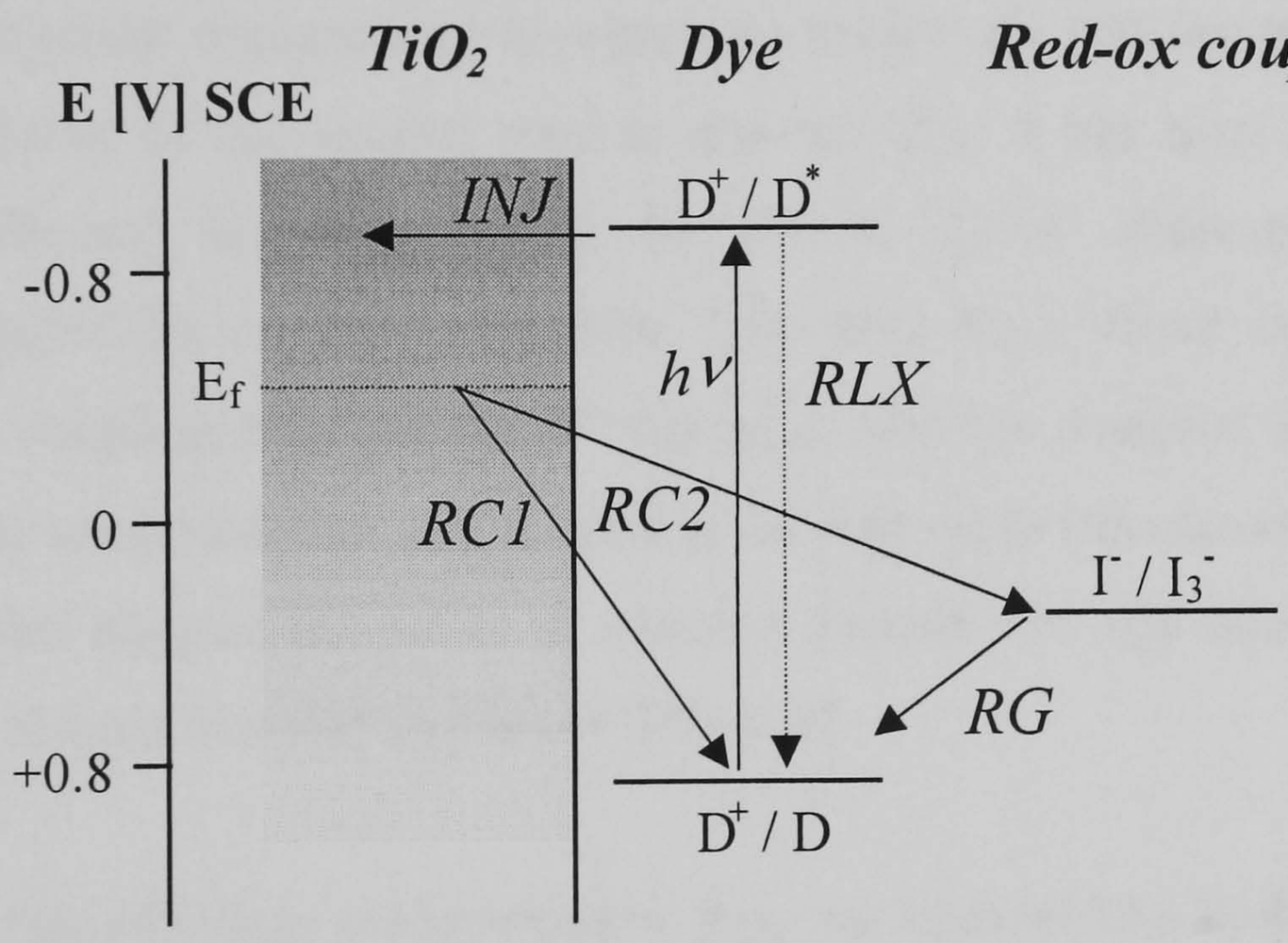


Figure 1.3 Diagram depicting the reactions occurring at the TiO_2 / dye / redox couple interface where process *INJ* represents the injection of electrons into TiO_2 by dye excited states, process *RG* represents the dye regeneration reaction by the redox couple, process *CR1* represents the charge recombination of injected electrons in TiO_2 with dye cations, process *CR2* represents the recombination or "dark reaction" between injected electrons in TiO_2 with the oxidised form of the redox couple, and process *RLX* represents the sum of radiationless and non-radiationless relaxation of dye excited states.

The kinetics of the reactions in Figure 1.3 are critical to the performance of the dye sensitised solar cell. Electron injection process (*INJ*) must to be faster than decay of the excited state to ground (*RLX*) to avoid the loss of dye excited states and allow electron injection into TiO_2 to occur with a high yield. Rates measured for the loss of dye excited states are generally quite rapid, with the decay half time of the range from 10^{-8} to 10^{-10} s^{-1}. Rather fortunately, the electron injection dynamics can be an extremely fast. It is now generally accepted that this reaction is one of the fastest chemical processes known to date, occurring in the femtosecond time region [17-19]. Furthermore, previous studies carried out in the Durrant group suggest that injection kinetics are only weakly sensitive to variations in experimental conditions, e.g. electrolyte composition, application of external bias to TiO_2, showing that the electron injection dynamics in an optimum device are just fast enough to compete with the decay of the excited state to ground [20]. It has been suggested that the highly efficient injection yields (> 90 % [17]) observed with the dye $Ru(dcbpy)_2(NCS)_2$ on nanocrystalline TiO_2 may be a direct consequence of the electronic coupling between the π^* orbital of the dye complex and the conduction band of the semiconductor (a manifold of 3d orbitals in the case of TiO_2). However, some studies suggest that efficient electron transfer can still occur from sensitisers which are remote from the surface of TiO_2 [21].

The rate of charge recombination, k_{CRI} has been widely studied in recent times. There are, however, great disparities regarding the measured rates for this reaction, ranging from hundreds of nanoseconds to tens of milliseconds [22-25]. What is clear is that electron recombination dynamics (*CR1*) is many orders of magnitude slower than the electron injection dynamics (*INJ*). Several reasons have been proposed for this, including the driving force for k_{cr1} being large enough to lie in the Marcus inverted region [22]. Other studies have shown millisecond charge recombination [25, 26] and have focused on the trapping of electrons in intra band gap defect states in the TiO_2 electrode [26, 27] to explain the extremely slow charge recombination kinetics routinely observed. In these investigations, k_{CRI} was found to be very sensitive to variations in applied bias to the TiO_2 electrode [25], and hence electron

occupancy of these trap states, with k_{CR1} accelerating by up to 10^9 as increasingly negative bias is applied to the TiO_2 electrode.

It is also crucial for high solar cell efficiencies that the regeneration reaction, *RG*, competes favourably with the electron recombination with the dye cation (*CR1*). Previous studies employing liquid state dye sensitised solar cells indicate that this is indeed the case for efficient sensitisers such as $Ru(L)_2(NCS)_2$ [14, 28, 29], with the regeneration reaction (*RG*) competing favourably with the recombination with the dye cation (*CR1*), even when a bias close to the maximum cell voltage (V_{oc}) is applied to the TiO_2 and the process (*CR1*) has accelerated by up to 1000 times [14].

The final reaction to be discussed, the dark reaction between electrons in TiO_2 and the oxidised form of the redox couple (*CR2*) is believed to be the principle loss reaction limiting cell voltages in liquid state dye sensitised solar cells [30, 31]. The advantage of the high surface area of nanocrystalline TiO_2 electrodes for dye adsorption also causes the complication of an extremely high contact area between the semiconductor and electrolyte. Leakage of electrons in TiO_2 into the electrolyte needs to be minimised for optimal cell performances, an issue returned to repeatedly within this thesis.

1.2.2 Comparison with silicon solar cells

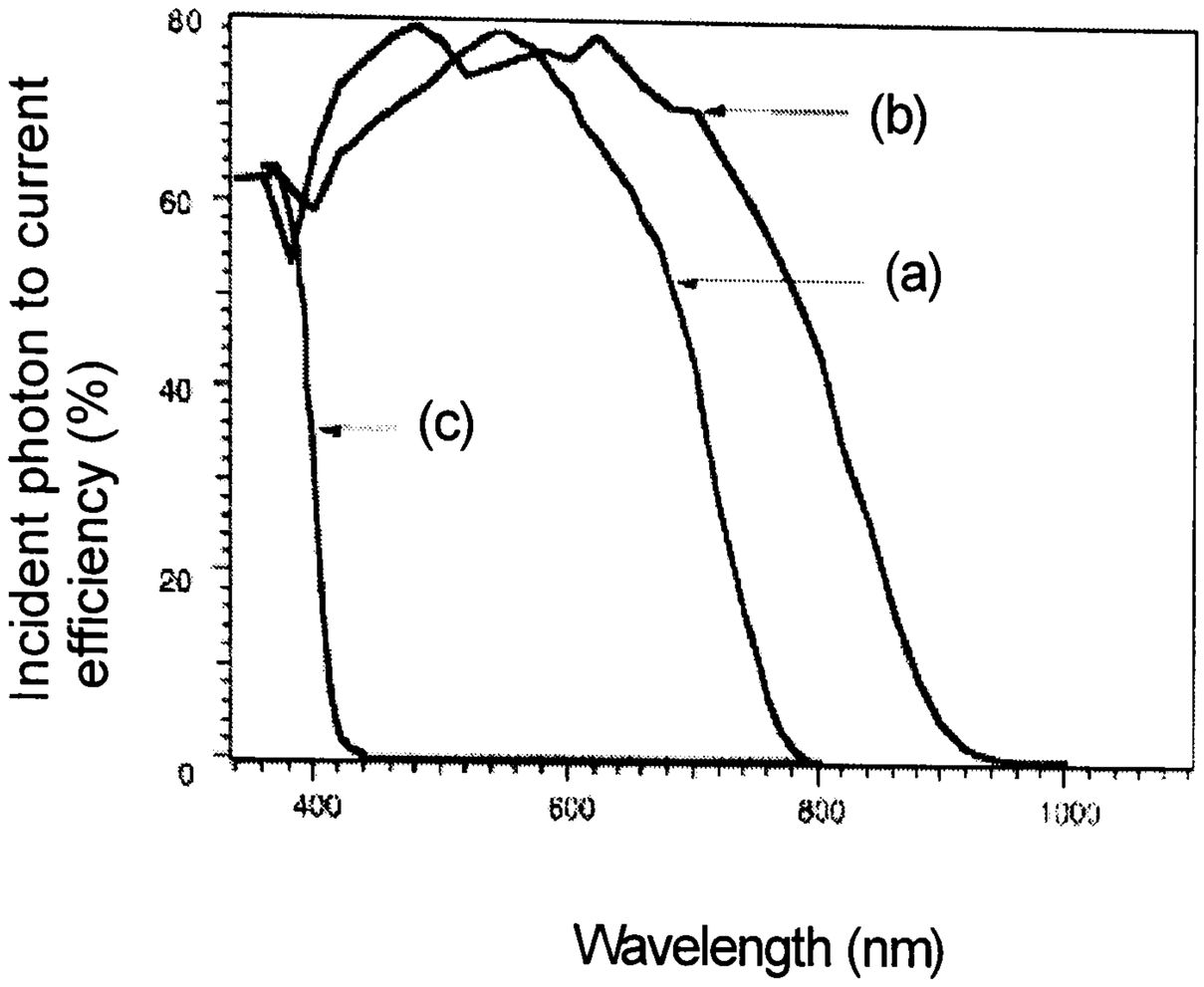
To optimize device performance not only each component material of DSSCs has been studied but also fabrication and construction issues such as a better sealing system. The research based on dye sensitised nanocrystalline semiconductors has grown very fast during the last 10 years, resulting in over 10% device efficiencies being reported. [10] The operating system of the DSSC has already been explained above and the device fabrication will be detailed in Chapter 2. However, at this point I shall focus on the differences in the operation between the DSSCs and the traditional semiconductor pn-junction solar cells for the better understanding of the experimental data explained in this thesis. Two of those differences are detailed below:

1) Contrary to the silicon solar cells, where light absorption, charge separation and charge transport occurs in the same material, the DSSC separate these functions: photons are absorbed by the dye molecules and the transport of charges is carried out in the TiO_2 electrode (electrons) and by the electrolyte (holes).
2) In the semiconductor pn-juntion cells the generated opposite changes travel in the same material, while in the DSSC, electrons travel in the nanoporous TiO_2 and holes in the electrolyte.

These DSSC features addressed above lead to slower recombination process compared to silicon cells, resulting in high-purity materials not being necessary for DSSCs, and therefore in potentially lower fabrication costs. Moreover, one of the most outstanding differences between silicon solar cells and DSSC is the use of dye molecules as photon absorbers.

1.2.3 Features of DSSCs

Well-designed dye molecules are synthesised through organic/inorganic chemistry to extend the photon absorption from the visible to the near-IR spectral regions (panchromatic dyes). Figure 1.4 represents the molecular structures of two leading photosensitizers for DSSCs and their Incident Photon to Current Efficiency (IPCE) spectra. The adsorption onto the surface of the nanocrystalline TiO_2 particles takes place via anchoring groups attached to the dye molecule. Generally, those anchoring groups are carboxylic groups (COOH), attached to the pyridyl rings. It is generally accepted that the carboxylic groups form a covalent bond between the TiO_2 surface and the dye, donating a proton to the TiO_2 lattice. The calculated surface area occupied by one dye molecule $RuL_2(NCS)_2$ at the TiO_2 surface is estimated to be $1.65nm^2$ [30].



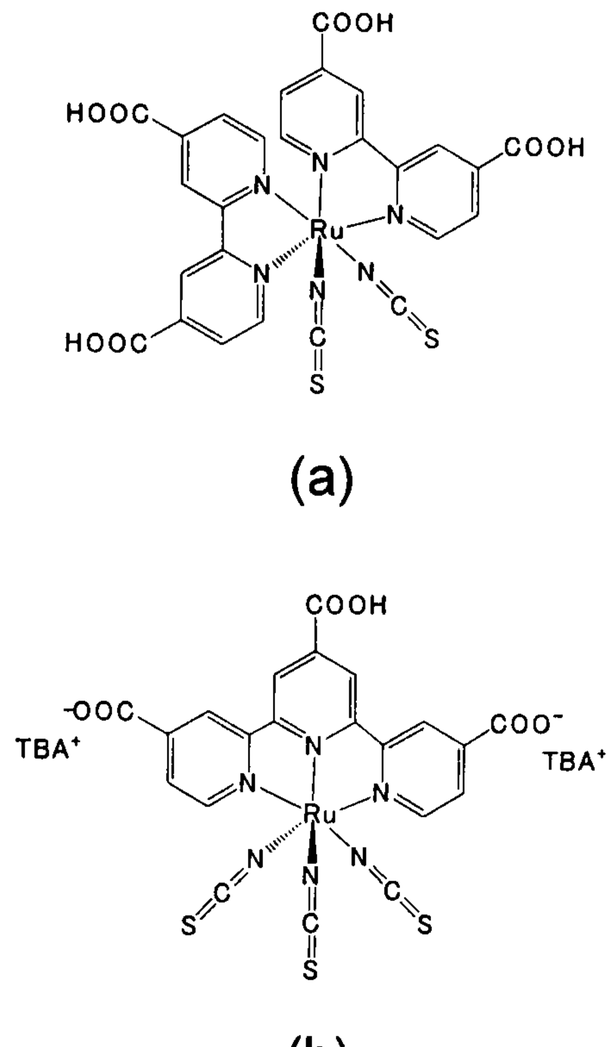


Figure 1.4 The molecular structures of two different sensitiser dyes and Incident Photon to Current Efficiency (IPCE) spectra for DSSCs employed nanocrystalline TiO_2 films sensitised with those dyes. Dye (a) is $RuL_2(NCS)_2$, where L represents 4,4'-dicarboxyl-2,2'-bipyridine (referred to as dye 1 in this thesis) and dye (b) is $(TBA)_3[Ru(Htcterpy)(NCS)_3]$, where tcterpy represents 4,4',4' '-tricarboxyl-2,2':6',2' '-terpyridine) and TBA represents tetra butyl amine. (c) is photocurrent for bare TiO_2 as a reference. Taken from ref [10].

As mentioned above, the fast electron injection process is one of the reasons for the success of these devices. It results from having high electronic coupling between the wavefunction of the LUMO (Lowest Unoccupied Molecular Orbital) of the dye and the conduction band of the TiO_2. Moreover, the HOMO (the Highest Occupied Molecular Orbital) of the dye is localized on the Ru-NCS ligand, making recombination with the oxidised dye more difficult for the injected electrons. Figure 1.5 illustrates the charge transfer processes taking place between the dye and the TiO_2

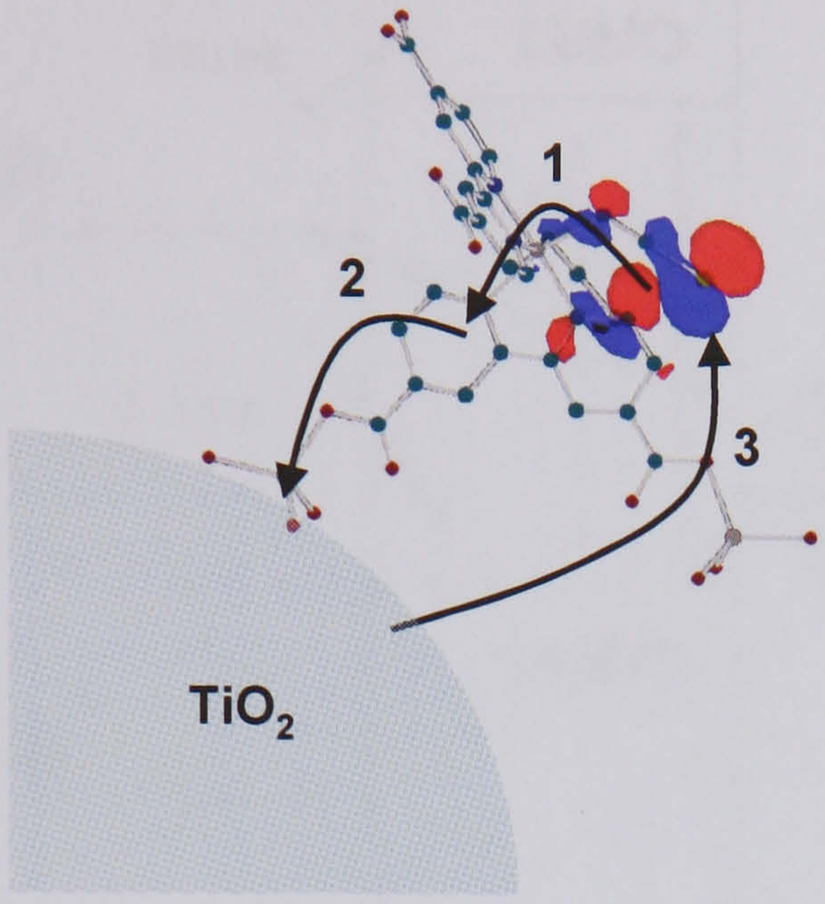


Figure 1.5 Charge transfer processes between the $RuL_2(NCS)_2$ dye and the TiO_2 lattice: (1) MLCT excitation, (2) Electron injection and (3) charge recombination. The Figure includes the semi empirical calculation of the HOMO orbital, adapted from ref [32].

The operation of the cell is an outcome of competing chemical reactions having different rate constants. A desired direction of the electrochemical reactions is achieved by fast wanted reactions (high rate constants) and slow unwanted reactions (low rate constants). The greater the difference between these rate constants, the higher the efficiency of the system is. Typical rates for these kinetics are summarized in Scheme 1.6. The interfacial electron transfer processes between the semiconductor/dye and the semiconductor/electrolyte interface will be the most important limiting factors for the DSSC device operation. Optimisation of these processes will increase device efficiency.

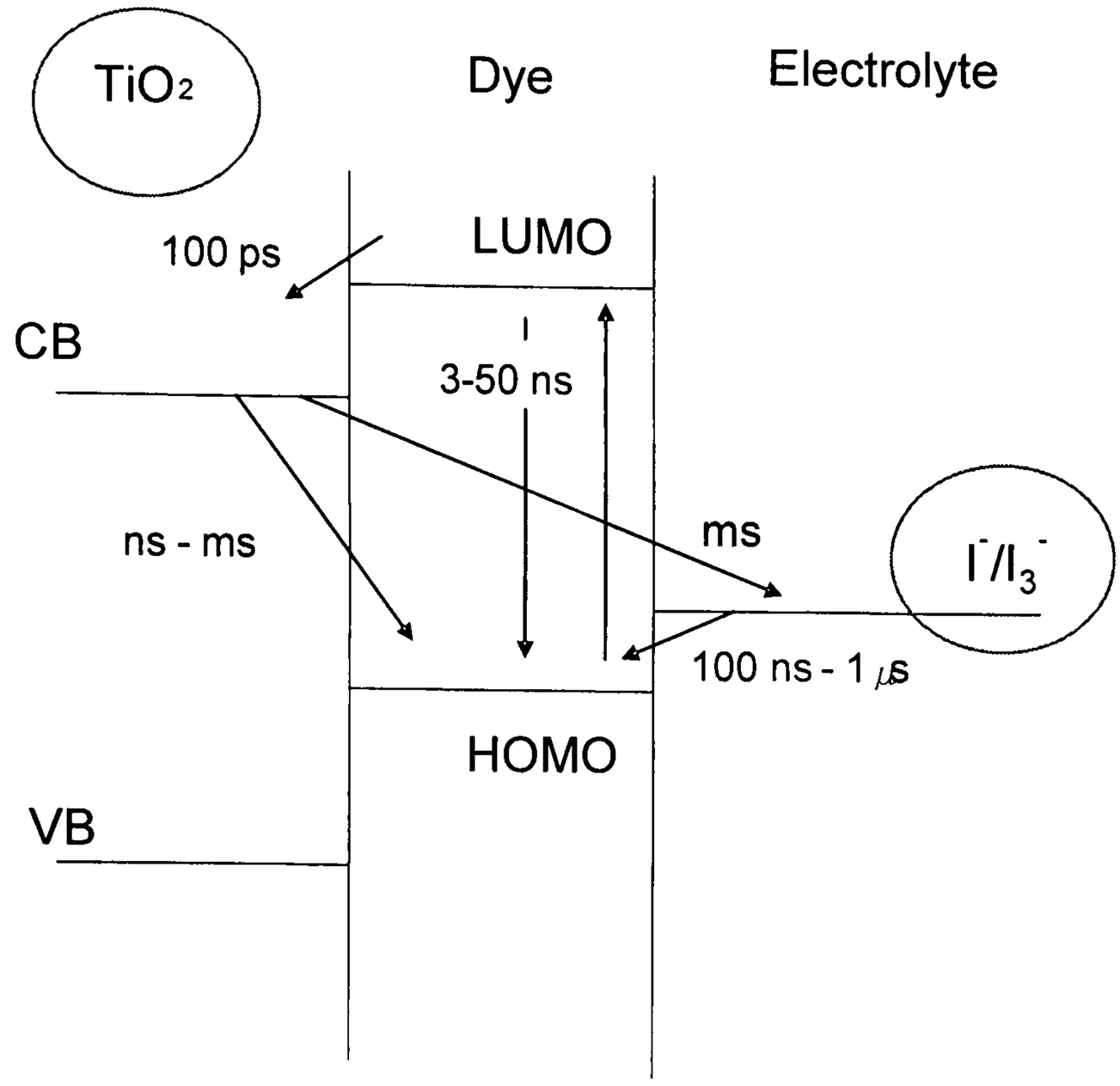


Figure 1.6 A summary of the kinetics of the DSSC. Electron injection dynamics from the excited state of the dye to the conduction band of TiO_2 has recently been found to be just fast enough to compete with excited state decay to ground [20]. Recombination dynamics have been observed to exhibit a dependency upon not only applied bias but also electrolyte composition [24, 25, 33]. Another desirable reaction, the regeneration of the electrolyte is also very fast (100 ns) in normal conditions [14].

1.2.4 Improvement of solar cell performance

Approaches to the improvement of efficiency of DSSC performance can be basically divided into two: (1) the development of light harvesting systems for stronger red / near infrared light absorption and (2) the development of more efficient electron transfer and transport processes leading to a reduction of recombination processes.

For the first issue, much research has focused on organic dyes such phthalocyanines which show intense absorption bands in the red and / or near IR

spectral region [ref]. Despite problems for such dyes with regard to aggregation and the unsuitable energetics of the dye LUMO level, which can be too low for electron transfer to the TiO_2 conduction band, Arakawa and co-workers have recently used coumarin and polyaniline type sensitizer to obtain solar to electric power conversion efficiencies of up to 7.7% [34, 35]. Other approaches include approaches to extending the spectral response of ruthenium bipyridyl dyes [36], the use of two sensitiser dyes [37] and quantum dot sensitisers [38].

For the second issue, efficient electron transfer and transport processes, a wide range of approaches have been employed, including modifications to the metal oxide film, electrolyte composition and dye structure. Several studies have, for example, investigated replacing the nanocrystalline TiO_2 substrate with ZnO [39], $SrTiO_3$ [40] or Nb_2O_5 [41] films in an attempt to improve conductivity. The influence of electrolyte composition upon charge transport has been studied for solid or quasi solid state DSSCs by optimisation of electrolyte viscosity and the selection of suitable hole transport materials [42-46]. Several studies have addressed the correlation between dye structure and interfacial dynamics [22, 47, 48], although quantitative determination of structure / function have been relatively limited to date.

1.3 This Thesis

The aim of my PhD studies has been to develop quantitative structure / function relationships which can lead to the further optimisation of DSSC performance. Experimentally my studies have focused on the use of transient absorption spectroscopy to interrogate interfacial electron transfer dynamics at the TiO_2 / dye / electrolyte interface, and the correlation of such dynamics with device current / voltage performance. The first half of my thesis (chapters 3-5) addresses sensitiser function in DSSC, employing both established sensitiser dyes and novel dyes synthesised by external research partners. The second half of my thesis focuses on the development on solid state alternatives to the liquid electrolyte in DSSC, employing both novel molecular and polymer hole transport materials (Chapters 6 and 7) and novel polymer electrolytes (chapter 8).

Chapter 2 details the experimental methodologies employed in my thesis studies.

Chapter 3 focuses upon the influence of protonation of the sensitiser dye upon device function. In this chapter, a series of ruthenium bipyrdyl dyes differing in their degree of protonation are studied by microsecond transient absorption studies, correlated with studies of device performance, as a function of dye loading on the nanocrystalline TiO_2 films. This study has been published in part in reference [49].

Chapter 4 presents a study of a supermolecular sensitizer dye encorporating a secondary electron donor ligand to retard interfacial recombination dynamics. Transient absorption studies of recombination dynamics are correlated with semi-empirical calculations of dye HOMO orbitals. Recombination dynamics with a 0.7 s half time are reported, the slowest dynamics reported to date for such dye sensitised films. The results reported in this chapter have been published in reference [32].

In chapter 5 a variety of novel dyes are studies with regard to their interfacial electron transfer dynamics. Three series of novel dyes are studied, including ruthenium bipyridyl and platinum diimine dithiolate dyes. Interfacial electron

transfer dynamics, including not only charge recombination but also regeneration dynamics, are correlated with device performance. Data presented in this chapter has been published in references [50, 51].

Chapter 6 addresses the evaluation of novel, high hole mobility, molecular semiconductors to replace the liquid electrolyte in DSSC. A close correlation is observed between molecular weight, dye regeneration yield and device photocurrent. Data presented in this chapter has been submitted for publication.

Chapter 7 addresses the use of polymeric and molecular organic semiconductors to fabricate a redox cascade in solid state DSSC, resulting in a significant retardation of recombination losses. Data presented in this chapter has been submitted for publication.

Chapter 8 focuses on the development of novel polymer electrolytes as solid state alternatives to the liquid electrolyte in DSSC. A series of polymers are employed, and the interfacial electron transfer dynamics correlated with device performance. Data presented in this chapter has been submitted for publication.

1.4 References

1. Source: Energy Information Administration of the U.S. Government (EIA), 2005 estimate.

2. Source: National Climatic Data Center of US department of commerce / NESDIS / NOAA, 2005.

3. TSUGE, S., *Development and improvement of HIT (c-Si/a-Si heterojunction) solar cell.* OYO BUTURI, 2003. **72**(7): p. 0886.

4. Veenstra, S.C., et al., *Photovoltaic properties of a conjugated polymer blend of MDMO-PPV and PCNEPV.* Chemistry of Materials, 2004. **16**(12): p. 2503-2508.

5. Yu, G. and A.J. Heeger, *Charge Separation and Photovoltaic Conversion in Polymer Composites with Internal Donor-Acceptor Heterojunctions.* Journal of Applied Physics, 1995. **78**(7): p. 4510-4515.

6. Halls, J.J.M., et al., *Efficient Photodiodes from Interpenetrating Polymer Networks.* Nature, 1995. **376**(6540): p. 498-500.

7. Forrest, S.R., *The limits to organic photovoltaic cell efficiency.* Mrs Bulletin, 2005. **30**(1): p. 28-32.

8. René A.J. Janssen, J.C.H., and N. Serdar Sariciftci, *Polymer–Fullerene Bulk Heterojunction Solar Cells.* MRS BULLETIN, 2005. **30**(1): p. 33.

9. Oregan, B. and M. Gratzel, *A Low-Cost, High-Efficiency Solar-Cell Based on Dye-Sensitized Colloidal Tio2 Films.* Nature, 1991. **353**(6346): p. 737-740.

10. Nazeeruddin, M.K., et al., *Engineering of efficient panchromatic sensitizers for nanocrystalline TiO2-based solar cells.* Journal of the American Chemical Society, 2001. **123**(8): p. 1613-1624.

11. Gratzel, M., *Perspectives for dye-sensitized nanocrystalline solar cells.* Progress in Photovoltaics, 2000. **8**(1): p. 171-185.

12. Kalyanasundaram, K. and M. Gratzel, *Applications of functionalized transition metal complexes in photonic and optoelectronic devices.* Coordination Chemistry Reviews, 1998. **177**: p. 347-414.

13. Hagfeldt, A. and M. Gratzel, *Light-Induced Redox Reactions in Nanocrystalline Systems.* Chemical Reviews, 1995. **95**(1): p. 49-68.

14. Montanari, I., J. Nelson, and J.R. Durrant, *Iodide electron transfer kinetics in dye-sensitized nanocrystalline TiO2 films.* Journal of Physical Chemistry B, 2002. **106**(47): p. 12203-12210.

15. Green, A.N.M., et al., *Transient absorption studies and numerical modeling of iodine photoreduction by nanocrystalline TiO2 films.* Journal of Physical Chemistry B, 2005. **109**(1): p. 142-150.

16. Nazeeruddin, M.K., et al., *Conversion of Light to Electricity by Cis-X2bis(2,2'-Bipyridyl- 4,4'-Dicarboxylate)Ruthenium(Ii) Charge-Transfer Sensitizers (X = Cl-, Br-, I-, Cn-, and Scn-) on Nanocrystalline Tio2 Electrodes.* Journal of the American Chemical Society, 1993. **115**(14): p. 6382-6390.

17. Tachibana, Y., et al., *Subpicosecond interfacial charge separation in dye-sensitized nanocrystalline titanium dioxide films.* Journal of Physical Chemistry, 1996. **100**(51): p. 20056-20062.

18. Benko, G., et al., *Photoinduced ultrafast dye-to-semiconductor electron injection from nonthermalized and thermalized donor states.* Journal of the American Chemical Society, 2002. **124**(3): p. 489-493.

19. Ellingson, R.J., et al., *Dynamics of electron injection in nanocrystalline titanium dioxide films sensitized with Ru(4,4 '-dicarboxy-2,2 '-bipyridine)(2)(NCS)(2) by infrared transient absorption.* Journal of Physical Chemistry B, 1998. **102**(34): p. 6455-6458.

20. Haque, S.A., et al., *Charge separation versus recombination in dye-sensitized nanocrystalline solar cells: the minimization of kinetic redundancy.* Journal of the American Chemical Society, 2005. **127**(10): p. 3456-3462.

21. Argazzi, R., et al., *Remote interfacial electron transfer from supramolecular sensitizers.* Inorganic Chemistry, 1997. **36**(1): p. 2-3.

22. Kuciauskas, D., et al., *Electron transfer dynamics in nanocrystalline titanium dioxide solar cells sensitized with ruthenium or osmium polypyridyl complexes.* Journal of Physical Chemistry B, 2001. **105**(2): p. 392-403.

23. Heimer, T.A., et al., *Electron injection, recombination, and halide oxidation dynamics at dye-sensitized metal oxide interfaces.* Journal of Physical Chemistry A, 2000. **104**(18): p. 4256-4262.

24. Oregan, B., et al., *Vectorial Electron Injection into Transparent Semiconductor Membranes and Electric-Field Effects on the Dynamics of Light-Induced Charge Separation.* Journal of Physical Chemistry, 1990. **94**(24): p. 8720-8726.

25. Haque, S.A., et al., *Parameters influencing charge recombination kinetics in dye- sensitized nanocrystalline titanium dioxide films.* Journal of Physical Chemistry B, 2000. **104**(3): p. 538-547.

26. Hara, K., et al., *Molecular design of coumarin dyes for efficient dye-sensitized solar cells.* Journal of Physical Chemistry B, 2003. **107**(2): p. 597-606.

27. Nelson, J., et al., *Trap-limited recombination in dye-sensitized nanocrystalline metal oxide electrodes.* Physical Review B, 2001. **6320**(20): p. art. no.-205321.

28. Nasr, C., S. Hotchandani, and P.V. Kamat, *Role of iodide in photoelectrochemical solar cells. Electron transfer between iodide ions and ruthenium polypyridyl complex anchored on nanocrystalline SiO2 and SnO2 films.* Journal of Physical Chemistry B, 1998. **102**(25): p. 4944-4951.

29. Fisher, A.C., et al., *Intensity dependence of the back reaction and transport of electrons in dye-sensitized nanacrystalline TiO2 solar cells.* Journal of Physical Chemistry B, 2000. **104**(5): p. 949-958.

30. Hagfeldt, A. and M. Gratzel, *Molecular photovoltaics.* Accounts of Chemical Research, 2000. **33**(5): p. 269-277.

31. Kebede, Z. and S.E. Lindquist, *Donor-acceptor interaction between non-aqueous solvents and I-2 to generate I-3(-), and its implication in dye sensitized solar cells.* Solar Energy Materials and Solar Cells, 1999. **57**(3): p. 259-275.

32. Hirata, N., et al., *Supramolecular control of charge-transfer dynamics on dye-sensitized nanocrystalline TiO2 films.* Chemistry-a European Journal, 2004. **10**(3): p. 595-602.

33. Yan, S.G. and J.T. Hupp, *Semiconductor-based interfacial electron-transfer reactivity: Decoupling kinetics from pH-dependent band energetics in a dye-sensitized titanium dioxide aqueous solution system.* Journal of Physical Chemistry, 1996. **100**(17): p. 6867-6870.

34. Hara, K., et al., *Design of new coumarin dyes having thiophene moieties for highly efficient organic-dye-sensitized solar cells.* New Journal of Chemistry, 2003. **27**(5): p. 783-785.

35. Hara, K., et al., *A coumarin-derivative dye sensitized nanocrystalline TiO2 solar cell having a high solar-energy conversion efficiency up to 5.6%.* Chemical Communications, 2001(6): p. 569-570.

36. Klein, C., et al., *Engineering of a novel ruthenium sensitizer and its application in dye-sensitized solar cells for conversion of sunlight into electricity.* Inorganic Chemistry, 2005. **44**(2): p. 178-180.

37. Clifford, J.N., et al., *Multistep electron transfer processes on dye co-sensitized nanocrystalline TiO2 films.* Journal of the American Chemical Society, 2004. **126**(18): p. 5670-5671.

38. Plass, R., et al., *Quantum dot sensitization of organic-inorganic hybrid solar cells.* Journal of Physical Chemistry B, 2002. **106**(31): p. 7578-7580.

39. Rensmo, H., et al., *High light-to-energy conversion efficiencies for solar cells based on nanostructured ZnO electrodes.* Journal of Physical Chemistry B, 1997. **101**(14): p. 2598-2601.

40. Burnside, S., et al., *Nanocrystalline mesoporous strontium titanate as photoelectrode material for photosensitized solar devices: Increasing photovoltage through flatband potential engineering.* Journal of Physical Chemistry B, 1999. **103**(43): p. 9328-9332.

41. Guo, P. and M.A. Aegerter, *RU(II) sensitized Nb2O5 solar cell made by the sol-gel process.* Thin Solid Films, 1999. **351**(1-2): p. 290-294.

42. Wang, P., et al., *Gelation of ionic liquid-based electrolytes with silica nanoparticles for quasi-solid-state dye-sensitized solar cells.* Journal of the American Chemical Society, 2003. **125**(5): p. 1166-1167.

43. Kubo, W., et al., *Quasi-solid-state dye-sensitized solar cells using room temperature molten salts and a low molecular weight gelator.* Chemical Communications, 2002(4): p. 374-375.

44. Kosmulski, M. and W. Janusz, *Dispersions of anatase in ambient temperature ionic liquids.* Journal of Colloid and Interface Science, 2001. **242**(1): p. 104-105.

45. Bach, U., et al., *Solid-state dye-sensitized mesoporous TiO2 solar cells with high photon-to-electron conversion efficiencies.* Nature, 1998. **395**(6702): p. 583-585.

46. Nogueira, A.F., J.R. Durrant, and M.A. De Paoli, *Dye-sensitized nanocrystalline solar cells employing a polymer electrolyte.* Advanced Materials, 2001. **13**(11): p. 826-+.

47. Galoppini, E., et al., *Long-distance electron transfer across molecule-nanocrystalline semiconductor interfaces.* Journal of the American Chemical Society, 2001. **123**(18): p. 4342-4343.

48. Dang, X.J. and J.T. Hupp, *Interfacial charge-transfer pathways: Evidence for Marcus-type inverted electron transfer in metal oxide semiconductor/inorganic dye systems.* Journal of the American Chemical Society, 1999. **121**(36): p. 8399-8400.

49. Hirata, N., et al., *THE INFLUENCE OF DYE PROTONATION UPON THE PERFORMANCE OF DYE SENSITISED SOLAR CELLS.* ECS meeting proceedings for session N1, 2005.

50. Geary, E.A.M., et al., *Synthesis, structure and properties of Pt(2,2 '-bipyridyl-5,5 '-dicarboxylic acid)(3,4-toluenedithiolate) : tuning molecular properties for application in dye-sensitised solar cells.* Dalton Transactions, 2003(19): p. 3757-3762.

51. Geary, E.A.M., et al., *Synthesis, structure, and properties of Pt(II)(diimine)(dithiolate) dyes with 3,3 '-, 4,4 '-, and 5,5 '-disubstituted bipyridyl: Applications in dye-sensitized solar cells.* Inorganic Chemistry, 2005. **44**(2): p. 242-250.

2

Experimental

This chapter begins with a section describing the procedures involved in the preparation of samples. The remainder of the chapter describes the experimental techniques used for functional analysis of these samples.

2.1 Sample preparation

This section describes in detail the preparation of nanocrystalline TiO_2 films, the dye sensitisation of these films and finally the fabrication of dye-sensitised solar cells using these films. All chemicals were research grade, purchased from Sigma-Aldrich and used without further purification.

2.1.1 Preparation of nanocrystalline TiO_2 films

The preparation of nanocrystalline colloidal films can be best described in three simple steps:

1. Preparation of an aqueous solution of colloidal 15 nm size particles of TiO_2 (concentration 12.5 % TiO_2 by weight).
2. Deposition of the colloidal solution on a conducting glass substrate.
3. Sintering the deposited film at a high temperature to achieve electrical contact between the particles.

2.1.1.1 Preparation of TiO_2 colloidal paste

An aqueous suspension of colloidal TiO_2 particles was synthesised by using a sol-gel reaction, details of which are given in Willis, R. L. et al [1]. The TiO_2 particles used in this thesis were synthesised in Prof. James Durrant's laboratory at Imperial College by Dr. Emilio Palomares, Alex Green and Dr. Jessica Kroeze.

The basic synthetic procedure developed to obtain nanocrystalline TiO_2 is described below. 20mL of titanium isopropoxide is injected into 5.5 g of glacial acetic acid under argon atmosphere and stirred 10 minutes for hydrolysis of the titanium isopropoxide. The mixture is then injected into 120 mL of 0.1 M nitric acid under anhydrous atmosphere at room temperature in a conical flask and stirred vigorously. The flask is left uncovered and heated at 80°C for 8 h. After cooling, the solution needs to be filtered using a 0.45 mm syringe filter to remove aggregates and big particles (See Figure 2.1 showing 5 nm particles of TiO_2.) The filtered solution was then diluted to 5wt% TiO_2 by the addition of H_2O and then autoclaved at 220°C for 12 h for peptization. Finally, the colloids are re-dispersed with a 60s cycle sonication employing a LDU Soniprobe horn and the solution is concentrated to 12.5% on a rotary evaporator using a membrane vacuum pump at 40°C.

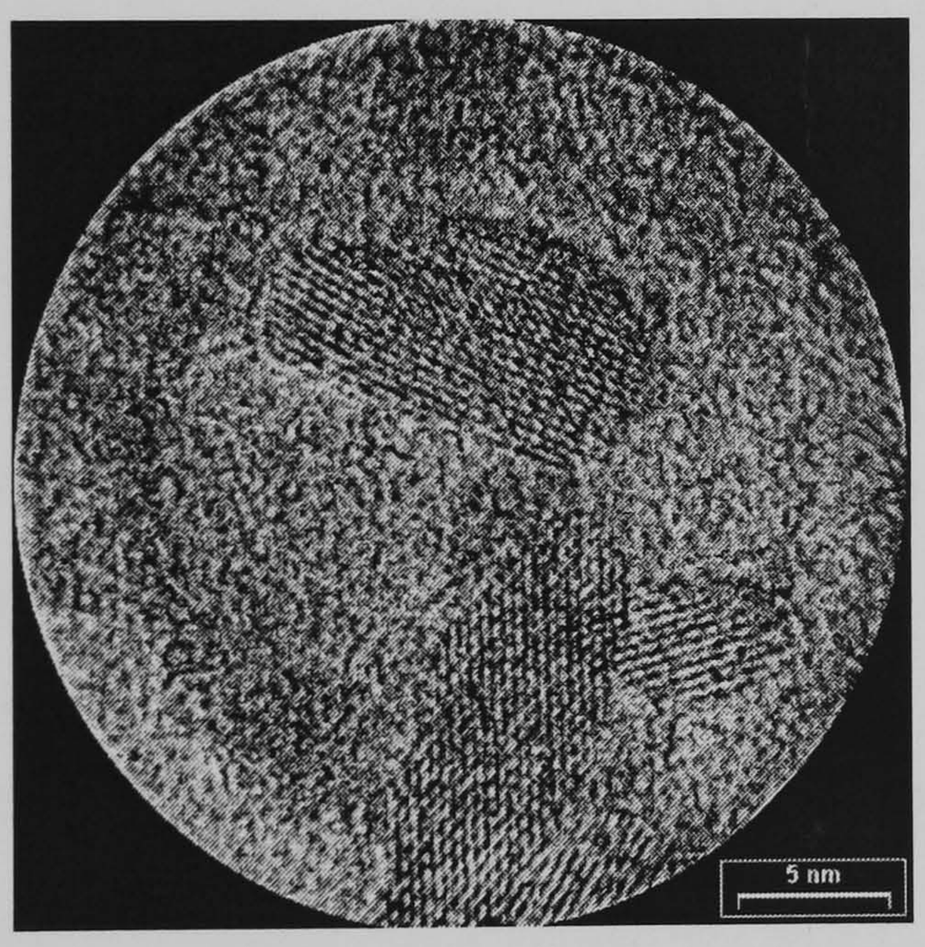


Figure 2.1 High Resolution Transmission Spectroscopy image of two nanoparticles of TiO_2 before autoclaving the sol-gel solution.

Subsequently, the resultant titanium dioxide paste is mixed with the polymer Carbowax, Mw 20,000, 50:50 TiO_2 : Carbowax (w/w). The Carbowax provides a support matrix for the film while it forms and improves its homogeneity. In addition, it increases the porosity of the titanium dioxide film and consequently allows more dye adsorption. The TiO_2 / Carbowax mixture was left stirring very slowly for at least 5

hours at room temperature to ensure complete blending of the Carbowax and the titanium dioxide paste. The stirring must be very slow in order to avoid the generation of bubbles that can cause inhomogeneity in films. The resultant TiO_2 paste is referred to as IC paste in this thesis.

The advantage of this IC paste is the transparency of the films after sintering, which allows transient optical absorption studies to be performed. However, this paste has two disadvantages. One is that the IC paste is more acidic than those commonly used in other research groups, i.e. with a pH of 1 as compared to 4 for the organic paste applied in Prof Micheal Grätzel's group. This might possibly lead to misinterpretation of the direct comparison of our results and those obtained by other research groups, since the pH of the TiO_2 films may be a crucial factor to device performance. It has for example been reported that there is a considerable effect of protons in nanocrystalline TiO_2 on the conduction band energetics, and hence on the interface electron transfer dynamics. [2] [3] Another disadvantage of the acidic IC paste is the technically poor reproducibility of the paste synthesis. For these reasons, an alternative organic TiO_2 paste, recently developed at The Energy research Centre of the Netherlands (ECN) for high-efficiency DSSCs, was employed for the studies reported in Chapter 4, 5, 6 and 7 of this thesis. This paste, referred to as ECN35, is synthesized under similar conditions as the IC paste, except for the peptization process in an autoclave, in which a basic chemical, tetraethylammonium, hydroxide is added to the TiO_2 solution, resulting in a paste pH of 6.0. The detailed synthetic procedure is described elsewhere [4].

2.1.1.2 Deposition of TiO_2 on glass substrates

The following two sections describe the procedures of deposition of TiO_2 on conductive glass substrates and of the sintering process. The same procedure was conducted for both IC and ECN35 paste. The titanium dioxide paste was deposited onto fluorine doped tin oxide (SnO_2:F) coated conducting (TEC8) glass slides purchased from Hartford Glass, Indiana, USA, which have a resistance of 8 Ω/sq. Prior to deposition, the 2.5 x 7.5 cm glass slide was cleaned by sonication in acetone at room temperature and then wiping with acetone soaked clean tissues to ensure that the

surface of the slide was entirely clean so that the TiO_2 nanoparticles would achieve a good contact when deposited. Great care was taken not to damage the conducting surface while cleaning. The clean glass slide was then carefully placed onto a flat clean surface, with the conducting side exposed. Both edges were fixed firmly with strips of a layer of Scotch Magic Tape™ while allowing a separation of 1 cm as shown in Figure 2.2. Then a sufficient amount (0.2 ml) of TiO_2 paste was introduced onto one of the un-taped ends of the glass slide and was quickly and evenly spread down the length of the conducting glass slide using a Pasteur pipette. This if done correctly, gives an even, homogeneous film. This film making technique is commonly referred to as "doctor blading". After the deposition of the paste, the strips of tape were carefully removed.

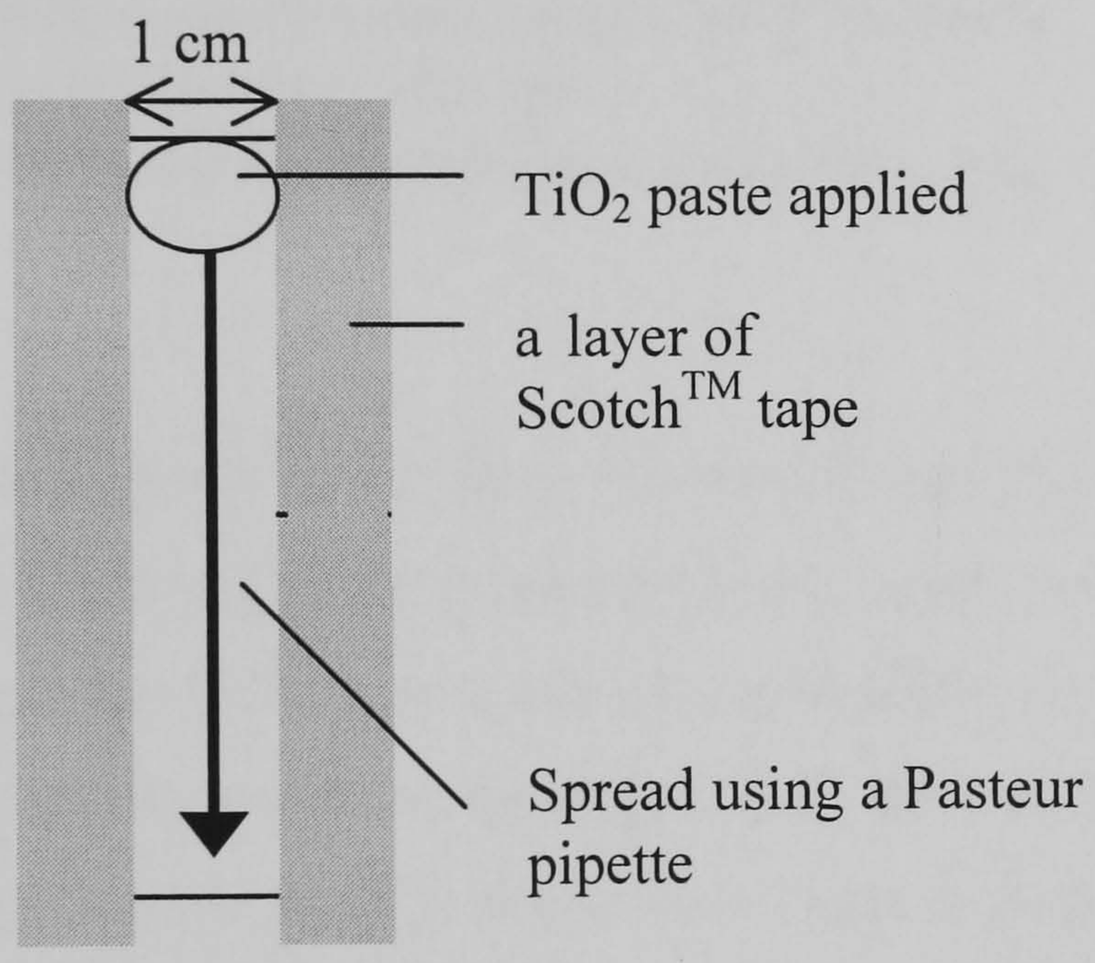


Figure 2.2 "Doctor blade" technique of preparing nanocrystalline TiO_2 films.

2.1.1.3 Film sintering

The films were then transferred to a furnace and sintered at 450°C for 30 minutes. Great care was taken not to exceed sintering temperatures above 500°C as the conversion of the crystal phase TiO_2 particles from anatase to rutile may be accelerated above this temperature. The prolonged heating removed all organic components such as the Carbowax, leaving only the nanocrystalline TiO_2 particles behind. The heat also sintered the nanocrystalline particles together, providing good electrical contact throughout the film. Once the heating was finished, the films were allowed to cool

gradually to room temperature. All sintered films were then stored in a sealed plastic box under anhydrous conditions.

Table 2.1 Characteristics of both IC and ECN35

	IC	ECN35
pH of paste *1	~1	~6
particle size (nm)	~15 *2	~25 *3
crystallinity	>99% anatase *4	>99% anatase *5
transparency of sintered film *6	>80%	>24%

*1 The pH of paste was determined by pH paper.

*2 The particle size was determined by BET analysis.

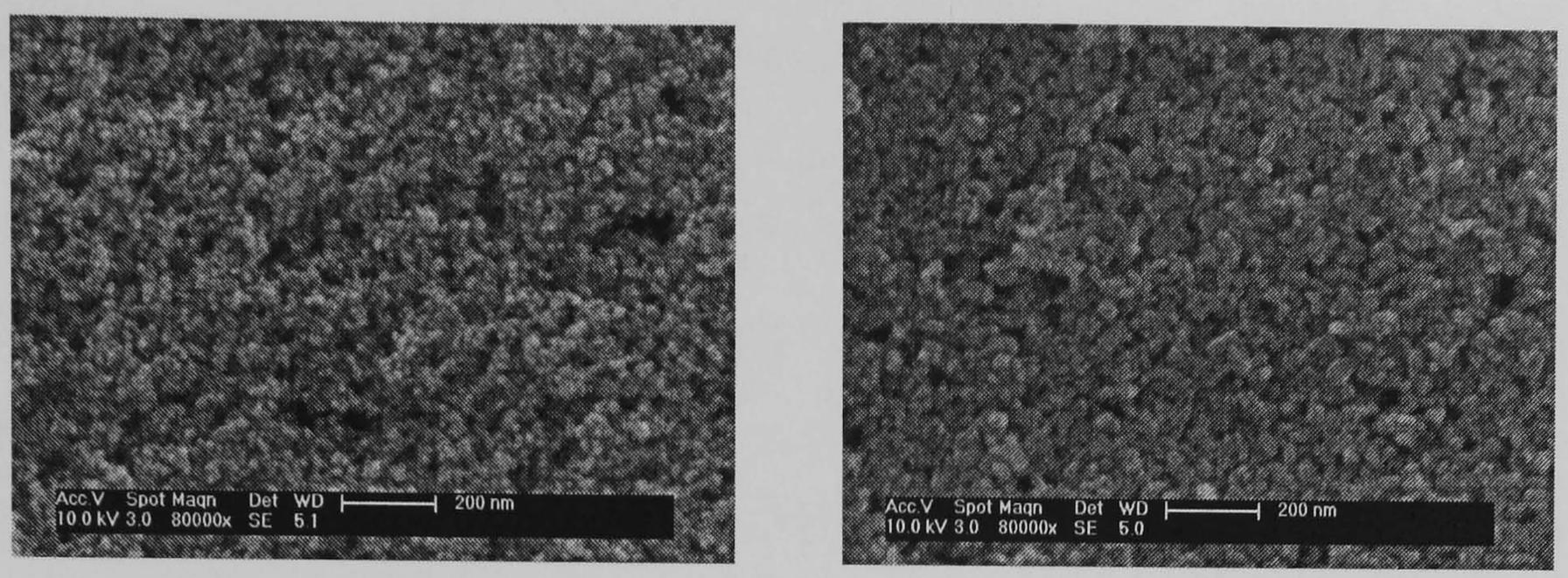
*3 The particle size was determined by SEM picture.

*4 The crystallinity was determined by resonance Raman spectroscopy.

*5 The crystallinity was determined by XRD.

*6 The transparency calculated by transmission of sintered films at 450 nm and above.

Some characteristics for the films made of IC and ECN35 paste are summarised in Table 2.1. The thickness of the resultant films was determined to be 4 ±0.2 μm for IC paste and 5±0.2 μm for ECN35 by employing a DekTak step-profilometer. The sintered films have a sponge-like structure (see Figure 2.3). BET analysis of the film made from IC paste show the average particle size to be ~15 nm with pore sizes of 16 - 18 nm and a surface area of 80 – 100 m^2 / g, while the average particle size for ECN35 was around three times as large, as also shown in Figure 2.3. The IC TiO_2 films were highly transparent with a transmission of > 80% (effective OD < 0.1) for wavelengths > 450 nm, while the ECN films were more scattering with a transparency of 24%, which is however transparent enough to measure transient absorption.



(a) (b)

Figure 2.3 SEM picture of the surface of a ~5 μm thick nanocrystalline TiO_2 film made from IC paste (a) and ECN35 paste (b), showing a sponge-like structure for both films with a slightly larger particle size for ECN35.

Consistency in film preparation is vital because the crystalline nature of the film and the quality of the electrical contact between the particles are influenced by the preparation conditions.

2.1.2 Dye sensitisation

Many different classes of dyes were used in this thesis, requiring different conditions for successful preparation of dye-sensitised TiO_2 films. These conditions include different solvents, different additives aiding sensitisation and different lengths of sensitising time. However, the procedure is essentially the same for all the samples prepared.

2.1.2.1 Preparation of sensitising solution

The ruthenium complex $Ru(dcbpy)_2(NCS)_2$, the most frequently employed sensitiser during my PhD studies, was dissolved in a 1:1 mixture of acetonitrile / *tert*-butanol. For nearly all experiments described in this thesis, 1 mM sensitisation solutions were used. Details of the sensitising conditions used for different experiments involving different dyes are given in the experimental sections of each chapter.

2.1.2.2 The sensitisation procedure

When the TiO_2 films and the dye solutions are prepared, the sensitisation process can begin. If sensitisation is not undertaken immediately then prior to sensitisation, both the sensitising solution was sonicated to break-up aggregation which may have formed and also the TiO2 films were heated at 450°C for 10 minutes to remove any water or organic molecules which may have adsorbed to the surface of the film. The sensitisation process simply involved immersing a piece of TiO_2 glass slide (1.5 cm x 2.5 cm) in the appropriate dye solution and leaving it in the dark for a period ranging from a few hours to over a full day, as detailed in the relevant chapters. The duration of the sensitisation period depends upon the type of experiment and the sensitiser employed. Generally, for a film that will be used in a transient laser spectroscopy experiment and to make a complete cell, the film was left overnight at room temperature to achieve maximum coverage of the film. However, for some experiments the dipping time was varied from a few minutes to a few hours in order to control the dye loading and hence the optical density of the dye-coated film. Details are given in the experimental sections of each chapter.

2.1.2.3 Calculation of dye coverage

Dye coverage on surface of the TiO_2 particles was simply calculated by the following two steps.

(1) To calculate the mole of dye per 1 cm^2 of the surface of the TiO_2

If Lambert-Beer law is applied and the equation 2.1 is mathematically rearranged for dye sensitised films, equation 2.2 will be obtained

$$OD = \varepsilon \times l \times C \qquad \text{(equation 2.1)}$$

where OD is optical density, ε is molar extinction coefficient of the dye ($M^{-1}cm^{-1}$), l is the path length (cm), C is the concentration of sample solutions (mol/l).

$$OD = \varepsilon \times (t \times 10^{-4}) \times [x/(t \times 10^{-7})] \qquad \text{(equation 2.2)}$$

where t is the thickness of the sample films (μm), x is the number of the dyes in the cube of 1 cm * 1 cm * t μm of film (mol). Consequently, x, the mole of dye per 1 cm^2 of the surface of the TiO_2, is simply calculated by using equation 2.3.

$$x = OD/(\varepsilon \times 10^3) \qquad \text{(equation 2.3)}$$

(2) To evaluate the dye coverage

By using the value x obtained from equation 2.3, the dye coverage, y, can be calculated by using an equation 2.4.

$$y = x \times Na \times s/450 \times 100 \qquad \text{(equation 2.4)}$$

where Na is Avogadro number, s is the area occupied by a molecule of the dye (~7*10^{-15} cm^2 for the $RuL_2(NCS)_2$ dye), and 450cm^2 is the surface area of TiO_2 nanoparticles in 1 cm^2 of the film. y is the possible percentage of the dye coverage on the surface of the TiO_2. Note that if the y is 100%, it could be a monolayer.

2.1.2.4 Storage of sensitised films

The samples studied in this thesis can be divided into three: liquid type cells, quasi-solid type cells and solid type cells. In this section, fabrication of liquid type cells, which were commonly studied in this thesis, is addressed. For the others, details are described in relevant chapters.

When the sensitisation process was finished, the films were rinsed in an appropriate solvent to remove any unbound dye from the pores of the film. For ruthenium complex dyes dry ethanol was employed. Afterwards, the sensitised films were covered with a drop of inert solvent, propylene carbonate, and a thin glass cover slide and stored under anhydrous conditions in the dark to prevent the degradation of dyes.

2.1.3 Fabrication of dye-sensitised solar cells

The fabrication of liquid type dye-sensitised solar cells can be described in four steps:

(1) Preparation of dye-sensitised nanocrystalline TiO_2 films.

(2) Preparation of electrolyte.

(3) Preparation of platinized conducting glass counter electrodes.

(4) Adhesion of working and counter electrodes, addition of electrolyte to the cell and cell sealing.

The preparation of dye-sensitised TiO_2 films has been described in the previous sections. In addition, any excess dye-sensitised TiO_2 film is scratched off using a scalpel leaving a 1 cm^2 square of dye-sensitised TiO_2 film in the centre of the 1.5 cm x 2.5 cm glass piece. This is the standard area over which cells are characterised in this thesis.

The electrolyte solution used varied with the type of dye used. For $Ru(dcbpy)_2(NCS)_2$, the electrolyte used consisted of 0.1 M lithium iodide, 0.8 M tetra butyl ammonium iodide, 0.5 M *tert*-butylpyridine and 0.05 M iodine in acetonitrile.

Platinized counter electrodes were prepared as follows. A conductive glass slide of TEC15, which has a transparency at 550 nm <85% and resistance>9 Ohm cm^{-2}, was broken up into pieces of the same size as the TiO_2 working electrodes (1.5 cm x 2 cm). Such a piece of glass was coated with a thin layer of 0.5 M hexachloroplatinic acid [H_2PtCl_4] in iso-propanol on the conductive side using the "doctor blade" technique (see Section 2.1.1.2). The slide was then heated to 450 ^0C for 20 minutes and subsequently allowed to cool at room temperature. Two small holes were drilled in these electrodes using a diamond tipped drill, the purpose of which will become apparent in the following paragraph. These finished counter electrodes were used immediately or were stored under anhydrous conditions.

The working and counter electrodes can now be assembled together to make the dye-sensitised solar cell. The electrodes can be made to adhere together using the

polymer Surlyn 1702 (DuPont). A frame of polymer was placed around the 1 cm^2 dye-sensitised TiO_2 square on the working electrode and then the counter electrode was placed on top of this with the drilled holes placed at either corner of the square. The two electrodes could be made to adhere permanently to each other by placing them under pressure at 100 ^0C for 60 seconds. The pressure was applied manually with a relatively soft material such as a wooden rod in order to prevent scratching the surface of the glass. As a criterion for whether the procedure for sealing was finished, the transparency of the Surlyn was used, *i.e.* the film becomes transparent as adhesion is reaching completion. Great care was taken to make sure there were no bubbles between the film and the electrodes, which could lead to electrolyte leakage. The electrolyte was then injected into the cell cavity between the electrodes with a syringe through one of the drilled holes. The second hole serves as a means of allowing the air to escape as the electrolyte enters through the first hole. The two holes can then be sealed by putting a piece of 1 cm^2 square cover glass on them, and a small amount of fast-drying epoxy glue (Araldite) was put around the cover glass to adhere to the back of the counter electrode. The cell is now entirely sealed and can be characterised immediately or at a later date: the cell will remain sealed for a few days. However, it is best for cell characterisation to begin immediately. Figure 2.4 shows a schematic diagram of a complete dye-sensitised solar cell.

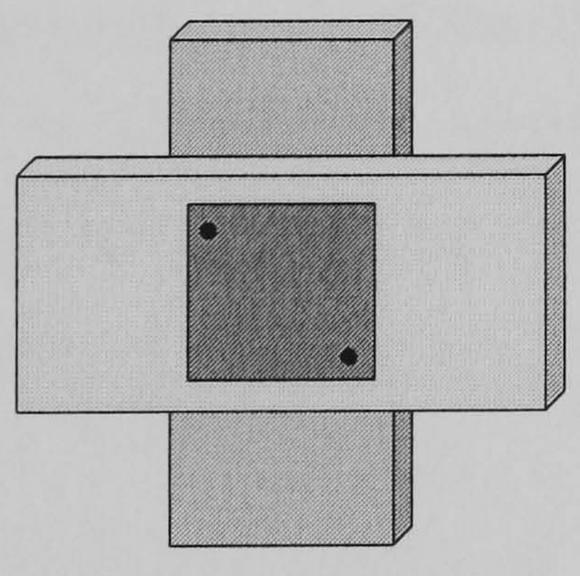


Figure 2.4 Schematic structure of a dye-sensitised solar cell. The dimensions of each electrode is 1.5 cm x 2 cm. The dark square represents the dye-sensitised TiO_2 with 1 cm^2 area. The small black circles represent the holes through which the electrolyte was injected.

2.2 Transient absorption spectroscopy

Transient absorption spectroscopy (TAS) has in many ways been the most important (definitely the most frequently employed) technique for analysing samples during the course of my PhD. Characterisation of cells using a solar simulator apparatus (see Section 2.5) enabled a quantitative assessment of cell performance, but the transient laser system was the means of gaining deeper insight into the processes occurring at the different interfaces within the cell.

2.2.1 Principle

This technique allows us to look at transient species in physical and chemical reactions that only have a very short life-time. It was originally developed by Lord Porter [5] for which he awarded the Nobel Prize for Chemistry in 1967. The apparatus may be viewed as an elaborate spectrometer that is capable of observing absorption spectra of transient species and also the formation and decay kinetics of these species.

The technique involves irradiation of a sample with a short intense pulse of light (the excitation pulse) and observing the consequent change in the sample optical density. The change in optical density is determined by monitoring the transmission of a less intense light beam passing through the sample known as the "probe". This technique yields information from a single excitation wavelength at a single probe wavelength but over a broad range of timescales (micro-millisecond) to provide kinetic data on the transient decay. In addition, our system allows the probe wavelength to be changed over a broad range (400 - 1000 nm) to give absorption spectra of transient species in the sample at chosen time delays (e.g. 100 μs) after the excitation pulse.

2.2.2 Apparatus

The transient absorption system assembled was capable of monitoring kinetics from microsecond to millisecond timescales. The system was based on a system designed and developed by Prof. James Durrant [6] during his PhD studies at Imperial College. A schematic of the system is shown below in Figure 2.5.

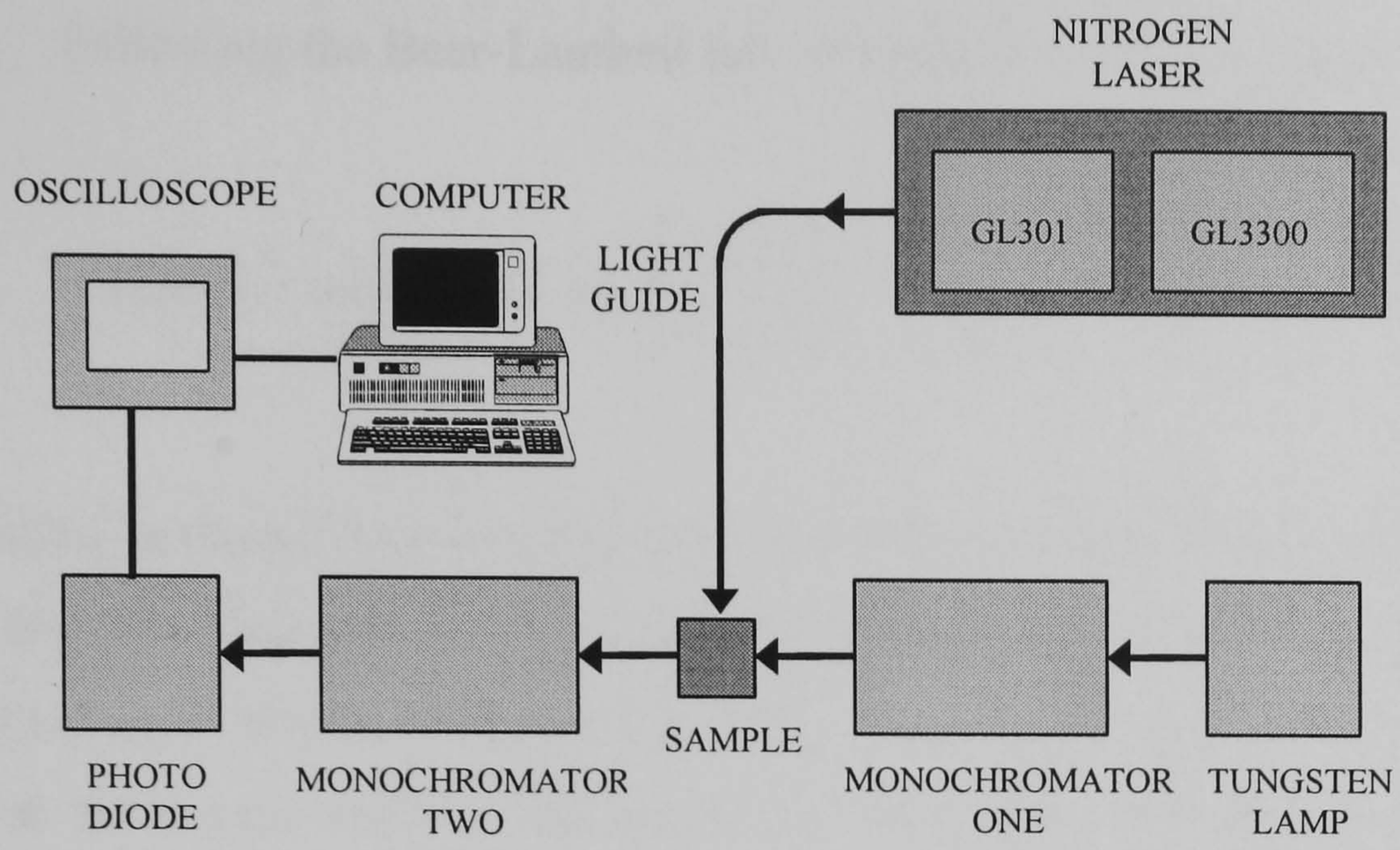


Figure 2.5 The microsecond to millisecond transient absorption system.

The excitation source used was a GL-3300 Nitrogen Laser (Photon Technology International). This laser produced 600 ps laser pulses at a wavelength of 337.1 nm with a pulse energy of 1.45 mJ at 5Hz. The repetition rate could be varied using a frequency generator. A GL-301 Dye Laser (Photon Technology International) was used in conjunction with the nitrogen laser to provide a variable excitation wavelength range of 400 – 750 nm. The energy of the pulse at the various wavelengths depended on the type of dye employed in the dye laser. A light guide was used to transmit the excitation pulse to the sample.

A 150 W Tungsten halogen lamp was used as the probe-light source. The monitoring wavelength from the lamp was selected by using monochromator one. Appropriate band-pass filters can be placed at the exit of the first monochromator to block "second harmonic" frequencies, which arise when white light passes through the monochromator. A second monochromator with appropriate band-pass filter was used behind the sample to reduce the amount of laser light scatter reaching the photodiode detector. The detection system comprised a silicon photodiode and an optical transient voltage amplifier coupled to a Tektronix oscilloscope. The detection system electronics were designed by Richard Monkhouse.

2.2.3 Calculation of ΔOD

Following the Beer-Lambert law, the optical density of a sample is defined as:

$$OD(\lambda) = \varepsilon(\lambda)cl = Log_{10}\left[\frac{I_i(\lambda)}{I_t(\lambda)}\right] \qquad \text{(Equation 2.5)}$$

where λ is the probe wavelength, ε is the extinction coefficient of the absorbing species at the probe wavelength, c is the concentration of the absorbing species and l is the optical path length through the sample. I_i represents the intensity of the incident light upon the sample and I_t is the intensity of the transmitted light through the sample. The change in optical density (ΔOD) can simply be written as:

$$\Delta OD(\lambda,t) = OD_1(\lambda,t) - OD_2(\lambda) \qquad \text{(Equation 2.6)}$$

It therefore follows that, using Equation 3.1, ΔOD can be rewritten as:

$$\Delta OD(\lambda,t) = Log_{10}\left[\frac{I_i(\lambda)}{I_{t1}(\lambda,t)}\right] - Log_{10}\left[\frac{I_i(\lambda)}{I_{t2}(\lambda)}\right] \qquad \text{(Equation 2.7)}$$

On simplification of Equation 2.7, Equation 2.8 is obtained:

$$\Delta OD(\lambda,t) = Log_{10}\left[\frac{I_{t2}(\lambda)}{I_{t1}(\lambda,t)}\right] \qquad \text{(Equation 2.8)}$$

where $OD_1(\lambda,t)$ and $I_{t1}(\lambda,t)$ are the optical density and transmitted light intensity, respectively, at delay time t after excitation. $OD_2(\lambda)$ and $I_{t2}(\lambda)$ are the optical density and transmitted light intensity without excitation of the sample.

Practically, the data collected by the oscilloscope was converted to units of ΔOD. The change in optical density was calculated by using Equation 2.9.

$$\Delta OD(t) = \log_{10} \times \left[\frac{V_0}{V(t)} \right] \qquad \text{(Equation 2.9)}$$

where $V(t)$ is the transient signal size which is proportional to the light intensity. V_0 is the DC voltage level, which is proportional to the intensity of the probe light.

2.2.4 Comparison with other apparatus

The transient absorption system was designed by Prof. James Durrant and Richard Monkhouse to enable very small transient signals to be observed; typically of 1 mΔOD for the radical cation of $Ru(dcbpy)_2(NCS)_2$ (excitation at 600 nm ; probing at 800 nm). These signals are among the smallest observed by groups undertaking research in the dye-sensitised solar cell field. For example, in studies by Hupp et al [7] where recombination kinetics for a series of different dye-sensitised films were recorded to determine the effect of free energy on this reaction, all signals observed were > 20 mΔOD. The fact that we observe much smaller signals means that the system is extremely sensitive to changes in optical density, mainly as a result of very sensitive detection electronics. Furthermore, we use the following components, which are different from those typically used by other groups: a Tungsten halogen lamp instead of a xenon lamp as the probe source and a photodiode instead of a photomultiplier as the detector. In addition, the detection electronics are equipped with low and high pass filters to reduce noise.

The nitrogen laser coupled to the dye laser produces low intensity pulses (~ 40 μJ / cm^2 at 530 nm) that produce low densities of charge carriers (electrons) in the TiO_2 film (< 1 electron per particle) during the course of the experiment.[8] These conditions are more relevant than using higher laser intensities if we wish to compare the charge carrier dynamics in the dye-sensitised films to the kinetics in a solar cell under illumination of 1 sun. Using high laser intensities that result in high populations of photoinduced electrons in the nanoparticles of the TiO_2 film causes non-linear effects on the observed kinetics, i.e. recombination kinetics will start to become influenced by the concentration of electrons in the film induced by the laser pulse, not just on the nature of the materials used. Such non-linear effects are not observed when monitoring

electron transfer rates between donor and acceptor complexes in solution as there is a homogenous distribution of both species.

2.2.5 Types of experiments

The simplest experiments involved dye-sensitised TiO_2 films only, observing the kinetics of the charge recombination reaction between electrons injected into the TiO_2 by the dye following laser excitation, and the resulting dye cations on the surface of the film. Dynamic transient absorption spectra are obtained by recording transients over a particular probe wavelength range, and noting the transient signal amplitude at a fixed time delay after the laser flash. When these points are plotted as a function of probe wavelength they provide the difference absorption spectra of the transient species being monitored. Not only dye-sensitised films but also complete solar cells were studied, in particular to monitor the efficiency of regeneration of the dye cation by redox couples in the electrolyte. Transient absorption spectra were used to assign the characteristic absorption and bleaching features to the various transient species.

2.3 Other Experimental Techniques

2.3.1 Steady state UV / visible absorption spectroscopy

UV/visible absorption spectroscopy was employed to measure the optical density of dye-sensitised films. All steady state absorption spectra of films or solutions were obtained by using a Shimadzu UV-1601 spectrometer. Spectra were recorded with a detection bandwidth of 2 nm. As a blank for baseline correction, unsensitised TiO_2 films were used.

2.3.2 Photocurrent measurements under AM 1.5 solar simulation

To measure the global efficiency of the dye-sensitised solar cells a solar simulator was used. As its name suggests, this apparatus is capable of simulating the illumination conditions a solar cell will experience in its operational mode. This technique quantitatively examines the power output of solar cells under a load. This is done by gradually increasing the voltage applied to the cell and recording the current produced, resulting in a so-called current-voltage curve, which yields valuable information about the cell under scrutiny. A typical example of a current voltage curve is shown below.

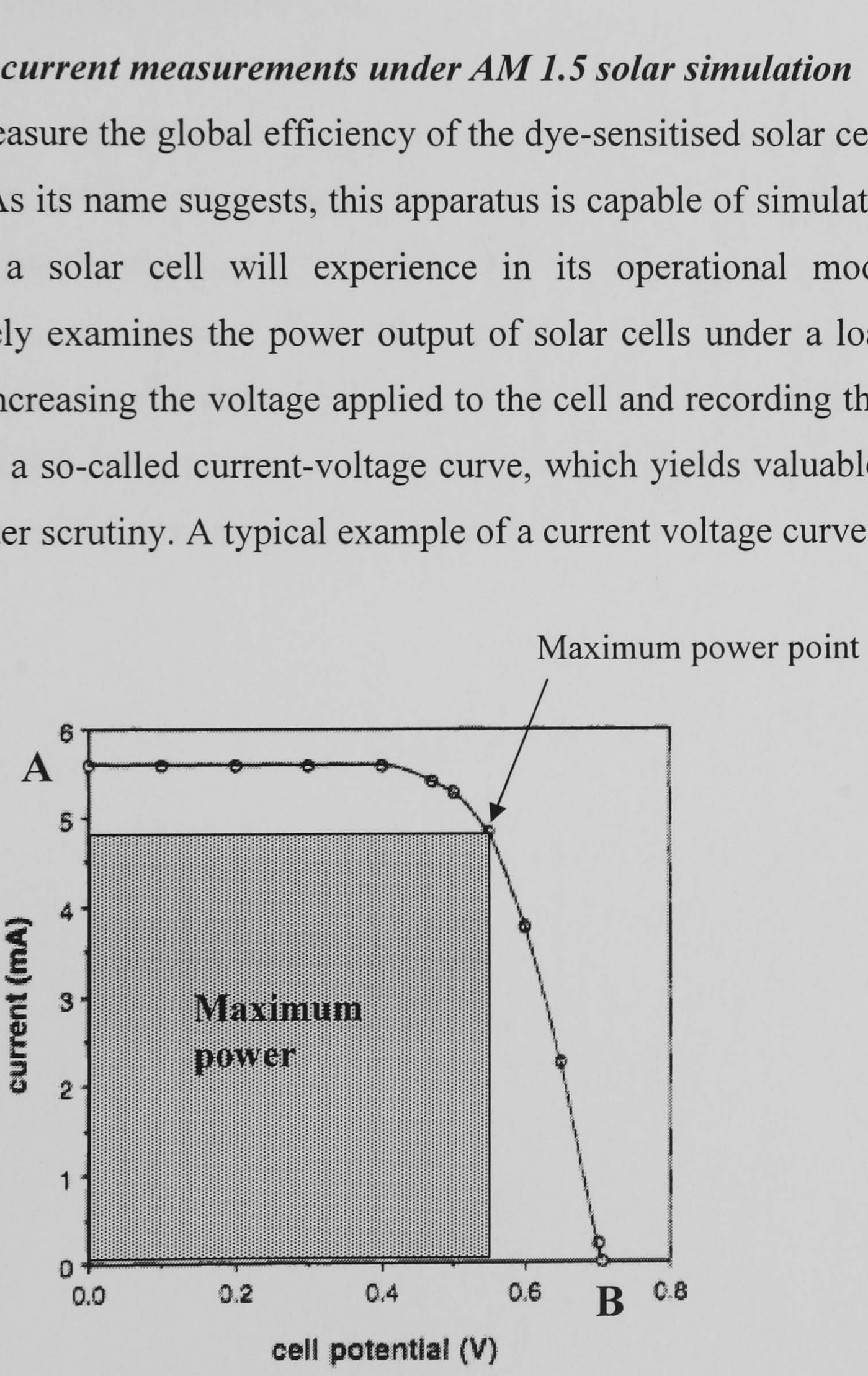


Figure 2.6 Current-voltage characteristics for a nanocrystalline TiO_2 dye-sensitised solar cell under simulated AM 1.5 solar radiation. This data is reproduced from reference [9].

The maximum power produced by the cell is recorded at the point indicated above. This power divided by the power of the incident light on the cell provides the overall conversion efficiency (η) of the cell. Points A and B correspond to the short circuit current (I_{sc}) and the open circuit voltage (V_{oc}), respectively, of the cell which are the maximum photocurrent and photovoltage obtainable from the cell. Using these values we can obtain the maximum theoretical power output of the solar cell. The ratio of the actual maximum power output to the maximum theoretical power output is known as the fill factor (*ff*). η, I_{sc}, V_{oc} and *ff* are all quoted when discussing the current-voltage curves of cells in this thesis.

Current-voltage measurements were made with a ScienceTech solar simulator and AM1.5 spectral filter. Calibration of the light intensity was achieved using band-pass filters of known transmission combined with a silicon photodiode with independently certified spectral response. The lamp intensity was adjusted to give a close (5%) agreement with the theoretical AM 1.5 intensity over the spectral region of dye optical absorption (450-700 nm). The intensity of this light can be further attenuated by using neutral density filters to give, for instance, "1/10 sun".

2.4 References

1. Willis, R.L., *Functional properties of nanocrystalline metal oxide films for dye sensitised solar cells*. 2002, University of London.

2. Tachibana, Y., et al., *Subpicosecond interfacial charge separation in dye-sensitized nanocrystalline titanium dioxide films.* Journal of Physical Chemistry, 1996. **100**(51): p. 20056-20062.

3. Tachibana, Y., et al., *Electron injection kinetics for the nanocrystalline TiO2 films sensitised with the dye (Bu4N)(2)Ru(dcbpyH)(2)(NCS)(2).* Chemical Physics, 2002. **285**(1): p. 127-132.

4. Spath, M., et al., *Reproducible manufacturing of dye-sensitized solar cells on a semi-automated baseline.* Progress in Photovoltaics, 2003. **11**(3): p. 207-220.

5. Porter, G., Proceedings of the Royal Society of London. Series A, Mathematical and Physical Sciences, 1950. **200**(1061): p. 284.

6. Durrant, J.R., *Transient absorption spectroscopy of photosystem II.* 1992, University of London.

7. Susan G. Yan, J.S.P., Youngjin Kim, and Joseph T. Hupp, *In Search of the Inverted Region: Chromophore-Based Driving Force Dependence of Interfacial Electron Transfer Reactivity at the Nanocrystalline Titanium Dioxide Semiconductor/Solution Interface.* J. Phys. Chem. B, 2000. **104**: p. 10871.

8. Haque, S.A., et al., *Parameters influencing charge recombination kinetics in dye- sensitized nanocrystalline titanium dioxide films.* Journal of Physical Chemistry B, 2000. **104**(3): p. 538-547.

9. M. K. Nazeeruddin, A.K., I. Rodicio, R. Humphry-Baker, E. Mueller, P. Liska, N. Vlachopoulos, and M. Graetzel, *Conversion of light to electricity by cis-X2bis(2,2'-bipyridyl-4,4'-dicarboxylate)ruthenium(II) charge-transfer sensitizers (X = Cl-, Br-, I-, CN-, and SCN-) on nanocrystalline titanium dioxide electrodes.* J. Am. Chem. Soc., 1993. **115**(14): p. 6382.

3

Electron transfer reactions on ruthenium based molecular dyes with different degree of protonation

In this chapter the influence of the extent of protonation in sensitizer dye upon charge separation and recombination dynamics, and thereby upon device performance, is addressed.

3.1 Introduction

In 1992 Rothenberger et al. used spectroelectrochemical techniques to investigate the dependence of the potential of conduction band energetics in nanocrystalline TiO_2 particles upon pH of the electrolyte composition. This potential was found to exhibit a Nernstein shift as a function of electrolyte proton activity, shifting by 59 meV per pH of the electrolyte. [1] (See Figure 3.1)

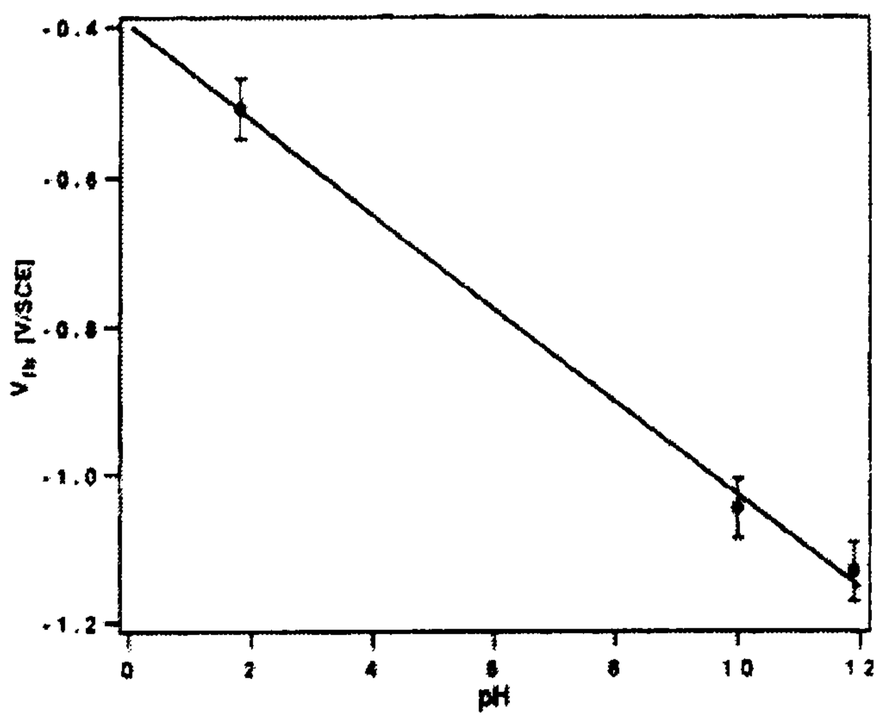


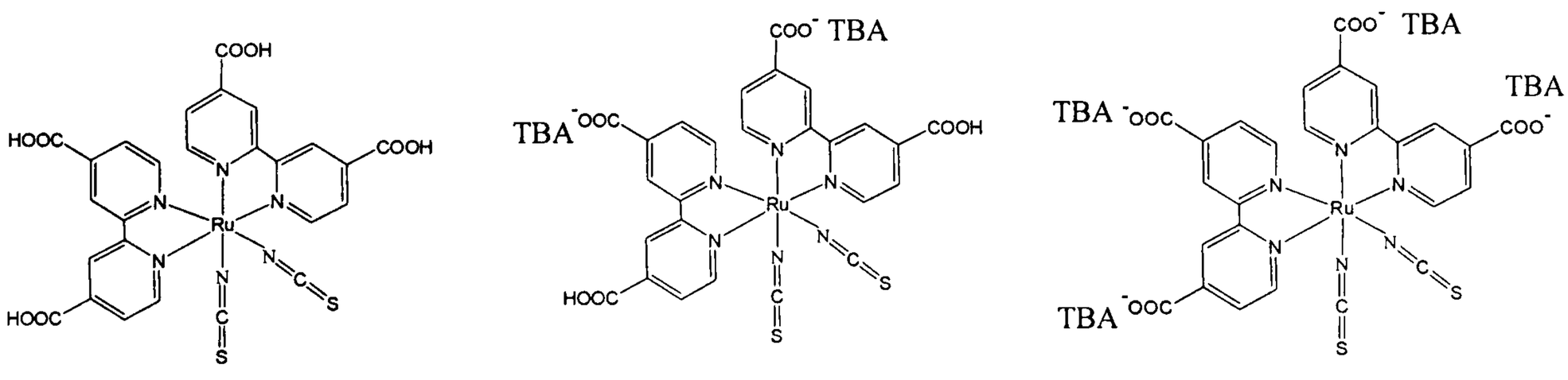
Figure 3.1 Plot of conduction band energetics of nanocrystalline TiO_2 as a function of pH the electrolyte composition, in agreement with a Nernstein shift (reproduced from [1]).

Further studies found that this shift of the conduction band energetics can result in striking effects upon the dynamics of both charge injection and recombination process, suggesting that the pH of the dye-sensitized TiO_2 interface could be crucial to the photovoltaic performance. [2, 3] Tachibana et al., for example, studied the influence of cations in the electrolyte upon electron injection kinetics from photoexcited dyes into the nanocrystalline TiO_2. In this study he found that the cations in the electrolyte such as Li^+ and H^+ led to a positive shift of the conduction band energetics, resulting in the faster injection dynamics. Similar research was carried out by Meyer el al. [4], who employed time-resolved absorption measurements of dye-sensitized TiO_2 films covered in electrolyte to demonstrate that the presence of lithium cations in the electrolyte increased the quantum yield for interfacial charge separation, with no significant influence on the charge recombination dynamics.

Regarding sensitizer dyes for DSSCs, carboxylic acid groups of the sensitiser dye are typically employed to anchor the dye on the surface of nanocrystalline TiO_2 particles. These acid groups are however not only critical in determining the extent of dye adsorption to the film, but also could influence the electrostatics of the TiO_2 / dye / electrolyte interface, following the findings described above. It has for example recently been reported that the kinetics of electron injection in dye sensitised TiO_2 films are a function of the protonation of the acid groups of the sensitiser dye. This observation is consistent with a study by Yan et al. which demonstrated that such protons released after dye adsorption onto the semiconductor, remained close to the dye at the surface of the nanoparticles, resulting in positive charging of the surface positive, and thereby in shifting the conduction band to more positive values [5]. Moreover, Tachibana et al. reported the observation of a similar trend by comparing two dyes with the different degrees of protonation of their carboxyl groups, observing that electron injection dynamics accelerated as the proton content in the dyes increased [3].

Building upon these studies of dye protonation, more practical research on this issue has been conducted for complete DSSC devices by Nazeeruddin et al [6]. In this study Nazeeruddin employed a series of ruthenium bipyridyl dyes differing only in the

protonation of their carboxylic acid groups: $[Ru(dcbpyH_2)_2(NCS)_2]$, $(Bu_4N)_2[Ru(dcbpyH)_2(NCS)_2]$ and $(Bu_4N)_4[Ru(dcbpy)_2(NCS)_2]$, where dcbpy represents 2,2'-bipyridyl-4,4'-dicarboxylate, (referred to as dye **1**, dye **2** and dye **3** respectively, in this thesis) [6]. Note that dye **1** has 4 protons, dye **2** has ~2 protons, and dye **3** has ~ 0 protons, as illustrated in Figure 3.2, with the missing protons in dye **2** and dye **3** being replaced by tetra butyl ammonium cations to balance the charges. The study by Nazeeruddin et al. found that the photovoltage increased as the dye proton content reduced, while the photocurrent was decreased. (See Figure 3.3) This observation was understood by a series of kinetic studies on both dye sensitized nanocrystalline TiO_2 films and complete DSSCs [3, 7], concluding that the higher value of V_{oc} for the dye **3**, which had no protons, was attributed to a negative shift of the TiO_2 conduction band compared to dye **1**, and on the other hand the low I_{sc} of dye **3** was attributed to slower kinetics of electron injection. However, these studies did not discuss any influence of different dye loading between the dyes they employed. Such variation in optical density (OD) could not be resolved in their study because they employed scattering TiO_2 layers, in which the OD of dye in the TiO_2 film could not be measured, in order to optimise devise performance. In the study reported herein, non-scattering TiO_2 films were employed to undertake an in-depth comparison of the electron transfer dynamics and DSSC device performance for this series of sensitiser dyes as a function of dye loading.



dye **1** dye **2** dye **3**

Figure 3.2 Chemical structures for dye **1** $[Ru(dcbpyH_2)_2(NCS)_2]$, dye **2** $(Bu_4N)_2[Ru(dcbpyH)_2(NCS)_2]$, and dye **3** $(Bu_4N)_4[Ru(dcbpyH)_2(NCS)_2]$. Note that tetra butyl ammonium is abbreviated as TBA.

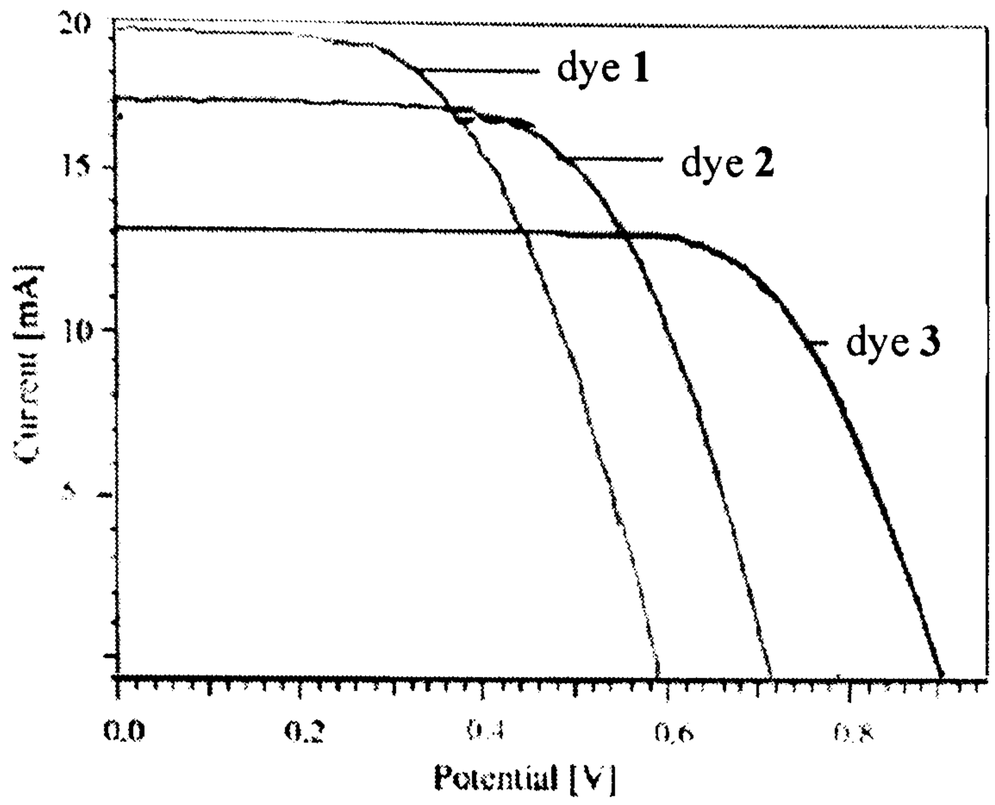


Figure 3.3 Device performance for the dye series reported by Nazeeruddin, showing that that the photovoltage is improved as the dye proton content reduces, while the photocurrent is decreased. [6]

The experiments were divided into two. The first part involves experiments under the condition of matched OD on the TiO_2 film with the three dyes. These data would be important because the correlation among the recombination, the injection yield, and the cell performance could be determined independent of the influence of dye loading. The same analyses were undertaken with varied dye coverages up to full dye loading in order to allow direct comparison to the Nazeeruddin paper, and to investigate more fully the potential of each dye for efficient photovoltaic device performance.

3.2 Experimental

All experiments were essentially carried out as described in Chapter 2. Here the only details specific to this chapter are addressed.

For the dye sensitisation, the optical density of the dye loaded on the 4 μm thickness TiO_2 films made from IC paste was controlled by changing the soaking time of the TiO_2 electrode in 1 mM dye solutions in 1:1 mixture of acetonitrile / *tert*-butanol. This soaking time was varied from a few minutes to overnight at room temperature. For the measurement of I/V data, sandwich cells filled with SB electrolyte, whose composition was addressed in Chapter 2, were employed. The active area was 1.0 cm^2. In order to minimize resistance losses, silver conductive paint (RS 186-3593) was put on the edge of the conductive glasses. All data were acquired under AM1.5 intensity illumination.

All laser experiments were carried out for the sensitised TiO_2 films covered in propylene carbonate to prevent decomposition of the dyes by water or oxygen, and then a piece of cover glass was put on top of the film. Transient absorption data were collected at 800 nm to monitor dye cation signals according to the assignment by previous studies [8], after excitation at 550 nm.

3.3 Results with same dye loading

The samples were prepared by controlling the immersion time of the TiO_2 electrodes in the dye solution to obtain the matched dye loading. The absorbance spectra of the TiO_2 films sensitised with the dye **1**, dye **2** and dye **3** are shown in Figure 3.4. ODs of all three films were around 0.6 at 535 nm. The strong absorption band at 520-530 nm corresponds to a metal-to-ligand charge transfer transition as reported previously [6]. The extinction coefficient for this transition has previously been determined to be ~14,000 $M^{-1}cm^{-1}$, independent of the extent of dye protonation [9].

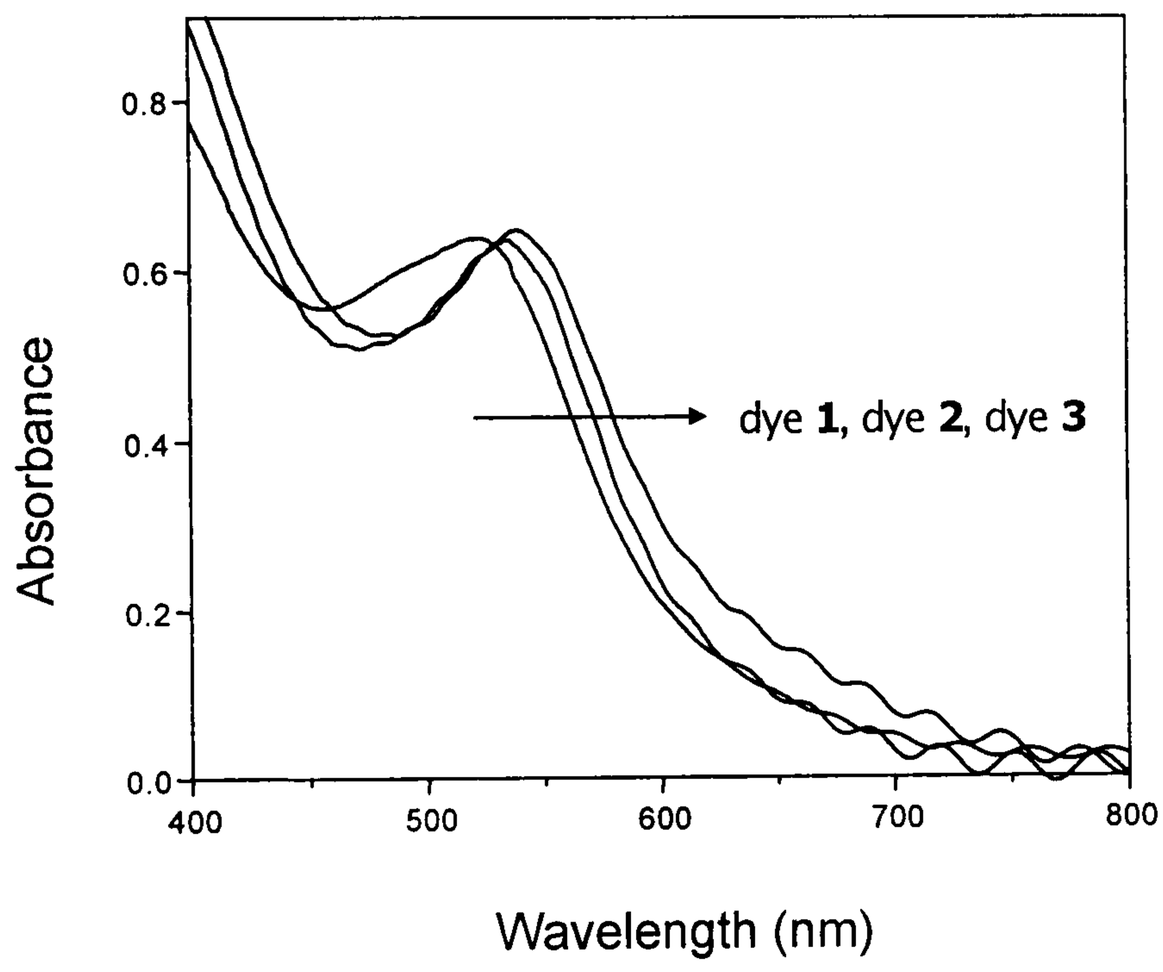


Figure 3.4 Uv-Visible measurements for nanoporous TiO_2 sensitised samples a) dye **1**, fully protonated dye, b) dye **2**, partially protonated dye and c) dye **3**, non-protonated dye.

Device performance of the DSSCs with matched dye loadings is shown in Figure 3.3. Note that as expected the efficiency (η) of the devices was low due to the low dye coverage. It is striking that under these conditions the differences in device performance were only rather modest compared to that reported by Nazeeruddin et al. (see Figure 3.3). Interestingly not only V_{oc} but also I_{sc} decreases as proton content increases [6]. It is noted that the results shown here are reproducible. This is also

different from the results reported by Nazeeruddin et al., carried out under full dye loading, who observed that the photocurrent was decreased as the dye proton content reduced. Regarding this issue, Tachibana has suggested that the higher value of V_{oc} for the dye **3**, can be attributed to a negative shift of the TiO_2 conduction band compared to dye **1**, while the low I_{sc} of dye **3** was attributed to slower kinetics of electron injection relative to the dye **1** [3]. These will be discussed later with the study for varied OD samples.

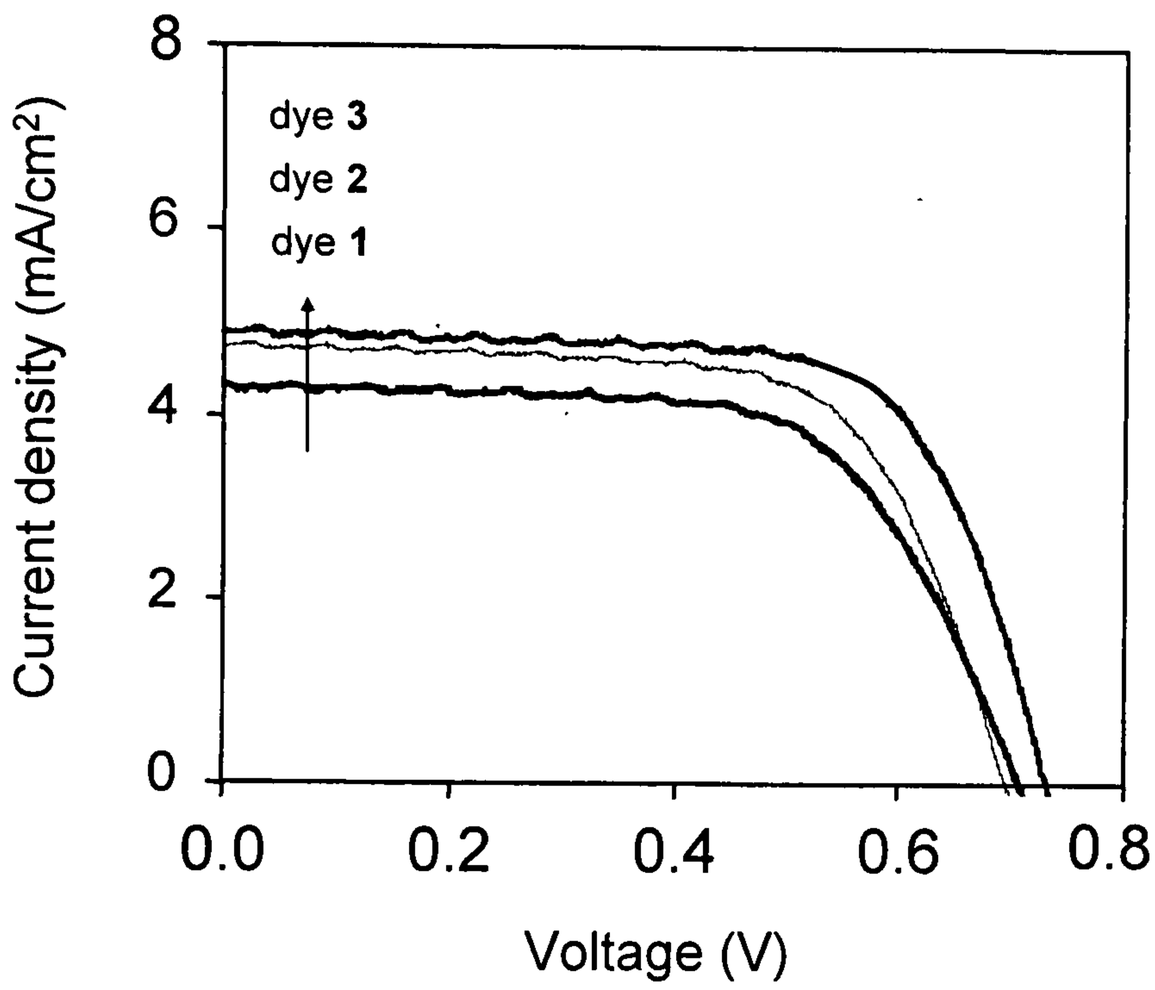


Figure 3.5 IV-characterization for dye **1**, dye **2** and dye **3** with efficiencies (η) of 1.9 %, 2.2 %, and 2.5 % respectively under AM1.5 one sun illumination.

Transient Absorption Spectroscopy (TAS) studies were carried out to measure the electron recombination dynamics and correlate them with device performance. Figure 3.6 illustrates typical electron recombination decays for each dye. As can be seen, the non-protonated dye **3** results in slower electron recombination dynamics compared with dye **2** (2 protons) and dye **1** (fully protonated). Although this difference was not large, these results were reproducible. Since the dye loading was the same for all samples, this difference is only attributed to the number of protons on the dye. It is also apparent from Figure 3.6 that the electron injection yields for the dyes are identical, determined for the initial amplitudes of the transient studies [3, 7] (assuming the same dye cation extinction coefficient for all 3 dyes), suggesting that the electron injection dynamics are

still fast enough to compete with the excited state decay, even though they would be changed as the TiO_2 conduction band is shifted by the protonation, as reported previously [3].

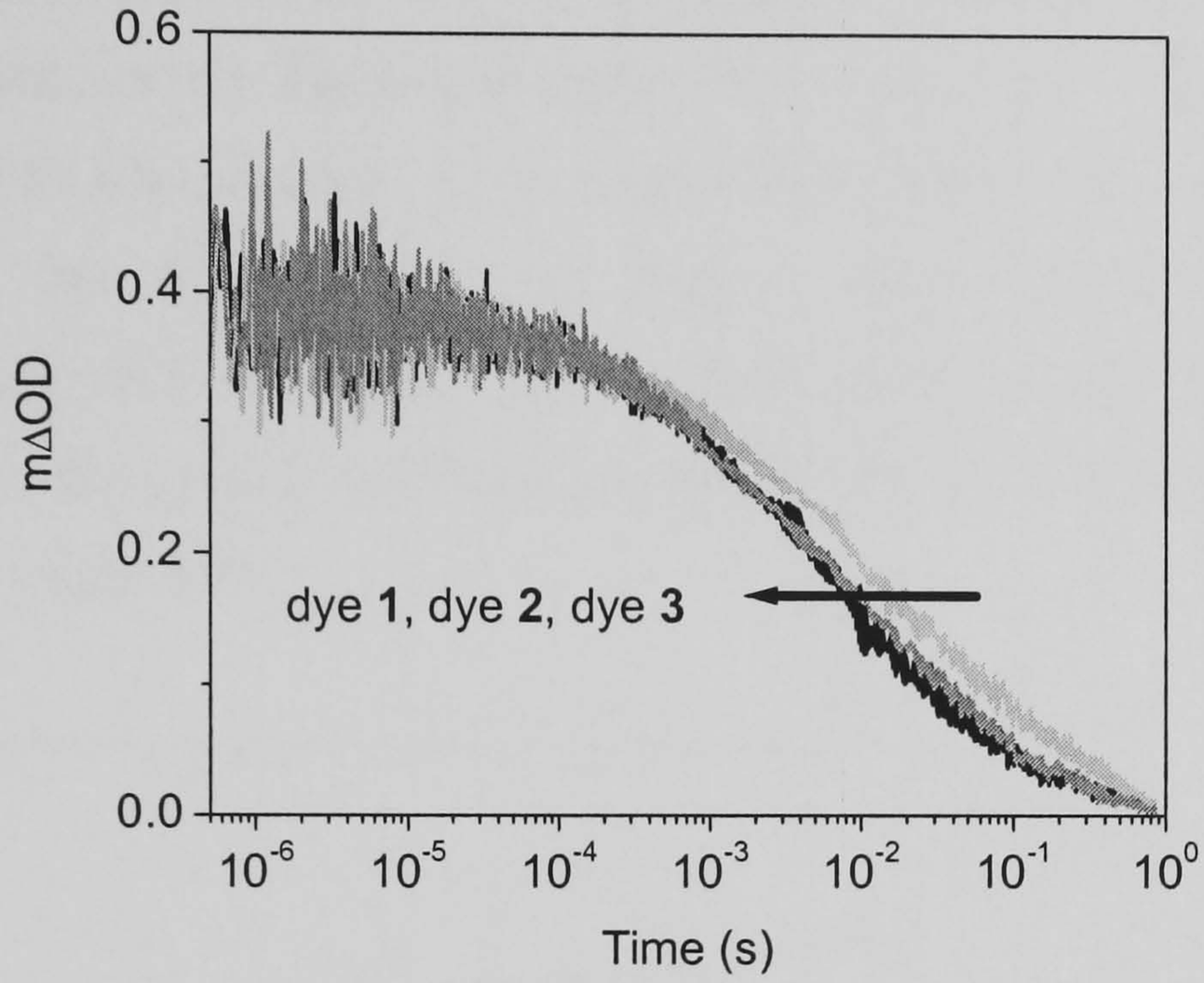


Figure 3.6 Transient absorption data monitoring photoinduced absorption of the dye cation. All data were collected under conditions of excitation at 550 nm and detection at 800 nm. The half times of the decay of dye **1**, dye **2** and dye **3** are 4.7 ms, 5.4 ms and 9.2 ms, respectively. Note that the amplitudes of these signals are not normalized.

3.4 Results under varied dye loading condition

In order to clarify the reason for the difference of the device performance from Nazeeruddin's data and seek the optimised condition for high device performance, a study with varied dye coverage was carried out. Figure 3.7 shows the dye adsorption kinetics for the three Ruthenium dyes as a function of soaking time. For these three dyes, dye absorbance on the TiO_2 films approached a maximum within 10 hours. This saturation behaviour was observed to be strongly dye dependent. As can be seen, the fully protonated dye **1** results in the highest optical density for 4μm thick nanocrystalline TiO_2 film while dye **3** (no protons) showed lower dye loading, giving for the first time a clear proof that more protons lead to more efficient binding of the dye to the surface of the TiO_2.

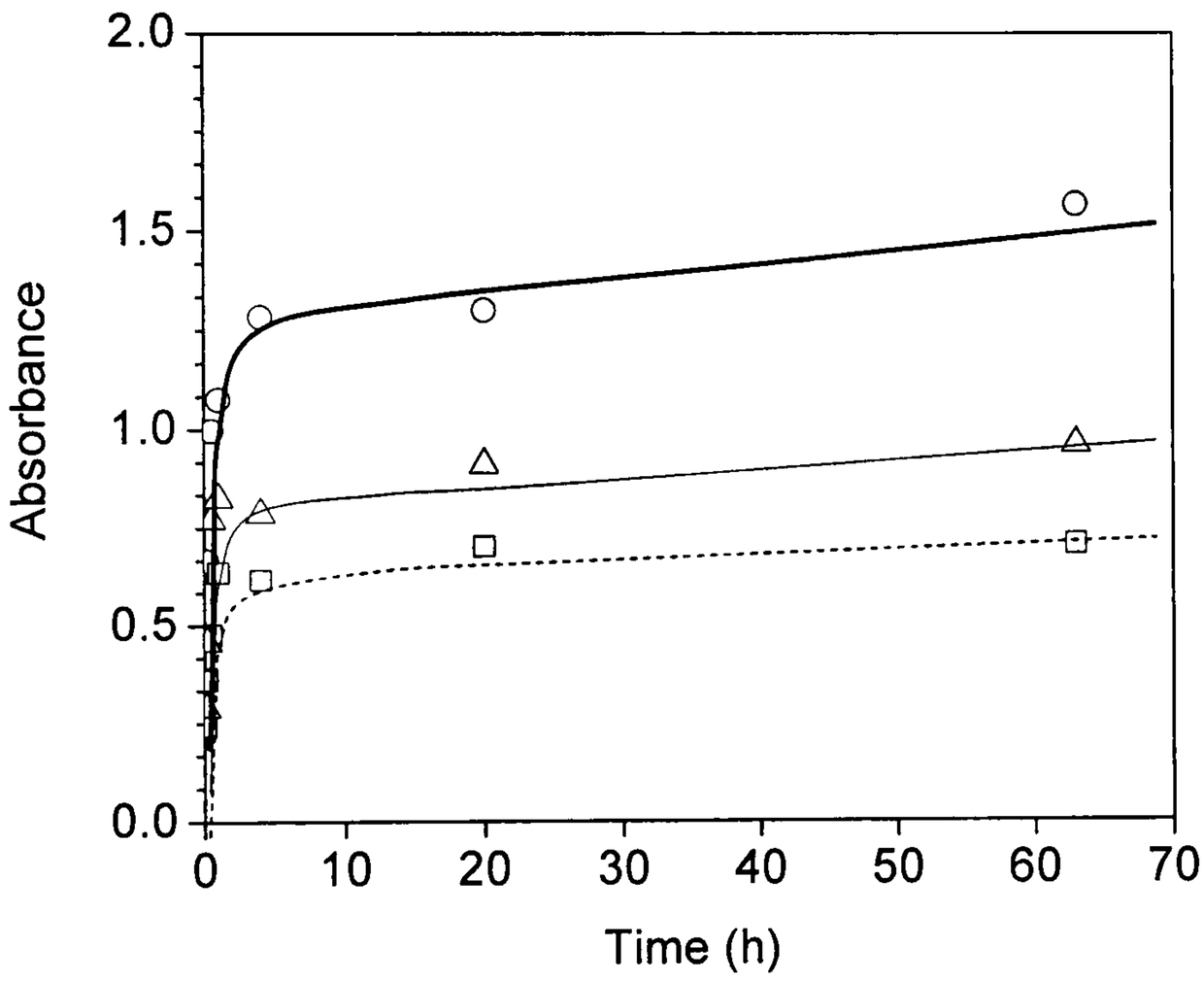


Figure 3.7 Adsorption maxima for dye **1** (bold line), dye **2** (thin line) and dye **3** (dashed line) as a function of sensitizing time in the dye solution at 23 °C.

Device characterization of these samples was carried out by measuring the IV curves. For a graphical comparison of the different parameters, Figure 3.8 shows separately the efficiency (η), fill factor (*ff*), short-circuit current (I_{sc}), and open-circuit voltage (V_{oc}). For each cell, dye loading was determined by the absorption maxima of the film optical density at around 530 nm, corresponding to the MLCT transition of the sensitiser dyes. It is apparent from Figure 3.8 that the device performance

characteristics were strongly dependent upon dye loading, with variations in performance between the different dyes at the same loading being of only secondary importance. In particular, I_{sc} was observed to be strongly dependent upon dye loading, increasing up to a maximum at an optimal dye loading (OD_{opt}) and then decreasing as the dye loading was increased further. Note that this trend was observed to be dye dependent. At low dye loadings, the deprotonated dye **3** gave the highest the currents, consistent with the data under the matched dye loading conditions, as shown in Figure 3.5. Furthermore, it was found from Figure 3.8 that the dye loading for this dye saturated at a relatively low level (OD ~0.7). The highest I_{sc} was observed for the dye **1**, at a dye loading corresponding to OD ~1.1. For all three dyes, increasing the dye loading beyond an optimal level (OD_{opt}) resulted in a decrease in device efficiency. OD_{opt} was found to be dye dependent, being 0.7, 0.8 and 1.1 for dye **1**, dye **2** and dye **3** respectively. Assuming extinction coefficient at 550 nm is 14,000 $M^{-1}cm^{-1}$ for all 3 dyes, these optimal OD is correspond to dye loading of 50, 57 and 78 nanomoles cm^{-2} for dyes **1**, **2** and **3**, respectively. Assuming dye areas of $7*10^{-15}$ cm^2, these values correspond to ~ 46, 53 and 73% of monolayer coverage for dye **1**, **2** and **3** respectively. (See section 2.1.2.3 in Chapter 2) Optimum overall device efficiency of 3.4% was observed for dye **1** with a dye loading of OD ~1 at 535 nm.

The influence of dye loading and protonation on the I_{sc} was closely matched to studies of electron injection yield determined by TAS. Transient studies such as those shown in Figure 3.4 were undertaken as a function of dye loading. The initial amplitude of the transient signal at 10^{-6} s is plotted as a function of film optical density in Figure 3.9 as an indication of the charge separation yield. It is apparent that for dye loadings beyond OD_{opt}, the electron injection yield decreases for all three dyes, with the highest yield for the most protonated dye, **1**, in good agreement with the current / voltage data. Surprisingly, the half time of the recombination dynamics as a function of dye loading shows a similar dependence upon dye loading, as shown in Figure 3.10. In this figure as the dye loading increases, the recombination accelerates to a maximal rate for the dye loading corresponding to OD_{opt}. Increasing the dye loading beyond this optimal level results in a retardation of the dynamics.

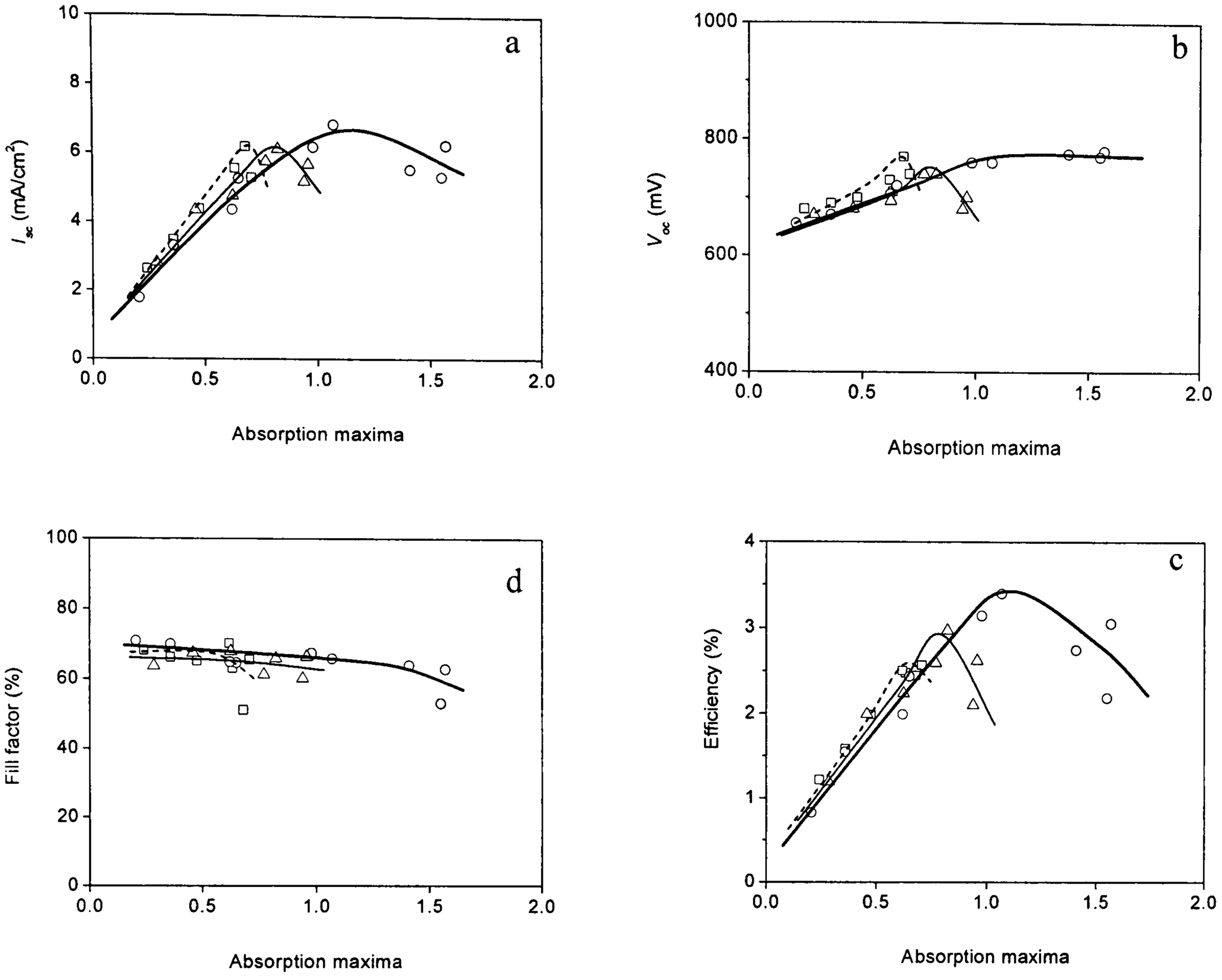


Figure 3.8 IV characterizations for the cells sensitised by dye **1** (bold line), dye **2** (thin line) and dye **3** (dashed line) as a function of dye loadings, as monitored by film absorbance at 525, 530 and 531 nm respectively, showing the effect of dye loading upon device performance. The figure shows I_{sc} (Fig. 3.8a), V_{oc} (Fig. 3.8b), efficiency (η) (Fig. 3.8c) and fill factor (*ff*) (Fig. 3.8d), in a clockwise direction from the top of left hand side. The effective area of a cell was 1 cm^2. All data were monitored under AM1.5 one sun illumination.

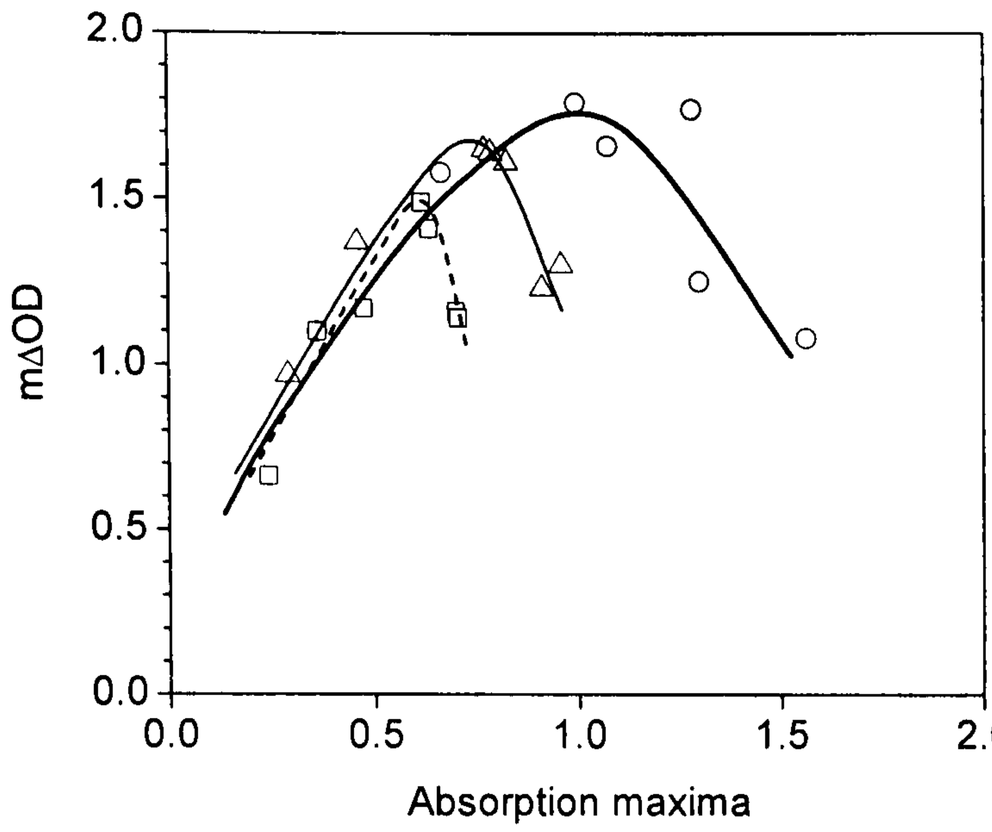


Figure 3.9 ΔOD for nanocrystalline TiO_2 films sensitised by dye **1** (bold line), dye **2** (thin line) and dye **3** (dashed line), monitoring at 800 nm in 1 μs after excitation at 550 nm, indicating the electron injection yield from dyes to TiO_2 conduction band, as a function the dye sensitised TiO_2 film absorption maxima. TAS data were collected for dye sensitised nanocrystalline TiO_2 film covered in propylene carbonate.

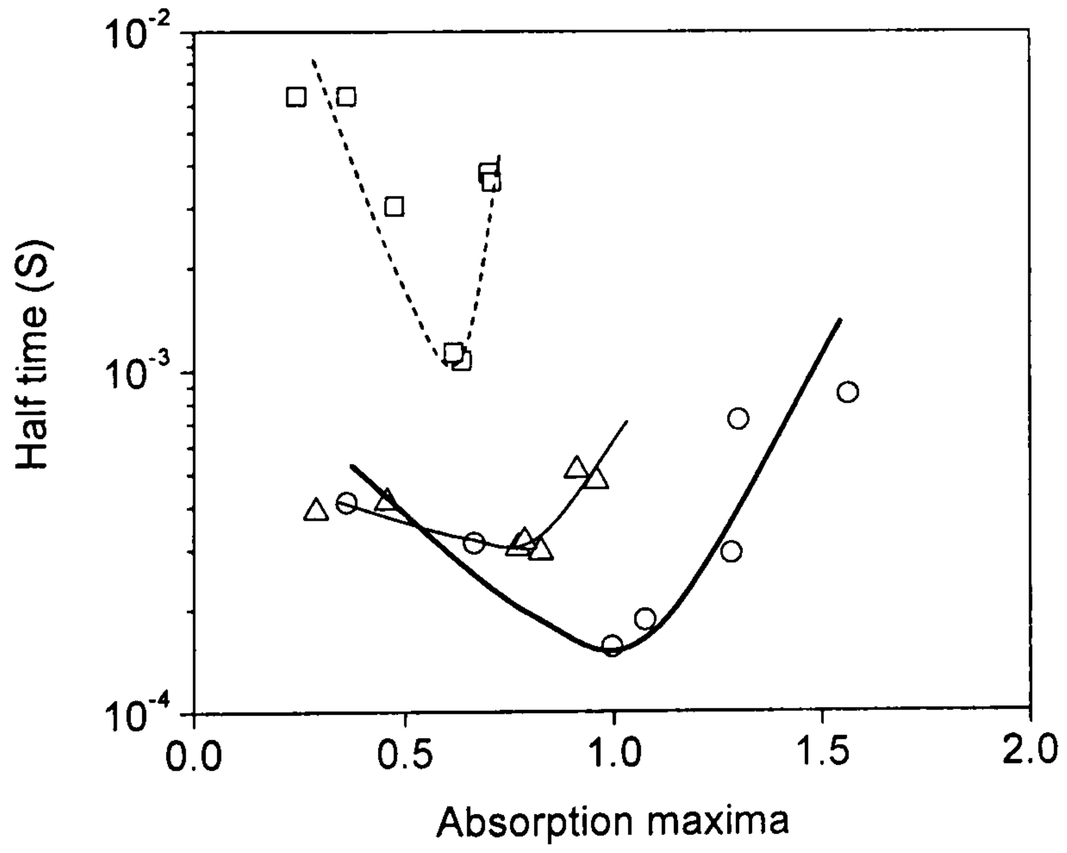


Figure 3.10 The half-time of decay for nanocrystalline TiO_2 films sensitised by dye **1** (bold line), dye **2** (thin line) and dye **3** (dashed line), monitored at 800 nm after excitation at 550 nm, indicating electron recombination dynamics with the dye cation, as a function of the dye sensitised TiO_2 film absorption maxima. The data were collected the dye sensitised TiO_2 films covered in propylene carbonate.

3.5 Discussion

3.5.1 Influence of dye loading upon proton content

The time resolved absorbance maxima data (Figure 3.7) clearly show the dye loading is improved as the dye proton content increases, with the highest OD of ~1.6 for dye **1**. This suggests that the protons have an important role in aiding the adsorption of dyes onto the surface of the TiO_2. This most probably results from the more neutral electrostatics of dye **1**, with dye **2** and dye **3** being increasingly negatively charged, resulting in electrostatistic repulsion between these dyes hindering absorption onto the TiO_2. This is in good agreement with a previous study done by Yan et al. which indicates that the protons released by dye adsorption would be localized adjacent to the dye carboxyl groups on the surface of TiO_2 [5], while TBA cations in dye **2** and dye **3** would remain solvated by the electrolyte.

3.5.2 Correlation between TAS and I/V data

It is apparent from the data obtained at matched dye loading shown in Figures 3.5 and 3.6 that the degree of protonation of the dye has an influence on the electron recombination kinetics and therefore on the DSSC device performance, although the extent of the influence is modest. The dye **3** based DSSC shows a higher V_{oc} relative to dye **1**, which can be attributed to a shift of the conduction band energetics on the semiconductor because of the influence of the protons, with for example the energetics being most negative for the dye **3** as discussed previously [3, 10]. Note that this trend in V_{oc} is consistent with the previous study by Nazeeruddin et al. [6].

In terms of photocurrent, it is found from the data obtained at matched dye loading that I_{sc} is also higher for dye **3** than for dye **1**. This difference can not be attributed to differences in injection yield, as the TAS data indicate the same injection yields for all three dyes. The improvement in J_{sc} is however consistent with the slower recombination dynamics observed for the dye **3** dye, which could be expected to result in lower recombination losses in the devices, and therefore potentially a higher J_{sc}.

The slower recombination dynamics observed for the deprotonated dyes can be most readily understood in terms of electrostatic repulsion between the negatively charged dye and the injected electrons. For the protonated dye **1**, the negative charge of the dye is compensated by the positive charge of co-adsorbed protons, allowing injected electrons to approach the TiO_2 surface and thereby accelerating recombination losses.

The lower I_{sc} observed for the dye **1** dye is not in agreement with the previous study by Nazeeruddin et al., in which the photocurrent for dye **1** was higher [6]. The higher current observed for the dye **1** by Nazeeruddin et al. was assigned to an improved injection efficiency. However the studies shown here suggest that this is probably not the case, and that the higher current should be attributed to the saturated dye loadings employed in this study, resulting in a relatively high optical density for the dye **1** sensitised film, as discuss the further below.

All the data shown in Figure 3.7 - 3.10 demonstrate a clear dependence of photovoltaic device performance upon film optical density. Figure 3.8c shows direct correlation between OD on film and overall device efficiency, mainly resulting from improvement of I_{sc} for higher OD sensitized films, as shown in Figure 3.8a. This observation is in good agreement with the data in Figure 3.9 showing an increase in injection yield as a function of OD.

It is apparent from both the current / voltage and the TAS studies (Figures 3.8 and 3.9) that there is an optimal dye loading for each dye, corresponding to OD_{opt}. This observation can be most readily understood by dye bi-layer or aggregation formation for dye loadings greater than OD_{opt}. In terms of the injection yield, more dye loading is observed to lead to a higher injection yield at the conditions below the OD_{opt}. This is consistent with a previous study by Haque showing that the electron injection dynamics are sufficiently fast to compete with the excited state decay, resulting in theoretically unity charge separation yield [7]. Therefore, the injection yield would be expected to increase with the dye loading. On the other hand, it is observed that as more dyes are adsorbed onto the TiO_2 surface beyond OD_{opt}, the injection yield is decreased as shown in Figure 3.9. This observation is clearly consistent with studies which have recently been reported, showing dye aggregation retards electron injection dynamics [11, 12]. It

is also found from Figure 3.9 that dye **1** is less prone to such dye aggregation formation compared to the other dyes, potentially due to the lower electrostatic repulsion between dyes for dye **1** as discussed previously, resulting in a denser dye monolayer for the dye.

An acceleration of recombination dynamics as the dye loadings are increased up to OD_{opt} is observed for all three sensitiser dyes. This can be tentatively assigned to cation hopping between adsorbed dyes, referred as to a lateral diffusion [13], resulting in accelerated recombination dynamics for a denser dye monolayer, as illustrated in Figure 3.11. On the other hand, the trend of slower dynamics beyond OD_{opt} can be attributed to dye aggregation increasing the spatial separation of dye cations from the TiO_2 surface (See Figure 3.11).

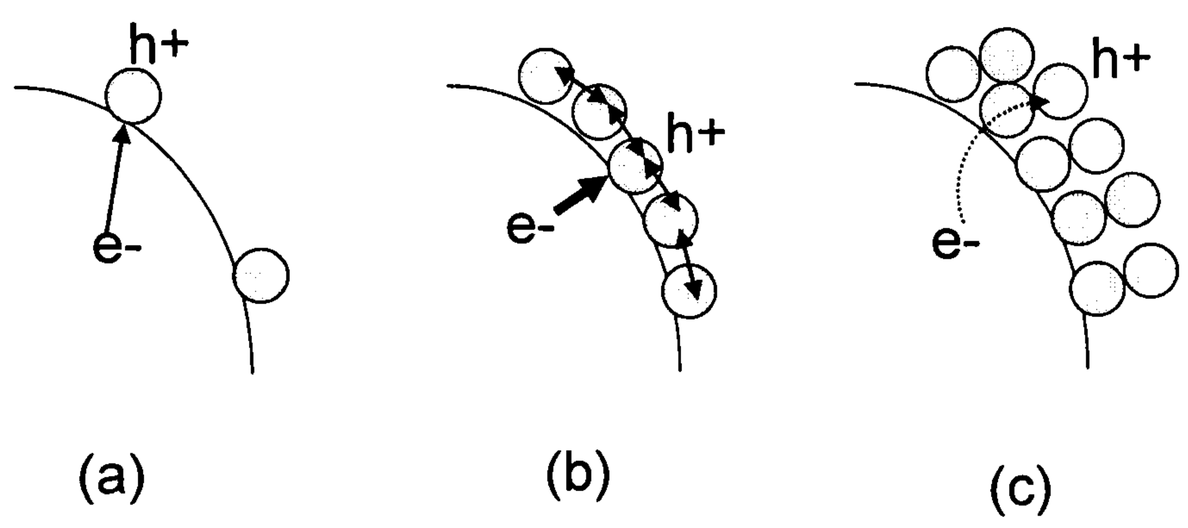


Figure 3.11 Schematic picture regarding the electron recombination dynamics at the condition of lower dye coverage (a), at optimal dye layer coverage (OD_{opt}) (b) and at higher dye coverages, $OD > OD_{opt}$ (c), showing faster dynamics due to lateral diffusion of dye cations. Note that small circles represent the adsorbed dyes on the TiO_2 surface.

In summary, according to these results, one can conclude that were the dye loading to be controlled properly at OD_{opt}, dye **1** would be the best dye out of the series. For example, in Figure 3.8c the highest efficiency of 3.5 % can be attained by using the dye **1**. Therefore, in terms of fabrication to optimize device performance the sensitising time is very critical. Another suggestion from these studies concerns the potential of dye **3** as a sensitizer dye. As shown in Figure 3.8c, the dye **3** can lead to modestly but

significantly higher performance than the other dyes under matched dye loading condition. A serious problem of dye **3** seems to be the difficulty in achieving high loadings, attributed to electrostatic repulsion between the adsorbed dyes. If this dye could be adsorbed onto TiO_2 at loading densities matching those of dye **1** without significant aggregation, it should have the capability to overtake the performance of dye **1**. Further studies to address this issue should be planned.

3.6 References

1. Rothenberger, G., D. Fitzmaurice, and M. Gratzel, *Optical Electrochemistry .3. Spectroscopy of Conduction-Band Electrons in Transparent Metal-Oxide Semiconductor-Films - Optical Determination of the Flat-Band Potential of Colloidal Titanium-Dioxide Films.* Journal of Physical Chemistry, 1992. **96**(14): p. 5983-5986.

2. Haque, S.A., et al., *Parameters influencing charge recombination kinetics in dye- sensitized nanocrystalline titanium dioxide films.* Journal of Physical Chemistry B, 2000. **104**(3): p. 538-547.

3. Tachibana, Y., et al., *Electron injection kinetics for the nanocrystalline TiO2 films sensitised with the dye (Bu4N)(2)Ru(dcbpyH)(2)(NCS)(2).* Chemical Physics, 2002. **285**(1): p. 127-132.

4. Kelly, C.A., et al., *Cation-controlled interfacial charge injection in sensitized nanocrystalline TiO2.* Langmuir, 1999. **15**(20): p. 7047-7054.

5. Yan, S.G. and J.T. Hupp, *Semiconductor-based interfacial electron-transfer reactivity: Decoupling kinetics from pH-dependent band energetics in a dye-sensitized titanium dioxide aqueous solution system.* Journal of Physical Chemistry, 1996. **100**(17): p. 6867-6870.

6. Nazeeruddin, M.K., et al., *Investigation of sensitizer adsorption and the influence of protons on current and voltage of a dye-sensitized nanocrystalline TiO2 solar cell.* Journal of Physical Chemistry B, 2003. **107**(34): p. 8981-8987.

7. Haque, S.A., et al., *Charge separation versus recombination in dye-sensitized nanocrystalline solar cells: the minimization of kinetic redundancy.* Journal of the American Chemical Society, 2005. **127**(10): p. 3456-3462.

8. Tachibana, Y., et al., *Subpicosecond interfacial charge separation in dye-sensitized nanocrystalline titanium dioxide films.* Journal of Physical Chemistry, 1996. **100**(51): p. 20056-20062.

9. Nazeeruddin, M.K., et al., *Acid-base equilibria of (2,2 '-bipyridyl-4,4 '-dicarboxylic acid)ruthenium(II) complexes and the effect of protonation on charge-transfer sensitization of nanocrystalline titania.* Inorganic Chemistry, 1999. **38**(26): p. 6298-6305.

10. Tachibana, Y., et al., *Modulation of the rate of electron injection in dye-sensitized nanocrystalline TiO2 films by externally applied bias.* Journal of Physical Chemistry B, 2001. **105**(31): p. 7424-7431.

11. Oekermann, T., et al., *Electron transport and back reaction in electrochemically self- assembled nanoporous ZnO/dye hybrid films.* Journal of Physical Chemistry B, 2004. **108**(24): p. 8364-8370.

12. Moser, J.-E., *Origin of the kinetic heterogeneity of ultrafast light-induced electron transfer from Ru(II)-complex dyes to nanocrystalline semiconducting particles.* Chimia, 2005. **59**(3): p. 123.

13. Bonhote, P., et al., *Long-lived photoinduced charge separation and redox-type photochromism on mesoporous oxide films sensitized by molecular dyads.* Journal of the American Chemical Society, 1999. **121**(6): p. 1324-1336.

4

Supermolecular sensitisation of nanocrystalline TiO_2 films

This chapter addresses the use of secondary electron donor groups attached to the sensitiser dye to retard interfacial charge recombination dynamics. This study specifically focussed on DSSCs, but also has wider relevance to control of interfacial electron transfer dynamics in general.

4.1 Introduction

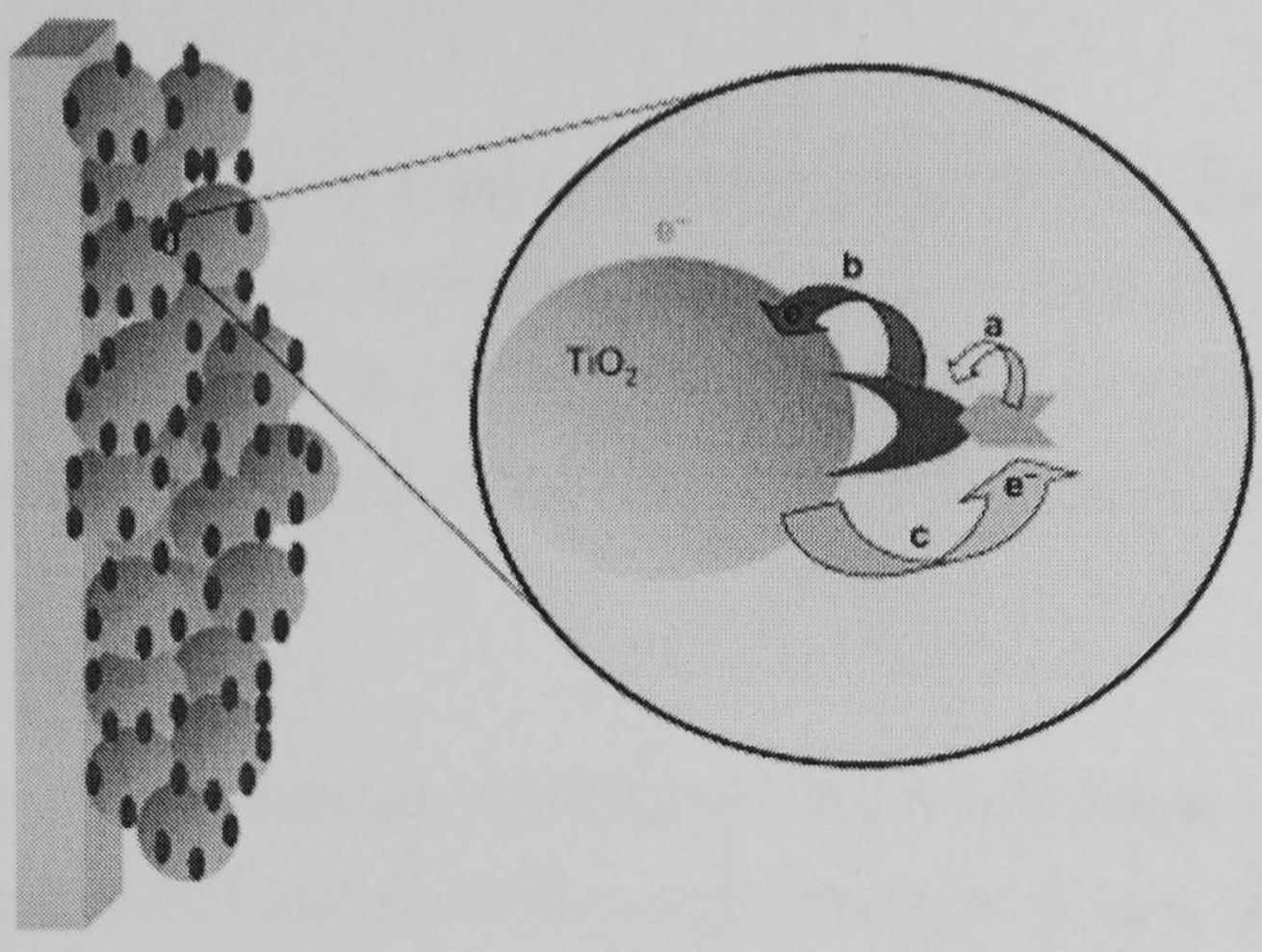
Light-driven electron-transfer processes between molecular adsorbates, semiconductor nanomaterials and adsorbed redox molecules have been a subject of intense research in recent years [1]. Such electron-transfer processes are fundamental to many applications of semiconductor nanomaterials in photography [2], photocatalytic degradation of pollutants [3], quantum dot devices [4] and solar energy conversion [5]. In all of these applications, a key requirement is that light absorption results in the efficient generation of a long-lived charge-separated state.

For photovoltaic devices including DSSCs, it is necessary to achieve high rates of charge separation and collection compared to interfacial charge-recombination processes in order to achieve high device efficiencies. A number of strategies are currently being developed to optimise these dynamics, including the insertion of inorganic barrier layers between TiO_2 and the sensitiser dye [6], the use of alternative redox couples [7], and the development of novel sensitiser dyes [8].

On the other hand, the synthesis of supermolecular (multicomponent) molecules is attracting strong interest due to their potential application in molecular electronic devices [9, 10]. Such supermolecular structures provide a potentially attractive

approach to controlling the charge separation, and recombination dynamics at the molecule/nanocrystal interfaces. In particular, by introducing a secondary electron transfer function, or "supersensitiser" into the supermolecular complex, as illustrated in Scheme 4.1, it is possible to retard the interfacial charge-recombination dynamics whilst retaining efficient light-induced charge separation. This approach has previously been employed by using either a Ru(II) tris-bipyridine derivate to demonstrate the supersensitiser function [11], although the relatively weak red optical absorbance of this dye relative to the most widely employed dyes, such as dye **2** as shown in Figure 3.2, precluded its practical device application, and by the use of organic molecules such as "molecular spacers" linked to the redox chromophore [12].

This chapter shows that by appropriate design of a ruthenium dye analogue of $RuL_2(NCS)_2$ it is possible to achieve molecular control of the back electron-transfer dynamics whilst maintaining good red-light absorption and efficient electron injection. This control is achieved by "supersensitising" the dye molecule by the addition of a secondary electron-donor group, in this case a *N*,*N*-(di-*p*-anisylamino)phenoxymethyl(DAP) group, referred to as $[RuLL'(NCS)_2]$ (dye **4**) where L' represents 4-[4-(*N*,*N*-di-*p*-anisylamino)phenoxymethyl]-4'-methyl-2,2'-bipyridine in this thesis. (Figure 4.1) It is shown that supersensitiser increases the physical separation of the dye cation from the electrode surface and results in remarkably slow, interface limited recombination dynamics.



Scheme 4.1 Schematic representation of electron-transfer (ET) processes in dye-sensitised solar cells showing photogeneration of the dye excited state: a) electron transfer from the secondary electron donor moiety, b) electron injection into the semiconductor and c) the wasteful charge-recombination pathway of the injected electron with the oxidised dye molecules.

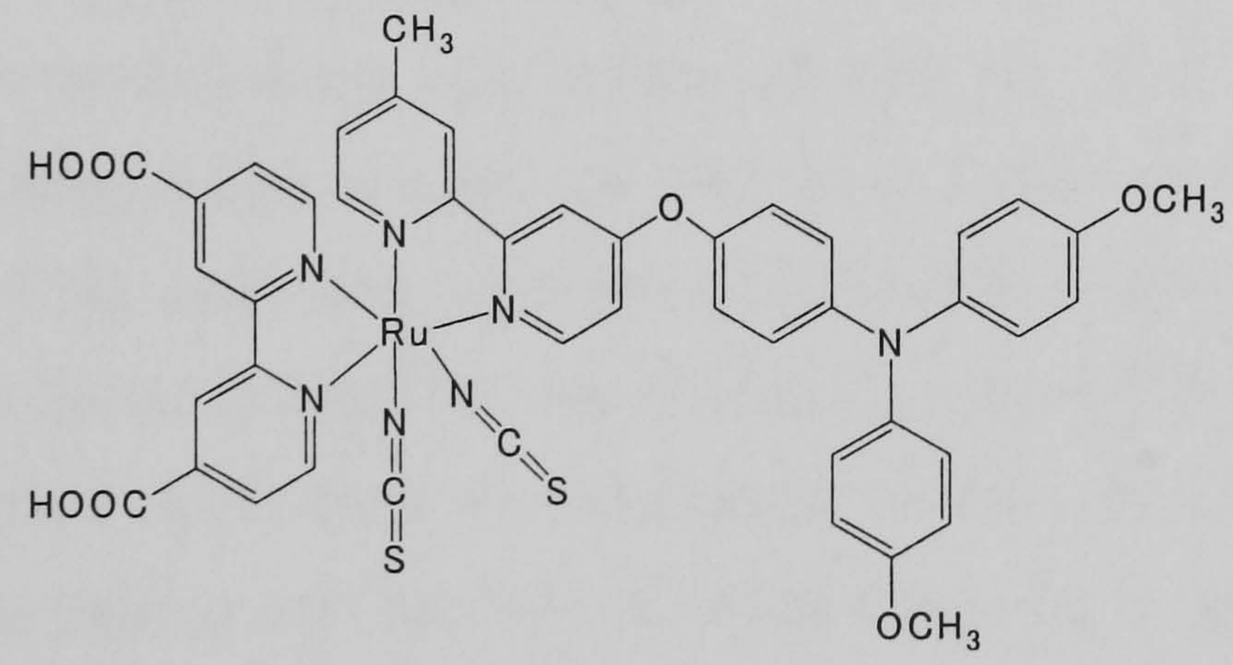


Figure 4.1 Chemical structure of [RuLL'$(NCS)_2$] (dye **4**), showing a secondary electron-donor moiety.

4.2 Experimental

The general procedures of experiments were carried out as described in Chapter 2. Here specific details are addressed. The dye **2** and **4** was synthesised by Nazeeruddin and Lagref et al. in EPFL [13]. The dye solution of dye **4** was prepared in the concentration of 0.2 mM in ethanol. It took approximately 12 hours to sensitise TiO_2 films.

An analogue of DAP group, 4-(diphenylamino)benzaldehyde was used for the purpose of assignment of spectra of the cation of dye **4**. It took overnight at room temperature to sensitise a film in 1 mM 4-(Diphenylamino)benzaldehyde solution in Ethanol.

Semi-empirical calculations were carried out by Dr Emilio Palomares (University of Valencia) to estimate the distance (r) between the positions of HOMO orbital on the dyes and the TiO_2 surfaces anchored by the carboxyl acid in the dye. Molecular orbitals and optimized geometeries for free molecules were calculated using Hyperchem 7 program package running on a PC AMD Athlon XP-2000+ 1.25 GHz. Geometrical optimizations were performed with the ZINDO/1 parameter set. The overlap weighting factors σ-σ and π-π were set at 1.265 and 0.585, respectively. For calculation of the optimized geometry of the Ru(II) polypyridyl dyes, it was assumed covalent bonds through the two carboxyl groups (-COOH) to Ti^{4+} atoms. These semi-empirical calculations were performed on the cation state of both dyes. The calculated Ru-N(bpy) and Ru-N(NCS) bond distances, as also summarised in Table 4.1 are within 1% of those obtained from crystallographic data supporting the validity of the calculations and indicating that the removal of one electron from the complexes does not induce dramatic geometry changes [14].

4.3 Results and discussion

4.3.1 Semiempirical calculations

For the optimised geometry of the Ru^{II} polypyridyl dyes, it was assumed that the two carboxyl groups (-COOH) are linked to the Ti^{4+} surface. The semiempirical calculations were performed on the cation state of both dyes.

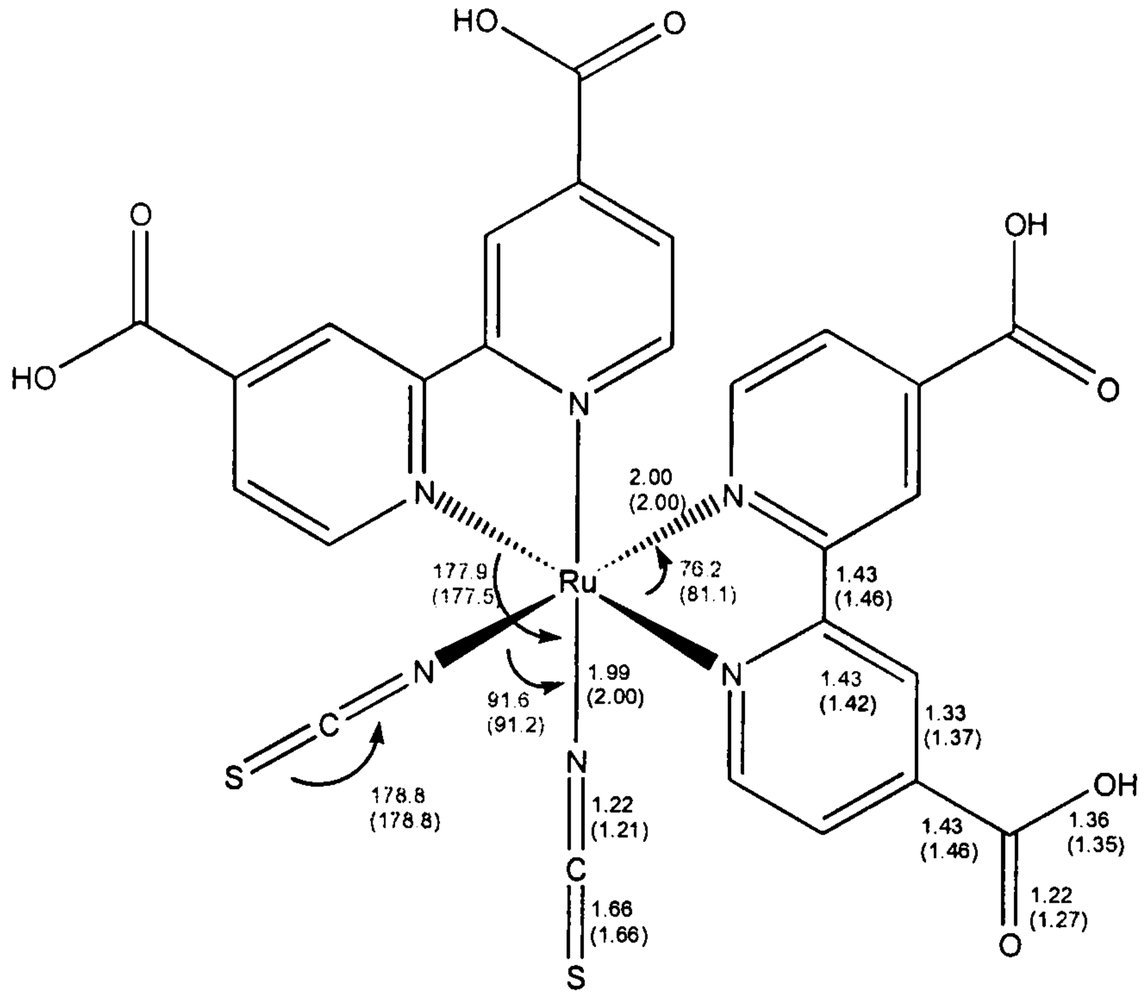


Figure 4.2 Comparison of bond (black) distances and angles (red) calculated using ZINDO/1 for the cation state of dye **2** with the corresponding experimental X-ray data [15]. The values in parentheses correspond to the X-ray data.

First of all the validity of the calculation was considered with the control dye (dye **2**). Figure 4.2 shows a comparison between the optimised geometry of the cation state determined by the semi-empirical ZINDO/1 calculations as detailed in section 4.2, against the X-ray structure of the fully protonated analogue of the dye **2** reported previously [15]. The calculated Ru-N(bpy) and Ru-N(NCS) bond lengths, as summarised in Table 4.1, are within 1 % of those obtained from crystallographic data, supporting the validity of this calculations [14]. These data also indicate that the removal of one electron from the complexes does not induce dramatic geometric changes. Furthermore these results are in good agreement with similar calculations

reported previously [15, 16], providing further support for the validity of this semiempirical calculations.

Table 4.1 Comparison of bond lengths (Å) and angles (^{0}) of crystallographic data for cis-$Ru(L)_2$ ($NCS)_2$ with ZINDO/1-optimized geometries for the cation states of dye **2** and dye **4**.

	cis-Ru $(bpy)_2(NCS)_2$ [c]	**dye 2 [d]**	**dye 4 [d]**
Ru-NCS [Å]	2.02	1.99	1.97
Ru-N(bpy) [Å]	2.06	2.04	1.99
NCS-Ru-NCS [a] [°]	91.9	91.6	87.5
N(bpy)-Ru-N(bpy) [°]	81.3	76.2	75.9
(bpy)-(bpy) [b] [°]	90.6	89.9	87.5

[a] NCS-Ru-NCS refers to the pby ligands to the cis to the NCS ligands.

[b] Dihedral angle between the mean planes of bipyridine ligands.

[c] Crystallographic data from Shklover et al. [14]

[d] Data from semi-empirical calculations.

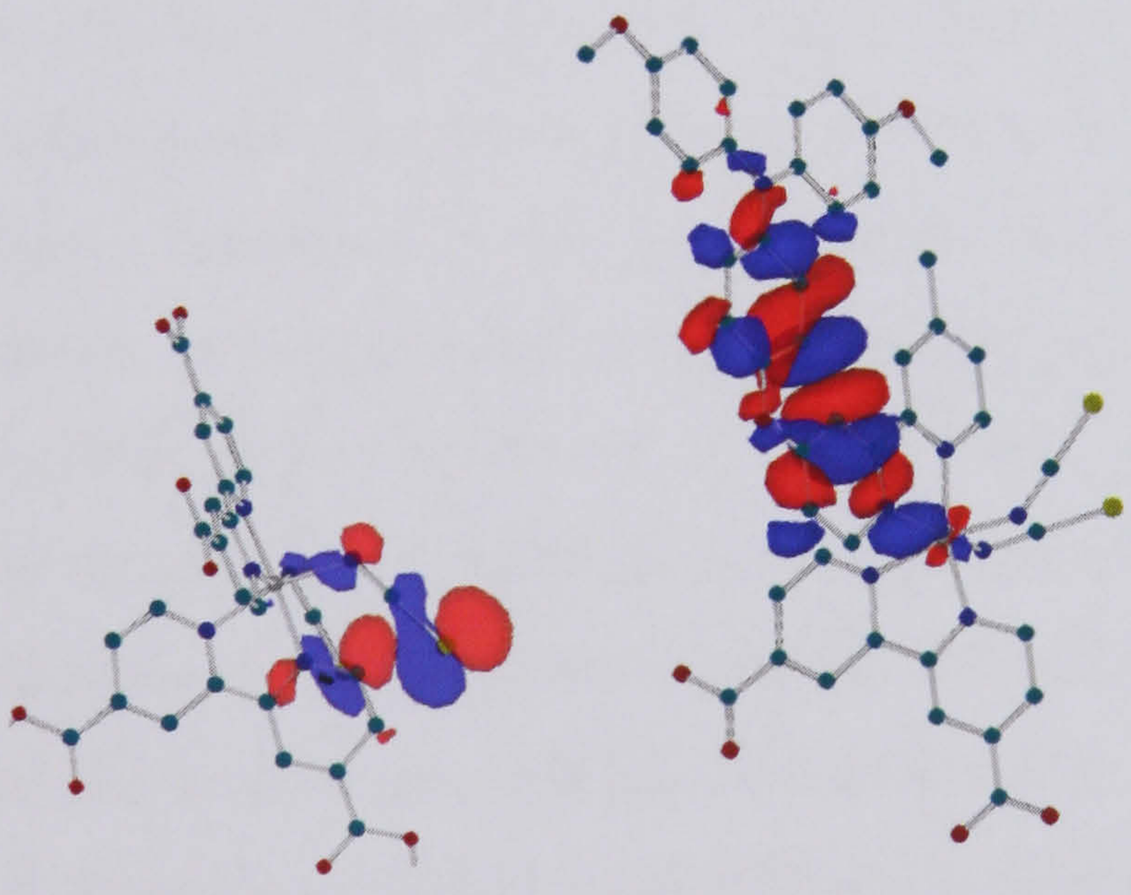


Figure 4.3 Graphical representation of the HOMOs of a) dye **2** and b) dye **4**. Atoms in turquoise, red, blue and pale yellow correspond to carbon, oxygen, nitrogen and sulfur, respectively.

These data in Table 4.1 show that the Ru metal co-ordination centres of both dyes are expected to be very similar, as seen by the close match of their optical absorbance spectra (Data published in ref [13]). The orbital profiles for the HOMO's of both dyes presented in Figure 4.3 show that the HOMO of the dye **2** has larger amplitude on NCS ligands, (similar results were obtained by Rensmo et al. [17]) and within the NCS ligands the amplitude is more on the sulfur atom. The HOMO for the dye **4** is clearly shifted to the secondary electron donor moiety (DAP), displacing the positive charge (hole) in the oxidised form of dye **4** from the NCS ligands closer to the DAP group. This results in an increased separation of the HOMO orbital from the TiO_2 surface, as desired in order to achieve slower charge-recombination dynamics.

4.3.2 Transient absorption study

4.3.2.1 Recombination dynamics

The primary function of the *N*,*N*-(di-*p*-anisylamino)phenoxymethyl (DAP) group is to accept the positive charge (hole) after electron injection from the dye-excited state into the conduction band of the nanocrystalline TiO_2. This results in an increase in the physical separation of the charged species. To assay this function, transient absorption spectroscopy was employed to measure the charge-recombination kinetics (reaction c, Scheme 4.1). The decay of the induced absorption of the dye **2** and dye **4** cations was monitored following pulsed laser excitation of the dye-sensitised TiO_2 films, in the absence of any applied bias or redox-active electrolyte. Typical data for the charge-recombination process is shown in Figure 4.4 while there is some complication in this data (see Appendix 4.5), it is apparent that the decay dynamics of the dye **4** cation are retarded 1000-fold relative to that of the dye **2** cation, with decay half times, $t_{50\,\%}$, of 0.71 s and 0.85 ms, respectively. It is noteworthy that this recombination for the dye **4** is the slowest dynamics reported to date for such dye sensitised films. This retardation cannot be attributed to differences in oxidation potential of the two dyes, as the recombination reaction is thought to occur in the Marcus "inverted region" [18]. This is where the smaller reaction free energy of the dye **4** would be expected to result in accelerated recombination dynamics, contrary to the experimental observation. Instead the retardation is attributed to an increased

distance of the dye cation from the electrode surface due to localisation of the dye **4** cation on the DAP moiety, consistent with the semiempirical calculations and electrochemical data detailed above.

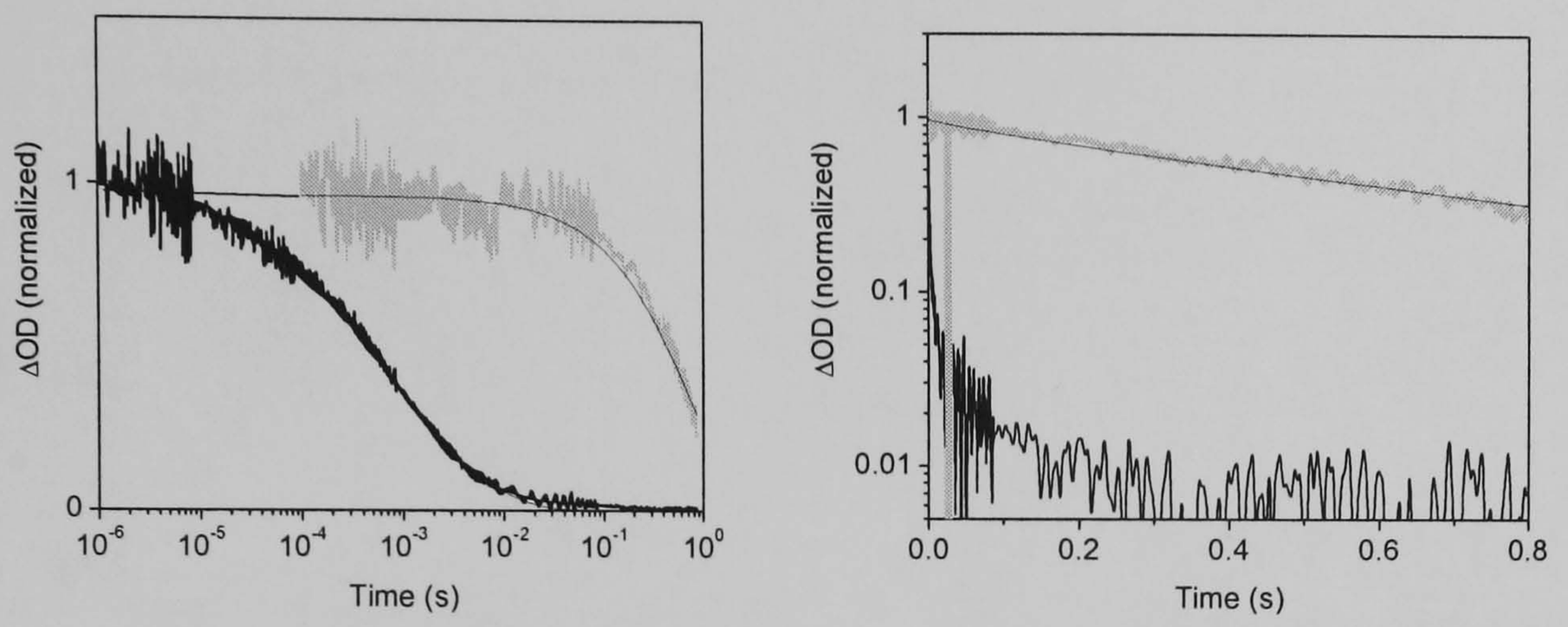


Figure 4.4 Transient absorption data monitoring charge-recombination dynamics for TiO_2 films sensitised with dye **2** (black trace) and dye **4** (grey trace). Both figures show the same data with being a linear/log plot (left hand side) and being log/linear plot (right hand side). The black thin lines are the fits to the decay kinetics corresponding to i) a stretched exponential (ΔO.D. $\propto$ exp $(-(t/\tau)^{\alpha})$, α=0.44) for liner/log plot and ii) a monoexponenetial decay for log/liner plot. The signal size has been normalised for comparison purposes. Data collected at a probe wavelength of 800 nm for dye **2** and 850 nm for dye **4**, following optical excitation at 550 nm.

4.3.2.2 Assignment of the dye cation

Localisation of the dye **4** cation on the DAP moiety is further supported by the transient absorption spectrum of the dye cation. Figure 4.5 compares the transient absorption spectrum of the dye cation generated following photoexcitation of the dye **4** adsorbed to the TiO_2 electrode (Figure 4.5a) with the transient spectrum observed for the 4-(diphenylamino) benzaldehyde, closely analogous to the DAP moiety alone (see inset to Figure 4.5b), adsorbed directly to the TiO_2 electrode (Figure 4.5b). In both cases, a photoinduced absorption maximum is observed at ~ 700 nm, assigned to an absorption maximum of the DAP cation, which could arise from the transfer of an electron in nitrogen lone pair in sp^2-orbital to the electrode. This is consistent with previous observations [19], and confirming the localisation of

the dye **4** cation on the DAP moiety. Note that in the case of Figure 4.5b, the photoinduced absorption exhibits rapid kinetics (8 μs), consistent with the expected small spatial separation of this cation from the electrode surface.

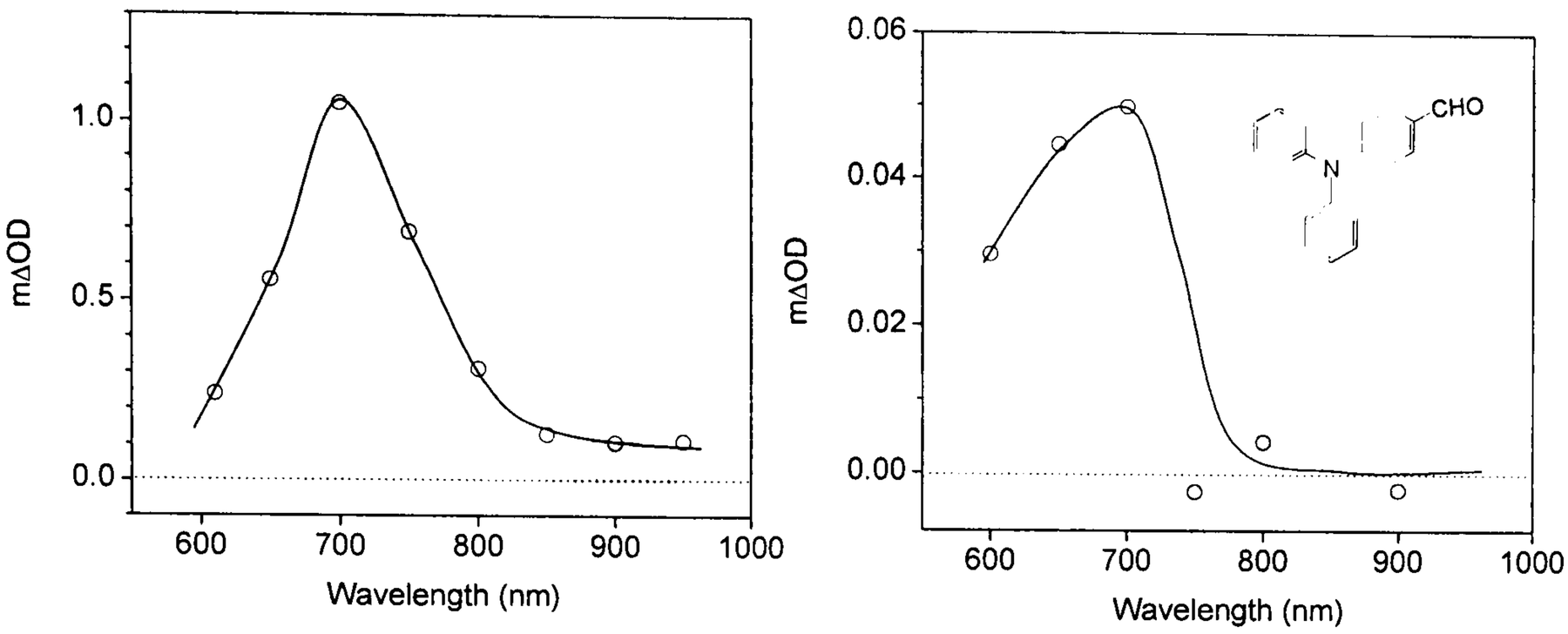


Figure 4.5 Transient absorption spectra shown in left hand side (4.5a) were collected for TiO_2 films sensitised with dye **4** monitored at 8 μs after excitation at 516 nm and the data shown in right hand side (4.5b) were for 4-(diphenylmaino) benzaldehyde (optical absorbance $\lambda_{410\,nm}$=0.35) monitored at 8 μs after excitation at 400 nm

4.3.2.3 Electron injection yield

It is noteworthy that the initial amplitudes of the dye cation transient absorption signals observed for both the dye **2** and **4** sensitised TiO_2 films were of similar magnitudes (ΔODs of 1 at 800 nm and 1.4 at 700 nm, respectively). This observation strongly suggests that the optical excitation of the dye **4** adsorbed to the TiO_2 films results in efficient electron injection into TiO_2 conduction band. However, uncertainty over the dye **4** cation extinction coefficient prevents quantitative analysis from these data alone.

4.3.2.4 Kinetic study of the decay

Electron transfer dynamics typically exhibit an exponential dependence upon spatial separation, as shown in Equation 4.1.

$$k_{et} \propto e^{-\beta r} \tag{4.1}$$

In which r is the edge-to-edge separation of the donor and acceptor wave-functions, and β is a measure of the barrier height of the intervening medium. Typically β varies from 2.8 $Å^{-1}$ for a vacuum to 1 $Å^{-1}$ for saturated-electron-orbital densities. From consideration of the HOMO orbital distributions shown in Figure 4.3, the dye-cation/electrode-surface distance is estimated to increase by 4 Å for dye **4** relative to dye **2**. Comparison with the ~1000 fold retardation of the observed recombination dynamics yields a value for β of 1.6 ± 0.2 $Å^{-1}$, typical of β values observed for through solvent electron transfer [20]. It can thus be concluded that the retardation of the recombination dynamics shown in Figure 4.4 is in good quantitative agreement with that expected from the increased dye-cation/electrode separation determined from the HOMO orbital calculations.

In addition to the retardation of the recombination dynamics shown in Figure 4.4, it is apparent that the temporal recombination shape differs significantly between these two dyes. For dye **2**, decay kinetics strongly suggest a stretched exponential (Δ O.D. ~$\exp(-(t/\tau)^{\alpha})$; α=0.44). Such stretched exponential recombination dynamics are typical of those we have observed previously for a range of different dyes under similar experimental conditions. In contrast, for dye **4** the recombination dynamics suggests an excellent fit to a near monoexponential decay (ΔO.D. ~$\exp(-(t/\tau)^{\alpha}$; α~ 0.9) as illustrated by the log/linear plot shown in Figure 4.4b.

It has previously been reported that the stretched exponential recombination dynamics, as observed here for the nanocrystalline TiO_2 films sensitised by dye **2**, are consistent with the charge-recombination dynamics being rate limited by electron transport within the metal oxide film [21]. The stretched exponential nature of these kinetics have been attributed to an inhomogeneous distribution of trap depths in the film, resulting in a broad distribution of detrapping (and therefore recombination) times. The observation that the dye **4** exhibits recombination dynamics three orders of magnitude slower than dye **2** in itself suggests that for this sensitiser, interfacial electron transfer is critical to determining the overall recombination dynamics. The near monoexponential behaviour is indicative of the recombination dynamics being

limited by the interfacial electron dynamics, as discussed previously in relation to experimental data obtained with two porphyrin dyes [21].

4.4 Conclusion

It can be concluded that this supermolecular approach translates the oxidising equivalent (hole) away from the nanostructured semiconducting surface. The increase in the distance between the surface and the hole, results in an extremely long-lived charge-separated pair, with the slowest recombination dynamics reported to date for such dye sensitised films, 0.7 s. The *N*,*N*-(di-*p*-anisylamino)phenoxymethyl secondary electron-donor group employed in this study can be expected to interface well with triarylamine-based hole conductors, making this sensitiser dye particularly attractive for applications in solid state dye-sensitised solar cells.

4.5 Appendix

4.5.1 Complication of electron recombination kinetics

This section addresses about complication of the transient absorption decay for the dye **4**. Transient absorption measurement for the dye **4** sensitized TiO_2 films covered in inert solvent was carried out. Typical data are shown in Figure 4.6A. In this figure, two phases were observed: a ms decay phase and a small μs decay phase with probe light wavelength dependence of amplitude. It is noteworthy that both phases showed dynamics that were significantly dependent upon the probe wavelength. This was understood by consideration of changes in build-up of long lived states in the conduction band in the TiO_2 due to the probe light wavelength dependency of the light intensity. To avoid this effect the data were recollected under steady light illumination, which is white light with 600 nm high pass filter to avoid the excitation of the electrons in valence band in the TiO_2 to the conduction band. Note that in this measurement the probe wavelengths were selected with the "monochrometer two" after the sample (See Figure 2.5 in Chapter 2). As a result, the decay half-times were observed to be indistinguishable on millisecond time scales as shown in Figure 4.6 B.

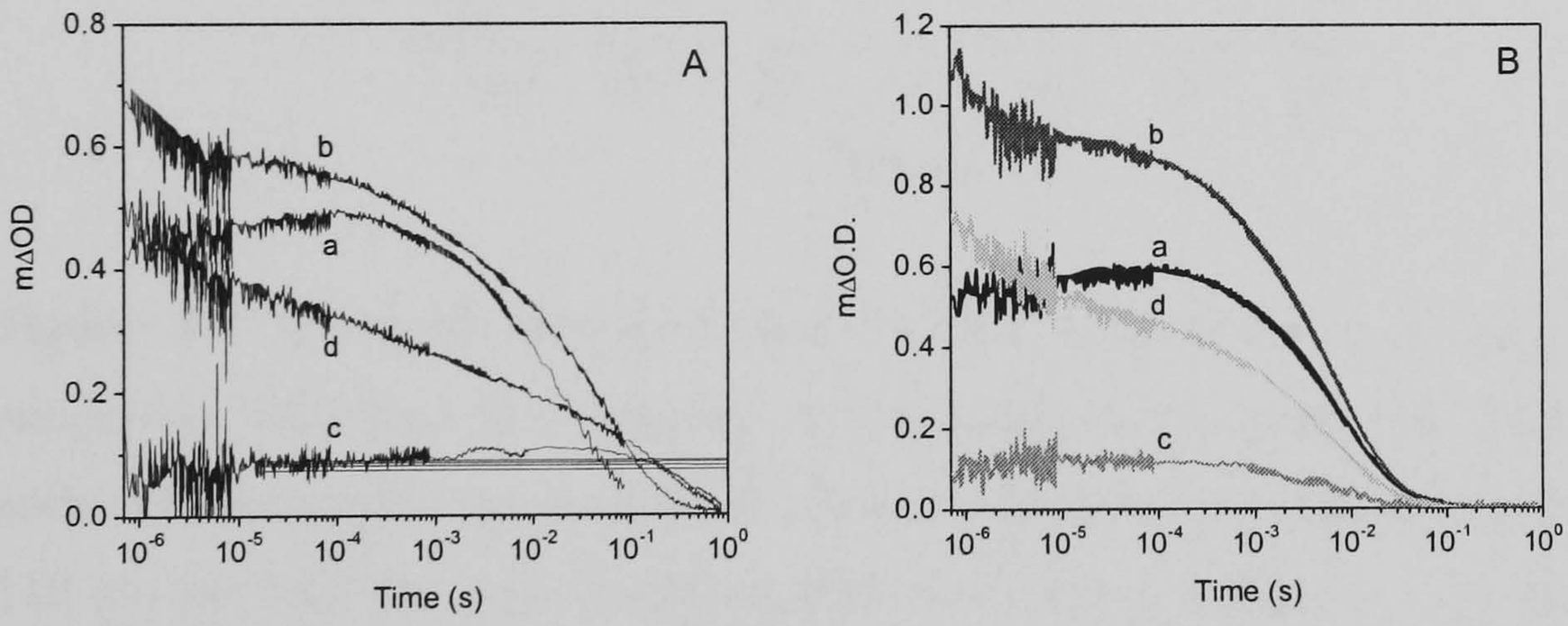


Figure 4.6 Transient absorption data for dye **4** adsorbed on TiO_2 films, collected with the 650 nm optical probe (a), 700 nm (b), 750 nm (c) and 950 nm (d) respectively, after the 550 nm optical excitation. For Figure A the data were collected by shining corresponding probe light. On the other hand, for Figure B the data were collected under white light illumination with 600 nm high pass filter, and the probe wavelength was controlled with a "monochrometer two" behind the sample. The optical density on 4 μm thick TiO_2 film is 0.88 at 516 nm.

Figure 4.6 shows the transient absorption spectra of dye **4** on nanocrystalline TiO_2 films under continuous light illumination. As can be seen in this figure it is also found that the faster phase (<10 μs) in the decay shows the dependency on the probe wavelength. Interestingly, even under steady light conditions the signals at 650nm remain steady while the signals at 700 nm decrease remarkably. This spectral evolution on microsecond timescales could be due to the relaxation processes of the dye cation by the dye molecular dynamics with surrounding solvent, not to the charge recombination. To clarify this, further experiments under different dye coverage were conducted.

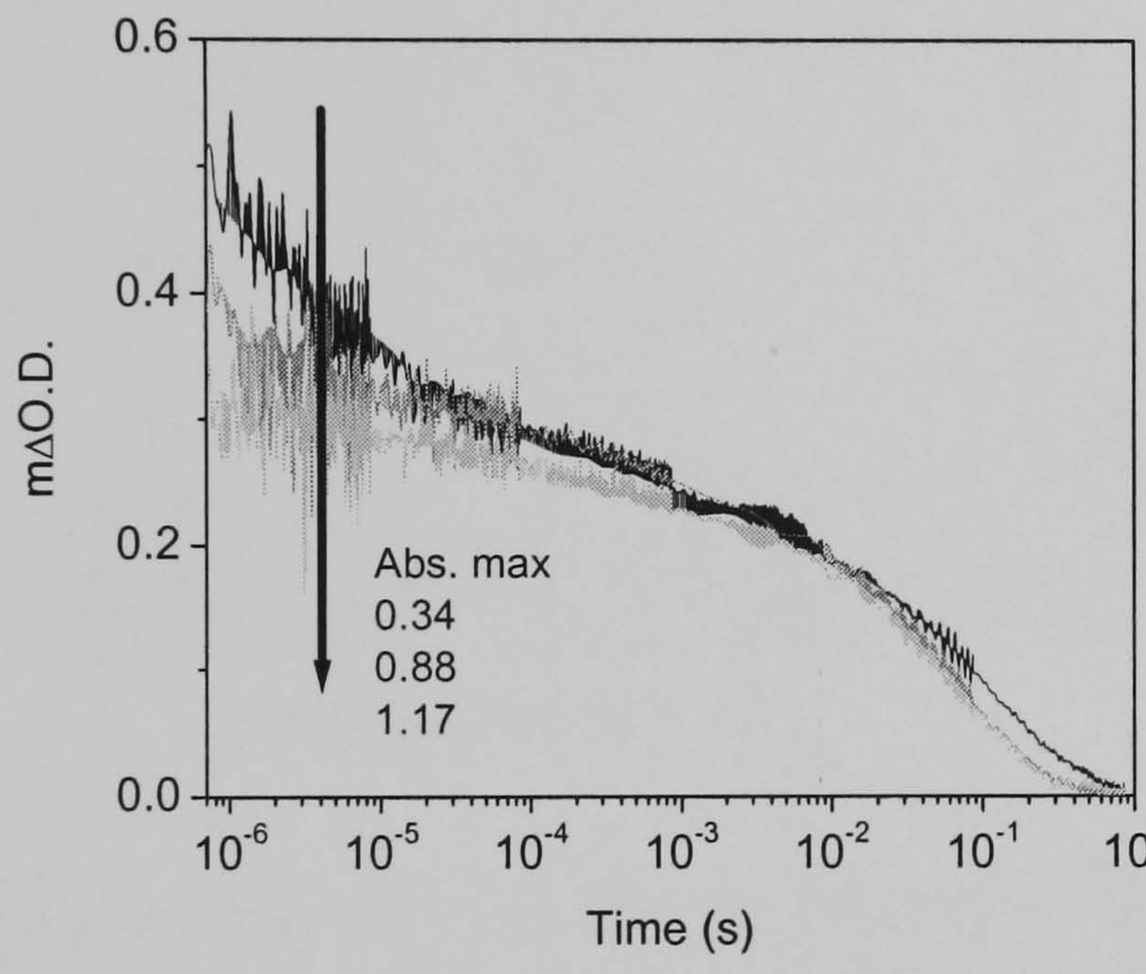


Figure 4.7 Transient absorption data for dye **4** adsorbed on 4 μm thick nonporous TiO_2 films as a function of dye coverage. The data were collected under 516 nm optical excitation and 700 nm detection. The optical densities at 518 nm are 0.34 (low dye coverage), 0.88 (mid. dye coverage), 1.17 (high dye coverage) nm. All data were collected under white light illumination with 600 nm high pass filter, and the probe wavelength was controlled with a monochrometer behind the sample.

If the transient spectroscopic absorbance decay is influenced by such molecular dynamics relaxation on the time scales, the dye coverage would affect the decay, because of increasing steric hindrance. Therefore, the decays under three different dye coverage conditions were monitored. The experiments employing varied dye coverage samples show that the decay in the faster phase depends on the extent of dye

loading, suggesting the higher extent of the dye loading leads to the unlikely relaxation. (Figure 4.7) This is consistent with the expectation; the dye could have slow molecular vibration and rotation because of the dense concentration of the dye on the surface of the TiO_2. Therefore, it can be concluded that the fast phase decay at around microseconds arises from relaxation of the dye **4**, and therefore that the slower phase in the decay would be associated with the recombination.

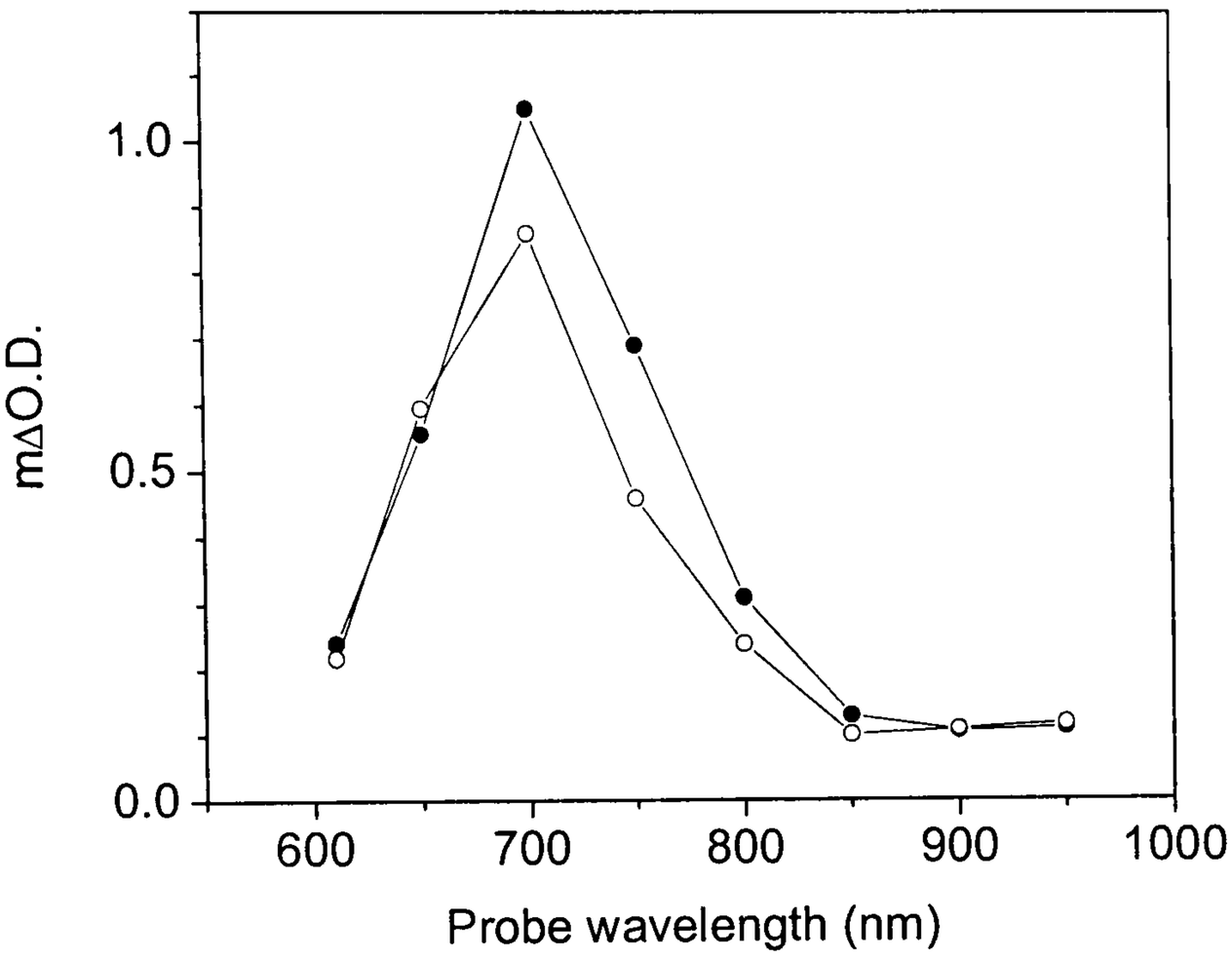


Figure 4.8 Transient absorption spectra of dye **4** on TiO_2 film under steady light illumination. The transient absorption spectra of dye **4** are shown at 10^{-6} s (filled circle) and at 10^{-4} s (open circle) after excitation at 550 nm. The optical density on 4μm TiO_2 film was 0.88 at 516 nm. The data were collected under white light illumination with 600 nm long pass filter, and with the probe wavelength selected after the sample.

Because such fast decay at micro seconds have never been seen in case of dye **2** (See Figure 3.6 in Chapter 3), the DAP group would be the causal effect for this relaxation. As can be seen in Figure 4.1, DAP group seems to be likely to move due to the flexibility of the junction ether bond. Therefore, as a future plan, the change from ether bond to ester bond, which could be more rigid, would be effective to prevent this relaxation.

4.5 References

1. Koval, C.A. and J.N. Howard, *Electron-Transfer at Semiconductor Electrode Liquid Electrolyte Interfaces.* Chemical Reviews, 1992. **92**(3): p. 411-433.

2. Gould, I.R., et al., *New approach to silver halide photography using radical cation chemistry.* Pure and Applied Chemistry, 2001. **73**(3): p. 455-458.

3. Fox, M.A. and M.T. Dulay, *Heterogeneous Photocatalysis.* Chemical Reviews, 1993. **93**(1): p. 341-357.

4. Meier, A., et al., *Fast electron transfer across semiconductor-molecule interfaces: GaAs/Co(Cp)(2)(+/0).* Journal of Physical Chemistry B, 1999. **103**(12): p. 2122-2141.

5. Oregan, B. and M. Gratzel, *A Low-Cost, High-Efficiency Solar-Cell Based on Dye-Sensitized Colloidal Tio2 Films.* Nature, 1991. **353**(6346): p. 737-740.

6. Palomares, E., et al., *Control of charge recombination dynamics in dye sensitized solar cells by the use of conformally deposited metal oxide blocking layers.* Journal of the American Chemical Society, 2003. **125**(2): p. 475-482.

7. Nusbaumer, H., et al., *Co-II(dbbiP)(2)(2+) complex rivals tri-iodide/iodide redox mediator in dye-sensitized photovoltaic cells.* Journal of Physical Chemistry B, 2001. **105**(43): p. 10461-10464.

8. Yanagida, M., et al., *Dye-sensitized solar cells based on nanocrystalline TiO2 sensitized with a novel pyridylquinoline ruthenium(II) complex.* New Journal of Chemistry, 2002. **26**(8): p. 963-965.

9. Marguerettaz, X. and D. Fitzmaurice, *Heterosupramolecular Chemistry - Long-Lived Charge Trapping by Vectorial Electron Flow in a Heterotriad.* Journal of the American Chemical Society, 1994. **116**(11): p. 5017-5018.

10. Marguerettaz, X., R. Oneill, and D. Fitzmaurice, *Heterodyads - Electron-Transfer at a Semiconductor Electrode Liquid Electrolyte Interface Modified by an Adsorbed Spacer Acceptor Complex.* Journal of the American Chemical Society, 1994. **116**(6): p. 2629-2630.

11. Argazzi, R., et al., *Long-Lived Photoinduced Charge Separation across Nanocrystalline Tio2 Interfaces.* Journal of the American Chemical Society, 1995. **117**(47): p. 11815-11816.

12. Hoertz, P.G., et al., *Organic rigid-rod linkers for coupling chromophores to metal oxide nanoparticles.* Nano Letters, 2003. **3**(3): p. 325-330.

13. Hirata, N., et al., *Supramolecular control of charge-transfer dynamics on dye-sensitized nanocrystalline TiO2 films.* Chemistry-a European Journal, 2004. **10**(3): p. 595-602.

14. Shklover, V., et al., *Structure of organic/inorganic interface in assembled materials comprising molecular components. Crystal structure of the sensitizer bis (4,4 '-carboxy-2,2 '- bipyridine)(thiocyanato) ruthenium(II).* Chemistry of Materials, 1998. **10**(9): p. 2533-2541.

15. Srikanth, K., V.R. Marathe, and M.K. Mishra, *Role of electronic structure of ruthenium polypyridyl dyes in the photoconversion efficiency of dye-sensitized solar cells: Semiempirical investigation.* International Journal of Quantum Chemistry, 2002. **89**(6): p. 535-549.

16. Nazeeruddin, M.K., et al., *Synthesis, spectroscopic and a ZINDO study of cis- and trans- (X-2)bis(4,4 '-dicarboxylic acid-2,2 '-bipyridine)ruthenium(II) complexes (X = Cl-, H2O, NCS-).* Coordination Chemistry Reviews, 2000. **208**: p. 213-225.

17. Rensmo, H., S. Lunell, and H. Siegbahn, *Absorption and electrochemical properties of ruthenium(II) dyes, studied by semiempirical quantum chemical calculations.* Journal of Photochemistry and Photobiology a-Chemistry, 1998. **114**(2): p. 117-124.

18. Fukuzumi, S., *New perspective of electron transfer chemistry.* Organic & Biomolecular Chemistry, 2003. **1**(4): p. 609-620.

19. Bhasikuttan, A.C., et al., *Study of spectral characteristics, kinetics, and equilibria of radicals derived from hydroxy benzophenones.* Journal of Physical Chemistry A, 1999. **103**(24): p. 4703-4711.

20. Bendall, D.S., *Protein Electron Transfer.* 1996.

21. Clifford, J.N., et al., *Molecular control of recombination dynamics in dye sensitised nanocrystalline TiO2 films.* Chemical Communications, 2002(12): p. 1260-1261.

22. Tachibana, Y., et al., *Subpicosecond interfacial charge separation in dye-sensitized nanocrystalline titanium dioxide films.* Journal of Physical Chemistry, 1996. **100**(51): p. 20056-20062.

5

Optimisation of sensitiser function in dye sensitised solar cells

5.1 Introduction

The ruthenium bipyridyl based sensitiser dye $RuL_2(NCS)_2$ where L = 2,2'-bipyridyl-4,4'-dicarboxylate, such as dye **2** shown in Chapter 3, was one of the first dyes reported by Grätzel and co-workers for use in DSSCs in the early 1990s. Remarkably, despite extensive studies of alternative dyes, this dye remains one of the front runner dyes for DSSC, yielding superior devices efficiencies to almost all other sensitiser dyes tested [1]. The merits of such ruthenium dyes include strong, broad band absorption in visible region (450 – 600 nm), good monolayer immobilisation on the surface of nanocrystalline TiO_2 as addressed in Chapter 3, and energetics well matched to both the TiO_2 conduction band and the I^- / I_3^- redox couple, allowing in efficient electron transfer processes [2]. Continuing optimisation of device design has led to device efficiencies of up to 10 % with the $RuL_2(NCS)_2$ dye [3].

Despite the success of the $RuL_2(NCS)_2$ sensitiser dye, there are clear limitations in the utility of this dye, including poor red / near infrared light absorption and expensive synthesis costs of the dye. Moreover recent developments in understanding of the electron transfer function of DSSC, including appreciation of aspects of device function exhibiting 'kinetic redundancy' [2, 4], have led to innovative strategies to modify dye design such as to minimise recombination losses. Note that the kinetic redundancy in this context implies a situation that there are too fast electron transfer reactions for better device performance and the efficiency could be improved by retardation of the reaction kinetics. Considerations relating to the issue of kinetic redundancy based on the application that most modifications to dye design affect not

just one but several of the interfacial electron transfer processes determining device function. A previous study [2] has focussed on the correlation between electron injection and charge recombination to the electrolyte (*CR2*) showing that changes of electrolyte composition which retard *CR2* also retard electron injection. Optimum device performance was observed when electron injection was just fast enough to compete with excited state decay to the ground state, conditions under which 'kinetic redundancy' of the injection process has been minimised. Such considerations are motivating extensive studies of alternative sensitiser dyes. Such research can be basically divided into two directions; iterative modification of the $RuL_2(NCS)_2$ dye, and the development of new classes of sensitiser dyes including Fe [5], Os [6] and Re [7] metal complexes and organic dyes [8].

During my thesis studies, I have addressed structure / function relationships for a broad range of sensitiser dyes [9-13]. In this chapter, a selection of these studies are presented, focusing on three distinct series of dyes; this chapter is therefore split into three sections. The first section presents studies of a series of ruthenium bipyridyl analogues of $RuL_2(NCS)_2$ with long alkyl sidechains. These chains were incorporated with the intension of forming a hydrophobic layer over the sensitiser dye layer, with the primary motivation of forming a barrier layer to protect the dye layer against water contamination in the electrolyte. However, my interest in these dyes is that this barrier layer could retard electron transfer dynamics at the TiO_2 / dye / electrolyte interfaces, potentially addressing the issue of kinetic redundancy in the device.

The second section focuses on $RuL_2(NCS)_2$ analogues with extended ligand conjugation. These dyes were synthesised for the purpose of extension of the long wavelength absorption of the dye. In this section the influence of the introduced moieties upon the electron recombination dynamics and the influence of resultant lower LUMO levels of the dyes upon electron injection yields will be addressed.

Finally as an alternative metal complex to ruthenium dyes, a series of platinum complexes are studied, focusing particularly upon the relationship between the position of carboxylic acid group on the dye and its function.

5.2 Characterisation of a series of ruthenium complexes with long alkyl chains

5.2.1 Introduction

One of the issues to be addressed for DSSCs is device stability. Many efforts have been made to improve the stability of DSSCs for the last few years. It has been found that water contamination in the electrolyte causes device performance to degrade seriously, showing over a 15 % drop of photocurrent for a complete DSSC containing 10% of water within 40 days [14]. Motivated by these observations, co-workers at EPFL succeeded in synthesising a series Ruthenium dye with two hydrophobic chains attached to a bipyrdine unit. The intention was to form a hydrophobic layer to keep water away from the interface between the nanocrystalline TiO_2 and the sensitiser dyes, resulting in improved device stability. The validity of this concept was proved by stability studies of device performance with dye $[Ru(H_2dcbpy)(mhdbpy)(NCS)_2]$ (where the ligands H_2dcbpy = 4,4'-dicarboxy-2,2'-bipyridine, mhdbpy = 4-methyl-4'-hexadecyl-2,2'-bipyridine), which has a C_{16} chains as shown in Figure 5.1, showing no degradation in the device performance under the same 40 day trial conditions [14].

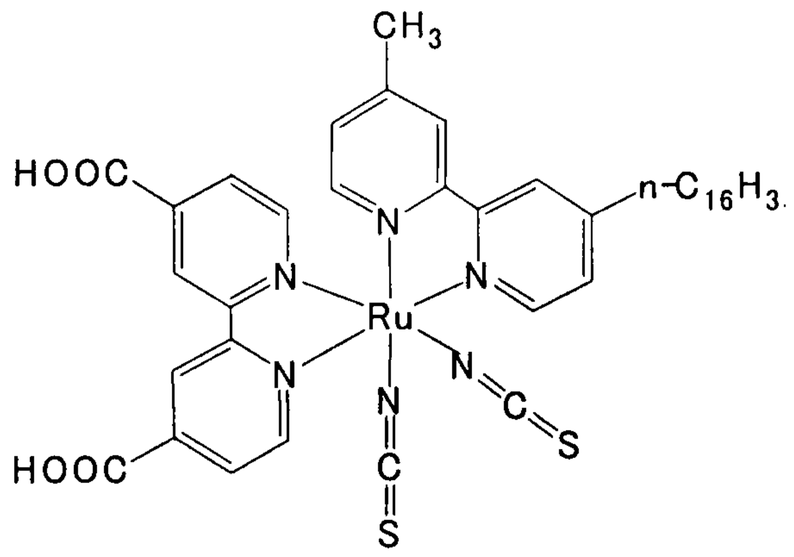


Figure 5.1 Chemical structure of $[Ru(H_2dcbpy)(mhdbpy)(NCS)_2]$ (where the ligands H_2dcbpy = 4,4'-dicarboxy-2,2'-bipyridine, mhdbpy = 4-methyl-4'-hexadecyl-2,2'-bipyridine)

DSSC performance for dyes based on the same concept described above with a variety of side chains were studied by Lagref et al. Higher V_{oc} was observed for a dye with two C_6 sidechains, relative to dye **1**, whilst retaining a IPCE values of about 80%

[15]. However, the functional mechanism of this superior performance was not addressed.

In terms of electron transfer dynamics, dyes with long side chains are of interest because of their potential influence upon electron transfer dynamics induced by the physical barrier layer of the alkyl chains. Figure 5.2 shows schematically the three relevant electron transfer processes. The key advantage of such barrier layers would be to potentially reduce recombination losses to the redox electrolyte (*CR2*). As Montanari et al. studied previously, and also addressed later in this section, in liquid type DSSCs the dynamics of regeneration of the oxidised dye by the redox species in the electrolyte are normally more than fast enough ($t_{50\%(RG)}$ ~1 μs) to compete with the recombination process with the dye cations ($t_{50\%(CR1)}$ ~1 ms) [16]. This can be regarded as an example of "kinetic redundancy". Therefore, a limited retardation of these regeneration dynamics due to a physical barrier layer would not necessarily reduce regeneration efficiency. It is noteworthy that both regeneration (*RG*) and the recombination with the redox couple (*CR2*) are predicted to be affected due to the physical barrier from the alkyl chain layer, while the dynamics of recombination with the dye cation (*CR1*) would not be effected by the barrier layer. This implies that the introduction of such barrier layer can control the electron transfer kinetics independently.

To address this concept, electron transfer kinetics were studied with TAS for a series of dyes with the alkyl chains of C_1 though C_{18}. These electron transfer dynamics are correlated with device performance to allow the rational optimisation of dye function.

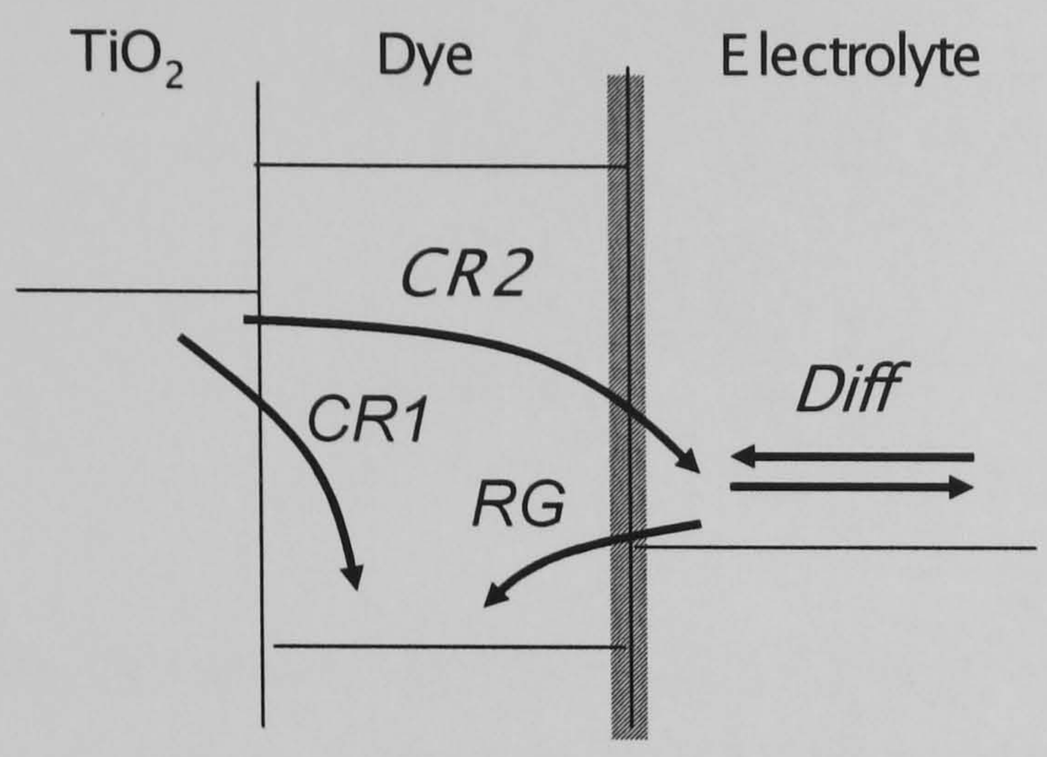


Figure 5.2 Schematic diagram showing the different interfacial electron transfer processes: regeneration of the dye cation by electron transfer from the redox couple (*RG*); recombination of electron with the dye cation (*CR1*); electron recombination to the redox couple (*CR2*); diffusion of the redox couple (*Diff*). Oblique lines represent the barrier layer over the dye layer.

5.2.2 Experimental

All experiments basically followed those detailed in Chapter 2. In this study four dyes received from the Grätzel group at EPFL were employed: [Ru(H_2dcbpy)(4,4'-dimethyl-2,2'-bipyridine)(NCS)$_2$] (dye **5.1**); [Ru(H_2dcbpy)(44'-dihexyl-2,2'-bipyridine)(NCS)$_2$] (dye **5.2**); [Ru(H_2dcbpy)(44'-tridecyl-2,2'-bipyridine)(NCS)$_2$] (dye **5.3**); [Ru(H_2dcbpy)(44'-octadecyl-2,2'-bipyridine)(NCS)$_2$] (dye **5.4**) as shown in Figure 5.3.

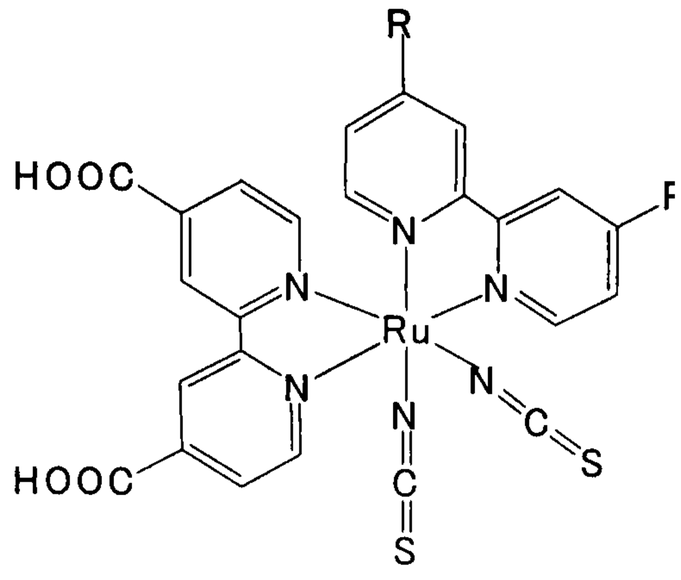


Figure 5.3 Chemical structure of the four dyes employed, where R = CH_3 (dye **5.1**), n-C_6H_{13} (dye **5.2**), n-$C_{13}H_{27}$ (dye **5.3**), n-$C_{18}H_{37}$ (dye **5.4**).

4 μm thick nanocrystalline TiO_2 films, which were made from the ECN35 paste, were soaked at room temperature overnight into 1 mM dye solutions in the mixture of acetonitrile and 2-methyl-2-propanol (1:1 in volume ratio), resulting in reasonable dye coverage on the surface of TiO_2 as measured by UV-visible absorption spectra of those films as shown in Figure 5.4. For laser measurements without the redox couple, the films were covered with a drop of propylene carbonate to prevent the degradation of dyes. Sandwich type 1 cm^2 DSSC cells were fabricated as detailed in chapter 2, with the electrolyte 'SB'.

5.2.3 Results

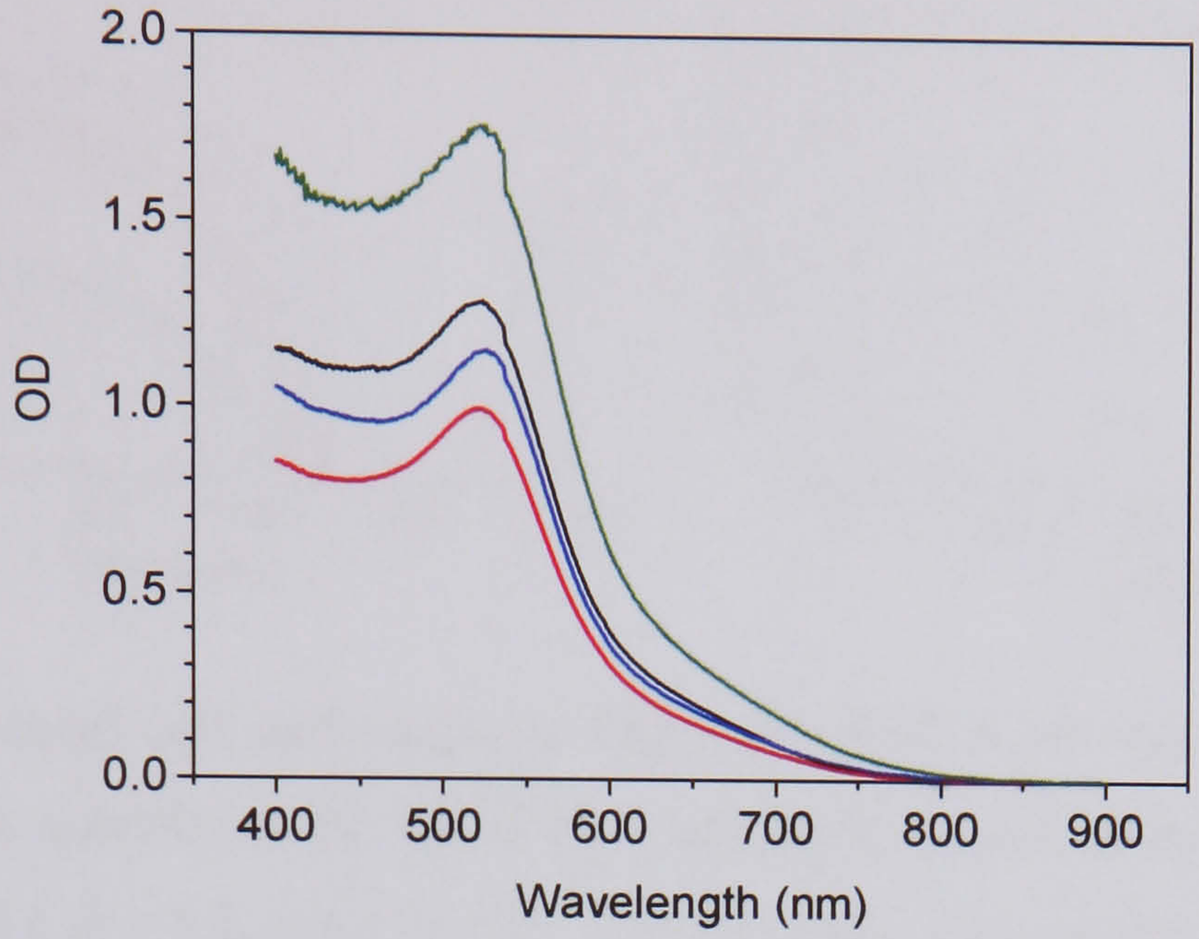


Figure 5.4 UV-visible absorption spectra for nanocrystalline TiO_2 films sensitised with a series of dyes with different side chain lengths. Black line represents the absorption spectra for dye **5.1**, red line for dye **5.2**, blue line for dye **5.3**, green line for dye **5.4**.

Figure 5.4 shows UV-visible absorption spectra of the films sensitised with the dye series. As can be seen, optical densities greater than 0.8 were obtained for all four dyes, indicating at least monolayer dye coverage. It is noteworthy that the dye **5.4** sensitised film exhibited a considerably higher absorbance than the others. This high absorbance indicates greater than monolayer coverage, potentially due to dye aggregation resulting from entanglement of the dye long chains. Such aggregation may also result in a lower injection yield, due to the difficulty for electrons in aggregated dyes to inject into the conduction band of the TiO_2, and therefore in a lower I_{sc}. Note that such a loss of device I_{sc} was observed for the N3 dye as addressed in Chapter 3.

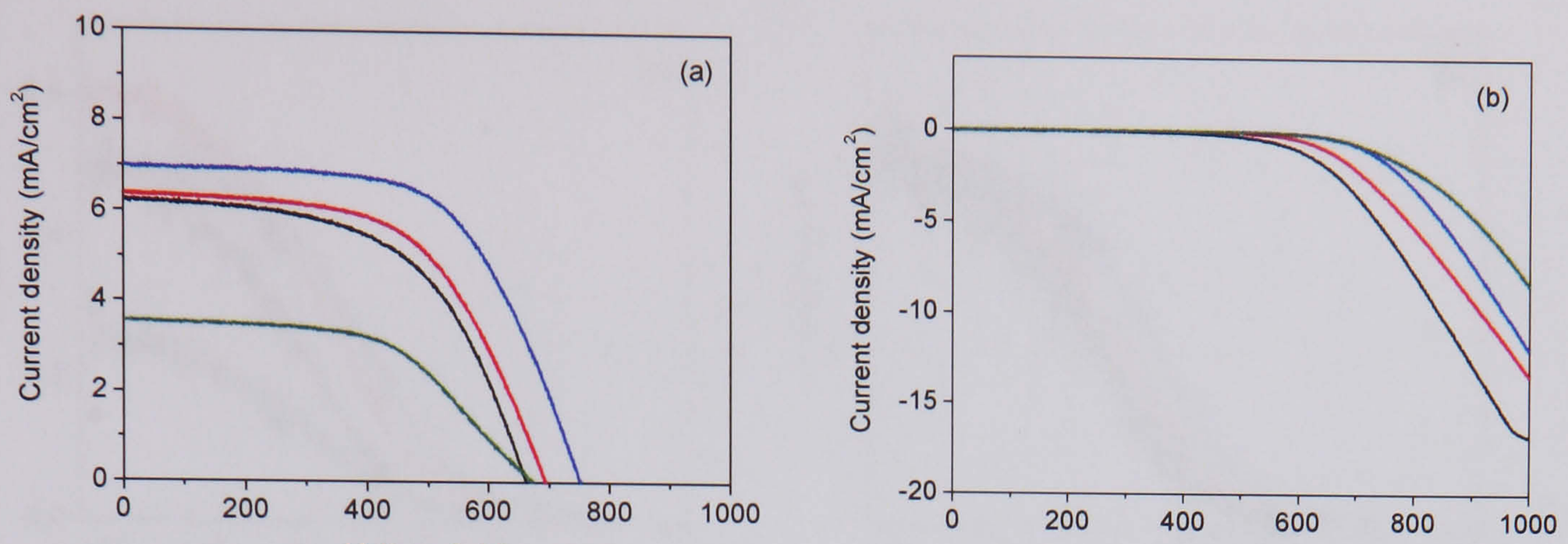


Figure 5.5 Overall cell performances both under AM1.5 one sun illumination (a) and under dark conditions (b). Black line represents the absorption spectra for dye **5.1**, red line for dye **5.2**, blue line for dye **5.3**, green line for dye **5.4**. The device efficiencies are 2.4%, 2.6%, 3.2% and 1.3%, respectively.

The IV data of DSSC cells with the four sensitiser dyes are shown in Figure 5.5. It is apparent that longer alkyl chains exhibited higher V_{oc}s except for the dye **5.4**, consistent with the trend of the V_{oc} data obtained by Nazeeruddin for the same dyes at EPFL (Data not published). As for the dark currents, the trend observed in the figure also correlates with the chain length, suggesting the chains can retard the recombination dynamics to the redox couple (*CR2*). The poor performance of the dye **5.4** can be attributed to a lower charge separation yield, resulting in the low short circuit current relative to the other dyes. The lower V_{oc} of the dye **5.4** is discussed later.

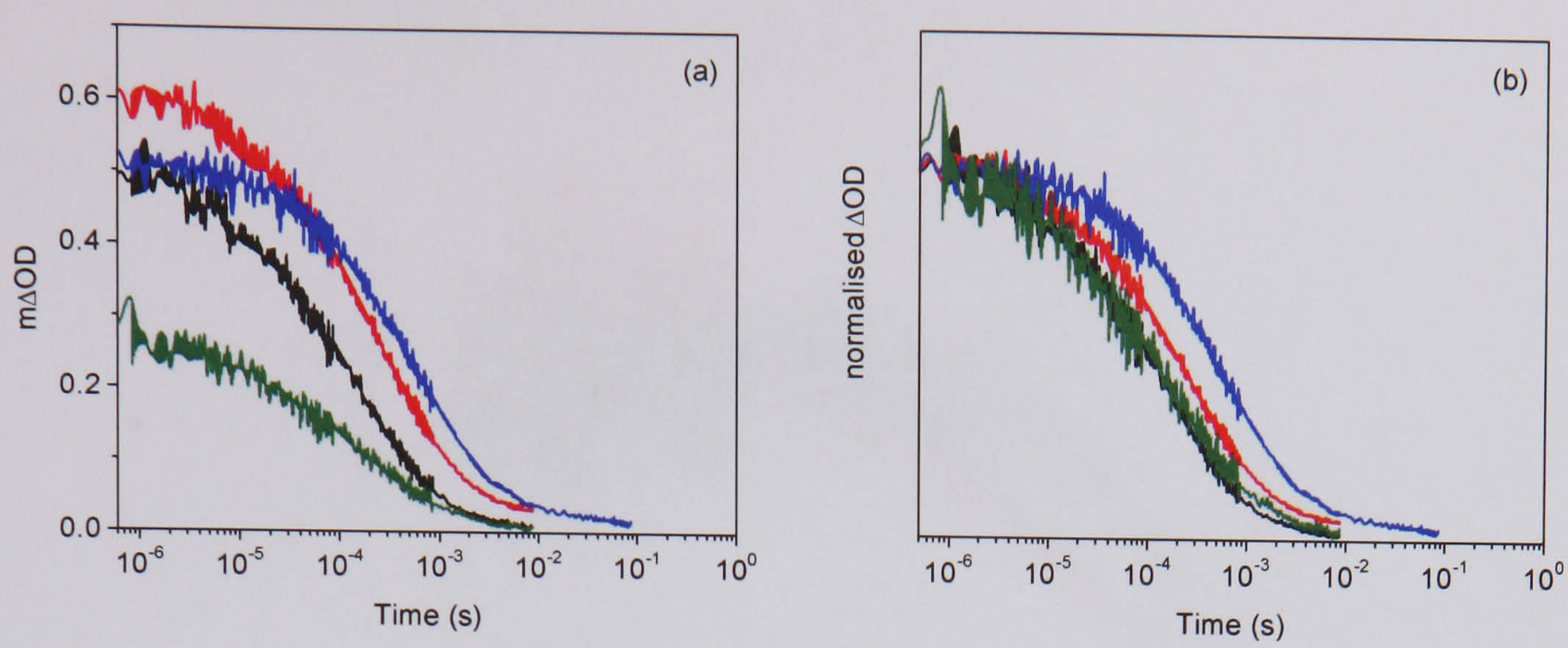


Figure 5.6 A series of transient absorption data for nanocrystalline TiO_2 films sensitised with dyes **5.1-5.4** with different length of alkyl chain monitoring the dye cation absorption at 775 nm. In the figure (a), signal amplitude is corrected based on the densities of absorbed photons determined from sample optical densities. The data in Figure (b) were normalised for the same signal amplitudes at 10^{-6} s to compare the kinetics. Black line represents the absorption decay for dye **5.1**, red line for dye **5.2**, blue line for dye **5.3**, green line for dye **5.4**. The half times ($t_{50\%}$) of the decays are 9.8 x 10^{-5} s, 1.8 x 10^{-4} s, 4.6 x 10^{-4} s and 1.1 x 10^{-4} s, respectively.

TAS studies for both TiO_2 films and sandwich type cells were performed. The electron injection yields of the dyes, as monitored by the initial magnitudes of the transient signals for the dye sensitized TiO_2 films as shown in Figure 5.6(a), were observed to be reasonably similar except for the dye **5.4**. Note that it was assumed that for all dyes, the dye cation extinction coefficient at the probe wavelength, 775 nm, is the same, justified by the expected similarities of their NCS localised HOMO orbitals. For the dye **5.4**, the injection yield was considerably smaller, consistent with the high optical density in Figure 5.4 indicating dye aggregation. Interestingly, the normalised data in Figure 5.6(b) shows clearly a trend in which the longer alkyl chain leads to the slower recombination, with dye cations (*CR1*) by up to one order of magnitude with the exception of the dye **5.4**.

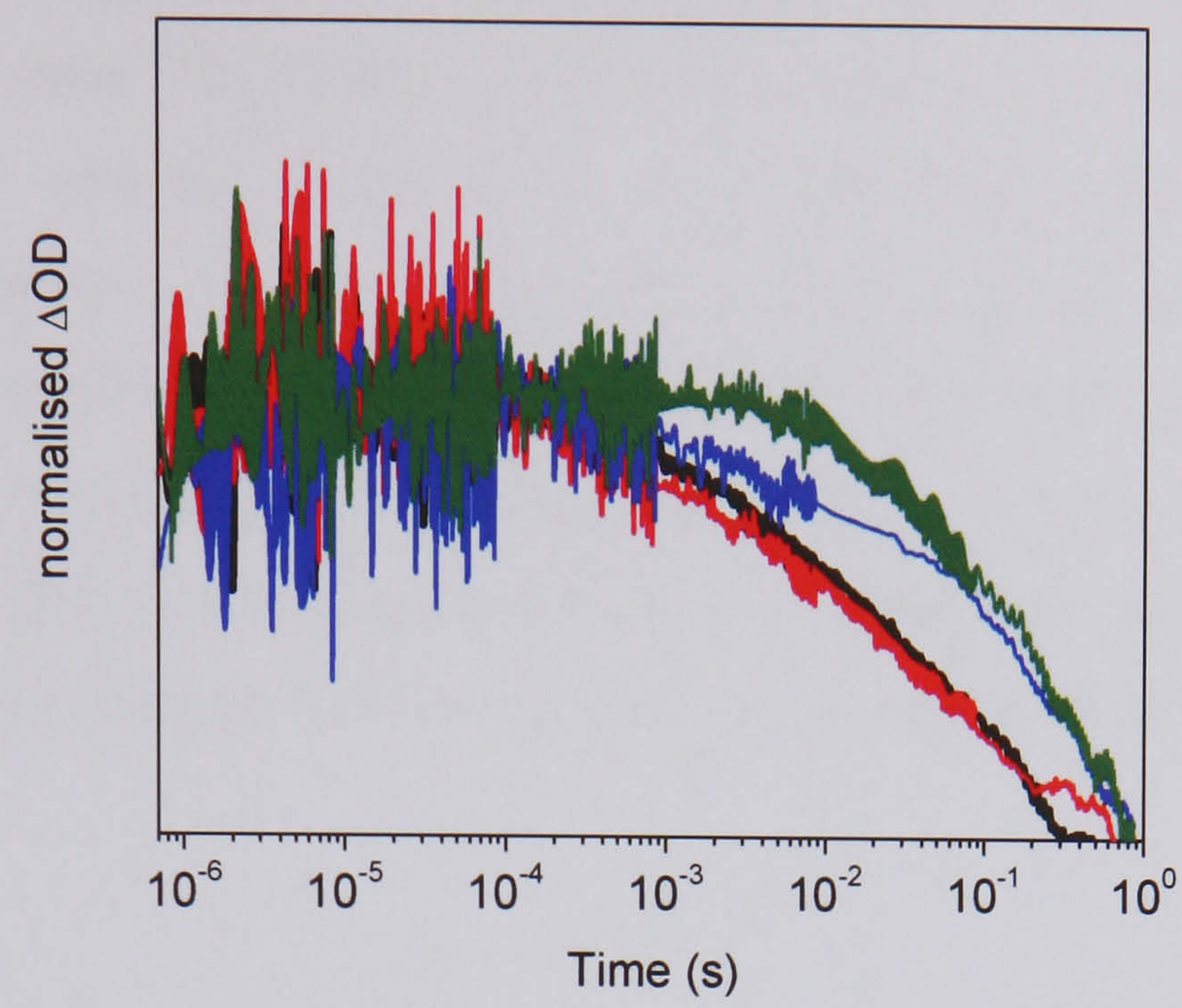


Figure 5.7 A series of transient absorption data for complete sandwich type cells employing sensitiser dyes with different length of alkyl chain lengths monitoring the injected electrons in TiO_2 at 1000 nm. Black line represents the absorption spectra for dye **5.1**, red line for dye **5.2**, blue line for dye **5.3**, green line for dye **5.4**. The half times ($t_{50\%}$) of the decays are 2.5×10^{-2} s, 1.9×10^{-2} s, 1.2×10^{-1} s and 1.7×10^{-1} s, respectively.

In order to monitor recombination dynamics with the redox electrolyte (*CR2*), the TAS of the complete DSSCs were studied employing a probe light of 1000 nm, monitoring absorption of electrons into the TiO_2 (at this wavelength absorption of injected electrons ($e^-_{(TiO2)}$) dominates the transient signal compared to that of dye cations or redox couple absorption [17].) As shown in Figure 5.7, the dyes with longer chains demonstrated a reasonable retardation of recombination kinetics. Note that the data in Figure 5.7 were normalised by matching all initial signal size at 10^{-6} s to make the comparison of kinetics clear.

(A paragraph was deleted.)

TAS data monitoring the dye cation signal at 775 nm for the cells with the different dyes is shown in Figure 5.8, representing absorption signals originated from two species: the dye cations and I_2^- [16]. The faster decay phase between 10^{-6} and 10^{-3}

s is assigned to the dynamics of regeneration of the dye cation by electron transfer from the redox couple. The residual long lived (millisecond lifetime) is assigned to absorption of I_2^- species generated by the re-reduction reaction *RG*, and the concomitant absorption of long lived electrons. Decay of this long lived signal is assigned to I_2^- dismutation and charge recombination with TiO_2 electrons, *CR2*. It is apparent that the long chains retard the regeneration process by over two orders of magnitude. Note that for the dye **5.4**, these two phases are no longer kinetically resolved as the regeneration is now so slow as to overlap with the recombination reaction *CR2*.

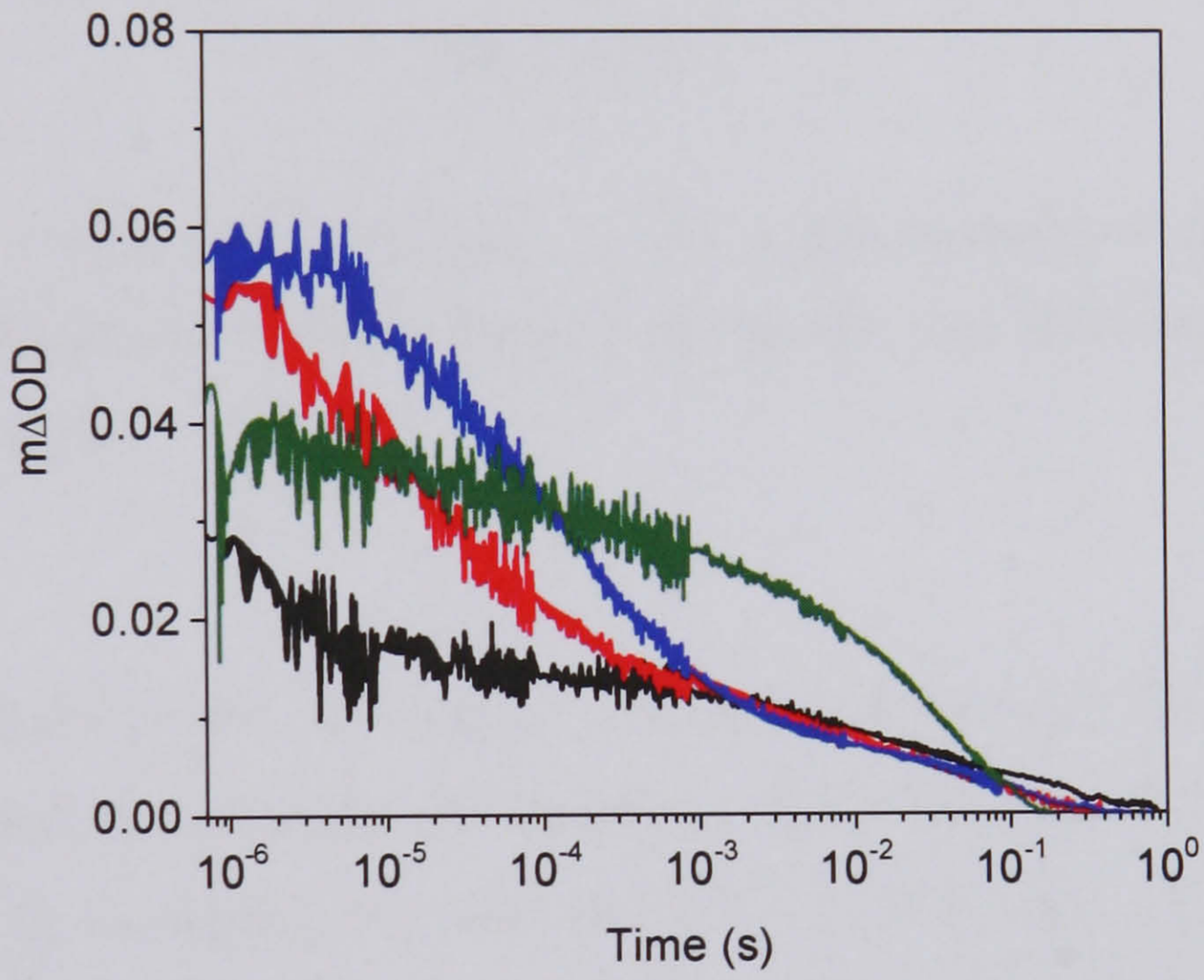


Figure 5.8 Transient absorption data monitored at 775 nm for complete DSSC cells employing sensitiser dyes with different length of alkyl chains. Note that the signal sizes were corrected on the basis of the injection yields obtained by monitoring at 1000 nm for the same dye sensitized TiO_2 films.

5.2.3 Discussion

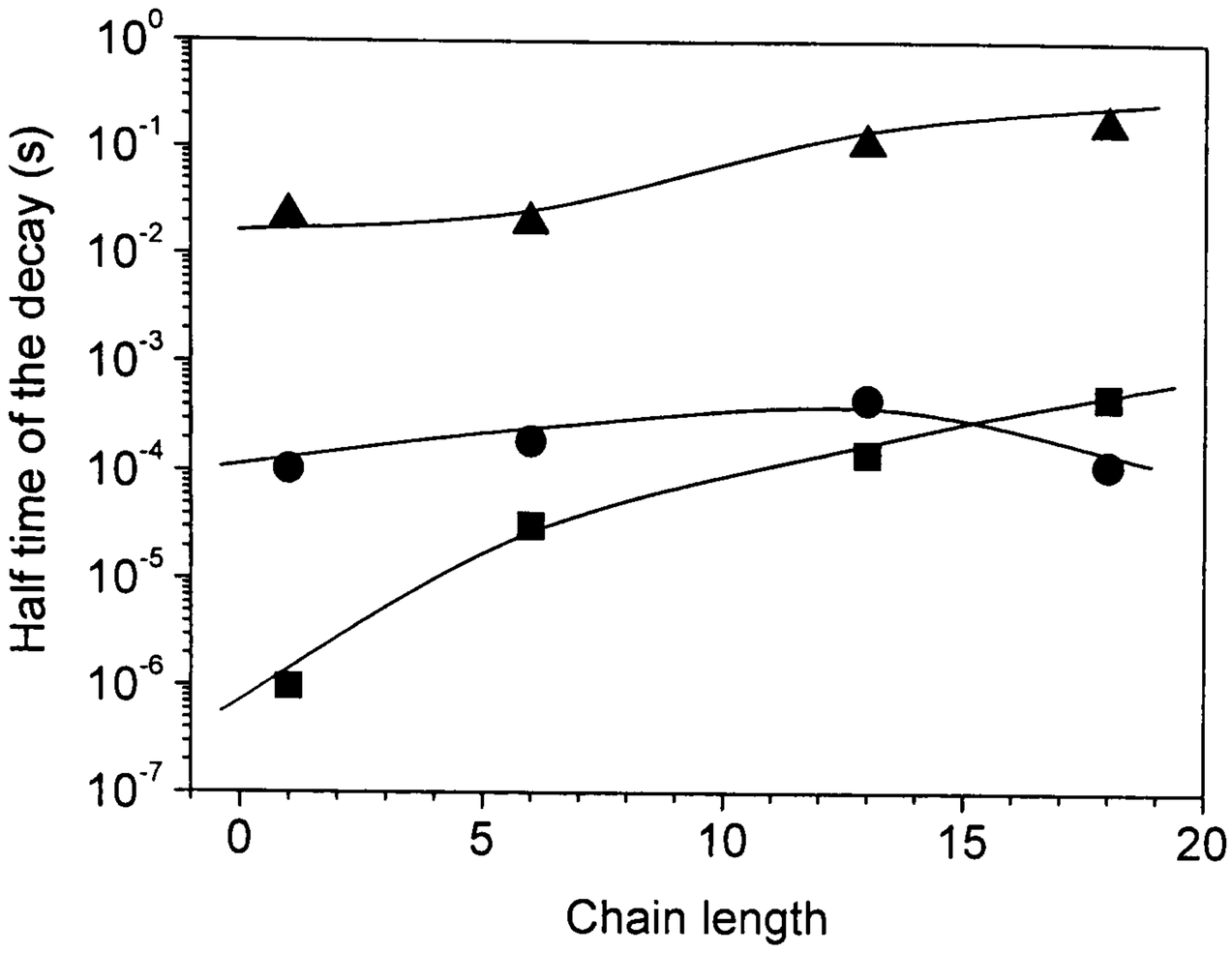


Figure 5.9 A plot of the half-time of the interfacial electron transfer reactions, *CR1*(circle), *CR2*(triangle) and *RG*(square), as a function of the alkyl chain length.

The half-times of the interfacial electron transfers for the dye series as a function of the alkyl chain length are summarised in Figure 5.9. It is apparent that as the chain length is increased, the recombination to the redox electrolyte (*CR2*) is retarded, consistent with the observed reduced dark current and high V_{oc} observed in complete cell performance. It is furthermore apparent that the regeneration reaction (*RG*) rapidly retards as the chain length is increased, and for chain lengths greater than C_{13} the regeneration (*RG)* is actually slower than recombination to the dye cation (*CR1)*, implying that dye **5.3** (C_{13}) results in near optimal conditions in terms of kinetic competition, consistent with the observed trend in device I_{sc} data as shown in Figure 5.10.

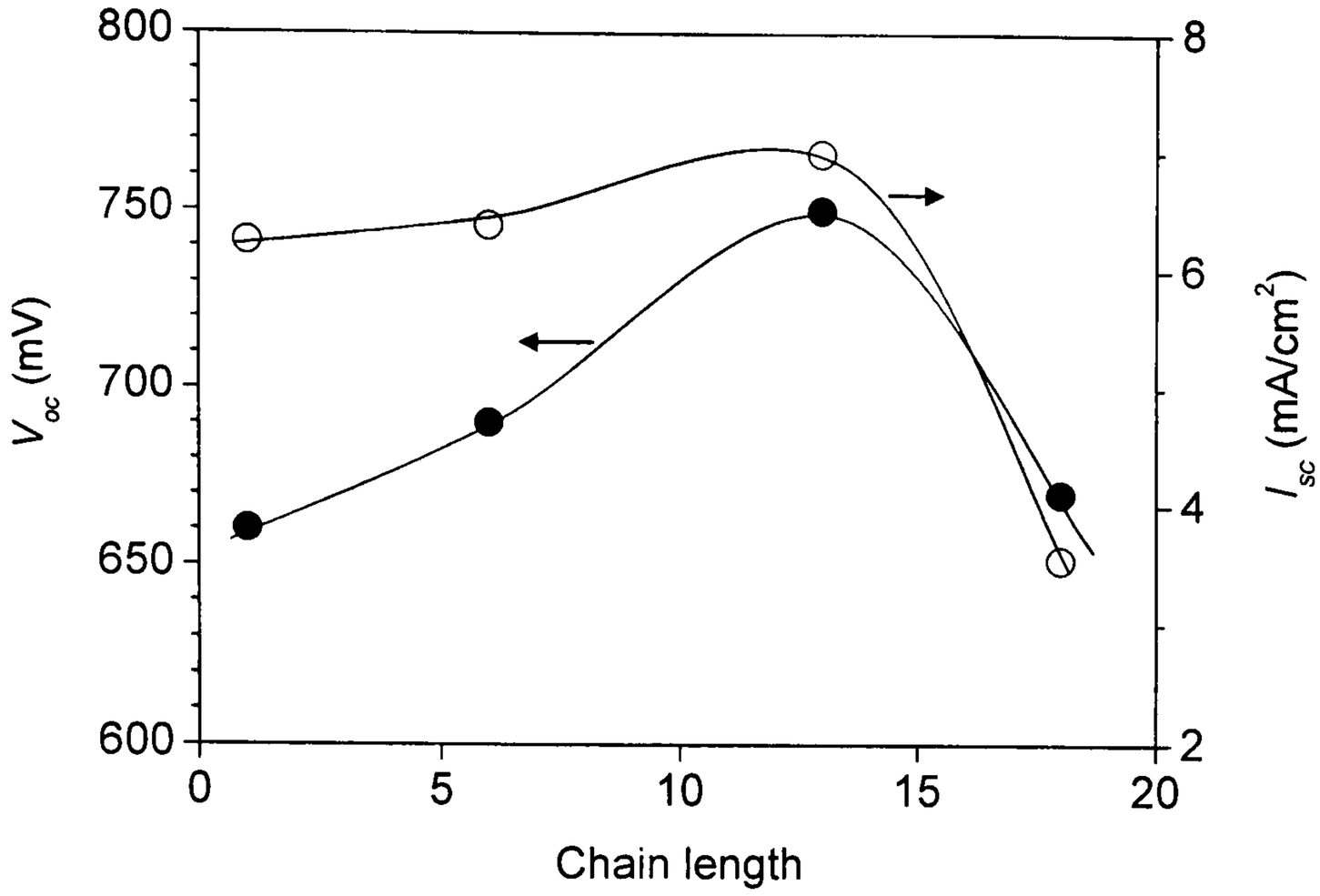


Figure 5.10 A plot of V_{oc} and I_{sc} for the dye series versus the alkyl chain length, showing the length of C_{13} resulted in the highest performance out of them, highly consistent with the TAS studies.

It is found that the introduction of long alkyl chains to ruthenium dyes retarded both recombination dynamics with the redox couple and regeneration in liquid DSSCs. Contrary to expectations, the recombination dynamics with the dye cation was also observed to be retarded by long chain lengths. (See in Figure 5.6(b)) It is noteworthy that the recombination dynamics for all dyes were faster than those observed for the standard dye **2**. This could imply that the molecules of this dyes studied here are be orientated flatter relative to the surface of the TiO_2, resulting in the shorter distance between the injected electrons in TiO_2 and the HOMO of the dye cation. Note that electron transfer dynamics are strongly dependent on a distance between a donor and an accepter. As stated in Chapter 4, the remarkable retardation of recombination dynamics was observed by lengthening the distance. This movement of the dye **5.1** to **5.4** may result from the presence of only two carboxyl groups, which have the function of anchoring to the surface of the TiO_2, per dye to attach to the surface in contrast to four carboxyl groups of the dye **2**. As such, it is

possible that the dyes with the longer chains could orientate more perpendicular to the surface of the TiO_2, resulting in the observed slower recombination dynamics.

These observations addressed in this chapter are perfectly consistent with reduction in the 'kinetic redundancy of the device [2, 4]. Previous studies of kinetic redundancy have focused on correlation between electron injection into TiO_2 conduction band and recombination to the redox electrolyte. The study addressed here is the extension of the kinetic redundancy argument to the regeneration dynamics of the dye ground state suggesting the importance of scrutinising charge transfer dynamics in DSSCs to design all the reactions optimised for high device performance.

5.3 Characterisation of a series of ruthenium complexes with unsaturated side chains

5.3.1 Introduction

As addressed in the introduction (section 5.1), while the $RuL_2(NCS)_2$ dyes, such as dye **1**, lead to superior device performance, a significant limitation of these sensitizers is their lack of absorption in the red region of the visible spectrum, coupled with only reasonable molar extinction coefficient in the blue/green (peak values of ~ 14,000 M^{-1} cm^{-1}[18]. Several groups have tried to overcome these shortcomings, without significant success, by modification of dye **1**, such as alteration of ligands [19] and alteration of the stereochemical position of ligands [20, 21]. To increase optical absorbance in the red / near IR, the band gap between the HOMO and LUMO levels of the sensitizer needs to be reduced. Strategies to address this have included alteration of the position of carboxyl acid ligands [22] and extension of the π conjugation system by the introduction of other benzene rings [23].

However the tuning of this LUMO energy level needs careful consideration with regard to the issue of electron transfer dynamics. Efficient electron injection into the TiO_2 conduction band requires the excited state of the dye to be sufficiently energetic such as to provide a thermodynamic driving force for injection into the conduction band. Yanagida et al. found that panchromatic sensitizer dyes exhibited poor photocurrents, suggesting a reduced efficiency for electron injection [23]. Recently Klein and Nazeeruddin reported significantly higher IPCE values with an IPCE value of 66% at 700 nm for a novel panchromatic sensitizer dye, referred to as dye **5.5** as shown in Figure 5.11, synthesised by introduction of an unsaturated moiety into the dye **1** to extend the π conjugation system of the bpy rings [24].

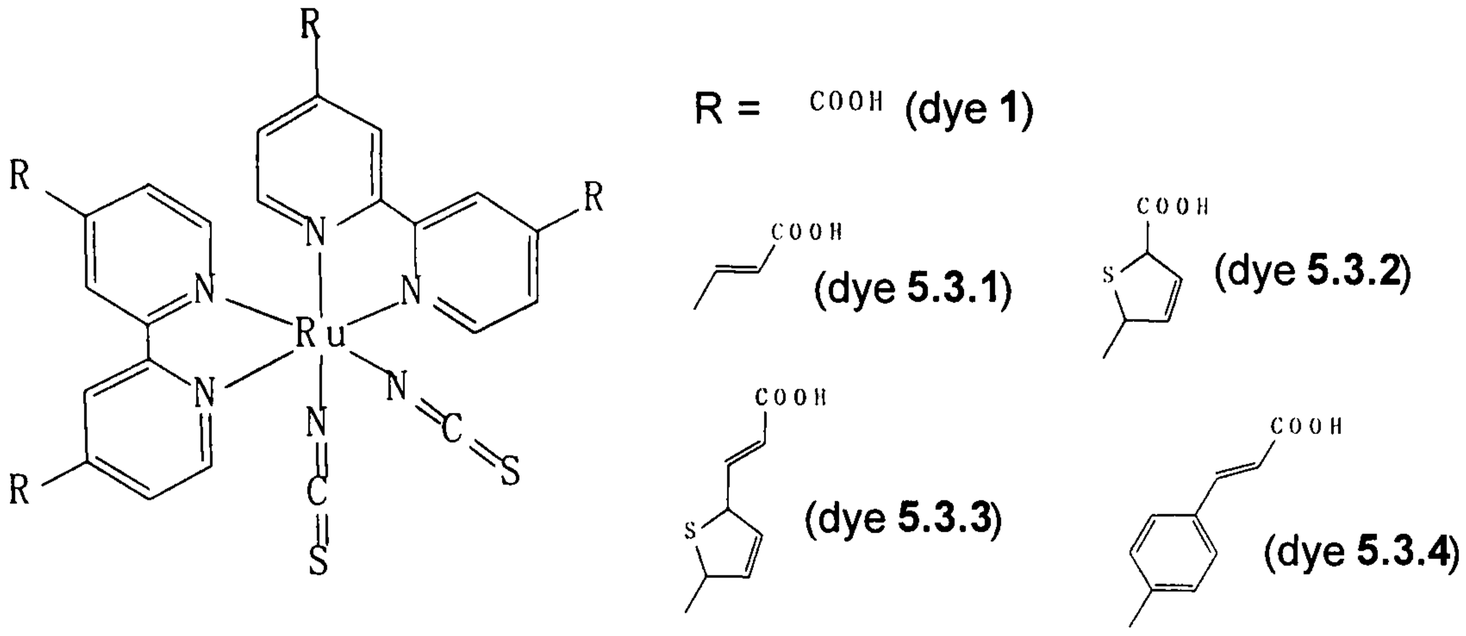


Figure 5.11 Chemical structure of a series of dyes, showing the dye **1** with no introduced side chain spacer, and dye **5.5**, dye **5.6**, dye **5.7** and dye **5.8** having vinyl, thiophene, vinyl thiophene, and vinyl phenyl groups as spacers between the pyridine group and carboxyl groups.

In this section electron transfer kinetics study are addressed not only for the dye **5.5** but also three other ruthenium complex dyes synthesised by Klein at EPFL on the basis of the same concept, as illustrated in Figure 5.11. As shown in Table 5.1, extension of the the π conjugation system results in a red shift of the dye absorption maximum. For these dyes not only the electron injection process, as mentioned above, but also potentially the electron recombination process CR1 could be altered by the introduced moieties because they could lead to an increased spatial separation between injected electrons in the TiO_2 electrode and dye cations. Both electron transfer processes are, therefore, studied with TAS for a series of the dyes, dye **5.5**, **5.6**, **5.7** and **5.8** with the dye **1** as a control material.

Table 5.1 Absorption maximum for the series of sensitizer dyes

	λ_{max} (nm)[a]
dye **1**	534
dye **5.5**	546
dye **5.6**	556
dye **5.7**	559
dye **5.8**	551

[a] Absorption spectra were collected for the dye solution in ethanol with the low concentration of around 0.1 mM.

5.3.2 Experimental

All experiments were carried out with nanocrystalline TiO_2 films sensitised by the Ru dyes. The dye **1** has no introduced side chain spacer, and the dye **5.5**, **5.6**, **5.7** and **5.8** have vinyl, thiophene, vinyl thiophene, and vinyl phenyl group as spacers between pyridine group and carboxyl group, respectively. These dyes were synthesized by Klein et al. [13]. Sensitization of TiO_2 films with dyes dye **1**, dye **5.5** and dye **5.8** was achieved by immersing the electrode at room temperature for three days in 1 mM solutions of these dyes in 1:1 mixture of acetonitrile and 2-methyl-2-propanol. As for dye **5.6** and **5.7**, 0.5 mM solutions were used because of shortage of these dyes. However, this difference in concentration would be immaterial for the studies mentioned in this section, because the dye concentration influences mainly how long the adsorption takes to reach the saturation, not on the maximum of the dye loading. Three days was found to be long enough for such Ru complexes to achieve adsorption saturation. (See Figure 3.7 in Chapter 3) All nanocrystalline TiO_2 films were fabricated with ECN35 paste. The thickness of the films was controlled to be 4 μm with doctor blade technique with single scotch tape.

All TAS data were collected for samples covered by a drop of propylene carbonate with a piece of cover slide to protect degradation of dyes. Samples were excited at 540 nm for all dyes to allow the difference in OD of each sample to minimize, and the data monitored the photoinduced absorption of injected electrons in the TiO_2 electrode at 1000 nm, as reported in [17].

5.3.3 Results

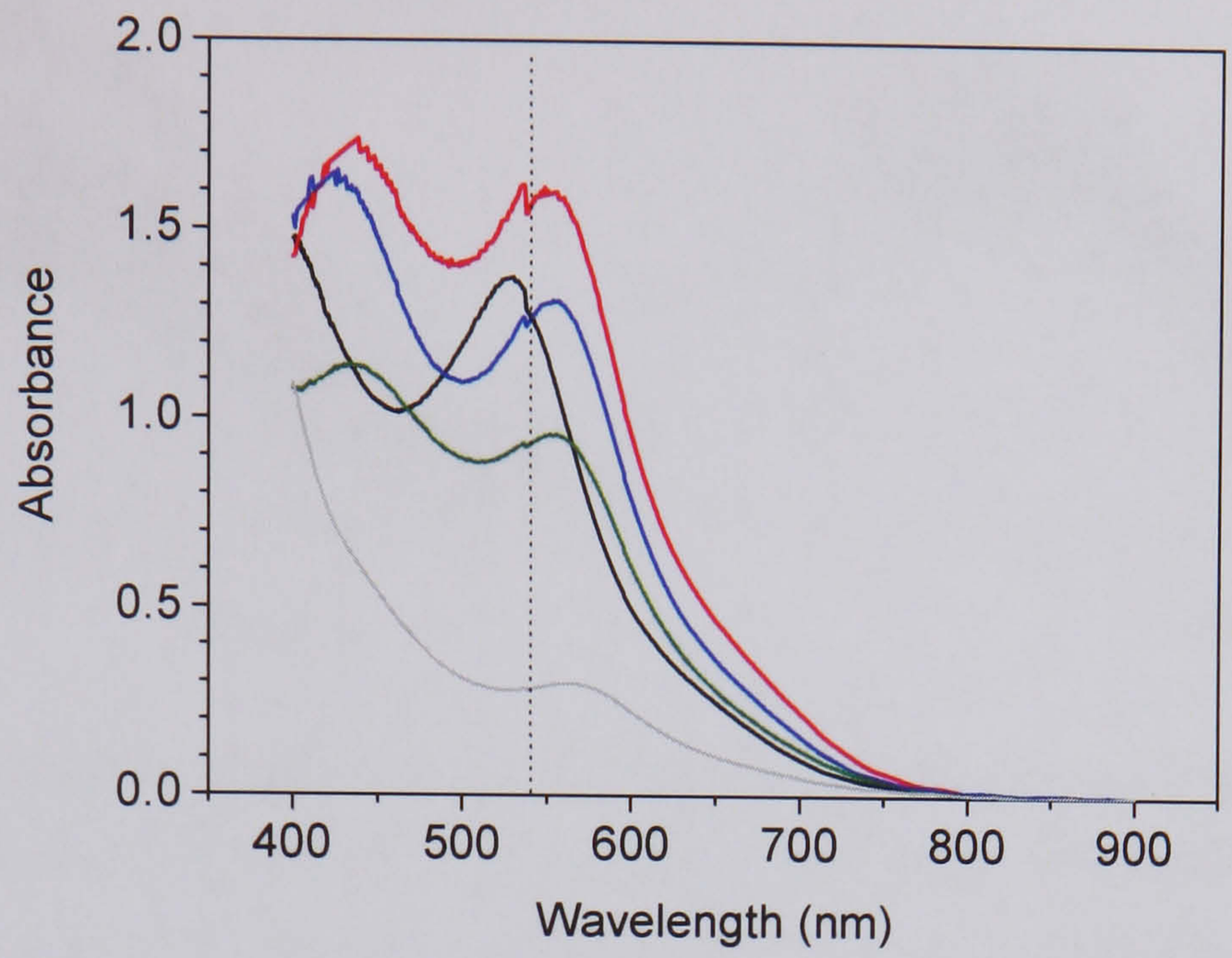


Figure 5.12 UV-visible absorption spectra of the nanocrystalline TiO_2 films sensitised with a series of dyes with different spacers: dye **5.5** (red), dye **5.6** (green), dye **5.7** (blue), dye **5.8** (grey) and dye **1** (black). Dotted line shows the excitation wavelength for the TAS measurement.

Firstly, UV-visible absorption spectra of the sensitised films were measured, as shown in Figure **5.12**. It is apparent that all absorption spectra for the dyes are reasonably red-shifted compared to the dye **1**, consistent with the solution data shown in Table 5.1. Peak optical densities for all dyes except for dye **5.8** were between 0.9 and 1.7. For dyes **5.5** though **5.8** differences in peak OD may result from either differences in dye loading and / or differences in extinction coefficient. In this study, because of this poor dye coverage, dye **5.8** was omitted from the following experiments.

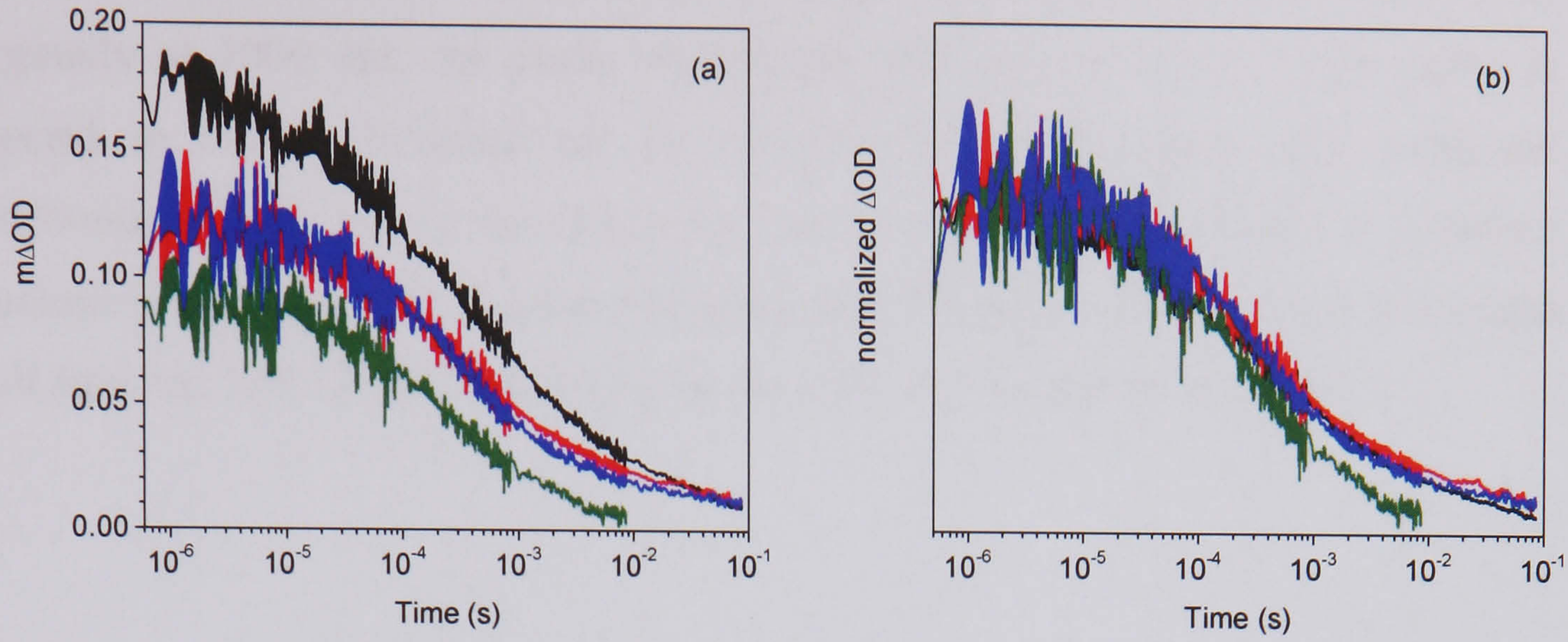


Figure 5.13 Transient absorption data monitoring at 1000 nm after excitation at 540 nm for TiO_2 films sensitised with dye **5.5** (red), **5.6** (green), **5.7** (blue) and **1** (black). The data are assigned to absorption of the injected electrons in the TiO_2 electrode. In Figure 5.13(a) signal amplitude is corrected based on the sample optical densities at 540 nm. Figure 5.13(b) shows normalised transient absorption data, showing the half times ($t_{50\%}$) of the decays of dye **5.5**, **5.6**, **5.7** and **1** are 1.8×10^{-4} s, 4.6×10^{-4} s, 1.1×10^{-4} s and 9.8×10^{-5} s, respectively.

Figure 5.13 shows the transient absorption data for the dyes, probed at 1000 nm to monitor photoinjected electrons in TiO_2 as assigned by Green et al. [17]. These data were also normalized at the signal size at 10^{-6} s to facilitate comparison of their recombination dynamics, as shown in Figure 5.13(b). It is apparent that the recombination dynamics for all samples were almost indistinguishable with half times between 9.8×10^{-5} s and 4.6×10^{-4} s. This observation is particularly striking because it indicates that the increase of the distance between the TiO_2 surface and dye metal centre does not significantly influence on the recombination dynamics. This can be understood by taking into account retention of the electronic coupling between the dye cation and the TiO_2 electrode due to the unsaturated nature of this moiety as shown for a tripod-shaped Ru complex containing triple C-C bonds studied by Galoppini [25].

On the other hand, in Figure 5.13(a) injection yields can be compared. It is apparent that the electron injection yields, monitored by the initial magnitude of the photoinduced absorption at 10^{-6} s, were observed to be 10-20% lower for the dyes **5.5**

– **5.7** relative to the control dye **1**. (For dye **1**, dye cation absorption contributes only marginally at 1000 nm, the probe wavelength. For dyes 5.5 to 5.7, the cation is expected to remain localised on the invariant Ru NCS group. Any increased contribution of dye cation absorption for dyes 5.5 to 5.7 would result in a further reduction in the estimated electron injection yield.) This lower injection yield might result from the low LUMO energetics for the dyes, as discussed further below.

5.3.4 Discussion

Figure 5.13(b) shows that the recombination dynamics for all four dyes in this study were reasonably similar. This observation contrasts with the distance dependence of the electron recombination with a series of ruthenium dyes reported by Clifford et al. [26]. However, as mentioned before in the results section, electronic saturation of the spacer could be a reason for this, even though the introduction of the spacers is expected to lead to longer distances between the injected electrons on the surface of the TiO_2 and the HOMO of the dye cations, which presumably remain localised on the NCS group as according previous study on dye **2**. (See Figure 4.3 in Chapter 4) This interpretation is in agreement with the spacer independent recombination dynamics observed by Galoppini et al for a tripod-shaped Ru complex with an unsaturated spacer unit [25].

On the other hand, there was a noticeable variation in injection yield with the introduction of the spacers, as shown in Figure 5.13. This may be due to the differences of the LUMO energy level of the dyes, which could arise from the extended conjugation introduced by the moiety. Assuming the HOMO energies for the dyes are the same due to maintenance of the chemical structure of the NCS ligands, where the HOMO tends to be localised [27], the red-shifted maximum absorption can be assigned to a lowering the LUMO level, which could result in poor injection yield. Supporting this argument, Figure 5.14 shows a good correlation between the injection yields extracted from Figure 5.13(a) and the energy gap of HOMO level and LUMO level of the dyes calculated from the solution absorption maxima shown in Table 5.1. This observation is consistent with studies done by Yanagida et al., showing the quantum yield (Φ_{inj}) of the charge injection is related to the free energy change ($-\Delta G_{inj}$), expressed as $-\Delta G_{inj} = E_{cb} - E_{Ru(III)/Ru(II)^*}$, where $E_{Ru(III)/Ru(II)^*}$ is the oxidation potential of the excited state of the dye [23]. Also these observations are corroborated by the fundamental studies on the electron injection process [28, 29], showing the dependence of electron injection dynamics upon $-\Delta G_{inj}$.

The direct relationship between the injection yield and the HOMO/LUMO energy gap implies that the LUMO of the dyes employed are close in the energy to the TiO_2 conduction band edge. For the HOMO level, the unvarying kinetics of the

electron recombination process for the dyes employed, as shown in Figure 5.13(b), imply a suitable energetic level of HOMO for the dyes.

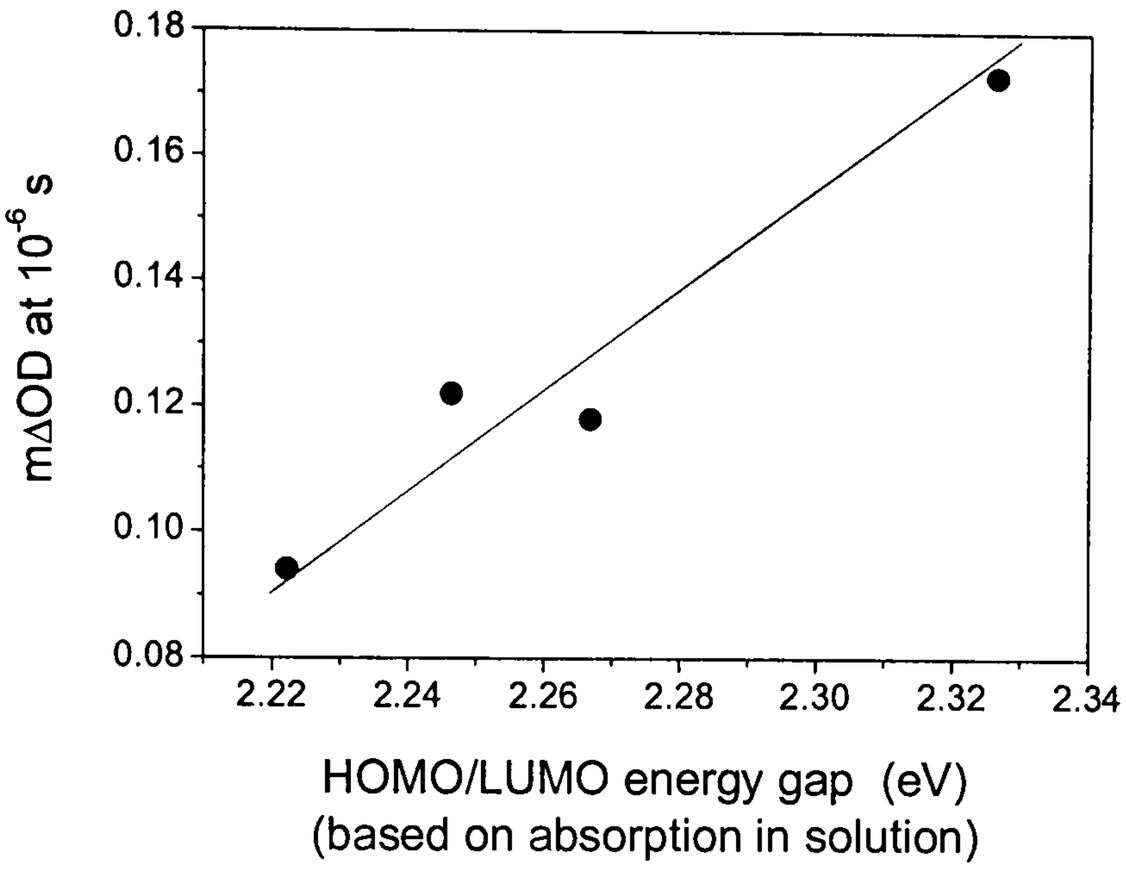


Figure 5.14 A plot of initial amplitude of transient absorption for dye sensitised TiO_2 films taken from Figure 5.13(a), indicating the electron injection yield, as a function of HOMO-LUMO energy gap based on absorption in dye solution from Table 5.1.

Regarding overall device performance, N3 could be predicted to be the best out of those 4 dyes due to its higher injection yield whilst exhibiting similar recombination dynamics. This prediction is partially supported by previous studies, showing the relatively lower saturated IPCE values for dye **5.5** (77%) relative to dye **1** (87%) [13, 30], although the shortcomings of injection yield are balanced by the improved red absorbance of the dye, resulting in comparable photocurrent generation efficiencies under AM1.5 one sun illumination. Further study on improvement of the injection yield should be planned. For example, electrolyte composition can affect the TiO_2 conduction band according to [2, 31, 32], depending upon the concentration of potential determining ions in the solution. The data demonstrated in this section were collected with dye sensitized nanocrystalline TiO_2 films covered in inert solvent. Therefore, suitable optimisation of electrolyte composition may lead to significant improvements in device performance.

5.4 Characterisation of a series of platinum complexes

5.4.1 Introduction

Since the advent of DSSCs in the early 1990s, ruthenium polypyridyl dyes have received much attention due to their outstanding performance as sensitizers in DSSCs, reaching efficiencies of up to 10% [30]. In parallel, other metal centred dyes have also been studied, including complexes of Fe [5, 33, 34], Os [35] and Re [7, 36]. In the past few years, [Pt(II)(diimine)(dithiolate)] compounds have been investigated for their use in solar cells [11, 12, 37, 38] as they possess a number of key features that make them of interest as sensitizers. These include an absorption band in the visible region with a relatively large molar extinction coefficient, and in some cases, luminescent properties in fluid solution.

The structure of a typical Pt(II)(diimine)(dithiolate) is shown in Figure 5.15. Visible light absorption by such dyes results from a charge-transfer transition assigned to a "mixed metal-ligand to ligand" charge transfer (MMLL'CT) absorption involving a HOMO that is a mixture of Pt(d) and dithiolate S(p) orbitals and a π^* bpy LUMO [37, 39]. Tuning these two molecular orbital energeties is crucial to optimising dye function for applications to DSSC. All dyes investigated for DSSCs contain a functionality that anchors the dye to the TiO_2 surface, and for the majority of dyes this anchor is {4,4'$(COOH)_2$-bpy}, where bpy is 2,2'-bipyridyl (e.g. the Ru$(dcbpy)_2L_2$ dye). The reason for the selection of the 4,4' position is mainly because of the favourable stereochemistry for anchoring to the surface of the TiO_2. Previous publications of Pt(II)(diimine)(dithiolate) have shown that the LUMO energy can be altered by changing the position of the carboxylic acid on the bpy ring [11, 40]. It was, for example, found that the electron density at the 4,4'-positions on a family of compounds of general formula [Pt$(X)_2$-bpy Cl_2] (X = H, Me, COOMe, COOEt, and NH_2) is significantly greater than the 3,3'- or 5.5'-positions [41].

No study has been reported of the correlation of the effect of the position of the substituents in such Pt(II)(diimine)(dithiolate) complexes with DSSC device performance. This chapter presents a comparison of the electrochemical and optical properties of dyes with carboxylic acid substituents at the 3,3'-, 4,4'-, and 5,5'-

positions in the bipyridyl moiety of [Pt(II)(diimine)(dithiolate)] dyes (referred to as pt**1**, pt**2** and pt**3** respectively through this thesis) and assessment of their device performances in a DSSC. In this section the relationship between chemical structure and the function will be addressed, focusing particularly upon their impact upon electron recombination processes and the device performance.

5.4.2 Experimental

Synthetic procedures for the 3 Pt complexes employed, [Pt{X,X'$(CO_2H)_2$-2,2'-bipyridyl}(maleonitriledithiolate)] (X,X'=3,3'(pt**1**), 4,4'(pt**2**), or 5,5'(pt**3**)) are reported elsewhere. [12] (See also Figure 5.15)

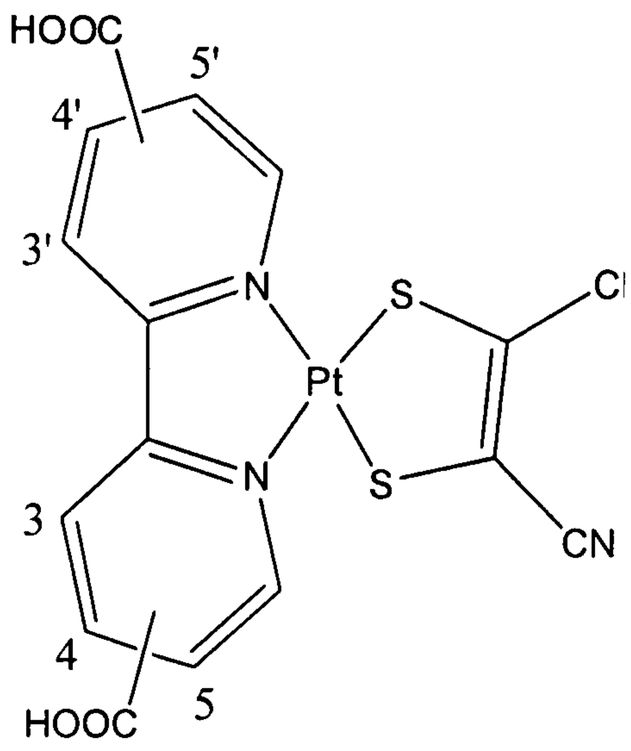


Figure 5.15 Chemical structure of [Pt{X,X'(dicarboxylato)-2,2'-bipyridyl}(maleonitriledithiolate)] (X,X'=3,3'(pt**1**), 4,4'(pt**2**), or 5,5'(pt**3**))

All experiments were conducted as described previously in Chapter 2 except for solvents employed for dye solutions. For these dyes DMSO and MeCN were selected as solvents because of the good dye solubility in these solvents. Nanocrystalline TiO_2 films were immersed in 1.72 mM pt**1** solution in DMSO, 1.72 mM pt**2** solution in DMSO, and 1.72 mM pt**3** solution of 1:1 DMSO/MeCN at room temperature overnight.

5.4.3 Results and Discussion

5.4.3.1 Sensitization of nanocrystalline TiO_2 films

Immersion of nanocrystalline TiO_2 in 1.7 mM solutions of pt**1** (in 1:1 acetonitrile / dimethyl sulfoxide), pt**2** (in dimethyl sulfoxide) and pt**3** (in dimethyl sulfoxide) resulted in a strong coloration of the films. UV/visible absorption spectra for the resulting dye sensitized films are shown in Figure 5.16.

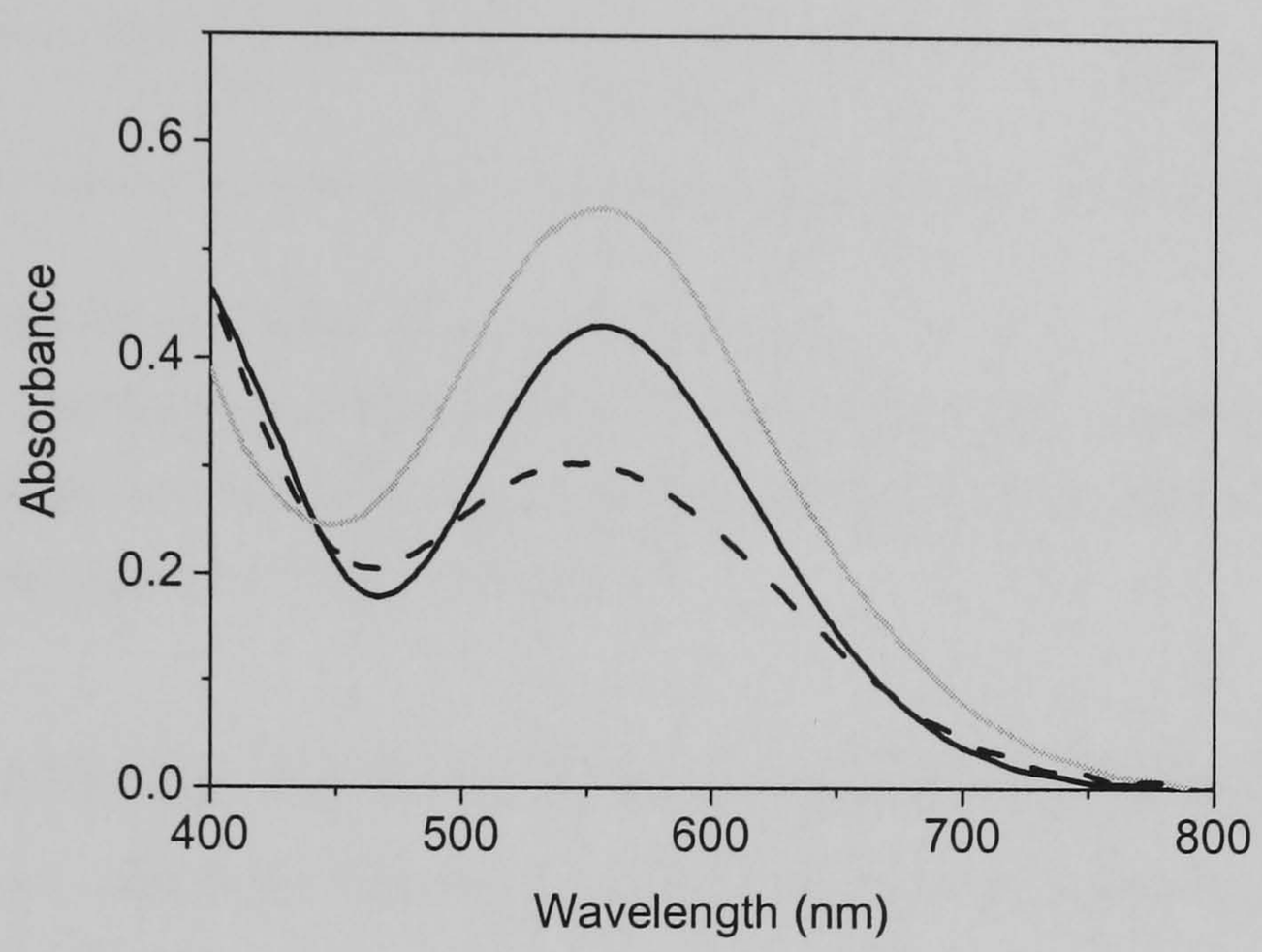


Figure 5.16 UV-visible measurement for nonporous TiO_2 sensitized by pt**1** (black solid line), **2** (grey solid line) and **3** (black dashed line).

Dye coverages for pt**1**, pt**2** and pt**3** were determined from these film spectra assuming the molar extinction coefficients determined in solution, 4,200, 5,600 and 3,100 $M^{-1}cm^{-1}$ respectively [12]. These are summarized in Table 5.2, indicating approximately 100% dye coverages for all three dyes. This suggests that approximately monolayer dye coverage is achieved for all three dyes, with differences in film optical density primarily arising from the differences in dye molar extinction coefficient.

Table 5.2 Summary of UV/Vis spectroscopy results obtained for nanocrystalline TiO_2 films sensitised with pt**1**, pt**2** and pt**3**.

	Optical density [a]	**Extinction coefficient** ($M^{-1}cm^{-1}$) [b]	**Dye coverage (%)** [c]
pt**1**	0.43	4200	105
pt**2**	0.54	5600	98
pt**3**	0.30	3100	101

[a] Optical densities were obtained at a maximum.

[b] Extinction coefficient was determined by UV/Vis spectroscopy for dye solutions [12].

[b] Dye coverages were calculated as described in section 2.1.2.3 in Chapter 2, assuming that a dye surface area is 7.73×10^{-15} cm^2.

Transient absorption data for the resulting dye sensitized films covered in inert solvent (PC) were obtained following pulsed laser excitation and are shown in Figures 5.17 and 5.18. In all cases, a broad absorption increase was observed between 700 and 1000 nm, assigned to induced absorption of the dye cation/$TiO_2(e^-)$ states generated by electron injection from the dye excited state (Fig. 5.17). For pt**1**, an absorption maximum was observed at 700 nm and is assigned as dye cation absorption. In contrast for pt**2** and pt**3**, the transient spectrum increases steadily towards longer wavelengths, indicating that for these dyes the transient signal is dominated by TiO_2 electron absorption, with cation absorption for these dyes being relatively weak over this spectral region. The relatively low signal amplitude for pt**3** is consistent with the low film optical density due to the low dye molar extinction coefficient.

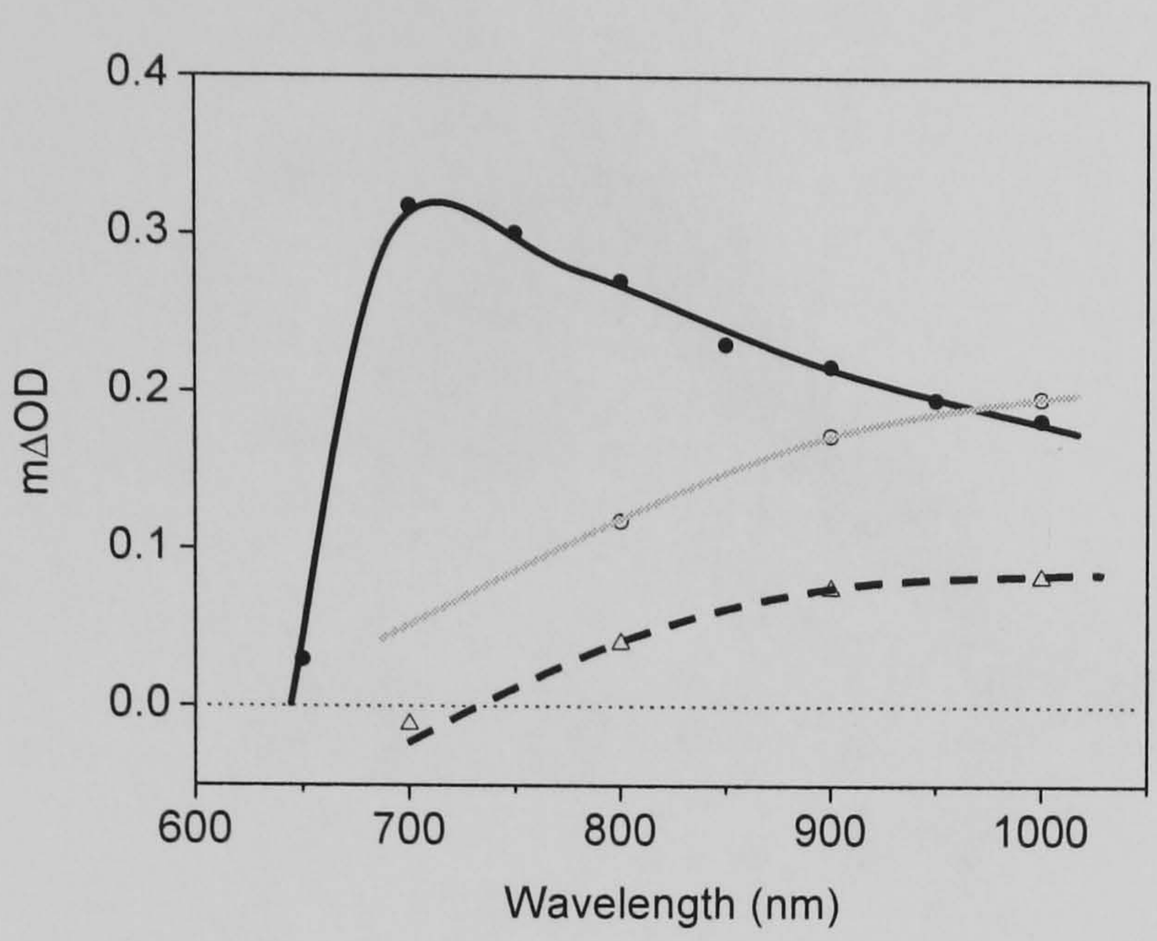


Figure 5.17 Comparison of the difference absorption spectra of pt**1** (black solid line), pt**2** (grey solid line) and pt**3** (black dashed line) on nanocrystalline TiO_2 film. The spectra were recorded with 550 nm excitation pulse at 10^{-6} s.

Decay dynamics of the transient absorption signal, assigned to the recombination of the TiO_2 electrons with dye cations, are shown in Figure 5.18. These dynamics are typical of charge recombination dynamics for such dye sensitized TiO_2 films [11, 42], with pt**2** showing faster, recombination dynamics relative to pt**1**.

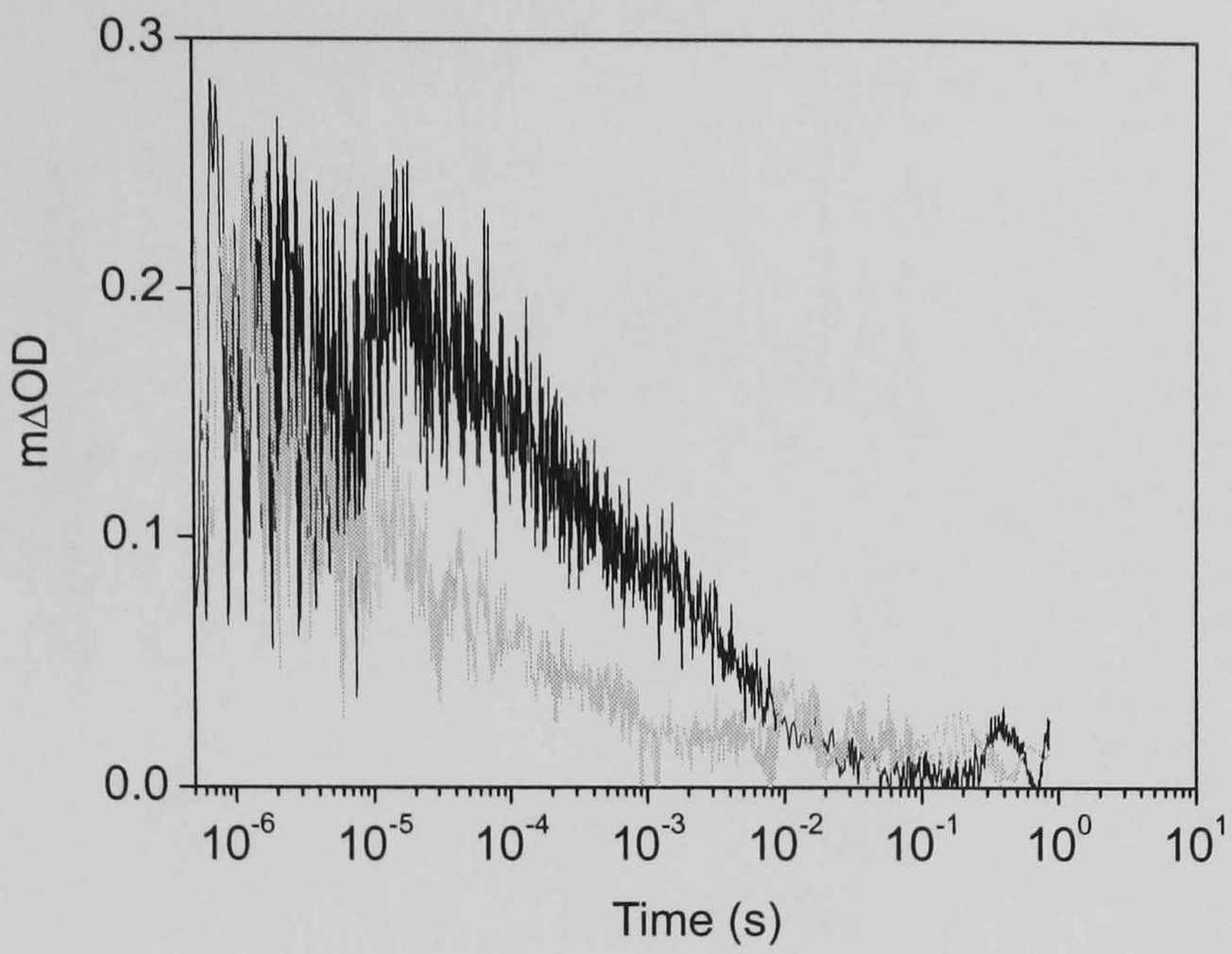


Figure 5.18 Transient absorption data monitoring the charge recombination kinetics for 4 μm TiO_2 films sensitized with pt**1** (black) and pt**2** (grey). Experiments employed 550 nm excitation and all data were collected at 900 nm probe wavelength. The half-life values for pt**1** and pt**2** are 3.2 x 10^{-4} s and 6.5 x 10^{-6} s respectively. The data for pt**3** were less reliable because of small signals.

Typical current/voltage characteristics for photoelectrochemical cells sensitized with pt**1**, pt**2** and pt**3** are shown in Figure 5.19. It is apparent that there is a good correlation between the UV/visible absorbance data, the transient absorption data and the device current/voltage characteristics. The pt**2** dye which has the highest optical density also has the highest short circuit current (I_{sc}), whilst pt**1** exhibits the slowest recombination dynamics and the highest open circuit voltage (V_{oc}).

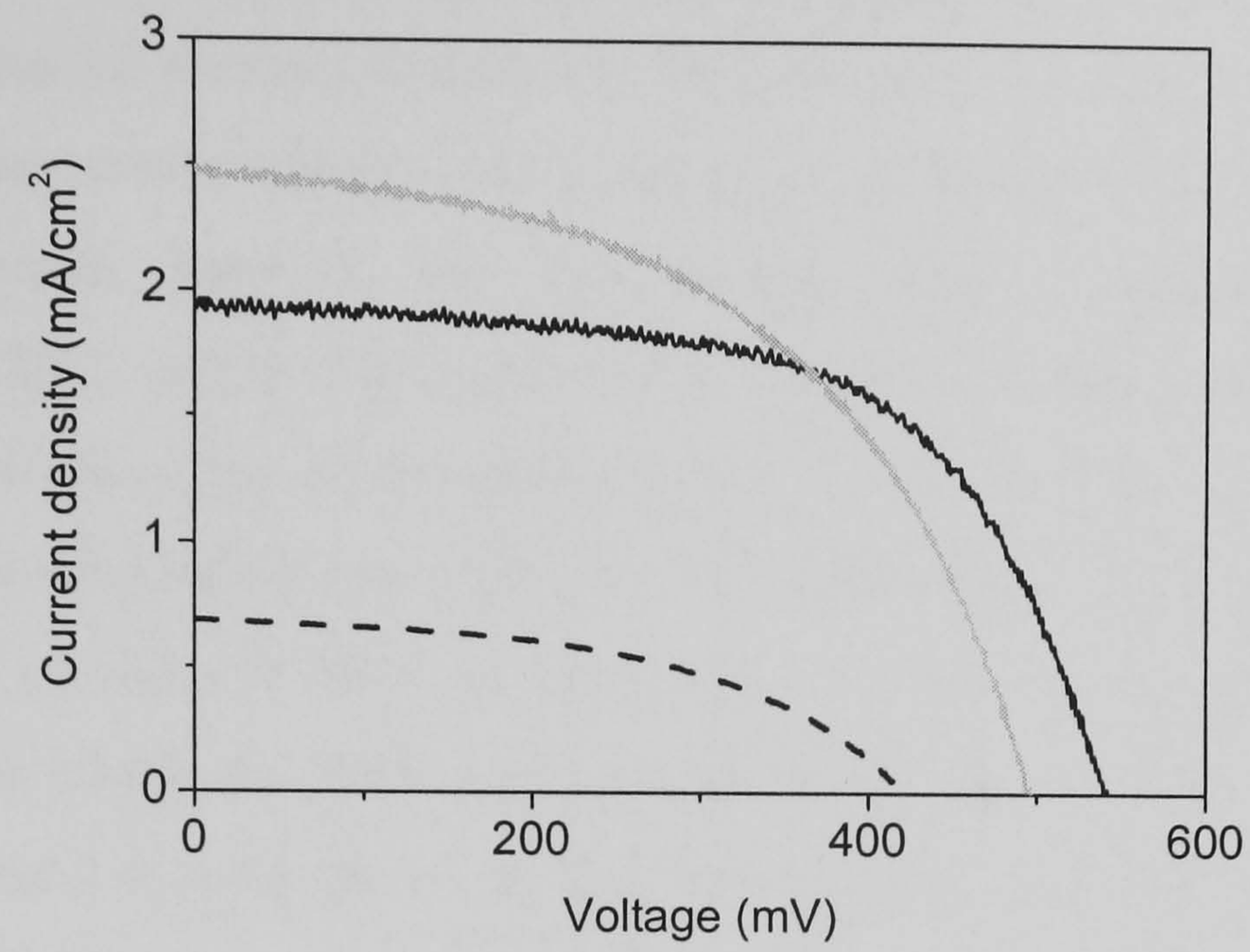


Figure 5.19 IV characterization for the liquid DSSC with pt**1** (black solid line), **2** (grey solid line) and **3** (black dashed line) under 1 sun AM1.5 light illumination. The areas of all samples were 1.0 cm^2. I_{sc}, V_{oc}, *ff* (fill factor) and efficiency were 1.94 mA, 540 mV, 61.4% and 0.64% for pt**1**; 2.49 mA, 490 mV, 51.3% and 0.63% for pt**2**; 0.68 mA, 420 mV, 50.5%, and 0.14% for pt**3** respectively.

From the data detailed above, it is apparent that pt**1** exhibits the highest photovoltaic device performance of the dye series studied. This device efficiency however remains relatively low compared to the more established sensitizer dye, the di-tetrabutylammonium salt of $[RuL_2(NCS)_2]$ (L = 2,2′-bipyridyl-4,4′-dicarboxylato). (See Figure 3.5 in Chapter 3) This lower device efficiency can be primarily attributed to the relatively low optical absorbance of pt**1** compared to $RuL_2(NCS)_2$ (with peak molar extinction coefficients in the visible of 5615 $M^{-1}cm^{-1}$ and 14000 $M^{-1}cm^{-1}$ respectively). As the devices presented here employed 4 μm, non-scattering TiO_2 films, this lower optical absorbance can be expected to have a strong effect on device performance. A significant improvement in device performance for pt**1** can be expected by the use of thicker TiO_2 films with the addition of light scattering layers.

5.4.3.2 Device optimization and comparison with Ruthenium complex (dye **2**)

A more detailed characterization of the photovoltaic performance and transient kinetics of devices employing pt**1** was undertaken to elucidate whether differences in device performance between pt**1** and widely used ruthenium dye, dye **2** ($Ru(dcbpy)_2(NCS)_2$), can be attributed to dye optical absorbance alone, or whether other parameters also limit device performance. Figure 5.20 shows current/voltage data for pt**1**/TiO_2 solar cells employing both the standard electrolyte **A** (containing the additive t-butyl pyridine (t-BP)), as employed in Figure 5.19, and an alternative electrolyte **B** in which the t-BP was omitted from the electrolyte. Control data employing the dye **2** are also shown for comparison, with the dye loading of the dye **2** being selected to give the same peak optical density as that of pt**1** (OD = 0.5 at 535 nm).

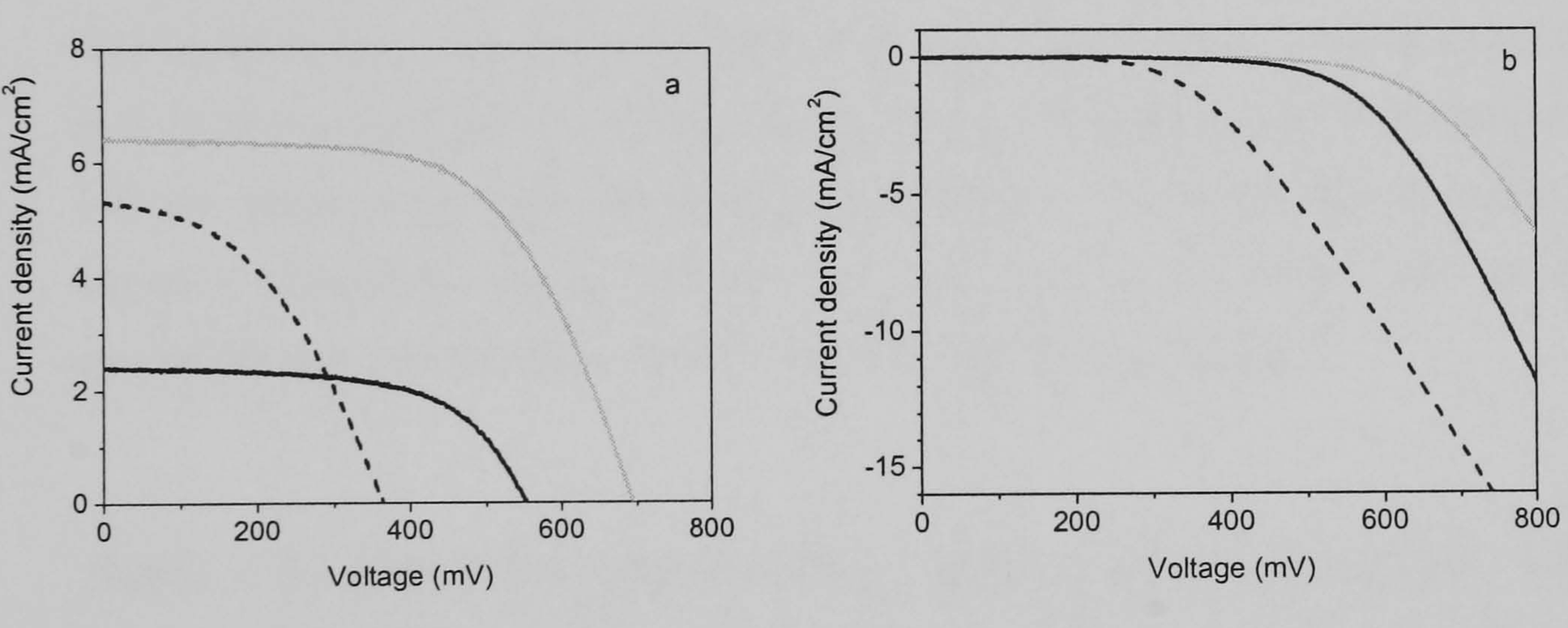


Figure 5.20 Comparison of cell performance obtained for DSSCs with sensitised pt**2** using electrolyte **A** (containing t-butyl pyridine (t-BP)) (black solid line) and electrolyte **B** (without t-butyl pyridine) (black dashed line). A cell employed the Ru dye **2** and electrolyte **A** was also measured as a control sample (grey solid line). Figure (a) represents I-V curve of all three cells under 1 sun illumination. The cell performance, I_{sc}, V_{oc}, ff and efficiency, were 2.4 mA, 550 mV, 62% and 0.80% for pt**1** using electrolyte **A**; 5.3 mA, 370 mV, 44% and 0.84% for pt**1** using electrolyte **B**; 6.4 mA, 700 mV, 60% and 2.69% for dye **2** using electrolyte **A**, respectively. Figure (b) shows the data collected under dark conditions.

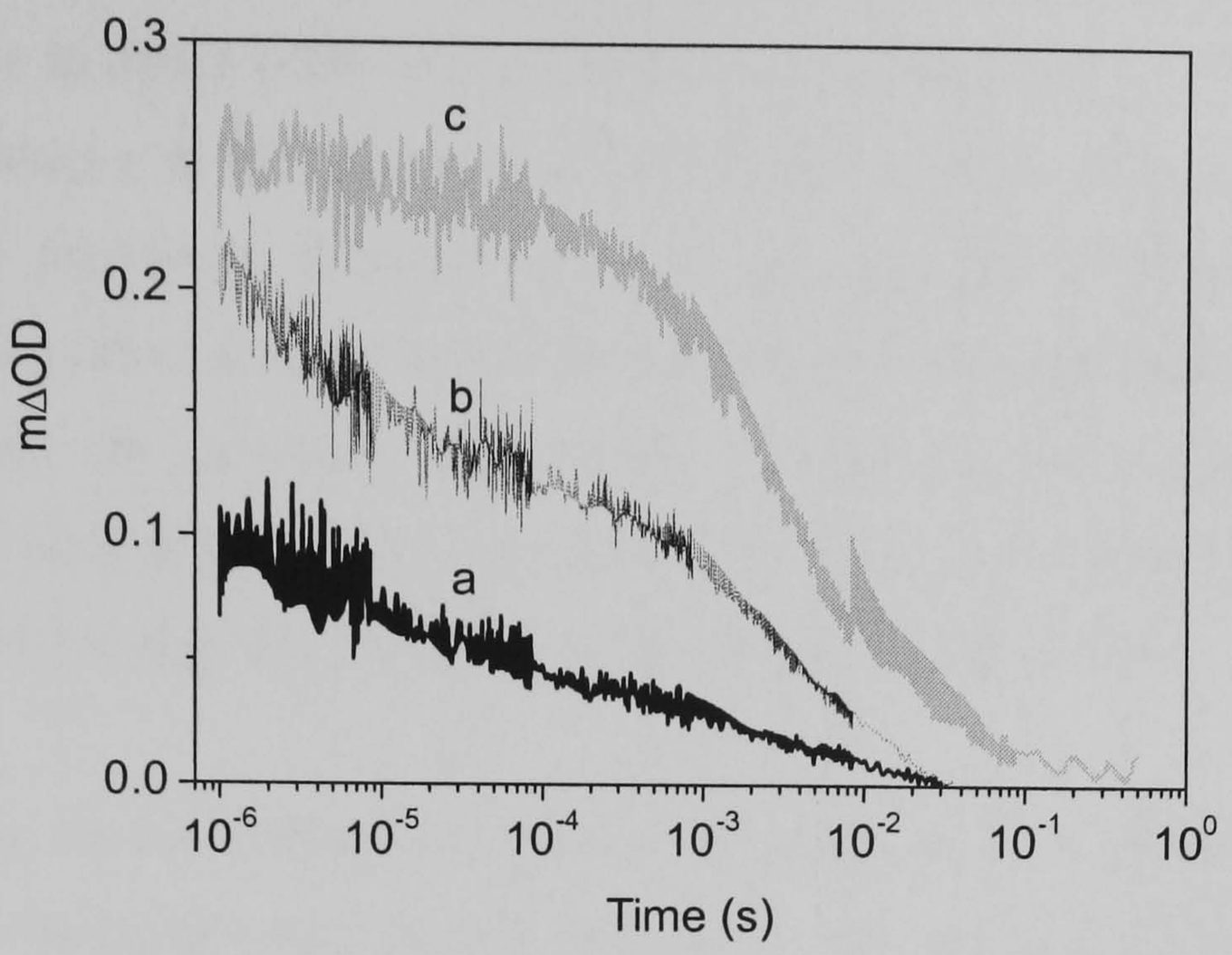


Figure 5.21 Comparison of transient absorption decays between the cell using electrolyte **A** (containing t-butyl pyridine (t-BP)) (a) and electrolyte **B** (without t-butyl pyridine) (b). A cell employed the dye **2** and electrolyte **A** was also measured as a control sample (c). The decays were monitored following optical excitation at 540 nm under white light and detected at 1000 nm. A comparison in terms of transient absorption decay between the cells with and without t-BP in the electrolyte suggests its effect on the LUMO energy level of the dyes.

Figure 5.21 shows the corresponding transient absorption signals, with the excitation wavelength of 540 nm corresponding to that at which the optical density of the dye **2** and pt**1** sensitized devices are identical. Note that these transient data were collected for complete devices rather than for dye sensitized films alone as employed in Figure 5.17, with the probe wavelength of 1000 nm being selected to correspond primarily to absorption of electrons injected into the TiO_2 by the optical laser pulse. It is apparent that for pt**1** the omission of t-BP from the electrolyte results in a significantly higher current density, but at the expense of a lower cell voltage. This observation is correlated with a larger transient signal, assigned to long lived I_2^- / e^- charge separated states. This effect is attributed to the established influence of t-BP on the TiO_2 conduction band energetics – the absence of t-BP lowers the TiO_2 conduction band, favoring electron injection and resulting in both the larger transient signal and higher short circuit current. The absence of efficient electron injection for

dye pt**1** in the presence of t-BP is attributed to the lower dye excited state oxidation potential relative to dye **2** (-770 mV vs. SCE for pt**1**, compared to -800 mV vs. SCE for dye **2**). Strikingly, in the absence of t-BP both the short circuit current density and transient signal amplitude obtained with pt**1** are of similar magnitude to those observed for the control data for dye **2.** These data are therefore indicative that in the absence of t-BP, the quantum efficiencies of both electron injection and dye regeneration for the pt**1**/TiO_2 system are near unity. The disadvantage for this pt**1** dye is its lower LUMO energetics, hindering efficient electron injection.

The lower device voltage obtained with sensitizer pt**1** relative to dye **2** is correlated with the higher dark current associated with this dye. This effect may be associated with the influence of the sensitizer dye on the TiO_2 conduction band energetics. Alternatively this effect may result from a dye induced acceleration of the rate constant for electron recombination with the redox electrolyte. Experiments to further address this point are in progress.

5.4.4 Conclusions

This is the first report of a Pt based dye sensitizer where the bpy has been substituted in the 3,3′ positions (pt**1**). Interestingly it shows the best performance of the three sensitizers tested. Transient absorption studies with different electrolyte compositions indicated that the disadvantage for this dye is lower LUMO energetics of this dye, resulting in hindering efficient electron injection, and therefore resulting in a lower photocurrent with the standard electrolyte. TAS and I/V characterization studies furthermore indicated that lower V_{oc} for pt**1** could rise from faster recombination dynamics.

The work reported in this article demonstrates the worth of looking at other anchor ligands in the rational design of solar cell dyes and broadens the scope for further investigations into potential dyes for use in DSSC.

5.4.5 References

1. Gratzel, M., *Photoelectrochemical cells.* Nature, 2001. **414**(6861): p. 338-344.

2. Haque, S.A., et al., *Charge separation versus recombination in dye-sensitized nanocrystalline solar cells: the minimization of kinetic redundancy.* Journal of the American Chemical Society, 2005. **127**(10): p. 3456-3462.

3. Nazeeruddin, M.K., et al., *Engineering of efficient panchromatic sensitizers for nanocrystalline TiO2-based solar cells.* Journal of the American Chemical Society, 2001. **123**(8): p. 1613-1624.

4. Durrant, J.R., S.A. Haque, and E. Palomares, *Towards optimisation of electron transfer processes in dye sensitised solar cells.* Coordination Chemistry Reviews, 2004. **248**(13-14): p. 1247-1257.

5. Ferrere, S., *New photosensitizers based upon Fe-II(L)(2)(CN)(2) and (FeL3)-L-II , where L is substituted 2,2 '-bipyridine.* Inorganica Chimica Acta, 2002. **329**: p. 79-92.

6. Sauve, G., et al., *Dye sensitization of nanocrystalline titanium dioxide with osmium and ruthenium polypyridyl complexes.* Journal of Physical Chemistry B, 2000. **104**(29): p. 6821-6836.

7. Asbury, J.B., et al., *Bridge length-dependent ultrafast electron transfer from Re polypyridyl complexes to nanocrystalline TiO2 thin films studied by femtosecond infrared spectroscopy.* Journal of Physical Chemistry B, 2000. **104**(50): p. 11957-11964.

8. Hara, K., et al., *Molecular design of coumarin dyes for efficient dye-sensitized solar cells.* Journal of Physical Chemistry B, 2003. **107**(2): p. 597-606.

9. Hirata, N., et al., *THE INFLUENCE OF DYE PROTONATION UPON THE PERFORMANCE OF DYE SENSITISED SOLAR CELLS.* ECS meeting proceedings for session N1, 2005.

10. Hirata, N., et al., *Supramolecular control of charge-transfer dynamics on dye-sensitized nanocrystalline TiO2 films.* Chemistry-a European Journal, 2004. **10**(3): p. 595-602.

11. Geary, E.A.M., et al., *Synthesis, structure and properties of Pt(2,2 '-bipyridyl-5,5 '-dicarboxylic acid)(3,4-toluenedithiolate) : tuning molecular properties for application in dye-sensitised solar cells.* Dalton Transactions, 2003(19): p. 3757-3762.

12. Geary, E.A.M., et al., *Synthesis, structure, and properties of Pt(II)(diimine)(dithiolate) dyes with 3,3 '-, 4,4 '-, and 5,5 '-disubstituted bipyridyl: Applications in dye-sensitized solar cells.* Inorganic Chemistry, 2005. **44**(2): p. 242-250.

13. Klein, C., et al., *Engineering of a novel ruthenium sensitizer and its application in dye-sensitized solar cells for conversion of sunlight into electricity.* Inorganic Chemistry, 2005. **44**(2): p. 178-180.

14. Zakeeruddin, S.M., et al., *Design, synthesis, and application of amphiphilic ruthenium polypyridyl photosensitizers in solar cells based on nanocrystalline TiO2 films.* Langmuir, 2002. **18**(3): p. 952-954.

15. Lagref, J.J., M.K. Nazeeruddin, and M. Gratzel, *Molecular engineering on semiconductor surfaces: design, synthesis and application of new efficient amphiphilic ruthenium photo sensitizers for nanocrystalline TiO2 solar cells.* Synthetic Metals, 2003. **138**(1-2): p. 333-339.

16. Montanari, I., J. Nelson, and J.R. Durrant, *Iodide electron transfer kinetics in dye-sensitized nanocrystalline TiO2 films.* Journal of Physical Chemistry B, 2002. **106**(47): p. 12203-12210.

17. Green, A.N.M., et al., *Transient absorption studies and numerical modeling of iodine photoreduction by nanocrystalline TiO2 films.* Journal of Physical Chemistry B, 2005. **109**(1): p. 142-150.

18. Nazeeruddin, M.K., et al., *Acid-base equilibria of (2,2 '-bipyridyl-4,4 '-dicarboxylic acid)ruthenium(II) complexes and the effect of protonation on charge-transfer sensitization of nanocrystalline titania.* Inorganic Chemistry, 1999. **38**(26): p. 6298-6305.

19. Islam, A., et al., *Synthesis and photophysical properties of ruthenium(II) charge transfer sensitizers containing 4,4 '-dicarboxy-2,2 '-biquinoline and 5,8-dicarboxy-6,7-dihydro-dibenzo 1,10 -phenanthroline.* Inorganica Chimica Acta, 2001. **322**(1-2): p. 7-16.

20. Zakeeruddin, S.M., et al., *Synthesis and photophysical properties of trans-dithiocyanato bis(4,4 '-dicarboxylic acid-2,2 '-bipyridine) ruthenium(II) charge transfer sensitizer.* Inorganica Chimica Acta, 1999. **296**(1): p. 250-253.

21. Renouard, T., et al., *Novel ruthenium Sensitizers containing functionalized hybrid tetradentate ligands: Synthesis, characterization, and INDO/S analysis.* Inorganic Chemistry, 2002. **41**(2): p. 367-378.

22. Argazzi, R., et al., *Enhanced Spectral Sensitivity from Ruthenium(Ii) Polypyridyl Based Photovoltaic Devices.* Inorganic Chemistry, 1994. **33**(25): p. 5741-5749.

23. Yanagida, M., et al., *Panchromatic sensitization of nanocrystalline TiO2 with cis- bis(4-carboxy-2- 2 '-(4- carboxypyridyl) quinoline)bis(thiocyanato-N)ruthenium(II).* Inorganic Chemistry, 2003. **42**(24): p. 7921-7931.

24. Klein, C., et al., *Amphiphilic ruthenium sensitizers and their applications in dye-sensitized solar cells.* Inorganic Chemistry, 2004. **43**(14): p. 4216-4226.

25. Galoppini, E., et al., *Long-distance electron transfer across molecule-nanocrystalline semiconductor interfaces.* Journal of the American Chemical Society, 2001. **123**(18): p. 4342-4343.

26. Clifford, J.N., et al., *Molecular control of recombination dynamics in dye-sensitized nanocrystalline TiO2 films: Free energy vs distance dependence.* Journal of the American Chemical Society, 2004. **126**(16): p. 5225-5233.

27. Srikanth, K., V.R. Marathe, and M.K. Mishra, *Role of electronic structure of ruthenium polypyridyl dyes in the photoconversion efficiency of dye-sensitized solar cells: Semiempirical investigation.* International Journal of Quantum Chemistry, 2002. **89**(6): p. 535-549.

28. Tachibana, Y., et al., *Modulation of the rate of electron injection in dye-sensitized nanocrystalline TiO2 films by externally applied bias.* Journal of Physical Chemistry B, 2001. **105**(31): p. 7424-7431.

29. Katoh, R., et al., *Efficiencies of electron injection from excited sensitizer dyes to nanocrystalline ZnO films as studied by near-IR optical absorption of injected electrons.* Journal of Physical Chemistry B, 2002. **106**(50): p. 12957-12964.

30. Nazeeruddin, M.K., et al., *Conversion of Light to Electricity by Cis-X2bis(2,2'-Bipyridyl- 4,4'-Dicarboxylate)Ruthenium(Ii) Charge-Transfer Sensitizers (X = Cl-, Br-, I-, Cn-, and Scn-) on Nanocrystalline Tio2 Electrodes.* Journal of the American Chemical Society, 1993. **115**(14): p. 6382-6390.

31. Tachibana, Y., et al., *Transient luminescence studies of electron injection in dye sensitised nanocrystalline TiO2 films.* Journal of Photochemistry and Photobiology a-Chemistry, 2001. **142**(2-3): p. 215-220.

32. Boschloo, G. and D. Fitzmaurice, *Electron accumulation in nanostructured TiO2 (anatase) electrodes.* Journal of Physical Chemistry B, 1999. **103**(37): p. 7860-7868.

33. Ferrere, S., *New photosensitizers based upon Fe(L)(2)(CN)(2) and Fe(L)(3) (L = substituted 2,2 '-bipyridine): Yields for then photosensitization of TiO2 and effects on the band selectivity.* Chemistry of Materials, 2000. **12**(4): p. 1083-1089.

34. Ferrere, S. and B.A. Gregg, *Chloride oxidation catalysis by a polymeric oxide derived from Ru(4,4 '-dimethyl-2,2 '-bipyridine)(Cl)(3)(H2O).* Journal of the Chemical Society-Faraday Transactions, 1998. **94**(18): p. 2827-2833.

35. Sauve, G., et al., *High quantum yield sensitization of nanocrystalline titanium dioxide photoelectrodes with cis-dicyanobis(4,4 '-dicarboxy-2,2 '-bipyridine)osmium(II) ortris(4,4 '-dicarboxy-2,2 '- bipyridine)osmium(II) complexes.* Journal of Physical Chemistry B, 2000. **104**(15): p. 3488-3491.

36. Wang, Y.Q., J.B. Asbury, and T.Q. Lian, *Ultrafast excited-state dynamics of Re(CO)(3)Cl(dcbpy) in solution and on nanocrystalline TiO2 and ZrO2 thin films.* Journal of Physical Chemistry A, 2000. **104**(18): p. 4291-4299.

37. Hissler, M., et al., *Platinum diimine complexes: towards a molecular photochemical device.* Coordination Chemistry Reviews, 2000. **208**: p. 115-137.

38. Islam, A., et al., *Dye sensitization of nanocrystalline titanium dioxide with square planar platinum(II) diimine dithiolate complexes.* Inorganic Chemistry, 2001. **40**(21): p. 5371-5380.

39. Cummings, S.D. and R. Eisenberg, *Tuning the excited-state properties of platinum(II) diimine dithiolate complexes.* Journal of the American Chemical Society, 1996. **118**(8): p. 1949-1960.

40. Paw, W., et al., *Luminescent platinum complexes: tuning and using the excited state.* Coordination Chemistry Reviews, 1998. **171**: p. 125-150.

41. McInnes, E.J.L., et al., *Mapping the unpaired electron density in Pt(bipy)L-2 (-) (bipy = 2,2 '-bipyridine; L = Cl-, CN-, (CN-)-C-13): A combined EPR-ENDOR-theoretical study.* Journal of the Chemical Society-Faraday Transactions, 1998. **94**(19): p. 2985-2991.

42. Kubo, K., et al., *X-ray crystal structure and electrical conductivity of Pt(2,2 '-bipyridine)(C8H4S8) BF4 C8H4S82-=2-{(4,5-ethylenedithio)- 1,3-dithiole-2-ylidene}-1, 3-dithiole-4,5-dithionate(2-).* Inorganica Chimica Acta, 2002. **336**: p. 120-124.

6

Parameters influencing charge separation in solid-state dye sensitized solar cells using novel hole conductors

6.1 Introduction

Dye sensitized solar cells employing liquid electrolytes are a promising, low-cost alternative to conventional silicon solar cells as mentioned previously in Chapter 1. However, several practical issues related to the presence of the liquid electrolyte, such as leakage of the electrolyte, dye desorption and the corrosive actions of the iodide/iodine redox couple, have withheld the large-scale technological development of such devices.

Approaches towards alternative electrolytes have resulted in the development of quasi-solid-state DSSCs, employing polymeric ionic gels [2], ionic liquids [3] and room temperature molten salts [4]. Full replacement of the liquid electrolyte, resulting in all-solid-state DSSCs, has been attempted using inorganic hole conductors such as p-type semiconductors [5] and organic low-molecular weight organic compounds [6].

Solid-state DSSCs employing the organic hole transport material (HTM) 2,2'-7,7'-tetrakis(N,N-di-p-methoxyphenyl-amine)9,9'-spirobifluorene, referred to as 'spiro-OMeTAD' in this thesis, have recently been reported with efficiencies of up to 4 % [7]. Although promising, this efficiency is still much lower than those reported for

analogous liquid-electrolyte devices. One of the limitations that has been suggested is the low hole mobility of spiro-OMeTAD (~10^{-4} cm^2/Vs), causing excessive interfacial recombination losses. A number of studies have focused on replacing spiro-OMeTAD by alternative, high-mobility hole conductors [8-14]. However, none of these have resulted in equaling the efficiency of spiro-OMeTAD-based devices, which has mainly been attributed to difficulties associated with the incomplete filling of the pores with the HTM.

Both hole mobility and pore filling of the HTM pertain to a central factor in the design of solid-state photovoltaic devices: the control of charge transfer at the device heterojunctions. The main charge transfer steps that take place at the dye/TiO_2/HTM interfaces are schematically represented in Figure 6.1, and will be discussed in more detail in what follows.

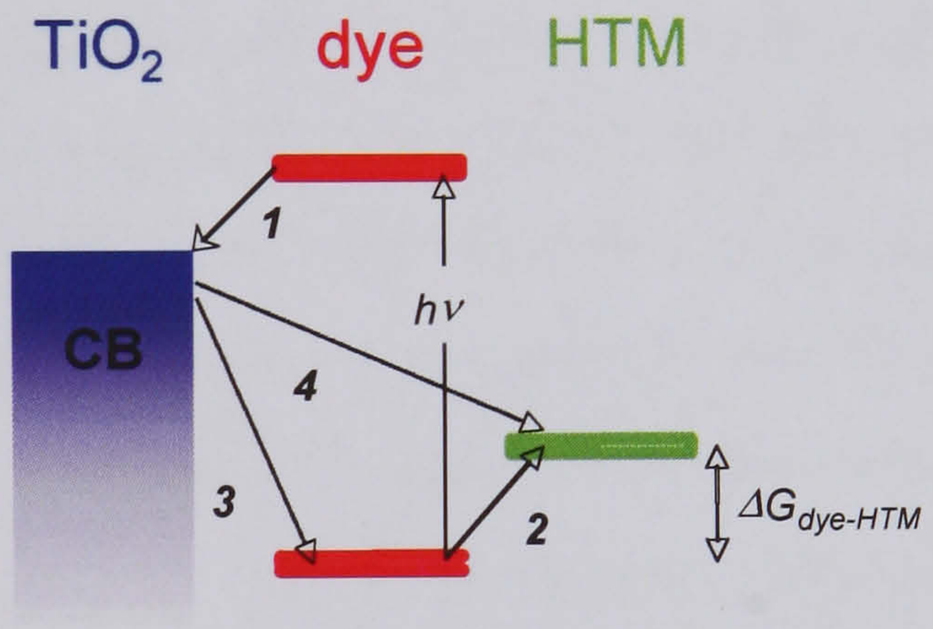


Figure 6.1 Schematic diagram of the charge-transfer processes occurring at the dye-sensitized nanocrystalline TiO_2/organic HTM heterojunction. Process **1**, **2**, **3** and **4** represent electron injection to nanoparticle TiO_2 conduction band (*INJ*), regeneration of the dye cation by hole transfer (*HT*), electron recombination with the dye cation (*CR1*) and with the HTM (*CR2*). Note that all arrows represent the flow of electrons except process **2**, in which the arrow shows the hole flow. $\Delta G_{(dye\text{-}HTM)}$ represents the difference of HOMO energy levels between sensitiser dye and HTM, indicating the driving force for *HT*.

Figure 6.1 shows schematic diagram of the charge-transfer processes occurring at the dye sensitized nanocrystalline TiO_2/organic HTM heterojunction. In principle all process are the same as those for liquid type DSSCs as shown in Figure 1.3 in Chapter 1. Visible light is absorbed by the sensitizer dye. After electron injection from the excited-state dye into the TiO_2 conduction band (*INJ*), the dye is regenerated by hole transfer from the dye cation to the HTM (*HT*). In a functioning device, the resulting charge carriers (electrons in the TiO_2 and holes in the HTM) are transported through their respective phases to external collecting contacts. Interfacial recombination pathways act as a loss mechanism in competition with these transport processes. The photoinjected electrons in the TiO_2 have two possible recombination pathways: direct recombination with dye cations (*CR1*), or with the HTM (*CR2*).

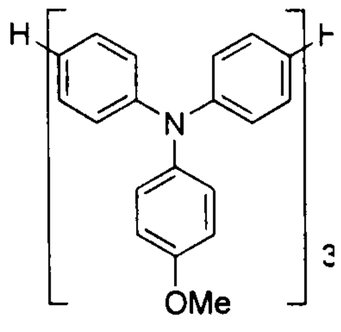
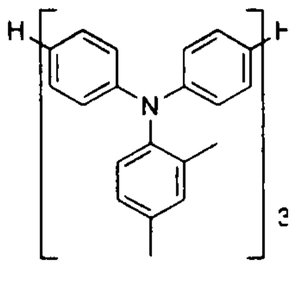
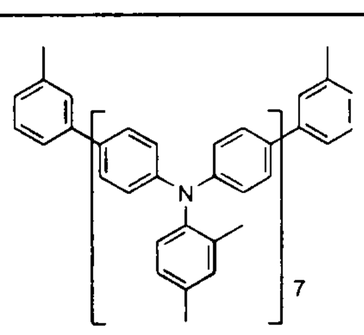
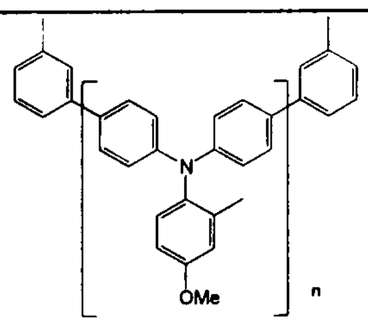
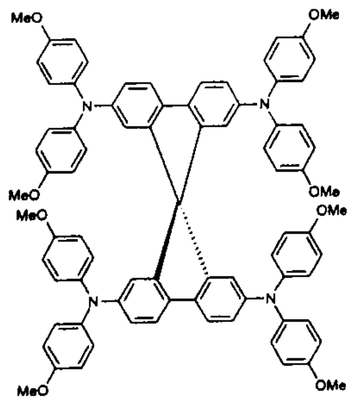
In previous transient optical studies on a TiO_2/dye/spiro-OMeTAD heterojunction it was demonstrated that hole transfer to spiro-OMeTAD (*HT*) occurs primarily on the picosecond timescale with multiphase kinetics, and that the yield of this dye regeneration step approaches unity at ~10 ns [15]. This reaction (*HT*) is much faster than the recombination reaction of the holes with the electrons injected in the TiO_2 (*CR2*), which typically occurs in the μs-ms time domain [16,17]. This suggests that the yield for the *HT* is not limited by kinetic competition between the rate of the hole-transfer process and the rate of the recombination process, but rather by the thermodynamic driving force, which is defined as ΔG_{dye}-HTM = $E_m(HTM^+/HTM) - E_m(D^+/D)$, of this reaction [18], where $E_m(HTM^+/HTM)$ and $E_m(D^+/D)$ represents the HOMO energy levels of HTM and sensitiser dye, respectively.

For both liquid-electrolyte and solid-state DSSCs, enhancement of device performance has been found upon addition of lithium salts, such as lithium bis(trifluoromethylsulfonimide) ($Li[CF_3SO_2]_2N$), dissolved in 4-*tert*-butyl-pyridine ('tBuPy') [19-22]. These additives are known to modulate the energetics of the cell components and hence influence the dynamics and yields of the interfacial charge transfer reactions. More specifically, lithium ions are known to shift the TiO_2 conduction band edge to more positive potentials [23,24], as well as to screen electrostatic interactions, resulting in an increased charge injection efficiency and

reduced recombination, whereas tBuPy shifts the conduction band edge to more positive potentials [25], leading to an increase of the device open circuit voltage V_{oc}.

This chapter addresses the results of functional studies on spiro-OMeTAD and a series of novel organic hole conductors, employing TAS and I/V characterization. These novel HTMs are substituted triarylamine oligomers, varying in conjugation length, HOMO energy level and hole mobility as summarized in Table 6.1. TAS was used to determine the hole transfer yields of the HTMs as well as to probe the extent of pore penetration in the nanostructured TiO_2 film. Furthermore, the influence of lithium ions and tBuPy on the charge separation yields is studied, showing excellent correlation with device performance. Finally, a number of parameters influencing charge separation in solid-state dye-sensitized solar cells are considered.

Table 6.1 Characteristics of the organic HTMs studied. Hole mobilities are FET mobilities. Ionization potentials were determined using solution-phase cyclic voltammetry by Kathryn Carr et al. in Avecia Research Centre, Manchester.
(a) Determined using the Time-of-Flight technique.

Compound	M_W	Hole mobility [cm^2/Vs]	HOMO level [eV]
 HTM1	821	4.86×10^{-4}	-4.97
 HTM2	815	8.07×10^{-4}	-5.0
 HTM3	~3,500	1.76×10^{-3}	-4.99
 n = 7 HTM4	~3,200	2.06×10^{-4}	-4.96
n = 15 HTM5	~6,500	8.23×10^{-4}	-4.98
n = 18 HTM6	~9,100	1.04×10^{-3}	-4.96
 spiro-OMeTAD	1230	2×10^{-4} (a)	-4.77

6.2 Experimental

The general experimental procedures were carried out as described in Chapter 2. Here specific details are addressed.

The triarylamine hole conductors and spiro-OMeTAD were supplied by Avecia Ltd., Manchester (now Merck). All solvents were purchased from Aldrich and were HPLC grade. Dye **2** was employed as a sensitiser dye for all experiments.

Solid-state device preparation has been described in detail previously [35]. After cleaning F-doped SnO_2 glass substrates (with acetone, methanol and Helmanex), a ~100nm compact layer of TiO_2 was deposited by spray-pyrolysis. A nanostructured TiO_2 layer was fabricated via doctor-blading the TiO_2 paste, followed by sintering at 450°C. Dyes were adsorbed to the TiO_2 film by immersion overnight in a 0.3 mM solution in acetonitrile:*tert*-butanol (1:1) and subsequently carefully rinsed with acetonitrile. The hole conductor matrix was applied by depositing a solution of the HTM (0.17 M in chlorobenzene) on the dye-coated substrate, allowing the HTM to penetrate the film during 1 min., followed by a spin-coating step at 1800 rpm. Samples were stored in the dark under vacuum prior to laser transient spectroscopy and/or gold evaporation.

In this study, FET (field-effect transistor) method were used to measure hole mobility. This is because for organic semiconductors the most common technique is via FETs. It is a rather simple and cheap method than other method such as Hall and Tof (time of flight). However, FET has a disadvantage, which is more indirect measurement compared to the others. The (drift) mobility (μ) of the carriers is defined as the ratio of carrier velocity v and electric field E:

$$v = \mu E$$

In FET, mobility is calculated by the value of current, which is measured for various electric fields. In Tof, the time for holes to move can be directly measured. However, FET is regarded to be a proper measurement in this study when all data are measured by this method.

6.3 Results and discussion

6.3.1 Recombination dynamics

Figure 6.2(a) shows the transient absorption kinetics at 520 nm for the dye sensitized nanocrystalline TiO_2 films in the absence and presence of HTM**1**. Note that at this wavelength, both the negative bleach signal assigned to the dye cation and positive absorption signal assigned to the HTM cation can be monitored as reported previously [18]. In the absence of HTM**1**, the kinetics follows the direct recombination between the injected electrons and the dye cations (*CR1*). Likewise, the decay kinetics of the positive 520 nm band follow the recombination between the injected electrons and HTM**1** cations (*CR2*). The absence of any increase of the HTM**1** cation absorption indicates that the formation of the cation species following *HT* is complete within the rise time of the detection system (1 μs). This observation is consistent with the findings of previous study, where spiro-OMeTAD was employed, that the process of *HT* occurs on the picosecond timescale [15].

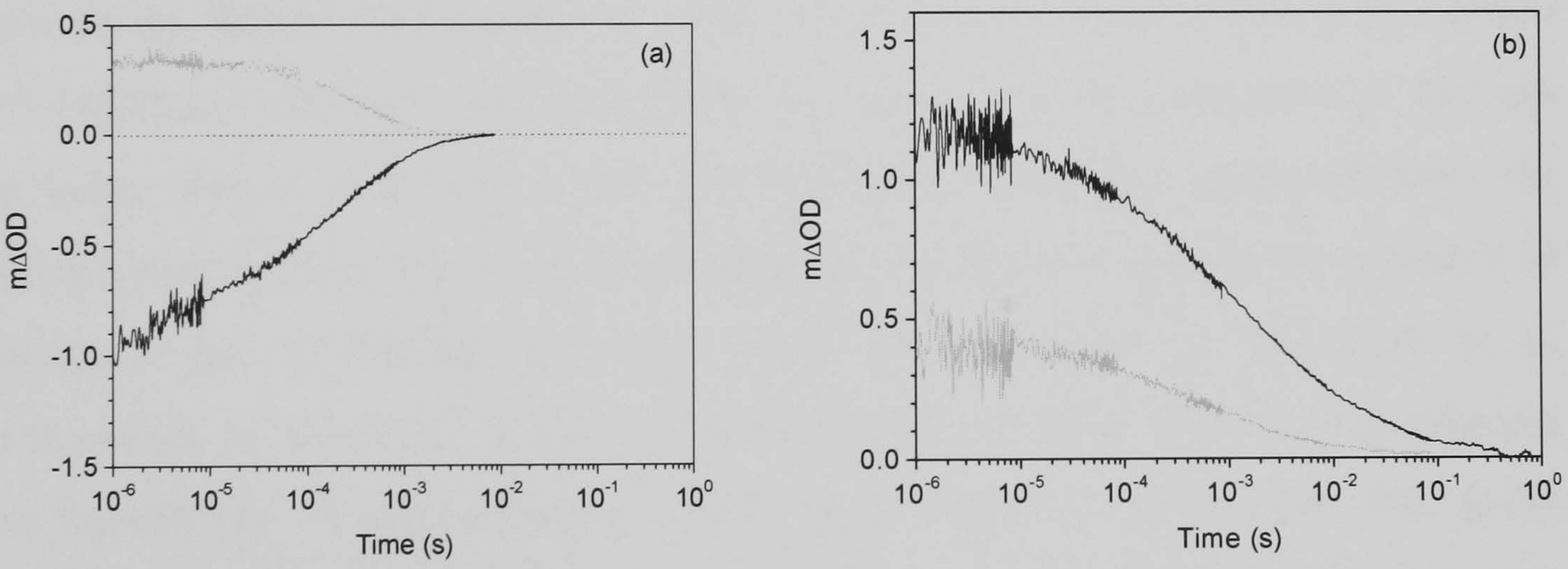


Figure 6.2 Transient absorption data of the dye **2** / nanocrystalline TiO_2 films in the absence (black trace) and presence (grey trace) of HTM**1**, monitoring recombination dynamics at (a) 520 nm following 620 nm excitation, and (b) 800 nm following 530 nm excitation.

Both decay dynamics assigned to the recombination reactions *CR1* and *CR2* exhibit the previously reported stretched-exponential behavior ($\Delta OD \propto \exp[-(t/t_{50\%})^{\alpha}]$) [26]. This behavior is consistent with a recombination reaction that is primarily controlled by electron trapping/detrapping dynamics in the TiO_2 particles as discussed

in Chapter 4. The values of $t_{50\%}$ are observed to be about 100 μs (no HTM**1**) and 400 μs (with HTM**1**), in agreement with previous studies [16, 22].

Figure 6.2(b) shows the transient absorption kinetics for the dye sensitized nanocrystalline TiO_2 films in the absence and presence of HTM**1** at 800 nm, probing the decay of the dye cation. Here a decreased amplitude of the transient absorption of the dye cation in the presence of HTM**1** is observed, consistent with rapid regeneration (*HT*) of the oxidized dye by the HTM.

6.3.2 Hole transfer yield

The determination of the yield for interfacial hole transfer process to the HTM (*HT*) can be considered using the TAS shown in Figure 6.2(a) and (b) in two different ways: (1) The amplitude of the dye cation band at 800 nm (Figure 6.2(b)) in the presence of the HTM is compared with that in the absence of the HTM; hole transfer yield=1-[ΔOD_{800}(+HTM)]/[ΔOD_{800}(-HTM)], or (2) the relative amplitudes at 520 nm of the traces shown in Figure 6.2(a) are compared, which are estimated from the difference between the respective molar extinction coefficients. Due to the presence of an absorption tail at 800 nm for electrons in TiO_2, method (1) may lead to an underestimation of the hole transfer yield. Method 2 is more accurate, but requires precise knowledge of the extinction coefficients of the HTM cations. For spiro-OMeTAD$^+$, this extinction coefficient is known (ε_{520} = 18,700 $Lmol^{-1}cm^{-1}$),[15] and by using method 2 a hole transfer yield of 90% for spiro-OMeTAD was calculated. Subsequently, all hole transfer yields were calculated according to method 1, and normalized on the basis of the yield (90%) for spiro-OMeTAD.

Recently, the extent of pore penetration of these HTMs has been evaluated by Scanning Electron Microscopy (SEM) studies [27]. Cross-sectional SEM images suggested superior pore penetration of spiro-OMeTAD as compared to the triarylamine series. Since this method is not quantitative, in this study TAS was employed to obtain

more detailed insight into the extent of pore penetration. To this end, samples were excited from either the front or back side, with no change in the position of the probe beam. Because of the high extinction coefficient of the dye at the excitation wavelength (530 nm), a strong concentration gradient of excitations is generated in the dye-coated films. Hence, if poor pore penetration produces a concentration gradient of the HTM in the film, this will result in discrepancy between the amplitude of dye cation signal monitored at 800 nm on front and back side illumination; *i.e.*, if the HTM is not able to penetrate homogeneously throughout the entire film, larger amplitudes dye cation signals are to be expected on backside illumination as compared to front side illumination. (See Figure 6.3)

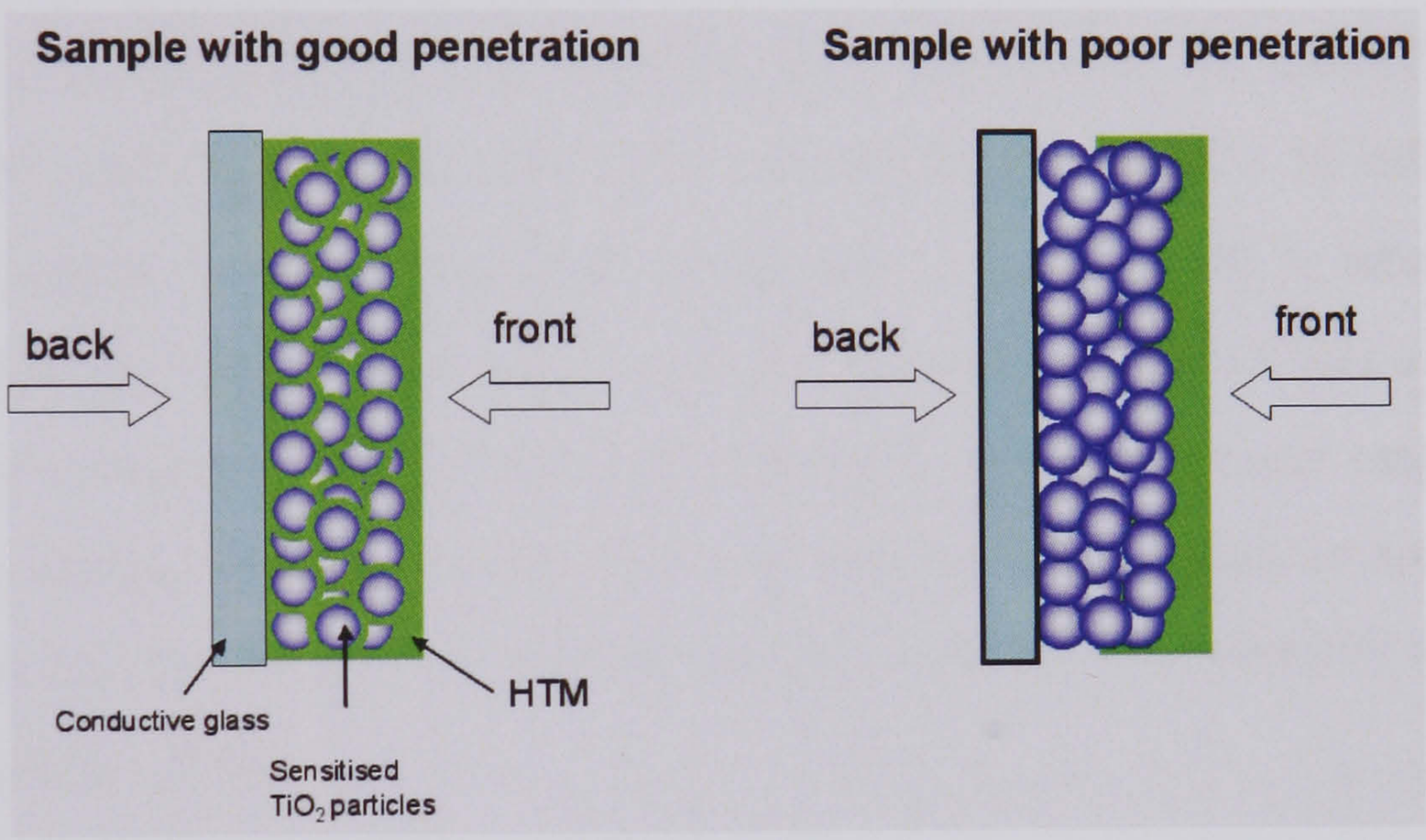


Figure 6.3 Schematic figure of the TAS measurements undertaken for quantitative determination of pore penetration. The excitation light is arriving at the front or back side of the sample. The amplitude of the dye cation signals for both measurements should be identical for samples with good penetration.

Table 6.2 Hole transfer yields determined by probing the transient absorption of the dye cation at 800 nm upon front- and backside excitation at 530 nm.

HTM	**Hole transfer yield [%]**			
	No additives		additives	
	front	back	tBuPy	Li^+/ tBuPy
HTM**1**	72	70	49	58
HTM**2**	50	50		
HTM**3**	52	49		
HTM**4**	41	40		
HTM**5**	49	50		
HTM**6**	50	51		
Spiro-OMeTAD	90	90	90	90

Table 6.2 summarizes the hole transfer yields determined for the HTMs using TAS, upon front- and backside excitation. For all HTMs, the kinetics of hole transfer were complete within the time resolution of the set-up (< 1 μs). It is interesting to observe that while the triarylamine hole conductors investigated are all less efficient in reducing the dye cation than spiro-OMeTAD with yields for hole transfer ranging from 41 to 72 %, the charge separation yields for front- and backside excitation are virtually identical. It is noted that there is no apparent relation between hole mobility (see Table 6.1) and hole transfer yield.

Recently, the reduced performance of solid-state devices based these hole conductors has been ascribed to inferior filling of the pores by the triarylamine oligomers [27]. In fact, the cross-sectional SEM images reported in ref [27] showed various degrees of incomplete pore wetting, with best pore penetration observed for HTM**1**. These observations are not only supported by the present TAS study, but at this point also quantified in terms of a quantum yield for hole transfer.

Variations in the hole transfer observed for the triarylamine hole conductors yield may also derive from differences in $\Delta G_{dye\text{-}HTM}$, as demonstrated previously [18]. However, with the present triarylamine HTM series differing no more than 40 meV in

HOMO energy level at most, this can not account for the observed variation in hole transfer yields. Hence, it can be concluded that the low charge separation yields for the triarylamine hole conductors must at least partially be due to incomplete filling of the pores of the nanostructured TiO_2 film.

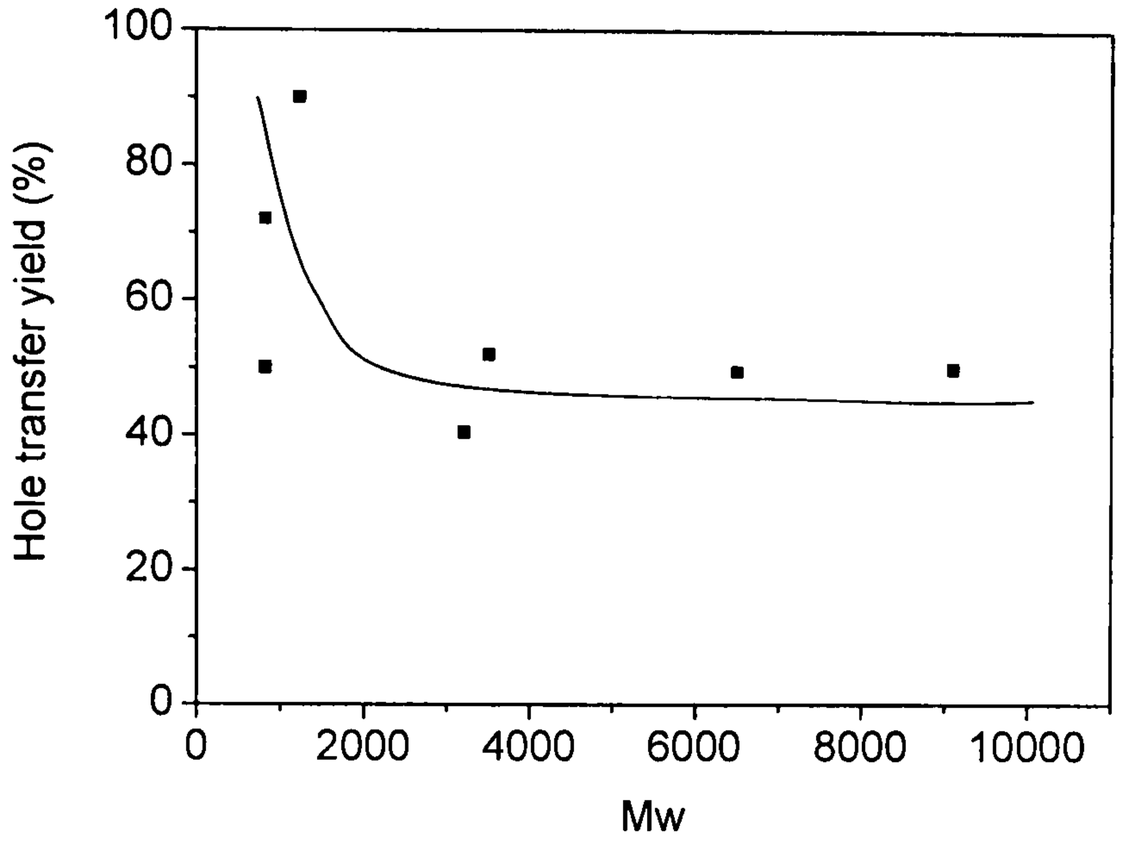


Figure 6.4 Hole transfer yield as a function of the average molecular weight (M_w) of the hole conductor.

By the aforementioned SEM study and TAS studies presented in this chapter, it was suggested that penetration of the triarylamine HTMs is not of uniform density throughout the TiO_2 film. In other words, although the macroscopic concentration of HTM is constant throughout the entire film, as indicated by identical hole transfer yields observed for front and back excitation, the filling of the smaller pores is less complete. This could be readily understood if it is taken into account that the nanostructured mesoporous TiO_2 films having an average pore size of 20 nm with FWHM of the pore size distribution of ~ 15 nm [28]. Additional evidence for this non-uniform pore filling can be found in Figure 6.4, which shows that the highest hole transfer yields are achieved for hole conductors with monodisperse, low molecular weights. Various methods of improving the pore penetration, including variation of solvent, soaking in dilute solution and heating of the spin-coating solution have so far proven unsuccessful. (Data not shown)

In addition to the poor pore penetration for the HTM series, considering the superior hole transfer yield of spiro-OMeTAD even to the low M_w triarylamine-type hole conductors, an additional factor should account for the lower charge separation yields. This will be addressed in the following section.

6.3.3 Effect of additives and $\Delta G_{dye\text{-}HTM}$

The hole transfer yield was also determined for HTM**1** and spiro-OMeTAD in the presence of the standard cell additives tBuPy and $Li[CF_3SO_2]_2N$, the results for which are given in Table 6.2. For spiro-OMeTAD, the hole transfer yield is unaffected by the addition of Li ions and tBuPy. In contrast, the yield for hole transfer from the dye cation to HTM**1** decreases from 72 % to 49 % upon the addition of tBuPy, and increases again to 58 % if Li ions are co-dissolved. Such a strong dependence upon additives is surprising in the light of the large free energy difference $\Delta G_{dye\text{-}HTM}$ as calculated on the basis of the individual dye (5.55 eV) and HTM**1** (4.97 eV) HOMO levels as summarized in Figure 6.5.

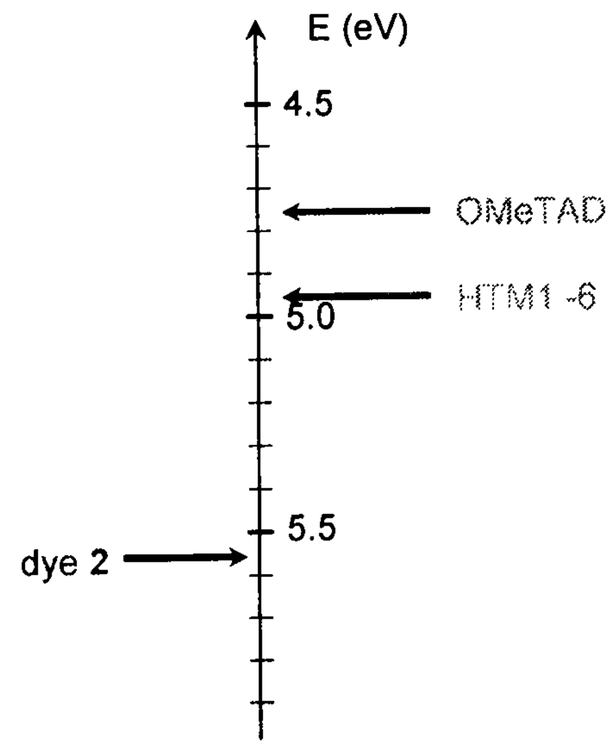


Figure 6.5 Schematic energetic diagram showing relationship between possible variation of the HOMO of dye **2** by additives and the HOMO level of the HTMs.

As mentioned in the introduction in this chapter, local electrostatic interactions play an important role in influencing the energetics of the interfacial redox reactions occurring in dye-sensitized solar cells. For instance, protonation/deprotonation of surface-adsorbed hydroxyl groups has been shown to shift the density of states of the nanocrystalline TiO_2 band by up to 1 eV [29], and to modulate the HOMO/LUMO levels of adsorbed dyes [30].

Furthermore, the addition of mobile ions, such as Li^+, to the liquid electrolyte or organic HTM has been demonstrated to screen electrostatic interactions deriving from coulombic interactions between photogenerated charges and interface dipoles [31,32]. Due to the greater physical separation of the HTMs from the TiO_2 interface, such local electrostatic interactions and the concomitant effects of potential-influencing additives are expected to have a smaller effect on the HTM HOMO level.

The HOMO level of the triarylamine HTMs, as determined using solution-phase cyclic voltammetry (CV), should provide sufficient driving force (> 0.5 eV) for the hole transfer (*HT*). However, only for spiro-OMeTAD (calculated $\Delta G_{dye\text{-}HTM} \sim 0.7$ eV) is such independence of the charge separation yield on Li^+ and tBuPy is observed. This provides strong support for the hypothesis that the actual HOMO difference between the dye and HTM in the TiO_2/dye/HTM heterojunction is considerably smaller than expected from the individual CV data. In other words, the prediction of interfacial charge separation yields based on independently obtained reduction/oxidation potentials may be misleading, resulting in overestimation of $\Delta G_{dye\text{-}HTM}$ and therefore of hole transfer yields and, consequently, device performance. It has previously been reported that local energetic inhomogeneous disorder also cause a broadening of $\Delta G_{dye\text{-}HTM}$ [18]. However, the present results are predominantly explained by an absolute reduction of the driving force for interfacial charge separation. Such considerations should be taken into account in the design of novel functional hole conductors for solid-state dye-sensitized solar cells.

It should be noted that for both HTMs, the addition of tBuPy results in a ~ 5-fold retardation of the recombination dynamics, and a further ~ 2-fold retardation upon dissolution of Li^+ in the tBuPy. This is consistent with the screening of electrostatic interactions by the Li^+ and the retardation of recombination previously reported by others [20,33,34].

6.3.4 Device characterization

(Some sentences about FET were added in Experimental.)

This section addresses a discussion of how the charge separation characteristics at the dye/HTM interface affect overall cell performance. Table 6.3 summarizes the device characteristics for solid-state dye-sensitized cells employing the triarylamine hole conductors as well as spiro-OMeTAD. Contrary to general expectations, no correlation between the HTM hole mobilities (see Table 1) and device parameters can be discerned. This supports to the conviction that pore filling and the control of interfacial energetics are stronger determinants in the development of efficient solid-state photovoltaic devices.

Table 6.3 Device parameters of solid-state dye-sensitized solar cells using different hole conductors. [b] Taken from ref [35].

Hole conductor	I_{sc} [mA/cm^2]	V_{oc} [mV]	Fill factor	η [%]
HTM**1**	3.8	789	67.1	2.01
HTM**2**	1.69	750	34.9	0.44
HTM**3**	1.96	778	59.2	0.9
HTM**4**	0.87	779	51.8	0.35
HTM**5**	2.29	815	56.6	1.05
HTM**6**	2.51	797	49.5	0.99
Spiro-OMeTAD[b]	6.3	738	64.3	2.8

It has been discussed above that both the extent of pore filling and the driving force ($\Delta G_{dye\text{-}HTM}$) contribute to the magnitude of the yield for interfacial hole transfer to the HTM. This hole transfer yield can be considered a measure of the number of charge carriers that are expected to be collected at the electrodes, which should hence be reflected in the short-circuit current of the device (I_{sc}). Figure 6.6 shows I_{sc} as a function of the hole transfer yields measured for the various hole conductors. Good linear correlation between the photocurrent and the charge separation yield is found.

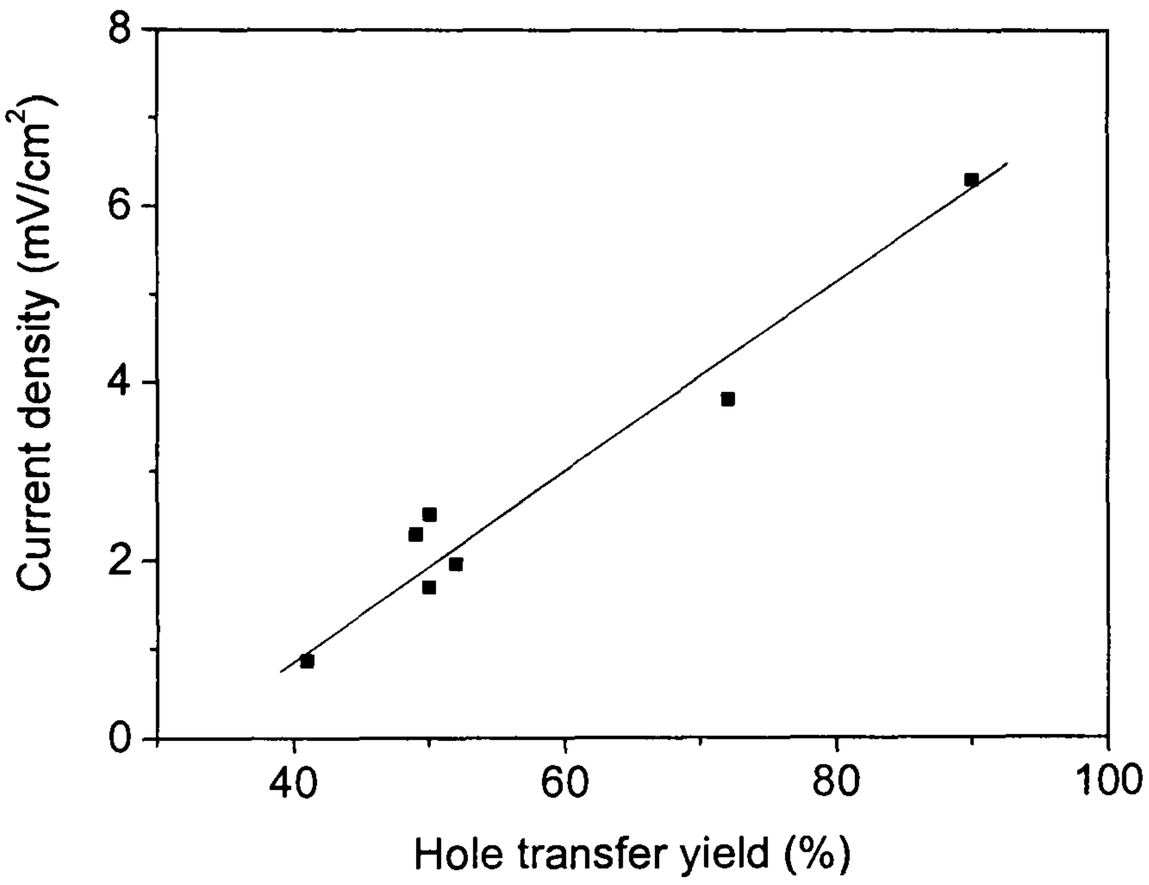


Figure 6.6 Short-circuit current (I_{sc}) as a function of the hole transfer yield determined by using transient absorption spectroscopy.

It is noteworthy that the larger ionization potential of the triarylamine hole conductors is reflected in the consistently higher open circuit voltage (V_{oc}) found for these devices as shown in Table 6.3. It is apparent though, that this positive influence of the shift of the HTM HOMO level on the V_{oc} does not sufficiently compensate for the adverse effect on the driving force for interfacial hole transfer, and hence the I_{sc}.

6.4 Conclusions

Interfacial charge transfer in a solid-state TiO_2/dye/HTM heterojunction have been studied by employing novel triarylamine hole conductors, using TAS and I/V characterization techniques to determine the yields for interfacial hole transfer and the extent of pore penetration. Pore penetration of the triarylamine hole conductors was found to be sub-optimal and non-uniform, with best hole transfer yields obtained for the smaller, low-molecular weight hole conductors. Local electrostatic interactions at the TiO_2/dye/HTM interface cause the driving force $\Delta G_{dye\text{-}HTM}$ for interfacial hole transfer to be smaller than anticipated on the basis of the individual ionization potentials of the dye and the hole conductor, resulting in losses in the hole transfer yield.

Contrary to general expectations, no relationship between hole mobility and device performance was found. However, the short-circuit photocurrent density was found to be directly proportional to the hole transfer yield.

Although it can be possible that hole mobility is also a critical factor in determining solid-state device performance, from the present findings the optimization of pore filling as well as the control of interfacial energetics should be the focus of the pursuit of alternative solid-state hole conductors. In conclusion, molecular level interface engineering to control charge transfer dynamics and yields is a key challenge in the development of efficient photovoltaic devices.

6.4 References

1. M. Grätzel, *MRS Bulletin* **2005**, *30*, 23.

2. F. Cao, G. Oskam, P. C. Searson, *J. Phys. Chem.* **1995**, *99*, 17071.

3. P. Wang, S. M. Zakeeruddin, J. E. Moser, M. K. Nazeeruddin, T. Sekiguchi, M. Grätzel, *Nat. Mater.* **2003**, *2*, 402.

4. N. Papageorgiou, Y. Athanassov, M. Armand, P. Bonhote, H. Pettersson, A. Azam, M. Grätzel, *J. Electrochem. Soc.* **1996**, *143*, 3099.

5. B. O'Regan, D. T. Schwartz, *Chem. Mat.* **1998**, *10*, 1501.

6. U. Bach, D. Lupo, P. Comte, J. E. Moser, F. Weissortel, J. Salbeck, H. Spreitzer, M. Grätzel, *Nature* **1998**, *395*, 583.

7. L. Schmidt-Mende, S. M. Zakeeruddin, M. Gratzel, *Appl. Phys. Lett.* **2005**, *86*.

8. C. Jäger, R. Bilke, M. Heim, D. Haarer, H. Karickal, M. Thelakkat, *Synth. Met.* **2001**, *121*, 1543.

9. B. O'Regan, F. Lenzmann, R. Muis, J. Wienke, *Chem. Mat.* **2002**, *14*, 5023.

10. K. Peter, H. Wietasch, B. Peng, M. Thelakkat, *Appl. Phys. A-Mater. Sci. Process.* **2004**, *79*, 65.

11. Y. Saito, N. Fukuri, R. Senadeera, T. Kitamura, Y. Wada, S. Yanagida, *Electrochem. Commun.* **2004**, *6*, 71.

12. R. Cervini, Y. B. Cheng, G. Simon, *Journal Of Physics D-Applied Physics* **2004**, *37*, 13.

13. K. R. Haridas, J. Ostrauskaite, M. Thelakkat, M. Heim, R. Bilke, D. Haarer, *Synth. Met.* **2001**, *121*, 1573.

14. S. Spiekermann, G. Smestad, J. Kowalik, L. M. Tolbert, M. Gratzel, *Synth. Met.* **2001**, *121*, 1603.

15. U. Bach, Y. Tachibana, J. E. Moser, S. A. Haque, J. R. Durrant, M. Grätzel, D. R. Klug, *J. Am. Chem. Soc.* **1999**, *121*, 7445.

16. S. A. Haque, Y. Tachibana, R. L. Willis, J. E. Moser, M. Grätzel, D. R. Klug, J. R. Durrant, *J. Phys. Chem. B* **2000**, *104*, 538.

17. J. Nelson, S. A. Haque, D. R. Klug, J. R. Durrant, *Phys. Rev. B* **2001**, *6320*, art. no 205321.

18. S. A. Haque, T. Park, A. B. Holmes, J. R. Durrant, *ChemPhysChem* **2003**, *4*, 89.

19. M. K. Nazeeruddin, A. Kay, I. Rodicio, R. Humphrybaker, E. Muller, P. Liska, N. Vlachopoulos, M. Grätzel, *J. Am. Chem. Soc.* **1993**, *115*, 6382.

20. J. Kruger, R. Plass, L. Cevey, M. Piccirelli, M. Grätzel, U. Bach, *Appl. Phys. Lett.* **2001**, *79*, 2085.

21. S. A. Haque, E. Palomares, B. M. Cho, A. N. M. Green, N. Hirata, D. R. Klug, J. R. Durrant, *J. Am. Chem. Soc.* **2005**, *127*, 3456.

22. S. A. Haque, T. Park, C. Xu, S. Koops, N. Schulte, R. J. Potter, A. B. Holmes, J. R. Durrant, *Adv. Funct. Mater.* **2004**, *14*, 435.

23. B. Enright, D. Fitzmaurice, *J. Phys. Chem.* **1996**, *100*, 1027.

24. Y. Liu, A. Hagfeldt, X. R. Xiao, S. E. Lindquist, *Sol. Energy Mater. Sol. Cells* **1998**, *55*, 267.

25. G. Schlichthörl, S. Y. Huang, J. Sprague, A. J. Frank, *J. Phys. Chem. B* **1997**, *101*, 8141.

26. J. Nelson, *Phys. Rev. B-Condens Matter* **1999**, *59*, 15374.

27. L. Schmidt-Mende, M. Gratzel, *Thin Solid Films* **2005**, submitted.

28. C. J. Barbe, F. Arendse, P. Comte, M. Jirousek, F. Lenzmann, V. Shklover, M. Gratzel, *J. Am. Ceram. Soc.* **1997**, *80*, 3157.

29. G. Redmond, D. Fitzmaurice, M. Graetzel, *J. Phys. Chem.* **1993**, *97*, 6951.

30. A. Zaban, S. Ferrere, B. A. Gregg, *J. Phys. Chem. B* **1998**, *102*, 452.

31. A. Zaban, A. Meier, B. A. Gregg, *J. Phys. Chem. B* **1997**, *101*, 7985.

32. S. Pelet, J. E. Moser, M. Grätzel, *J. Phys. Chem. B* **2000**, *104*, 1791.

33. T. Park, S. A. Haque, R. J. Potter, A. B. Holmes, J. R. Durrant, *Chem. Commun.* **2003**, 2878.

34. N. Hirata, J. E. Kroeze, T. Park, D. Jones, S. A. Haque, A. B. Holmes, J. R. Durrant, *Chem. Commun.* **2005**, submitted.

35. L. Schmidt-Mende, J. E. Kroeze, J. R. Durrant, M. K. Nazeeruddin, M. Gratzel, *Nano Lett.* **2005**, *5*, 1315.

7

Interface engineering for solid-state dye sensitised nanocrystalline solar cells: the use of an organic redox cascade

7.1 Introduction

As discussed in Chapter 1-5 the efficient operation of photovoltaic devices including DSSCs ultimately depends on the ability to control the charge transfer at the device heterojunction. Many research groups have recently been focusing upon a range of 'interface engineering' strategies to control electron transfer dynamics at nanostructured inorganic / organic interfaces [1-5]. Such dynamics are of particular interest for the development of solid state dye sensitised solar cells (DSSCs) [6-11], such as those addressed in Chapter 6 above. In this chapter the control of recombination dynamics in such solid state DSSCs is focussed. A novel strategy is foccessed to retard interfacial charge recombination in such devices, employing a organic redox cascade increase the spatial separation of photogenerated electrons and holes, as illustrated in Figure 7.1.

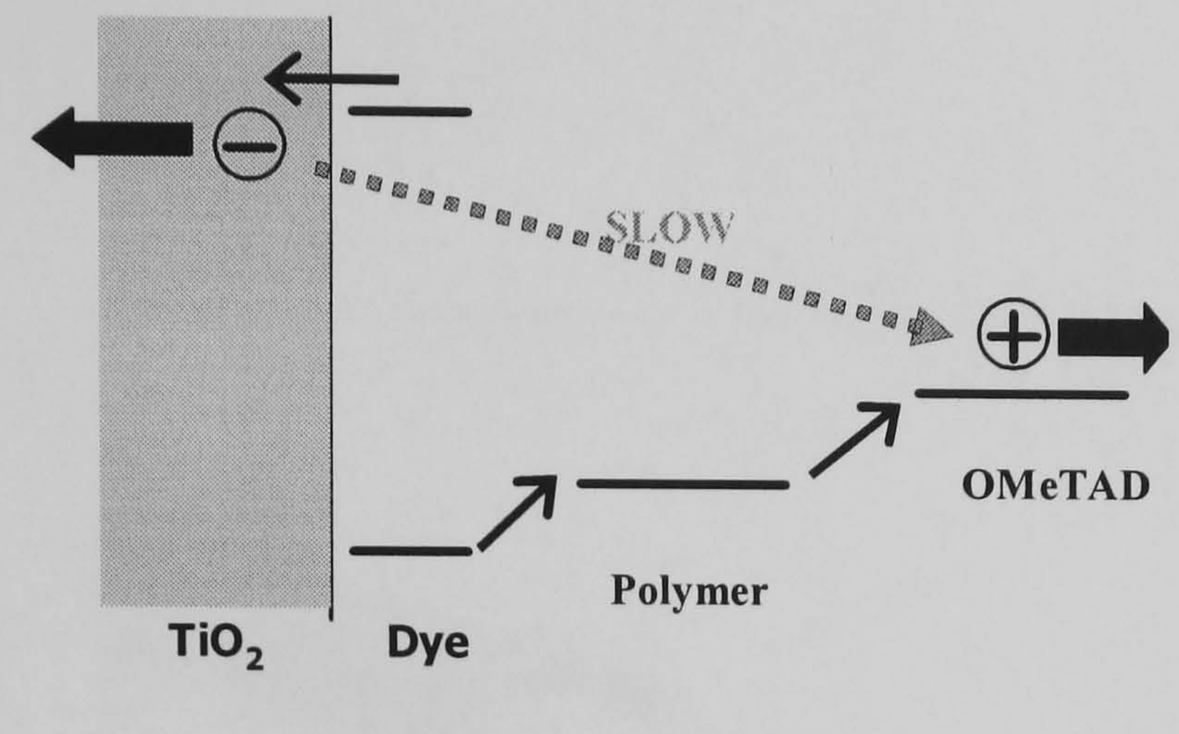


Figure 7.1 Illustration of the organic redox cascade strategy addressed in this study to retard interfacial charge recombination.

Solid state DSSC's employing the organic hole transporter spiro-OMeTAD have recently been reported with efficiencies of up to 4% [12]. This efficiency, whilst promising, remains however significantly below those reported for analogous devices employing iodide / iodine based redox electrolytes. For such sporo-OMeTAD devices, the yield of charge separation is > 90%, as described in Chapter 6, and is therefore not a significant factor limiting device erformance. Rather, the key factor limiting the performance of devices of spiro-OMeTAD DSSCs is their fast interfacial charge recombination dynamics relative to liquid electrolyte devices [8]. Figure 2 illustrates this point, showing typical recombination dynamics for these two device types employing the sensitiser dye **2**. It is apparent that charge recombination dynamics for the spiro-OMeTAD device are two orders of magnitude faster then those observed for the liquid electrolyte device, consistent with previous observations [13]. These faster recombination dynamics limit the diffusion length of photogenerated charges within the device, and therefore limit the maximum device thickness (and therefore light absorption) compatible with effcient charge collection.

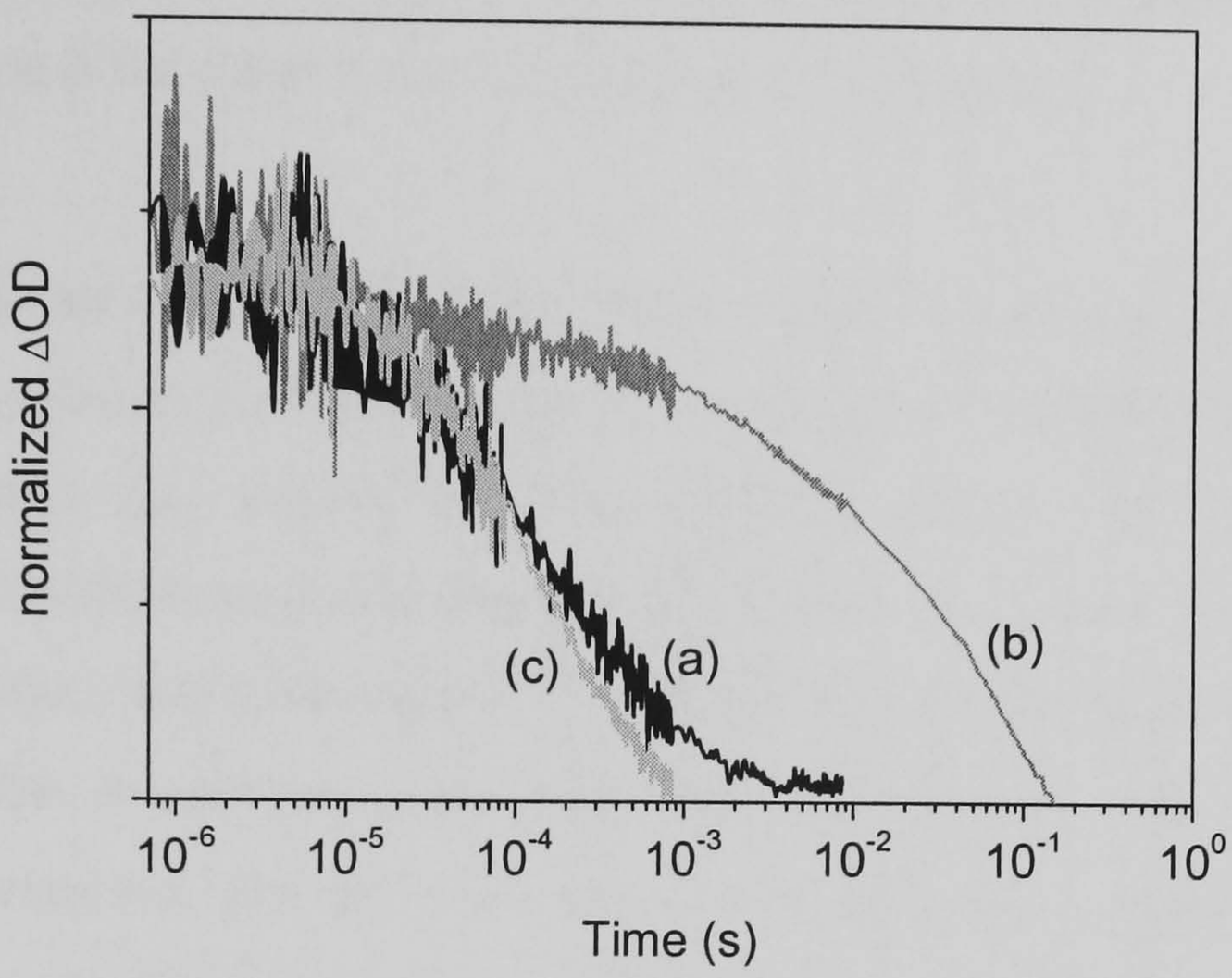


Figure 7.2 Transient absorption data monitoring charge recombination dynamics of (a) a $RuL_2(NCS)_2$ sensitised TiO_2 film, (b) the same film covered in redox electrolyte and (c) the same film following addition of spiro-OMeTAD. Data collected monitoring TiO_2 electron absorption at 1000 nm following optical excitation at 530 nm, with 25 mW cm^{-2} continuous white light bias. The spiro-OMeTAD was spin coated from chlorobenzene with no additives. The redox electrolyte comprised 0.1 M lithium iodide, 0.8 M tetra butyl ammonium iodide, 0.5 M *tert*-butylpyridine and 0.05 M iodine in acetonitrile.

Figure 7.2 also shows the corresponding charge recombination dynamics of injected TiO_2 electrons with dye cations, observed in the absence of any organic hole conductor or redox couple. It is striking that charge recombination to dye cations and spiro-OMeTAD cations are indistinguishable. It has previously been shown that recombination dynamics to dye cations are dependent upon both the dynamics of electron transport in the TiO_2 film and the spatial separation of the cation from the TiO_2 surface [14]. The observation of indistinguishable recombination dynamcis to both the dye and OMeTAD cations indicates that hole transfer from the dye to

OMeTAD does not result in a significant movement of the cation away from the TiO_2 surface. In other words, despite the OMeTAD largely filling the pores of the mesoporous film as shown Chapte 6, in these films the photogenerated OMeTAD cations remain localised close to the dye sensitised TiO_2 surface.

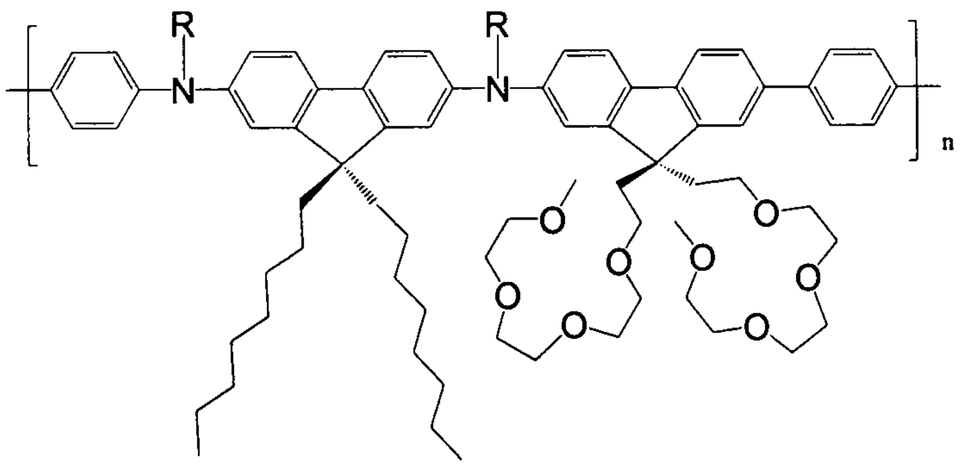
The localisation of the OMeTAD cations ('holes') on the TiO_2 surface can be readily understood in terms of local electric fields at TiO_2/dye/OMeTAD interface. Such electric fields may derive both from interface dipoles and from coulombic interactions of the photogenerated charges [15, 16] as disscussed in Chapter 6. One strategy to overcome this localisation of the OMeTAD cations is the introduction of mobile ions to the organic phase, such as lithium triflamide salts, to screen these electrostatic interactions. The addition of such salts results in a signficant retardation of recombination dynamics, consistent with an increased spatial separation of the OMeTAD cations from the TiO_2 surface, and results in an improvement in device efficiencies by upto an order of magnitude [8].

One limitation to this approach is however the requirement of the addition of volatile pydrine to the hole transport layer to solublise the lithium salt. Haque et al. have recently demonstrated an alternative solublisation strategy based upon the attachment of tetraethylene glycol (TEG) side groups to the organic hole transporter to ligate the lithium ions [17]. This strategy was futhermore employed to achieve an organic multilayer structure, depositing the dual function ion ligating and hole transport polymer between the sensitiser dye and spiro-OMeTAD to achieve a localised ionic screening of the interfacial electric fields. In this study, the multilayer approach is extended by modulating the HOMO energy level of the polymer layer to achieve an energetic redox cascade, as illustrated in Figure 6.1, and resulting in a further retardation of the interfacial charge recombination dynamics.

7.2 Experimental

7.2.1 Materials

All materials employed have already been addressed in section 6.2 in Chapter 6, except for 4 new polymers. These materials are triarylamine polymers with ion solvating tetra-ethylene glycol (TEG), synthesised in the group of Professor Andrew B. Holmes in University of Melbourne. Compounds and polymers were synthesised by using published procedures [17]. These materials provide a bicontinuous interpenetrating network morphology: the TEG network provides channels for additional ions such as lithium ions, whereas the triarylamine moieties provide pathways for hole transport. The chemical structure of the polymers is shown in Figure 7.3. P**1** is the material used in previous research performed by Haque et al. [17], while P**2**-P**4** have been synthesized by substitution of P**1** in order to vary the HOMO level suitably for the cascade system.



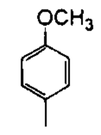
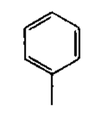
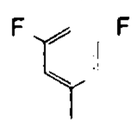
	R	HOMO (eV)
P1		4.82
P2		4.73
P3		4.76
P4		5.05
spiro-OMeTAD	-	4.77

Figure 7.3 Chemical structures of the ion ligating hole transport polymers employed in this chapter and corresponding HOMO energy level determined by cyclic voltammetry.

7.2.2 Experimental procedures

All experimental procedures have been described in Chapter 2 and section 6.2 of Chapter 6, except for cyclic voltammetry for **P1** through **P4** and the sample fabrication.

7.2.2.1 CV measurements of P1 through P4

The oxidation potentials for **P1** though **P4** were measured by using solution phase electrochemistry, cyclic voltammetry (CV), performed by Ms. Samantha Handa at Imperial College London. The CV cells used in this study consisted of a three-electrode configuration – a gold working electrode, a platinum wire as a counter electrode and $Ag^+/AgCl$ as a "pseudo" reference electrode. 0.1 M tetrabutylammonium hexafluorophosphate (Bu_4NPF_6) in N,N-Dimethylformamide (DMF) was used as the supporting electrolyte. The scan rate was 50 mV/s. Results are summarized in Figure 7.3, showing that the HOMO for the series of polymers are suitably varied from 4.73 – 5.05 eV.

7.2.2.2 Sample fabrication

The electrostatic assembly of the Li^+-HTM1 layer was achieved as follows: the dye-sensitized nanocrystalline TiO_2 films were immersed in a 1:9 acetonitrile/chlorobenzene solution containing 1.5 mM HTM1 and 18 mM lithium triflamide salt at 70°C for 30 minutes, followed by drying under ambient conditions. This procedure resulted in the formation of a conformal interface layer of the Li^+-HTM1 complex. Subsequently, the hole conductor matrix was applied by spin coating a 0.17 M solution of the hole-conductor in chlorobenzene. It has previously been demonstrated that polymer **P1** can be adsorbed by the dip coating to form a conformal monolayer on dye sensitised nanocrystalline TiO_2 films [17]. Subsequent spin coating of a spiro-OMeTAD bulk hole transport layer did not result in dissolution of this layer.

7.3 Results and discussion

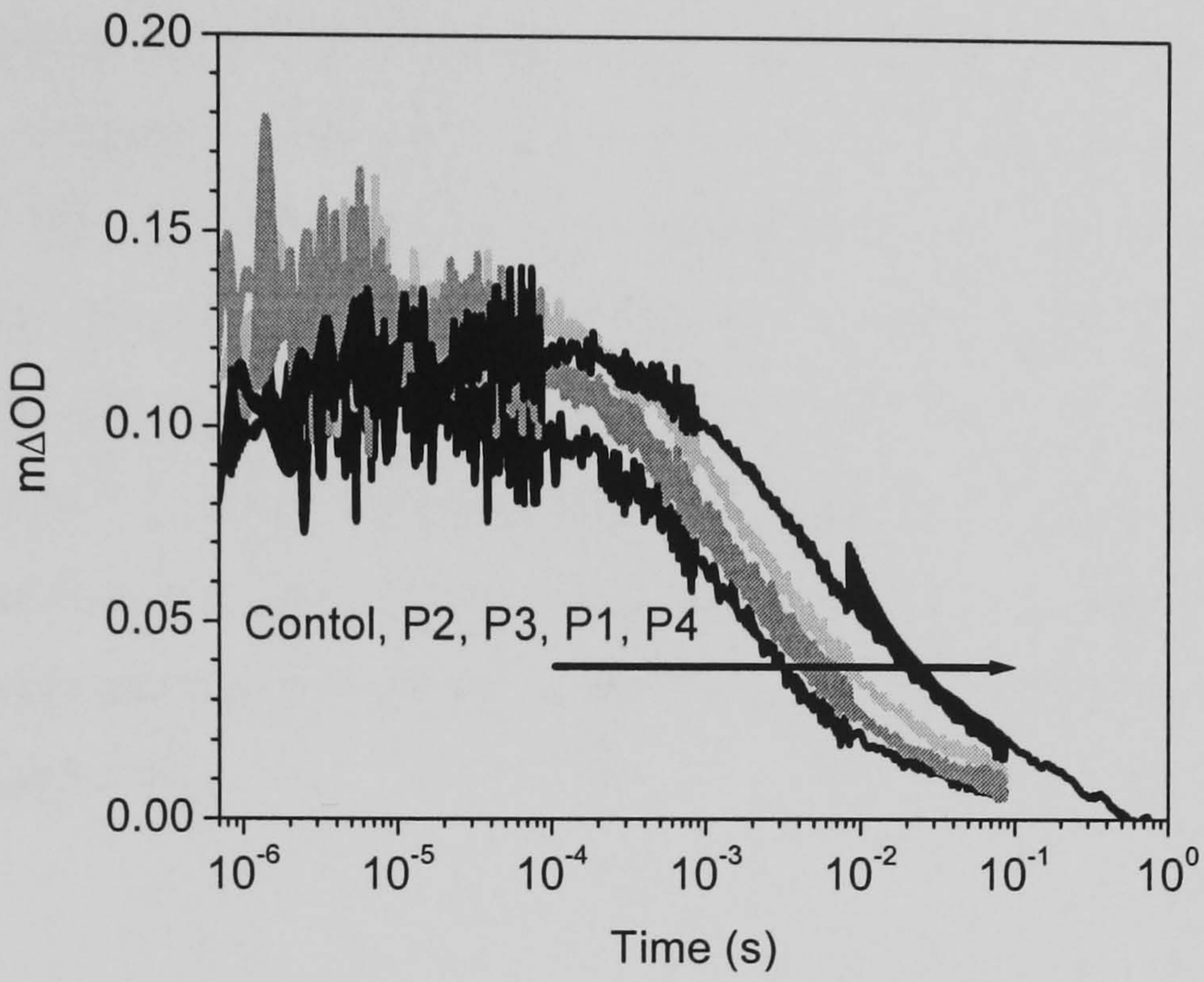


Figure 7.4 Transient absorption data monitoring charge recombination dynamics of TiO_2 / dye / polymer / spiro-OMeTAD films as a function of polymer employed. Data collected in dark monitoring TiO_2 electron absorption at 1000 nm following optical excitation at 530 nm. All data collected with lithium triflamide in the polymer deposition solutions, and without any additives to the OMeTAD spin coating solution. Control data collected without any polymer layer.

Figure 7.4 shows typical charge recombination dynamics obtained for multilayer structures employing polymers **P1** to **P4**. Control data was also obtained omitting the polymer layer. It is apparent that, depending upon which polymer is employed, the deposition of the polymer layer can result in a significant retardation of the interfacial charge recombination relative to the polymer free control.

The retardation of the recombination dynamics observed for polymers **P1** to **P4** shows an excellent correlation with the ionisation potential of these polymers, as shown in Figure 7.5. The recombination dynamics becoming progressively slower with increasing polymer HOMO energy level. This behaviour is consistent with the redox cascade strategty, as illustrated in Figure 6.1. For polymer HOMO energy levels close to that of spiro-OMeTAD, a significant proportion of photogenerated holes are likely to remain on the polymer layer. However polymer ionisation potentials greater than spiro-OMeTAD may allow the formation of a redox cascade as illustrated in Figure 1 increasing hole transfer from the polymer to the OMeTAD. This would increases the spatial separation of photogenerated holes from the TiO_2 surface and consequently result in slower charge recombination dynamics, as observed experimentally.

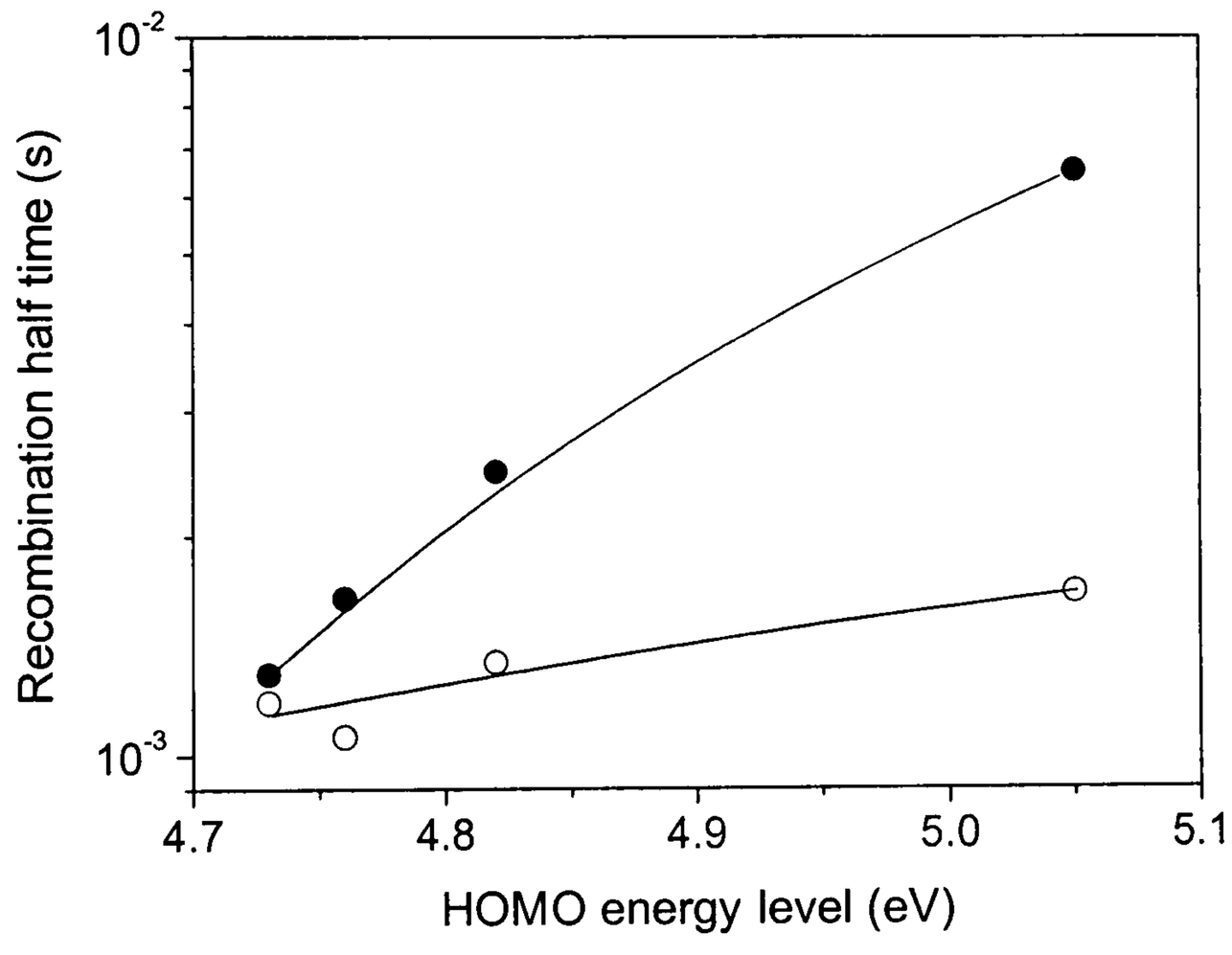


Figure 7.5 Recombination half times determined from transient absorption data such as that shown in Figure 5.4 as a function of polymer ionisation potential. Data shown with the inclusion (•) and omission (o) of lithium triflamide from the polymer dipping solution.

Note that the retardation of recombination dynamics observed due the insertation of the polymer layer is dependent upon the inclusion of lithium triflamide in the polymer deposition solution. A retardation of recombination dynamics with increasing polymer HOMO energy level is also observed in the absence of the salt (Figure 6.5, open symbols) but the effect is small compared to that observed in the presence of the salts. This observation is consistent with conclusion that the formation of an energetic redox cascade will be dependent not only upon the relative HOMO energy level of the materials employed but also upon the interfacial dipoles and coulombic attractions between the photogenerated charges. In the absence of ionic screening, these electrostatic interactions can be expected to dominate the interfacial energetics, and therefore prevent significant formation of an energetic redox cascade. However the presence of the co-deposited lithium triflamide can be expected to screen these electrostatic interactions, allowing the formation of an energetic redox cascade based upon the differing energetics of the polymer and spiro-OMeTAD layers, consistent with the experimental observations.

7.4 Conclusion

This chapter has demonstrated the successful fabrication of a nanostructured TiO_2 / dye / polymer / molecular hole transport multilayer structure, employing organic semiconducting materials with different HOMO energy levels to achieve an energetic redox cascade at a dye sensitised nanostructured interface. The solution processing of organic multilayer nanostructures is key challenge for a range of organic electronic and optoelectonic devices, including not only dye sensitised solar cells, but also polymer based devices and light emitting diodes [18]. The application of this strategy to the optimisation of solid state dye sensitised solar cells is currently on going. Several devices with the cascade system by employing P**4**, which have shown most significant retardation of the recombination, have been tested. However, no superiar device performance has been achieved while V_{oc} was observed to increase slightly. This may be attribute to poor pore penetration of the polymer. In this case, a breakthrough to obtain better pore penetration could be achieved by using a polymer with suitably short chain length. Further research should be planned.

7.5 References

1. Hagfeldt, A. and M. Gratzel, *Molecular photovoltaics.* Accounts of Chemical Research, 2000. **33**(5): p. 269-277.

2. Kopidakis, N., et al., *Transport-limited recombination of photocarriers in dye-sensitized nanocrystalline TiO2 solar cells.* Journal of Physical Chemistry B, 2003. **107**(41): p. 11307-11315.

3. Galoppini, E., et al., *Long-distance electron transfer across molecule-nanocrystalline semiconductor interfaces.* Journal of the American Chemical Society, 2001. **123**(18): p. 4342-4343.

4. Fisher, A.C., et al., *Intensity dependence of the back reaction and transport of electrons in dye-sensitized nanacrystalline TiO2 solar cells.* Journal of Physical Chemistry B, 2000. **104**(5): p. 949-958.

5. Heimer, T.A., et al., *Electron injection, recombination, and halide oxidation dynamics at dye-sensitized metal oxide interfaces.* Journal of Physical Chemistry A, 2000. **104**(18): p. 4256-4262.

6. Bach, U., et al., *Solid-state dye-sensitized mesoporous TiO2 solar cells with high photon-to-electron conversion efficiencies.* Nature, 1998. **395**(6702): p. 583-585.

7. Bach, U., et al., *Charge separation in solid-state dye-sensitized heterojunction solar cells.* Journal of the American Chemical Society, 1999. **121**(32): p. 7445-7446.

8. Kruger, J., et al., *High efficiency solid-state photovoltaic device due to inhibition of interface charge recombination.* Applied Physics Letters, 2001. **79**(13): p. 2085-2087.

9. Kruger, J., U. Bach, and M. Gratzel, *Modification of TiO2 heterojunctions with benzoic acid derivatives in hybrid molecular solid-state devices.* Advanced Materials, 2000. **12**(6): p. 447-+.

10. Kruger, J., et al., *Improvement of the photovoltaic performance of solid-state dye- sensitized device by silver complexation of the sensitizer cis- bis(4,4 '-dicarboxy-2,2 ' bipyridine)-bis(isothiocyanato) ruthenium(II).* Applied Physics Letters, 2002. **81**(2): p. 367-369.

11. Kruger, J., et al., *Recent developments in sensitized mesoporous heterojunction solar cells.* Materials Research Society Symposium Proceedings, 2002. **708**(Organic Optoelectronic Materials, Processing and Devices): p. 259-269.

12. Schmidt-Mende, L., S.M. Zakeeruddin, and M. Gratzel, *Efficiency improvement in solid-state-dye-sensitized photovoltaics with an amphiphilic Ruthenium-dye.* Applied Physics Letters, 2005. **86**(1): p. art. no.-013504.

13. Kruger, J., et al., *Charge transport and back reaction in solid-state dye-sensitized solar cells: A study using intensity-modulated photovoltage and photocurrent spectroscopy.* Journal of Physical Chemistry B, 2003. **107**(31): p. 7536-7539.

14. Nelson, J., et al., *Trap-limited recombination in dye-sensitized nanocrystalline metal oxide electrodes.* Physical Review B, 2001. **6320**(20): p. art. no.-205321.

15. Pelet, S., J.E. Moser, and M. Gratzel, *Cooperative effect of adsorbed cations and iodide on the interception of back electron transfer in the dye sensitization of nanocrystalline TiO2.* Journal of Physical Chemistry B, 2000. **104**(8): p. 1791-1795.

16. Zaban, A., A. Meier, and B.A. Gregg, *Electric potential distribution and short-range screening in nanoporous TiO2 electrodes.* Journal of Physical Chemistry B, 1997. **101**(40): p. 7985-7990.

17. Haque, S.A., et al., *Interface engineering for solid-state dye-sensitized nanocrystalline solar cells: The use of ion-solvating hole- transporting polymers.* Advanced Functional Materials, 2004. **14**(5): p. 435-440.

18. Tang, C.W. and S.A. Vanslyke, *Organic Electroluminescent Diodes.* Applied Physics Letters, 1987. **51**(12): p. 913-915.

8

Kinetic competition in flexible dye sensitised solar cells employing a series of polymer electrolytes

8.1 Introduction

As discussed in Chapter 6 and 7, many studies have recently focused on solid state alternatives to the liquid electrolyte employed DSSCs because of their possible short term and long term sealing problems. Moreover, the use of glass electrodes brings restrictions related to fragility and shape limitations. Several advantages can be obtained replacing the use of conducting glass substrates by plastic electrodes. There are related to their lower weights, increased flexibility, impact resistance and lower cost. Besides, the use of flexible substrates opens up the possibility of manufacture DSSC using a continuous roll-to-roll, high speed coating process and design prototypes in deferent shapes to be applies at different surfaces (e.g. glass windows). In addition, the ability to produce DSSCs in continuous steps would substantially lower the cost of the cells compared to the batch process used for glass based cells.

Many studies have therefore been of particular interest of low temperature encapsulation on flexible (e.g.: plastic) substrates, including molecular hole transporters [1-5], polymer electrolytes [6, 7] and polymer gel electrolytes [8-13]. The application of molecular HTM's to such plastic substrates has however been restricted by the requirement of a dense TiO_2 backing layer to prevent recombination

losses at the SnO_2 / HTM interface. No industrial, low temperature manufacture of a dense TiO_2 backing layer has been reported to date. Studies of DSSCs on plastic substrates such as polymer or polymer gel electrolytes have been restricted to systems retaining the I^- / I_3^- redox couple, where recombination losses at the SnO_2 surface are less critical. In this chapter the recombination losses in DSSC employing a series of polymer electrolytes are addressed.

In principle, as shown in Figure 1.3 of Chapter 1, there are two recombination pathways of importance in DSSCs, electrons photoinjected into the TiO_2 electrode can recombine with either dye cationsor the redox electrolyte (*CR1* and *CR2*). In liquid electrolyte devices, rapid re-reduction of dye cations by the redox electrolyte (*RG*) competes effectively with *CR1*, and therefore charge recombination to the redox electrolyte, *CR2*, is the primary recombination loss pathway limiting device efficiency [14]. A similar situation is observed for DSSCs employing molecule HTMs, as discussed in Chapter 7. However the increasing shift towards more solid state, and therefore typically more viscous, redox electrolytes raises the possibility that dye cation re-reduction by the redox electrolyte (*RG*) may no longer compete effectively with recombination pathway *CR1*. As a consequence, charge recombination to dye cations may become critical in limiting device efficiency as is discussed also above in Chapter 5 as a result of modifications to dye design. This chapter demonstrates that this can indeed be the case with DSSCs employing polymer electrolytes, and furthermore demonstrate that the extent of recombination losses due to *CR1* depend upon the chemical composition of the polymer employed.

8.2 Experimental

DSSCs (1 cm^2) were fabricated as previously elsewhere [15] employing a low temperature compression route [16] to deposit P25 (Degussa Ltd.) TiO_2 nanoparticles as 8 μm thick mesoporous film on ITO/PET sheets. The dye **2** shown in Figure 3.2 was employed as a sensitiser dye for this study. The polymer electrolyte was solution cast onto the sensitised film, followed by addition of a platinum coated ITO-PET film in the standard unsealed 'sandwich' configuration. The solution employed for polymer electrolyte deposition comprised 0.3 g of polymer dissolved in 25 ml. of acetone, with the addition of 0.03 g of NaI and 0.003 g iodine as redox couple and 0.15 g ethylene carbonate and 0.15g propylene carbonate as platicisers. Following polymer electrolyte casting, the film was allowed to dry in air to allow solvent evaporation. As discussed previously, the plasticisers were added to improve the ionic mobility of the polymer electrolyte. Two different co-polymers were used for the polymer electrolyte two co-polymers Epichlomer-16 (EP-16, Diaso Co. Ltd., Osaka, Japan) and Epichlomer-50 (EP-50 Aldrich, USA) (see Figure 8.1), in addition to a control polymer poly - ethylene oxide (PEO).

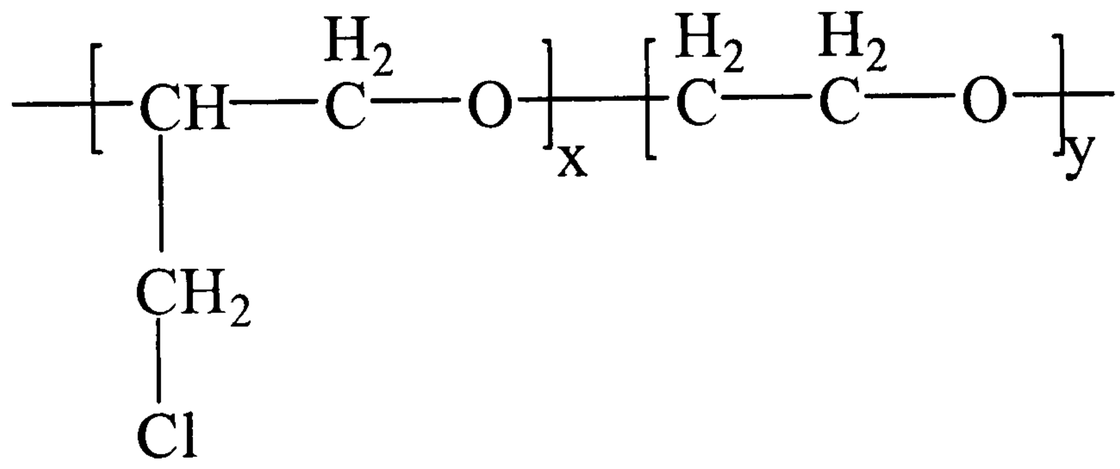


Figure 8.1 Chemical structure of the poly(epichlorohydrin-co-ethylene oxide) employed in this study: Epichlomer 50, x = y = 50 and Epichlomer-16, x = 16, y = 84. The control polymer poly - ethylene oxide corresponds to x = 0, y = 100.

8.3 Results and discussion

Figure 8.2 shows typical current / voltage data for DSSCs fabricated with the three different polymer electrolytes. Device performance characteristics are tabulated in Table 8.1 It is apparent that these data are strongly dependent upon the polymer composition, with the Epichlomer-50, comprising the highest epichlorohydrin content, yielding the highest short circuit current and fill factor, but also the highest dark current and lowest open circuit voltage.

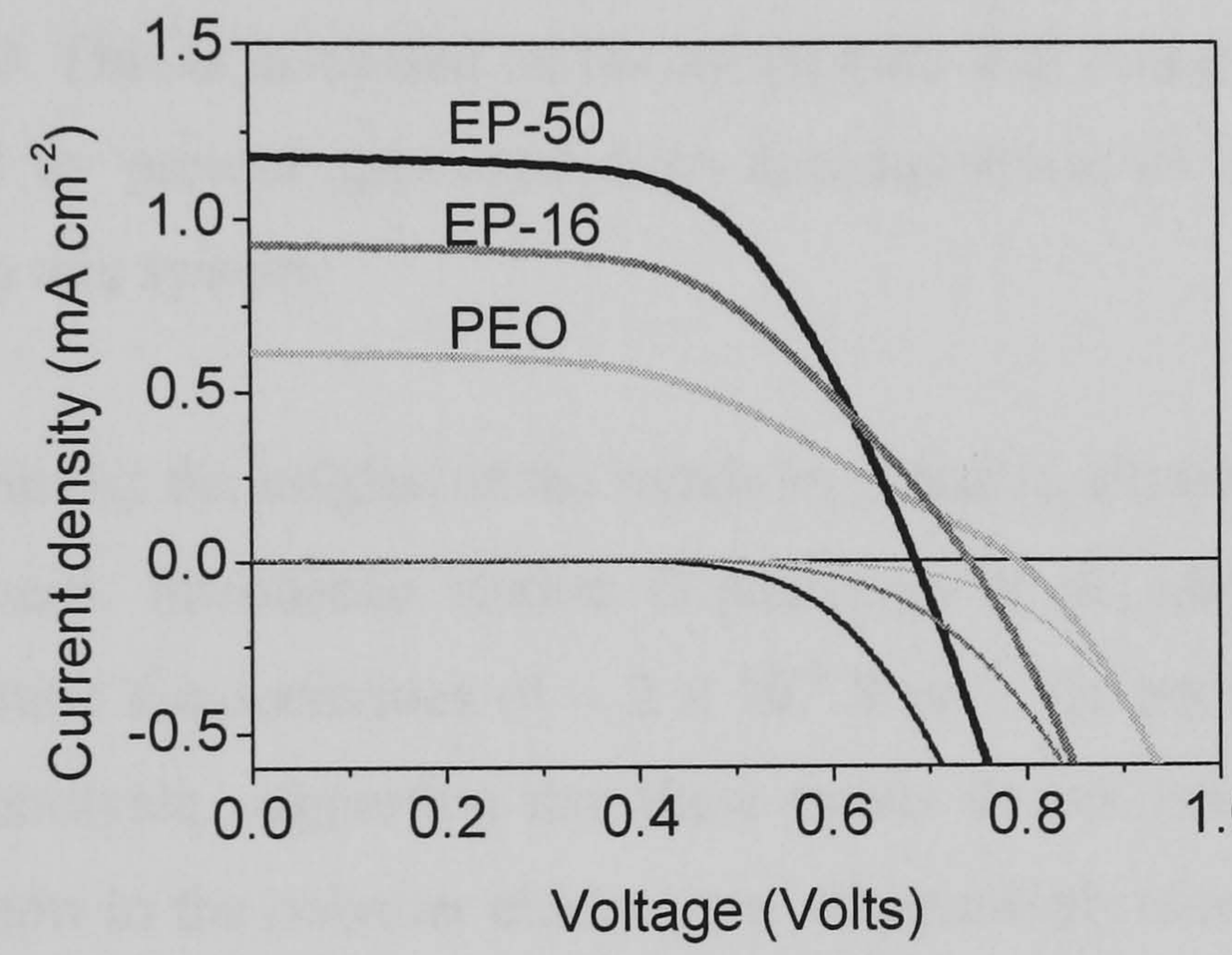


Figure 8.2 A comparison of the J-V characteristics of the typical flexible DSSCs using polymer redox electrolytes with EP-50, EP-16 and PEO in the dark (thin lines) and under 10 mW cm^{-2} AM1.5 simulated irradiation (bold lines). The device performance (J_{sc}, V_{oc}, *ff* and η) is 1.20 mA, 0.70 V, 62% and 5.2% for EP50; 0.95 mA, 0.76 V, 55% and 3.9% for EP16; 0.60 mA, 0.82 V, 48% and 0.2% for PEO.

The trend in V_{oc} observed for the three polymer electrolytes clearly follows the trend in dark current. This trend most probably originates from the Lewis acid / base properties of the polymer [6, 7]. This dark current originates from the recombination pathway *CR2* above. As disscussed in Chapter 3 more aprotic electolytes raise the conduction band energy of the TiO_2 electrode, resulting at a given voltage in a reduced TiO_2 electron density, and therefore in a lower dark current density. The dark current data shown in Figure 8.2 are consistent with this behaviour, with the most aprotic polymer (PEO) giving the highest V_{oc}; the inclusion of less aprotic epichlorohydrin groups into the polymer results in progressively lower V_{oc}'s for EP-16 and EP-50. This is discussed on the assumption that energy level of the electrode is influenced by protons generated from decomposition of contaminated water by Lewis base in this system.

Determining the origins of the trends in *ff* and I_{sc} shown in Figure 8.2 are less straight forward. Impedance studies (Upadhyaya et al., personal comminication) determined ionic conductivities of ~ 2 x 10^{-4} S cm^{-1} for both the EP-16 and EP-50 polymer electrolytes, suggesting that these trends do not result from differences in charge transport in the polymer electrolytes. Alternatively these trends may originate from differences in interfacial electron transfer dynamics. Transient absorption studies were therefore employed to address these dynamics directly.

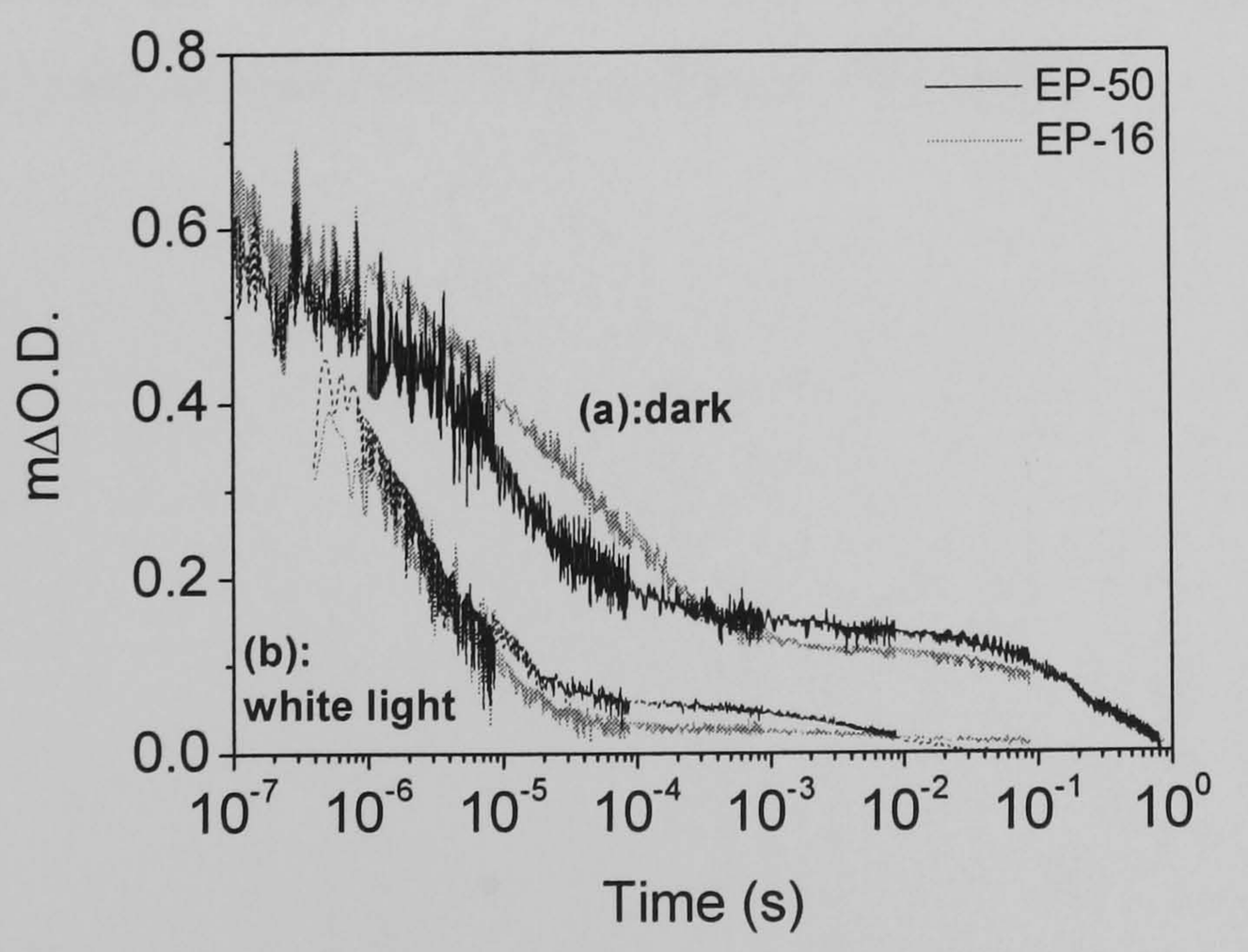


Figure 8.3 Transient absorption for $Ru(dcpby)_2(NCS)_2$ sensitised TiO_2 films covered in polymer electrolytes with EP-50 (black) and EP-16 (grey). Data collected at a probe wavelength of 800nm, in the absence (a) or presence (b) of ~ 25 mW cm^{-2} of continuous white light irradiance.

The data shown in Figure 8.3 provide clear evidence that kinetic competition between charge recombination to dye cations (*CR1*) and dye cation re-reduction by the polymer electrolyte limits the performance of DSSC employing these polymer electrolytes. The data collected in the absence of white light illumination (a) is considered first. Under such 'dark' conditions, charge recombination to the dye **2** cation (*CR1*) exhibits a half time of ~ 1 ms [7]. In liquid electrolytes, dye **2** cation re-reduction by iodide ions (*RG*) exhibits a half time of ~ 1 μs, and therefore competes efficiently with charge recombination to the redox electrolyte [14, 17]. The decay dynamics of dye cation absorption in Figure 8.3 (half times, $t_{50\%}$ of 20 and 6 μs for EP-16 and EP-50 respectively) are clearly indicative of slower re-reduction dynamics. For the EP-16 electrolyte, the yield of I_2^- product states of the re-reduction reaction is also reduced (apparent as the lower amplitude slow decay phase), indicating that for this polymer electrolyte, dye cation re-reduction is so slow that it no longer competes effectively with charge recombination *CR1*. The 20 % lower yield of dye regeneration (*RG*) observed from these transient studies is in good quantitative agreement with the lower I_{sc} obtained for this polymer electrolyte. Note that the lower I_{sc} observed for EP-16 can not result from a lower injection yield into the TiO_2 electrode as the dye cation yields (as observed from the initial magnitidue of absorption transients in Figure 8.3) are independent of the polymer electrolyte.

The presence of continuous illumination raises the TiO_2 Fermi level (corresponding to open circuit conditions), resulting in an acceleration of both charge recombination pathways. As shown in Figure 8.3, this illumination results both in acceleration in dye cation decay dynamics ($t_{50\%}$ of 1 and 2 μs for EP-16 and EP-50 respectively) and a reduction in I_2^- yield, indicating increased charge recombination losses due to the acceleration of *CR1*. These observations contrast with our studies of MeCN based electrolytes where the faster re-reduction dynamics compete effectively with *CR1*, resulting in the dye cation decay dynamics and I_2^- yields being independent on bias light [17]. The recombination losses are most significant for EP-16, consistent with the slower dye re-reduction dynamics observed for this electrolyte, resulting in the observed lower fill factor observed in the device I/V data.

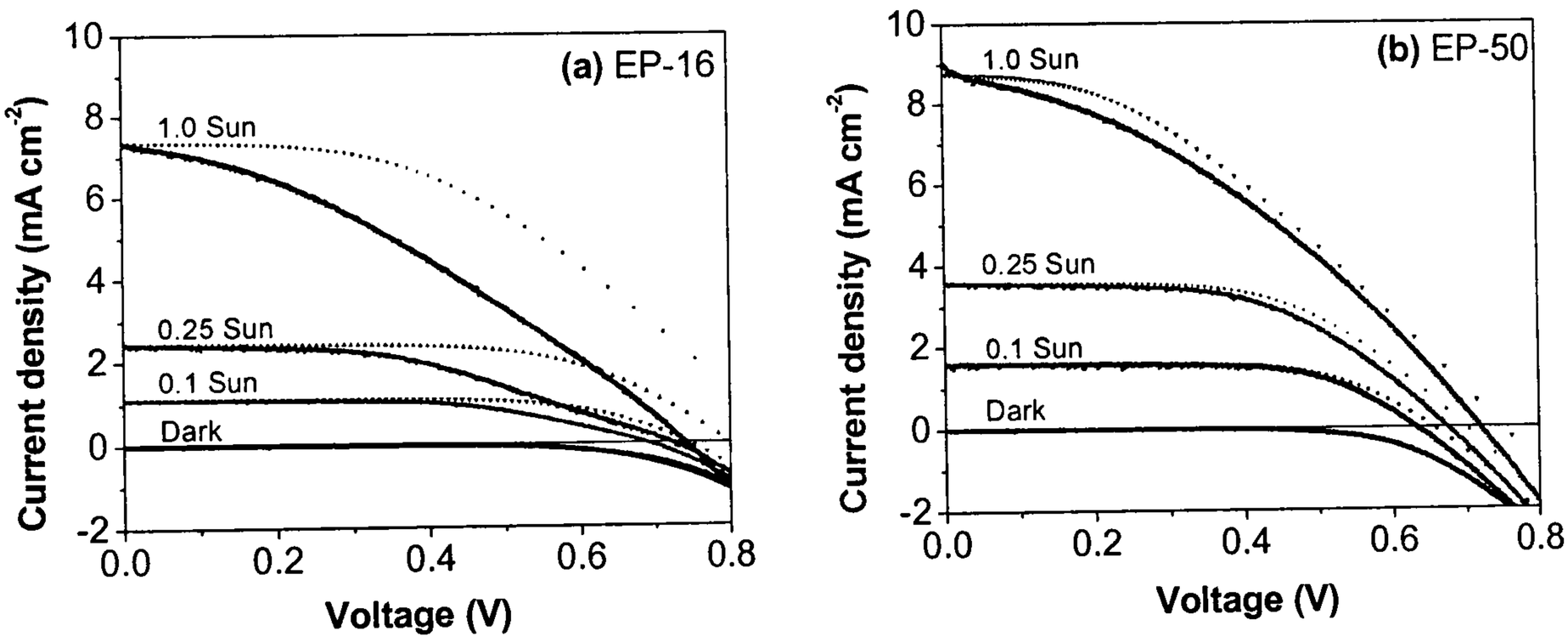


Figure 8.4 I/V characteristics (solid lines) of the flexible DSSCs using polymer redox electrolytes with (a) EP-16 and (b) EP-50 as a function of irradiation intensity. Also shown (dashed lines) are fits to the single diode model, equation 8.1, with all parameters except I_L being assumed to be independent of light intensity.

Further support for kinetic competition between *CR1* and *RG* limiting device performance can be obtained from simulating the device current / voltage data in terms of the non-ideal diode equation [7]:

$$I = I_L - I_0\left(e^{qV_j/mk_BT} - 1\right) \tag{8.1}$$

where I_L is the light intensity dependent short circuit current, k_B is Boltzmann's constant, T is temperature and I_0, m are fitting constants. The bias dropped across the internal junction, V_j can be related to the externally applied bias, V, through:

$$V_j = V + IR_S \tag{8.2}$$

where R_S is the series resistance of the system. I_0, m and Rs are assumed to be light intensity independent. As discussed previously [7, 17], deviations from this model can be most easily interpreted in terms of a voltage dependent loss of charge separation yield due to either lower electron injection yields or kinetic competition between *CR1* and *RG*. For MeCN based electrolytes, experimental data show an excellent fit to this model, indicating that recombination losses are limited only to recombination with the redox electrolyte *CR2*. For the EP-50 polymer electrolytes, the experimental data only deviate marginally from this model (Figure 8.4 (a)), indicating minor recombination losses from *CR1*, whilst for the EP-16 polymer electrolyte, the experimental data show significantly lower fill factors than that predicted by the model calculations, confirming significant efficiency losses due to charge recombination to dye cations. Note that the deviation from model calculations in Figure 8.4 is observed even at low light intensities, confirming these deviations can not result from series resistance losses.

It can be concluded that the improved I_{sc} and *ff* observed for the EP-50 polymer electrolyte originate from faster dye cation re-reduction by iodide ions (*RG*). These faster dynamics may also result from the less aprotic nature of EP-50 compared to EP-16 and PEO. Pelet et al. have previously reported faster re-reduction dynamics for less aprotic electrolytes, assigned to a more positive TiO_2 surface charge [18]. Alternatively the faster dynamics may result from a higher iodide mobility in this polymer electrolyte due to the epi-chlorohydrin component resulting in a less packed polymer structure (Note that impedance conductivity measurements primarily depend upon cation rather than anion conductivity.)

8.4 Conclusion

In this study transient absorption spectroscopy has been employed to study electron transfer dynamics in dye sensitised solar cells employing a series of polymer electrolytes, and correlated with device current / voltage characteristics. Kinetic competition between charge recombination with dye cations and regeneration of the dye ground state by the polymer electrolyte has been shown to be critical in determining device efficiency.

The observation of kinetic competition between *CR1* and *RG* reported herein contrasts with the conclusion of the previous study of DSSCs employing a polymer electrolyte without added plasticizers. In the previous study [7], the absence of plasticizers resulted in a lower ionic conductivity, resulting in accumulation of I_2^- and I_3^- species in the film pores under illumination, and therefore causing recombination losses to the redox electrolyte *CR2* to limit device performance.

A study has previously demonstrated that careful consideration of the correlations between charge separation and recombination are critical to optimisation of the efficiency of dye sensitised solar cells, with optimisation requiring the minimisation of 'kinetic redundancy' within the device [19]. The study has focused on the correlation between dye regeneration and charge recombination to the redox electrolyte in liquid electrolyte devices. The study emphasises that the use of higher viscosity, more solid state electrolytes may result in the secondary charge step, electron transfer from the electrolyte to the dye cation, also playing a key role in determining device efficiency.

8.5 References

1. Bach, U., et al., *Solid-state dye-sensitized mesoporous TiO2 solar cells with high photon-to-electron conversion efficiencies.* Nature, 1998. 395(6702): p. 583-585.

2. Schmidt-Mende, L., et al., *Effect of hydrocarbon chain length of amphiphilic ruthenium dyes on solid-state dye-sensitized photovoltaics.* Nano Letters, 2005. 5(7): p. 1315-1320.

3. Kruger, J., et al., *High efficiency solid-state photovoltaic device due to inhibition of interface charge recombination.* Applied Physics Letters, 2001. 79(13): p. 2085-2087.

4. Oregan, B. and D.T. Schwartz, *Efficient dye-sensitized charge separation in a wide-band-gap p-n heterojunction.* Journal of Applied Physics, 1996. 80(8): p. 4749-4754.

5. Oregan, B. and D.T. Schwartz, *Efficient Photo-Hole Injection from Adsorbed Cyanine Dyes into Electrodeposited Copper(I) Thiocyanate Thin-Films.* Chemistry of Materials, 1995. 7(7): p. 1349-1354.

6. Nogueira, A.F., J.R. Durrant, and M.A. De Paoli, *Dye-sensitized nanocrystalline solar cells employing a polymer electrolyte.* Advanced Materials, 2001. 13(11): p. 826-+.

7. Nogueira, A.F., et al., *Electron transfer dynamics in dye sensitized nanocrystalline solar cells using a polymer electrolyte.* Journal of Physical Chemistry B, 2001. 105(31): p. 7517-7524.

8. Nogueira, A.F., C. Longo, and M.A. De Paoli, *Polymers in dye sensitized solar cells: overview and perspectives.* Coordination Chemistry Reviews, 2004. 248(13-14): p. 1455-1468.

9. Durr, M., et al., *Low-temperature fabrication of dye-sensitized solar cells by transfer of composite porous layers.* Nature Materials, 2005. 4(8): p. 607-611.

10. Stathatos, E., et al., *Dye-sensitized photoelectrochemical solar cells based on nanocomposite organic-inorganic materials.* Journal of Photochemistry and Photobiology a-Chemistry, 2005. 169(1): p. 57-61.

11. Stathatos, E., et al., *A quasi-solid-state dye-sensitized solar cell based on a sol- gel nanocomposite electrolyte containing ionic liquid.* Chemistry of Materials, 2003. 15(9): p. 1825-1829.

12. Stergiopoulos, T., et al., *Binary polyethylene oxide/titania solid-state redox electrolyte for highly efficient nanocrystalline TiO2 photoelectrochemical cells.* Nano Letters, 2002. 2(11): p. 1259-1261.

13. Wang, P., et al., *A stable quasi-solid-state dye-sensitized solar cell with an amphiphilic ruthenium sensitizer and polymer gel electrolyte (vol 2, pg 402, 2003).* Nature Materials, 2003. 2(7): p. 498-498.

14. Montanari, I., J. Nelson, and J.R. Durrant, *Iodide electron transfer kinetics in dye-sensitized nanocrystalline TiO2 films.* Journal of Physical Chemistry B, 2002. 106(47): p. 12203-12210.

15. Haque, S.A., et al., *Flexible dye sensitised nanocrystalline semiconductor solar cells.* Chemical Communications, 2003(24): p. 3008-3009.

16. Lindstrom, H., et al., *A new method for manufacturing nanostructured electrodes on plastic substrates.* Nano Letters, 2001. 1(2): p. 97-100.

17. Green, A.N.M., et al., *Charge transport versus recombination in dye-sensitized solar cells employing nanocrystalline TiO2 and SnO2 films.* Journal of Physical Chemistry B, 2005. 109(25): p. 12525-12533.

18. Pelet, S., J.E. Moser, and M. Gratzel, *Cooperative effect of adsorbed cations and iodide on the interception of back electron transfer in the dye sensitization of nanocrystalline TiO2.* Journal of Physical Chemistry B, 2000. 104(8): p. 1791-1795.

19. Haque, S.A., et al., *Charge separation versus recombination in dye-sensitized nanocrystalline solar cells: the minimization of kinetic redundancy.* Journal of the American Chemical Society, 2005. 127(10): p. 3456-3462.

9

General conclusions and future work

In this thesis the quantitative relationship between material structure and device function in the dye sensitised photovoltaic solar cells (DSSCs) has been studied for the future development of DSSCs. This has been achieved by correlating the interfacial electron transfer dynamics of nanocrystalline TiO_2 film / sensitiser dye / hole conductor heterojunctions observed using nanosecond and millisecond transient absorption spectroscopy techniques, which were related to device current / voltage performance. Chapters 3 to 5 focus on the function of a range of dye sensitisers, which were synthesized based on the conventional ruthenium bipyrdyl dye, in liquid electrolyte DSSCs. In Chapter 6 and 7 studies of solid type DSSCs were directed towards the application of novel molecular and polymer hole transport materials as well as novel polymer electrolytes.

The carboxylic groups of ruthenium bipyridyl dyes have an important function in DSSCs, not only for anchoring the dye on to the surface of nanocrystalline TiO_2 particles, but also at determining the local pH environment, which can influence electron transfer dynamics. It was found from the study herein that the influence of dye protonation upon the performance of dye sensitised solar cells primarily derives from the influence of protonation upon the dye loading, rather from differences in the underlying electron transfer kinetics. It can be furthermore concluded that overloading of the TiO_2 film with sensitiser dye can result in lower device performance, resulting from a reduced yield of electron injection, suggesting that optimal dye loading is very crucial to device performance. Another suggestion from

these studies concerns the high potential of the least protonated dye, dye **3**. This dye can lead to modestly but significantly higher performance under matched dye loading condition. If this dye could be adsorbed onto TiO_2 at loading densities matching those of the most protonated dye, dye **1**, without significant aggregation, it should have the capability to overtake the performance of dye **1**.

A supermolecular sensitizer dye was studied by employing a ruthenium bipyridyl dye incorporating a secondary electron donor ligand in order to retard the dynamics of electron recombination, which is an unfavourable process for device performance. It was found that the increase in the distance between the TiO_2 surface and the dye cation results in an extremely long-lived charge-separated pair, with the slowest recombination dynamics (CR1) reported to date for such dye sensitised films, 0.7 s. This long lifetime correlates well with semi-empirical calculations of dye HOMO orbital positions. This dye can be expected to interface well with triarylamine-based hole conductors, making this sensitiser dye particularly attractive for applications in solid state dye-sensitised solar cells.

Interfacial electron transfer dynamics, including not only charge recombination but also regeneration dynamics, were correlated with device performance for a series of novel functional dyes with long alkyl chains. It was found that the regeneration reaction (*RG*) rapidly retards as the chain length is increased, and for chain lengths greater than C_{13} the regeneration (*RG*) is actually slower than recombination to the dye cation (*CR1*), implying that dye with C_{13} chains results in near optimal conditions in terms of kinetic competition, consistent with the observed trend in device I_{sc} data. This study addressed that the extension of the kinetic redundancy argument to the regeneration dynamics of the dye ground state suggesting the importance of scrutinising charge transfer dynamics in DSSCs to design all the reactions optimised for high device performance.

For solid state DSSCs, interfacial charge transfer in TiO_2 / dye / HTM heterojunctions have been studied by employing novel triarylamine hole conductors, using TAS and I/V characterization techniques to determine the yields for interfacial

hole transfer and the extent of pore penetration. Pore penetration of the triarylamine hole conductors was found to be sub-optimal and non-uniform, with best hole transfer yields obtained for the smaller, low-molecular weight hole conductors. It was found that local electrostatic interactions at the TiO_2 / dye / HTM interface could cause the driving force $\Delta G_{(dye\text{-}HTM)}$ for interfacial hole transfer to be smaller than anticipated on the basis of the individual ionization potentials of the dye and the hole conductor, resulting in losses in the hole transfer yield. Although it can be possible that hole mobility is a critical factor in determining solid-state device performance, from the present findings the optimization of pore filling as well as the control of interfacial energetics should be primary considerations in the pursuit of alternative solid-state hole conductors.

The successful fabrication of a nanostructured TiO_2 / dye / polymer / molecular hole transport multilayer structure was done by employing organic semiconducting materials with different HOMO energy levels to achieve an energetic redox cascade at a dye sensitised nanostructured interface. Such solution processing of organic multilayer nanostructures is a key challenge for a range of organic electronic and optoelectonic devices, including not only dye sensitised solar cells, but also polymer based devices and light emitting diode. The application of this strategy to the optimisation of solid state dye sensitised solar cells is currently on going.

A series of studies on electron transfer dynamics in dye sensitised solar cells employing a series of polymer electrolytes were undertaken. Significantly slower regeneration (*RG*) was observed, consistent with the suggestion that the shift towards more viscous, redox electrolytes increases the possibility that dye cation re-reduction by the redox electrolyte (*RG*) may no longer compete effectively with recombination pathway (*CR1)*. As a consequence, charge recombination to dye cations may become critical in limiting device efficiency. It can furthermore be concluded that the improved I_{sc} and *ff* observed for a polymer (EP-50) electrolyte originate from faster dye cation re-reduction by iodide ions (*RG*). These faster dynamics may also result from the less aprotic nature of EP-50 compared to the other polymer electrolytes. The study reported here emphasises that the use of higher viscosity, more solid state

electrolytes may result in the secondary charge step, electron transfer from the electrolyte to the dye cation, also playing a key role in determining device efficiency.